Deposit & Copying of Thesis Declaration

UNIVERSITY OF CAMBRIDGE

Please note that you will also need to bind a copy of this Declaration into your final, hardbound copy of thesis - this has to be the very first page of the hardbound thesis.

1	Surname (Family Name)	Forenames(s)	Title
	Kelly	Elaine	Ms.

2	Title of Thesis as approved by the Degree Committee
	Self-Assembly of Azobenzene Photosurfactants and the Relationship with Macroscopic Properties

In accordance with the University Regulations in *Statutes and Ordinances* for the PhD, MSc and MLitt Degrees, I agree to deposit one print copy of my thesis entitled above with the Secretary of the Postgraduate Committee who shall deposit the thesis in the University Library under the following terms and conditions:

1.   Thesis Author Declaration

I am the author of this thesis and hereby give the University the right to make my thesis available in print form as described in 2. below.

My thesis is my original work and a product of my own research endeavours and includes nothing which is the outcome of work done in collaboration with others except as declared in the Preface and specified in the text. I hereby assert my moral right to be identified as the author of the thesis.

The deposit and dissemination of my thesis by the University does not constitute a breach of any other agreement, publishing or otherwise, including any confidentiality or publication restriction provisions in sponsorship or collaboration agreements governing my research or work at the University or elsewhere.

2.   Access to Dissertation

I understand that one print copy of my thesis will be deposited in the University Library for archival and preservation purposes, and that, unless upon my application restricted access to my thesis for a specified period of time has been granted by the Postgraduate Committee prior to this deposit, the thesis will be made available by the University Library for consultation by readers in accordance with University Library Regulations and copies of my thesis may be provided to readers in accordance with applicable legislation.

| 3	Signature		Date
	Elaine Kelly		02/12/21

Corresponding Regulation

Before being admitted to a degree, a student shall deposit with the Secretary of the Postgraduate Committee one copy of his or her hard-bound thesis, in a form approved by the Committee. The Secretary shall deposit the copy of the thesis in the University Library where, subject to restricted access to the thesis for a specified period of time having been granted by the Postgraduate Committee, it shall be made available for consultation by readers in accordance with University Library Regulations and copies of the thesis provided to readers in accordance with applicable legislation.

Self-Assembly of Azobenzene Photosurfactants and the Relationship with Macroscopic Properties
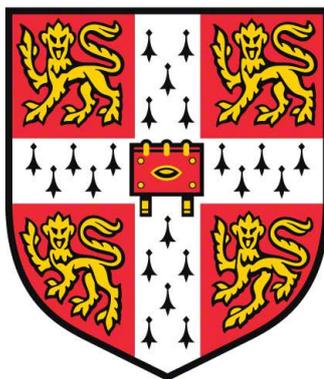
Elaine Kelly

King's College

Department of Materials Science & Metallurgy

University of Cambridge

This thesis is submitted for the degree of

Doctor of Philosophy

September 2021

Declaration

This thesis is the result of my own work and includes nothing which is the outcome of work done in collaboration except as declared in the preface and specified in the text.

It is not substantially the same as any work that has already been submitted before for any degree or other qualification except as declared in the preface and specified in the text.

It does not exceed the prescribed word limit for the Faculty of Physics & Chemistry Degree Committee.

_____

Elaine Kelly

Abstract

Self-Assembly of Azobenzene Photosurfactants and the Relationship with Macroscopic Properties
Elaine Kelly

Azobenzene photosurfactants (AzoPS) demonstrate the combined ability to change their shape upon irradiation with light and to self-organise into polymolecular assemblies. Photoisomerisation changes the polarity and shape of the surfactant on demand, which has led to the exploration of these materials in a diverse range of applications. The interplay between these properties also affects the concentration-dependent self-assembly of azobenzene photosurfactant into micelles.

This thesis focuses on four non-ionic azobenzene photosurfactants, which have been systematically varied in terms of their structure to study their self-assembly behaviour as a function of molecular structure, isomeric form, concentration, temperature and applied shear. The reciprocal effect of self-assembly behaviour on macroscopic properties such as viscosity, viscoelasticity, optical anisotropy and soft-templating ability is also investigated, emphasising how control over self-assembled structure can be used to modulate key properties and applications. In general, non-ionic photosurfactants have been less studied compared to their ionic counterparts and there are very few reports of their behaviour under shear, formation of lyotropic liquid crystal phases and use as templating agents. In this work, small-angle scattering is used extensively to probe the shape and dimensions of the self-assembled surfactant aggregates in solution. It will become apparent this is a key technique in the characterisation of dynamic and soft matter systems.

Chapter 3 of this thesis will focus on the dynamic self-assembly behaviour of two AzoPS under photoisomerisation, with an initial study on the flow behaviour. Chapter 4 will take a more detailed look into the relationship between the self-assembled structure and flow behaviour of an AzoPS, using combined rheology and small-angle scattering measurements. In Chapter 5, the formation of lyotropic liquid crystal phases by all four AzoPS as a function of concentration, temperature and isomeric form, will be investigated, and binary concentration-temperature phase diagrams for each AzoPS constructed. In Chapter 6, the ability of AzoPS to act as soft-templating agents to form porous titania nanoparticles will be proven, along with an investigation on the effect of template structure and irradiation conditions on the photocatalytic ability of the product titania. Finally, conclusions will be drawn on the basis of the above results, along with a discussion of the evolution of the field during the time this work took place, with signposting for potential future work.

Acknowledgements

This thesis would not have been possible without the support of many people, the most significant of whom I hope to remember to thank here.

Firstly, to my supervisor Dr Rachel Evans, thank you so much for your support and care over the past (many!) years. I am truly grateful for your guidance, insight and friendship. It has been such a pleasure working with you and I'm glad to have been a part of the Evans Group.

Thanks also to the members of the Evans Group, past and present. From the original surfactant duo, Camille and Judith, whose guidance and wisdom I have consistently relied on, to the current group members. Thank you Tom, Morton, Kieran, Mike, Nell, Abi, Bolong, Bethan, Bea, Shomik and Anne for your support, help and insight, it's been really great to get to know you all. In particular, thank you Kieran for being my chauffeur for various excursions to the sea-side and picturesque English villages, as well as providing a loving home for my former plants. Thank you Tom for introducing me to the best burgers of my life and to Morton for his friendship and funny conversations. You both made me feel really welcome when it was just the three of us in the beginning! Mike, you've improved my lab confidence and organic chemistry capabilities by an order of magnitude, thank you for sharing your wisdom! Thanks to Bolong for sharing my love of different kinds of tea, and Bea for picking up the mantle of AzoPS life. Thank you Bethan for adopting Magnus and Nell for her positivity and good company. Special thanks also to Angelika, Jeronimo, Adarsh and Andrew, for their company pre-covid. We had great pub trips, lunch-breaks and burrito endeavours together! I also want to thank Bill and Drew, former housemates and forever BikeGang. You are both amazing friends and I'm glad we got the chance to live together.

I owe a great deal of thanks to the technical and administrative staff in the Department of Materials Science & Metallurgy, in particular to Nicola Daily for her help with all things administrative in the group, to Mary Vickers and Andrew Moss for X-ray support, Dr Giorgio Divitini for his help with TEM, Dr Cate Ducati for her help with SEM and Sue Gymer to her help with all things calcination. Thank you also to Jan and Nana in the tea-room, particularly for giving our office a head start on any free coffee and snacks! This project relied on help from people across different departments, and to that end thank you to Dr Sian Dutton, Dr Niamh Willis-Fox, Andrew Mason, Dr David Fairen-Jiminez, Dr David Madden and Dr Ceren Çamur. Some of the work in this thesis is the result of experiments outside of Cambridge and as such I would like to thank Dr Judith Houston (beamtime scientist version), Dr Nathan Cowieson and Dr Katie Weigandt for their help with many different beamtimes.

Finally, thank you to my friends, family and cats, particularly to my parents for their continuous support. Most importantly, I would like to thank my partner, Friedrich, for being in equal parts a source of motivation and distraction.

Table of Contents

Chapter 4 –Probing the Structure-Flow Relationship of an AzoPS using RheoSANS

Chapter 5 – Formation of Light-Responsive Lyotropic Liquid Crystal Phases

Chapter 6 – AzoPS as Templating Agents for Photocatalytic Titania

List of Symbols

a_0 – Equilibrium Area of Surfactant Head Group

A_f – Alignment Factor

B – Full-Width Half-Maximum

C - Concentration

D – Diffusion Coefficient

d – Inter-Planar Distance (crystallography)

d – Periodicity (LLC phases)

D_H – Hydrodynamic Diameter

G' – Storage Modulus

G'' – Loss Modulus

G_0 – Plateau Value of Storage Modulus

H – Hexagonal Phase (LLC)

h – Plank's constant

I – Intensity

I_0 – Isotropic Phase (Micellar Solution)

k – Rate Constant (kinetics)

k/s – Kubelka-Munk function

k_b – Boltzmann Constant

L – Length (cylinder)

L_c – Contour Length (wormlike micelle)

l_c – Surfactant Tail Length

L_K – Kuhn Length (wormlike micelle)

L_α – Lamellar Phase

L_β – Lamellar Phase

n – Non-bonding electrons (electronic transition)

P – Packing Parameter

q – Scattering Vector

r – Radius (cylinder)

R – Reflectance

R_{CS} – Cross-Sectional Radius

T – Temperature

t – Time

V – Cubic Phase (LLC)

v – Volume of Surfactant Tail

γ_c - Critical Shear Rate

δ – Lamellar Membrane Thickness

ε – Molar Absorptivity Coefficient

η – Viscosity

η^* - Complex Viscosity

η_0 – Zero-Shear Viscosity

θ – Bragg Angle

λ – Wavelength

ν – Frequency

π – Pi Bonding Orbital

π^* - Pi Anti-Bonding Orbital

τ – Average Crystallite Size

τ_b – Breaking Time

τ_R – Relaxation Time

τ_{rep} – Reptation Time

ϕ – Volume Fraction

ω – Angular Frequency

ω_c – Crossover Frequency

χ^2 – Goodness-of-Fit Parameter

Abbreviations

AzoPS – Azobenzene Photosurfactant(s)

AzoTAB – Azobenzene Trimethylammonium Bromide

2D – 2-Dimensional

3D – 3-Dimensional

BET – Brunauer-Emmett-Teller

CIF – Crystallographic Information Framework

CMC – Critical Micelle Concentration

CTAB – Cetyltrimethylammonium bromide

DCM – Dichloromethane

DFT – Density Functional Theory

DLS – Dynamic Light Scattering

DRUV – Diffuse Reflectance UV-Vis

DSC – Differential Scanning Calorimetry

EC – Elliptical Cylinder

EISA – Evaporation-Induced Self-Assembly

FC – Flexible Cylinder

FEC – Flexible Elliptical Cylinder

FTIR – Fourier Transform Infra-Red Spectroscopy

HDA – Hexadecylamine

JCNS – Jülich Centre for Neutron Science (Germany)

LED – Light-Emitting Diode

LLC – Lyotropic Liquid Crystal

LVR – Linear Viscoelastic Range

NIST – National Institute for Neutron Science (U.S.A)

NMR – Nuclear Magnetic Resonance Spectroscopy

PDI – Polydispersity Index

POM – Polarised Optical Microscopy

PSS – Photostationary State

PSD – Pore-Size Distribution

RBF – Round-Bottomed Flask

SANS – Small-Angle Neutron Scattering

SAXS – Small-Angle -X-ray Scattering

SEM – Scanning Electron Microscopy

SDT - Simultaneous Differential Scanning Calorimetry-Thermogravimetric Analysis

TEM – Transmission Electron Microscopy

TGA – Thermogravimetric Analysis

TR-SANS – Time-Resolved Small-Angle Neutron Scattering

TR-SAXS – Time-Resolved Small-Angle X-ray Scattering

TTIP – Titanium (IV) Isopropoxide

UV – Ultraviolet

VSANS – Very Small-Angle Neutron Scattering

WLM – Wormlike Micelle

XRD – X-ray Diffraction

Chapter 1

Introduction

1.1   Introduction

Stimuli-responsive materials that significantly alter their behaviour and properties on-demand are fascinating, often elegantly highlighting cause and effect between initially disparate entities, for example, relationships between temperature, pH and electromagnetic field with volume, conformation and colour. Such materials emphasise how the environment can determine the material's behaviour, through the domino-effect of changes in physicochemical properties ultimately altering the bulk system behaviour. This effect is often non-linear, with small changes in the environment precipitating a huge change in the material properties, facilitating interesting and useful phenomena such as locomotion, sensing and controlled release.

Examples of adaptability to the environment[1-4] and non-linear response to a stimulus are abundant in the natural world,[5,6] but their replication remains much sought after in scientific research. As well as representing a sort of cooperative Rube Goldberg machine,[a] fascinating to construct in its own right, stimuli-responsive materials also offer the possibility of developing new technologies and innovation, such as artificial muscles,[7-9] adaptive wound dressings[10,11] and controlled delivery of small molecules.[12-14] Soft matter systems, such as surfactants, have a lot of potential in this regard as their dynamic self-association makes them extremely sensitive to changes in their environment. Surfactants are ubiquitous to many industries as foaming, dispersing, emulsifying and wetting agents. Their usefulness stems from their amphiphilic nature; they possess both hydrophobic and hydrophilic components on the same molecule. This duality imparts surfactants with interesting properties, such as surface activity and self-assembly. To create stimuli-responsive materials using surfactants, significant changes to the key properties governing surfactant behaviour (conformation, polarity) need to be induced.

Stimuli-responsive materials of particular interest are simple, reversible, single-component systems with well-defined dimensions and morphologies and a rapid response to the stimulus. Specifically, light is a desirable stimulus as it is non-invasive with a high degree of spatiotemporal resolution, remote application and tunability.[15,16] Azobenzene, a simple light-responsive molecule, offers the possibility to create reversible, stimuli-responsive systems.[7,17] Subsequently, azobenzene has been integrated into many dynamic systems based on non-covalent interactions, particularly in the area of supramolecular chemistry.[18-20] Azobenzene-based systems show potential in a myriad of applications, for example, molecular machines,[7,21] locomotion[22] and actuators.[23] Azobenzene has a natural harmony with surfactants in that it changes its key properties

---

[a] a contraption which performs a series of simple tasks as a chain reaction.

of polarity and conformation in response to light. Using light, it is possible to photoisomerise azobenzene between the linear, non-polar *trans*-isomer and the bent, polar *cis*-isomer[24,25] (Figure 1.1). Therefore, integration of azobenzene with surfactants allows control over the parameters essential to surfactant behaviour to be achieved. It becomes possible to tune the conformation and polarity of the surfactant using light *via* photoisomerisation of the azobenzene. In theory, this can create 'on' and 'off' states for the macroscopic behaviours of the surfactant, *e.g.,* foaming, emulsifying, viscosity.

The integration of azobenzene with surfactants creates a class of materials known as *azobenzene photosurfactants* (AzoPS), which change their conformation and dipole moment upon photoisomerisation between *cis*- and *trans*-isomers.[26] As well as light triggering key changes in physicochemical properties, causing a cascade effect on self-assembly and macroscopic properties, AzoPS create a novel type of surfactant. The inclusion of a bulky, aromatic azobenzene group challenges current theories and frameworks used to understand surfactant behaviour, many of which were proposed with simple alkyl surfactants in mind, *e.g.* the *packing parameter* concept. AzoPS offer new breadth to an established field, by reaffirming conventional knowledge through the impact of photoisomerisation on physicochemical and bulk system properties of surfactants (surface tension, self-assembly, viscosity), as well as developing the theoretical frameworks used to predict and understand surfactant systems. AzoPS push the established boundaries of surfactant structures in terms of molecular conformation and composition.

AzoPS also offer the possibility to make existing surfactant technologies responsive to light and have been used in areas such as micellar catalysis,[27] microfluidics,[28,29] DNA compaction.[30–32] and foam-dyeing processes.[33,34] The most common AzoPS structures are cationic azobenzene trimethylammonium bromide surfactants (AzoTABs), whereas neutral AzoPS have been much less studied and integrated with applications. In this work, azobenzene will be embedded into the hydrophobic tail of non-ionic tetraethylene glycol surfactants (Figure 1.1). Tetraethylene glycol AzoPS have not been studied extensively,[35,36] despite their non-photoresponsive analogues receiving widespread scientific interest.[37–41] It is hoped this head group will facilitate interesting self-assembly behaviour through hydrogen bonding interactions, as well as neutral AzoPS having the benefit of a much lower critical micelle concentration than their charged counterparts. This means that, in general, less surfactant material is needed for a given application.
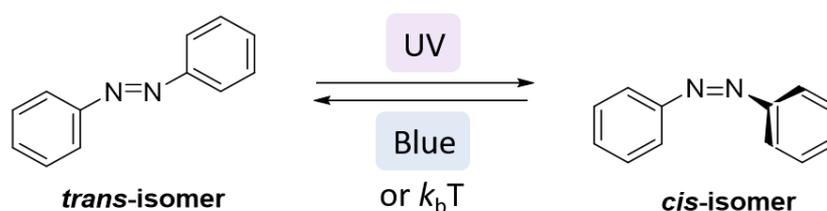
Figure 1.1. Azobenzene isomerises between the pseudo-stable *cis* and thermodynamically stable *trans*-isomers upon irradiation with UV or blue light, respectively. Reverse isomerisation to the *cis*-isomer can also be triggered with heat. The *trans*-isomer is planar, linear with a dipole moment of 0 D, while the *cis*-isomer is non-planar, bent and has a dipole moment of 3 D.[42,43]

In this work, the self-assembly behaviour of four non-ionic AzoPS will be investigated, along with the relationships between self-assembly and macroscopic system properties. Initially, the dynamic self-assembly behaviour of one model AzoPS under photoisomerisation will be probed by combining small-angle neutron scattering (SANS) with UV-Vis absorption spectroscopy. It will become apparent that light can cause drastic changes to the viscosity and viscoelastic behaviour of AzoPS systems *via* changes to the self-assembled structure. The flow behaviour and self-assembled structure under shear will also be examined in detail using combined rheology and SANS. The creation of light-responsive *lyotropic liquid crystal* (LLC) phases in AzoPS solutions will also be investigated; reports of LLC phases for AzoPS are still relatively uncommon. Having consolidated an understanding of the self-assembly behaviour of the AzoPS and how self-assembled structure impacts macroscopic properties, focus will then be turned to potential applications of these molecules. In particular, AzoPS will be trialled as photo-deformable templates for the creation of mesoporous titania nanoparticles. In the next section, a brief summary of the fundamentals of azobenzene and surfactant behaviour will be provided. This will be followed by a literature review of the relevant research required to contextualise the results and a more detailed presentation of the aims of the thesis.
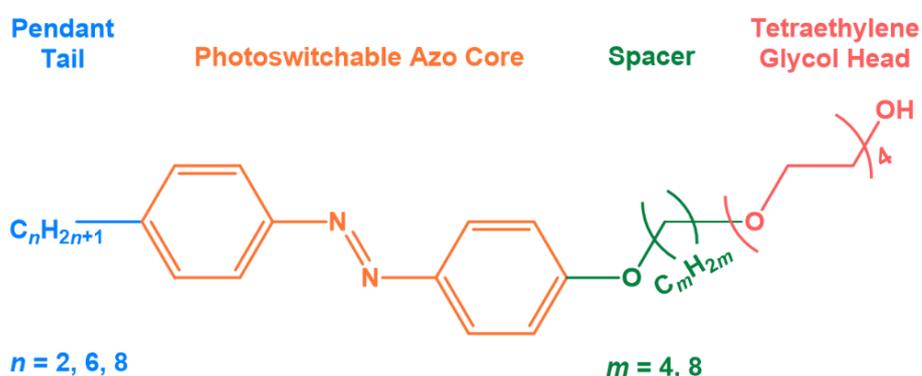
Figure 1.2. Molecular structure of the four tetraethylene glycol AzoPS used in this work. The number of carbons in the pendant tail was varied as 2, 6, 8, while the carbons in the spacer varied as either 4 or 8. Most AzoPS follow this general structure, with potential for varying the head group (*e.g.* trimethylammonium bromide, fewer or more ethylene glycol repeat units, betaine group), as well as the length of the carbon tail and location of the azobenzene group within the tail.

1.1.1 Photochemistry of Azobenzene

As aforementioned, azobenzene can exist in one of two isomeric forms: *cis* or *trans*. The latter is thermodynamically more stable than the *cis*-isomer by about 50 kJ mol^{-1} and so predominates at thermal equilibrium.[44] Importantly, photoisomerisation can still occur upon incorporation of the azobenzene group into an amphiphilic surfactant molecule.[45,46] The isomers can be distinguished using UV-Vis absorption spectroscopy; in water, the *trans*-isomer absorbs strongly in the UV region with an absorption band centred around 320 nm corresponding to the symmetry allowed $\pi\rightarrow\pi^*$ transition ($S_2\leftarrow S_0$ excitation, Figure 1.3).[25] Upon irradiation with UV light the *cis*-isomer is formed, the UV-Vis absorption spectrum of which displays a less intense $\pi\rightarrow\pi^*$ transition band in the UV region, centred around 270 nm, and a second absorption band at 450 nm, corresponding to the symmetry forbidden $n\rightarrow\pi^*$ transition ($S_1\leftarrow S_0$).[25,44,47] The *Laporte selection rule* states that there must be a change in symmetry upon an electronic transition, meaning that transitions can only occur between wavefunctions of different symmetry, *e.g.* $\pi\rightarrow\pi^*$ is allowed, while $n\rightarrow\pi^*$ is forbidden. The non-planarity of the *cis*-form allows the previously Laporte-forbidden $n\rightarrow\pi$ transition to occur. The *trans*-form can be recovered by irradiation with blue light or by leaving the molecule in the dark for several hours to allow thermal relaxation to occur. The mechanism of isomerisation is disputed, with solvent choice, irradiation wavelength, temperature and nature of substituents all playing a role in the isomerisation pathway taken.[47]

It should be noted that for the parent azobenzene chromophore it is usually not possible to obtain 100% conversion from the *trans*- to the *cis*-isomer due to the overlap of their respective absorption spectra.[48] However, the absorption spectra can be manipulated through the inclusion of substituents.[49] Similarly, the absorption maximum of AzoPS will red-shift relative to pure azobenzene, the extent of which depends on the nature of any substituent, *i.e.* electron-donating or withdrawing. Upon UV irradiation and photoisomerisation, typically a *photostationary state* (PSS) of *cis*-azobenzene is obtained, which consists of an assembly of mostly *cis*-isomers.[50] The exact composition of the PSS depends on factors such as solvent, irradiation wavelength, temperature and molecular structure.[47,48] Similarly, 100% *trans*-azobenzene generally cannot be recovered optically. When irradiated with blue light a second PSS is formed, consisting of majority *trans*-isomers.[51,52] An assembly of 100% *trans*-isomers is recovered by thermal relaxation.[48,53]
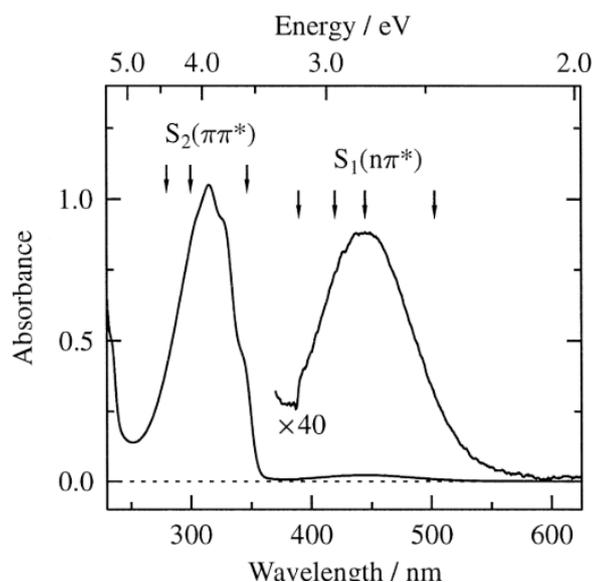
Figure 1.3. *Trans* and *cis*-azobenzene can be distinguished on the basis of their absorption spectra. Figure shows the UV-Vis absorption spectra of *trans*-azobenzene in hexane. Two peaks are evident, at 315 and 445 nm, corresponding to the $\pi{\rightarrow}\pi^*$ and $n{\rightarrow}\pi^*$ transitions, respectively. Figure reproduced from reference 25.

1.1.2 Self-Assembly of Surfactants

Having been introduced to the fundamentals of azobenzene and its spectroscopy, the next crucial fundamental is the self-assembly behaviour of surfactants; both are essential to the behaviour of AzoPS. Surfactants tend to self-assemble in solution (typically aqueous) into aggregates known as *micelles* (Figure 1.4). Understanding micelle formation is key to understanding the basic properties of surfactants so some time will be dedicated to the factors responsible. Micelles are formed primarily through the *hydrophobic effect* at concentrations above the *critical micelle concentration* (CMC). The hydrophobic effect is entropically driven and describes the interaction between water and a non-polar solute, in this case the surfactant. The introduction of a non-polar entity into water results in a decrease of entropy, as the water molecules structure themselves around the non-polar solute (*cf.* clathrate cages).[54,55] As a result, the creation of a cavity in the water to house the non-polar solute increases the free energy of the system, meaning the hydrophobic effect depends strongly on the area of contact between the water and the non-polar solute. The consequence is that surfactants tend to migrate to interfaces to minimise the free energy of the solution. The distortion of the water structure is also minimised through aggregation into micelles above the CMC, with polar head groups oriented outwards and hydrophobic tails in the micelle interior. The long-range hydrophobic effect facilitates the aggregation of surfactant alkyl chains, while at shorter distances repulsive forces (*e.g.* electrostatic, steric) between the hydrated surfactant head groups prevent large scale crystal formation or phase separation.[56,57] At the CMC, these two opposing forces are balanced and it becomes favourable for micelles to form.[58] As

there are no chemical bonds involved, the surfactant monomers in the micelles are in equilibrium with monomers in the bulk solution.[58] The CMC is identified by a change in the physicochemical properties of the system, such as surface activity and turbidity, and so can be measured through surface tensiometry or dynamic light scattering.[59,60]

Generally, the size and shape of the surfactant monomers determines the structure of the micelle adopted, with either spheres, cylinders or sheets typically formed. The key structural parameters for the monomers are the alkyl tail volume (v), the equilibrium surface area of the polar head group (a) and the critical alkyl tail length (l_c). It is worth noting that the above parameters presume linear alkyl chain surfactants, rather than surfactants with more complex or bulky conformations.[61,62] From simple geometric considerations it is possible to derive a relationship between the values required for these dimensions and the preferred shape adopted. For example, if a spherical micelle has an inner hydrophobic volume, V, this can be considered as Nv where N is the aggregation number and v is the alkyl tail volume of the monomer. Therefore, $Nv = 4\pi r^3/3$, where r is the radius of the spherical micelles and is roughly equivalent to the alkyl tail length, l_c. Similarly, the total surface area, A, can be considered as Na, which is $4\pi l_c^2$ for a spherical micelle. This leads to the relationship of $v/al_c = 1/3$. The relationship between v, a and l_c is called the *packing parameter*, P.[61]

$$P = \frac{v}{al_c}$$
(Eq. 1.1)

As derived above when $P < 1/3$, spherical micelles are formed. A similar approach can be used for cylinders and spheres, leading to the result that for $1/3 < P < 1/2$ cylindrical micelles are formed and for $1/2 < P < 1$ lamellar sheets tend to form.[61]
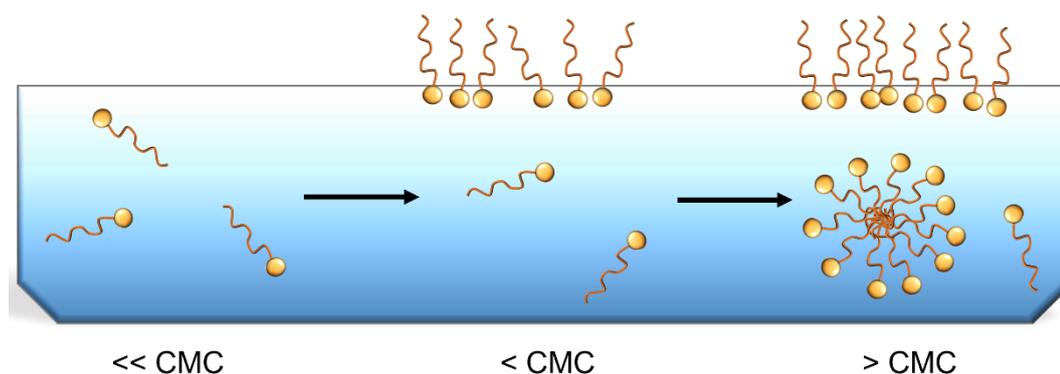

Figure 1.4. Surfactants have concentration-dependent self-assembly behaviour. Below the CMC, surfactant monomers are freely dispersed in solution, adsorbing to the surface with increasing concentration. Above the CMC, surfactant monomers in solution begin to form micelles. These micelles exist in equilibrium with monomers adsorbed to the surface.

Pertinent to this work is the *wormlike micelle* (WLM), a subset of the cylindrical micelle morphology. WLMs are elongated, flexible, self-assembled structures which entangle to form a dynamic network.[63,64] Due to the constant breaking and reforming of this network, WLMs are referred to as 'living polymers'.[65–67] WLMs are typically characterised in terms of four parameters (Figure 1.5): radius of gyration, R_g, contour length, L_C, Kuhn length, L_K, and cross-sectional cylinder radius, R_{CS}.[68,69] R_g indicates the size of the micellar aggregate,[69] L_C is the overall length of the WLM and ranges from several nanometres to micrometres.[69] L_K gives a measure of the distance over which WLM segments can be considered rigid,[70] and R_{CS} gives the cross-sectional radius of the constituent rigid cylinders. The structure of WLMs imparts them with interesting rheological behaviour. For example, WLMs in aqueous solution often have viscosities orders of magnitude higher than that of pure water.[67,71,72] Above a certain critical shear rate, WLMs frequently present non-Newtonian *shear-thinning behaviour*, whereby the viscosity of the WLM solution decreases as the applied shear is increased. This is due to the micelle chains aligning in the direction of the applied force.[73] The dynamic nature of the micelle network also grants viscoelastic behaviour to the WLM solution. Similar to polymer solutions, the viscoelasticity is a result of chain entanglement. It is well established that this behaviour can be described by a Maxwell model of a spring, with Hooke constant G_0.[65,74] From this, the *storage* and *loss moduli*, $G'(\omega)$ and $G''(\omega)$, respectively arise. G' and G'' (Equations 1.2, 1.3) can be measured through oscillatory rheology measurements, where a sinusoidal deformation is applied to the sample and the response measured:

$$G'(\omega) = \frac{\omega^2 \tau_R^2 G_0}{1+\omega^2 \tau_R^2}$$

(Eq. 1.2)

$$G''(\omega) = \frac{\omega \tau_R G_0}{1+\omega^2 \tau_R^2}$$

(Eq. 1.3)

where ω is the frequency of the applied deformation, τ_R is the relaxation time of the WLM and G_o is the plateaus modulus. A crossover from $G' < G''$ to $G' > G''$ with increasing frequency is consistent with viscoelastic, Maxwellian behaviour and is generally taken as a strong suggestion of wormlike micelles.[75–77] WLMs also have an additional breaking relaxation mechanism (τ_b) due to their constant breaking and reforming, unlike polymers, which can only relax *via* reptation (τ_{rep}) along their length.[65,74]
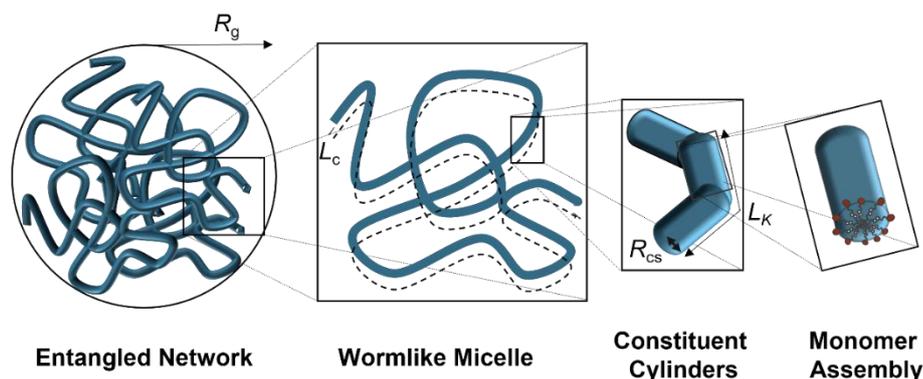
Figure 1.5. Pictorial representation of an entangled micelle network and a single wormlike micelle with radius of gyration, R_g, contour length, L_c, Kuhn length, L_K, and cross-sectional radius, R_{CS}.

1.1.3 Lyotropic Liquid Crystal Phases Formed by Surfactants

At higher concentrations, surfactants can also self-assemble to form a range of LLC phases. These are solvent-surfactant mesophases that have properties intermediate between liquids and crystals; they possess some long-range orientational order but the molecules also have molecular motion, allowing the liquid crystals to flow, albeit often with very high viscosities. By the reasoning that if the monomers are primary building blocks to forming micelles, the micelles themselves can be considered as secondary building blocks, whose size and shape control the liquid crystal structure.[78] Representative liquid crystal mesophases include *cubic phases*, (*I, V*) *hexagonal phases* (*H*) and *lamellar phases* (*L_α*) , either water-continuous (normal, identified by subscript 1) or surfactant-continuous (reversed, identified by subscript 2). These phases, their identification and how they relate to surfactant structure and properties, will be discussed in more detail below.

Cubic LLC phases consist of spherical micelles packed in a cubic lattice, such as body- or face-centred cubic. In some cases, bicontinuous or 'sponge-like' cubic phases can form (Figure 1.6).[46,79,80] Bicontinuous phases have a curvature intermediate between hexagonal and lamellar phases, with various mesh arrangements possible. Hexagonal LLC phases are cylindrical aggregates which arrange in a hexagonal packing array. It is possible for either normal H_1 or reverse H_2 hexagonal phases to be formed, depending on the concentration of the amphiphile and the solvent.[78,81] For a normal hexagonal phase, the surfactant tails are oriented inwards, forming the bulk of the cylinder, while the hydrophilic head groups are oriented outwards, in contact with the solution. In contrast, lamellar phase LLCs consist of surfactant molecules arranged as a planar bilayer (Figure 1.6). Typically the surfactant tails are oriented inwards to form a central hydrophobic region while the hydrophilic head groups form the interface with the aqueous solution. The lamellar phase can be described geometrically as a periodic stack, with a periodicity

d, of bilayer thickness, δ.[78,82,83] The most common lamellar phase is the fluid phase, L_α, but the gel phase, L_β, is also possible. The key difference between the two is the ordering of the hydrophobic chains within the bilayer. For the L_α phase, the hydrophobic chains are relatively fluid and disordered while for the L_β, phase the chains are ordered with the surfactants typically arranged with hexagonal symmetry.[84]

Cubic, hexagonal and lamellar mesophases have structures based on spherical, rod and bilayer micelles., respectively. In the first instance, it is useful to discuss LLC phases in terms of their intermicellar interactions, which will depend on the micelle shape and the packing efficiency/volume fraction of the micelles at high concentration. In general, a solution of spherical micelles will pack into cubic liquid crystals. The maximum volume fraction for close-packed spheres is 0.74;[85] at concentrations where this packing efficiency is exceeded, a change in packing will occur, typically to a hexagonal phase initially.[85] Likewise, cylindrical micelles will pack into a hexagonal liquid crystal array, the maximum close-packing fraction of which is 0.91,[85] upon which a change to either bicontinuous cubic or lamellar is most likely to occur. Finally, sheet-like micelles will pack into a lamellar phase, which has no maximum packing efficiency and has been observed for neat surfactant. At high surfactant concentration, reversed phases can be observed.[80,86] In this case, the surfactant forms the continuous medium, with water existing in small cavities within the phase. Generally, the trend with curvature is reversed for reverse phases, although a high degree of variability is possible for reversed phases.
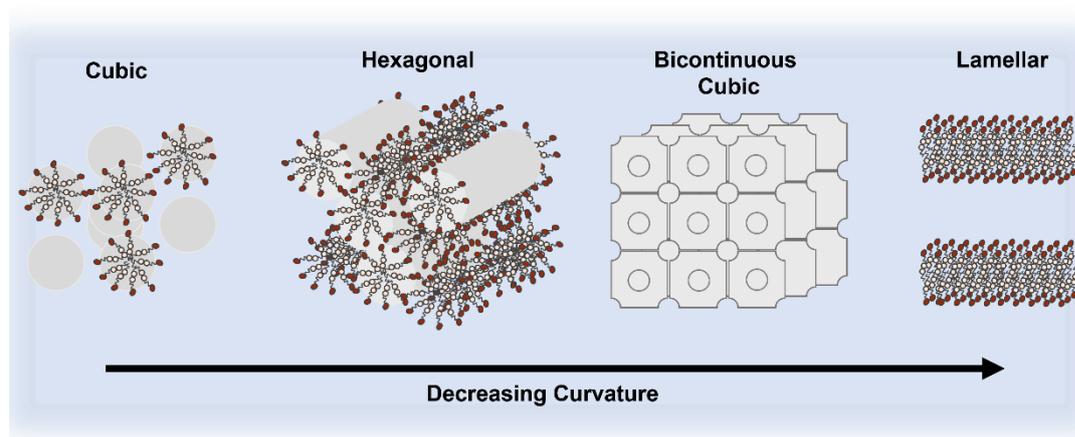
Figure 1.6. Schematic representation of possible lyotropic liquid crystal mesophases, arranged in order of decreasing spontaneous curvature. A cubic phase (*I*) is formed from spherical micelles arranged in a cubic-packing arrangement. A body-centred cubic arrangement is shown but a variety of packing types are possible. A hexagonal phase (*H*) is formed from cylindrical micelles packed in a hexagonal array. A bicontinuous phase (*Q*) is a second cubic phase, with various mesh arrangements possible. *Im3m* is shown here. The lamellar phase (*L*) is formed from micelles packed in a sheet-like arrangement.

Polarised optical microscopy (POM) can be used to characterise LLC phases. If, when viewed through crossed polars, the sample is anisotropic then it is implied that the sample is liquid crystalline with a non-cubic space group symmetry.[78] Cubic phases are optically isotropic so will appear dark between crossed polars.[39,87,88] The absence of any LLC phase formation will also appear dark. When present, the optical textures can be used to distinguish the phase formed (*e.g.* hexagonal or lamellar),[78] as each possesses characteristic textures and geometries.

Small-angle scattering (SAS) is also a useful technique to probe the self-assembly behaviour of surfactants, with the orientational order of LLC phases determined using small-angle X-ray scattering (SAXS). SAS is elastic scattering of either neutrons or X-rays off the nuclei or electron density in a sample.[89,90] SAS data are typically presented in terms of scattering intensity as a function of q, the *scattering vector* that corresponds to the change in momentum between the initial and final wavevectors. The scattering profile obtained can be analysed to give information about the size, shape and dimensions of the scattering bodies in solution, as well as the extent of any interparticle interactions.[89,90] Interference peaks can also be observed when long-range order is present and are used to characterise LLC phases.[86,91] For example, lamellar phases are often assigned from SAXS data on the basis of their interference peak repetitions; second, third and sometimes higher order reflections are present at integer multiples of the first order peak, q_0.[92,93]

1.1.4 Surfactants as Templating Agents

As well as spontaneous self-assembly in solution, surfactants can also interact with other species. This has resulted in their use as templating agents for the creation of porous of metal oxides.[94–98] Soft-templating to form mesoporous particles was first reported in 1992, with mesoporous silica (MCM-41) formed through a surfactant-mediated self-assembly approach.[99] This style of templating involves cooperative interactions between the surfactant species and inorganic precursor, driven by non-covalent interactions.[100–102] Mesoporous materials have pore sizes intermediate between micro- and macropores, generally 2 – 50 nm, which is the size range that surfactant micelles tend to form.[99,103,104] Metal oxide particles are formed through hydrolysis and condensation of the precursor material. During this synthesis, the added surfactant molecules form an ordered, self-assembled phase, interacting with the metal oxide precursors (typically $M(OR)_4$ where M is the (semi)-metal such as Si or Ti and R is an alkyl group) and intermediates.[98,100,105] The result is a metal oxide structure studded with self-assembled surfactant aggregates. The surfactant template is extracted, often through high-temperature calcination, resulting in a porous metal oxide product (Figure 1.7).[102,106]

The nature of the surfactant itself plays a significant role in the templating process. Depending on the surfactant charge, be it cationic, anionic or non-ionic, different interaction pathways with the metal oxide precursors and intermediates can occur.[102,106] Likewise, salinity and pH play a key role in determining the dimensions and quality of the porous product, with the former screening electrostatic interactions and controlling particle size, and the latter controlling the rates of hydrolysis and condensation, depending on the isoelectric point of the metal oxide species.[105–107] For example, a cationic surfactant used as a template for the formation of porous silica will experience stabilising electrostatic interactions between the cationic headgroup of the surfactant and the hydrolysed silica, $((^-O)_mSi(OR)_{4-m})$ deprotonated in a basic environment.[100,106] For the above scenario to proceed in an acidic environment, the electrostatic interaction would need to be mediated through an anionic counterion.[98] Many other factors also influence the synthesis, such as temperature, surfactant concentration and choice of solvent.[105–107]

The cooperative self-assembly method outlined above is not the only means to use surfactants as templates; liquid crystal templating is also possible. While the cooperative self-assembly method relies on simultaneous aggregation of the surfactant with the metal oxide reagents and intermediates to form an inorganic-organic composite phase, liquid crystal templating involves very high surfactant concentrations, such that ordered LLC phases are formed without the inorganic precursor materials.[97,99,108] This LLC phase is maintained upon addition of the metal precursors, which condense around the LLC network. As well as soft-templating using surfactants, porous materials can also be formed using hard templates (Figure 1.7). Hard templates include species such as silica spheres[109] or polystyrene beads[110] which facilitate the metal oxide material forming around the hard sphere. Upon removal of the hard template (by calcination or chemical etching), a porosity which is the 'negative' of the template is left in the material. [102,107]
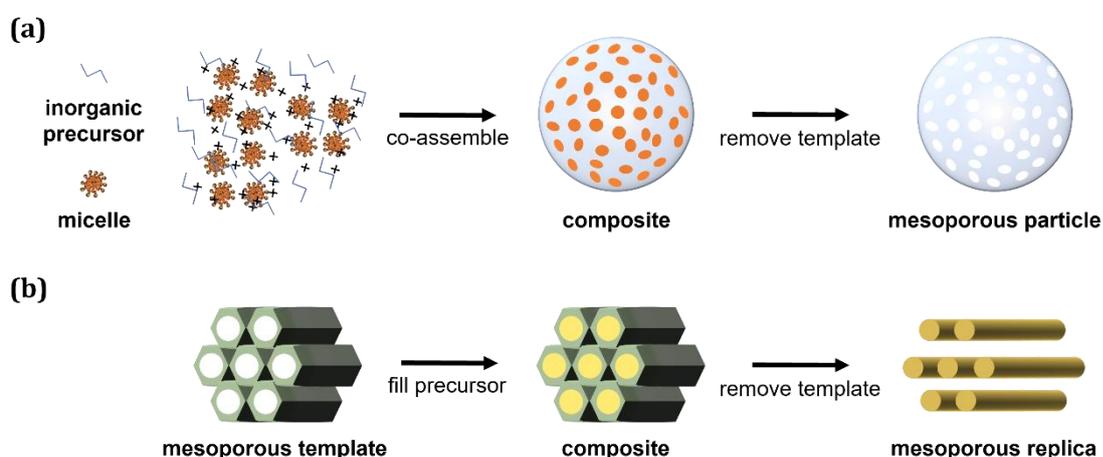

Figure 1.7. Mesoporosity can be created using soft- or hard-templating approaches (a) a schematic representation of soft-templating using a surfactant to form a mesoporous particle. (b) a schematic representation of hard templating to form a hexagonal array.

While silica initially attracted attention as a mesoporous material, a variety of metal and mixed oxide nanoparticles can be formed using surfactant templating, *e.g.* Ti, Zr, Al, Ta, W, Zn and Cu.[102,107] These materials have applications in catalysis,[111–113] sensing,[114,115] and adsorption.[116-118] Titanium dioxide is particularly interesting as it is photocatalytic and can be excited with UV light to produce electron-pairs[119] (Eq. 1.4). It is used in applications such as photocatalytic degradation of organic pollutants,[120–124] dye-sensitised solar cells,[125–127] and photolysis of water for hydrogen fuel production.[128,129] TiO_2 is also chemically stable, highly abundant, cheap to produce and with a low toxicity.[119] Upon reaction with water, the oxidising holes create hydroxyl radicals and can also create superoxide and hydrogen peroxide. These secondary radical species are highly oxidising and can be used to degrade organic contaminants and pollutants.[119,120,124]

$$TiO_2 + 2hv \rightarrow 2e^- + 2h^+ \hspace{3cm} \text{(Eq. 1.4)}$$

The photocatalytic activity of TiO_2 is strongly influenced by several parameters; templating TiO_2 allows control over the dimensions and porosity of the material which can be crucial to performance. In general, the desired properties of photocatalytic TiO_2 are: (1) a high surface area to increase access to catalytic sites; (2) a high porosity to allow reagents to diffuse into the particles and access reactive sites; (3) a high crystallinity to promote the formation, and prevent the recombination, of electron-hole pairs.[101,130–132] Crystalline TiO_2 usually adopts one of three phases: *anatase, rutile* or *brookite* (Figure 1.8). Rutile is the equilibrium phase and most common natural form of TiO_2, with brookite and anatase both irreversibly converting to rutile at high temperature (600–800 °C).[133,134] Rutile has a tetragonal unit cell and tends to form nanorods and wires due to preferential growth in the [001] direction. Brookite TiO_2 is a relatively rare form of TiO_2 and is historically difficult to synthesise phase pure.[135] It has an orthorhombic crystal structure of space group *Pcab* (Figure 1.8). Anatase TiO_2 has a tetragonal unit cell (Figure 1.8) and can be formed through calcination of amorphous TiO_2 at 350–700 °C.[136,137] Generally, higher temperatures leads to the formation of rutile titania, unless specific synthetic measures have been taken to prevent this.[134] All three phases of TiO_2 are photocatalytic but anatase phase is widely believed to offer the best photocatalytic performance.[125,130] This is possibly due to anatase phase TiO_2 being an indirect bandgap semi-conductor with a longer lifetime of photoexcited electrons and holes compared to the direct band-gap of rutile and brookite.[130] TiO_2 can be formed in a variety of morphologies, including columns, fibres, sheets, spheres and hollow structures.[122,138,139] Mesoporous spheres are a popular choice and can be synthesised with hard or soft templates.[98,101,102,140,141] In this thesis, AzoPS are trialled as templating agents for the formation of porous titanium dioxide.
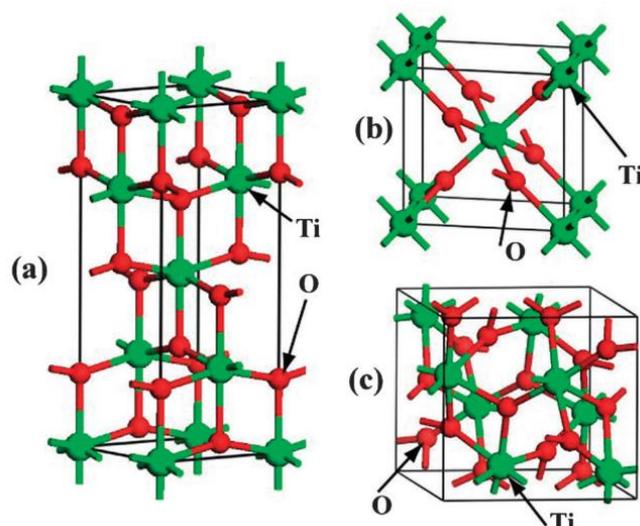
Figure 1.8. Unit cells for TiO$_2$ polymorphs of (a) anatase (b) rutile) and (c) brookie TiO$_2$. The Ti atoms are represented with green spheres, the O atoms with red. Figure taken from reference [130]

The basics of azobenzene photoisomerisation, surfactant self-assembly behaviour and the use of surfactants as templating agents now being familiar, the next section will focus on the relevant background literature required to support this thesis. This includes the prior research investigating azobenzene photosurfactants, as well as surfactant-based stimuli-responsive fluids, the formation of LLC phases by surfactants and the use of surfactants as templating agents for the creation of titanium dioxide nanoparticles.

1.2 Literature Review

1.2.1 Photosurfactants

Surfactants which contain a light-responsive group, such as spiropyran,[142–144] stilbene,[145,146] arylazopyrazole[147–149] or azobenzene,[35,50,51,150–153] are known as photosurfactants. Upon irradiation with light, a structural change is induced (*i.e.,* a photodimerisaion, photodestruction or photoisomerisation) which causes a change in the molecular dipole moment, geometry and self-assembly behaviour of the surfactant.[154] Photosurfactants are a relatively understudied class of materials, in comparison with 'regular' or non-photosurfactants. Considering the breadth of industries and applications that surfactants are integral to, photosurfactants pose exciting possibilities for developing the additional dimension of stimuli-responsiveness or on-demand control of physicochemical properties in a multitude of areas (*e.g.* dispersing, foaming, wetting, emulsification, templating). In this work, the focus is on azobenzene photosurfactants, which undergo a reversible photoisomerisation between *cis-* and *trans-*isomers upon irradiation with UV and blue light, respectively.

The first investigation into the effect of photoisomerisation on the properties of an azobenzene photosurfactant was reported by Shinkai *et al.* in 1982.[26] For three cationic

AzoPS — (4-octanoylamino-4'-(dimethylamino) azobenzene, 4-hexadecyloxy-4'-(dimethylaminomethyl) azobenzene and 4-octyloxy-4'-(di-methylaminomethyl) azobenzene) — they probed the effect of UV irradiation and formation of the *cis*-PSS on the CMC of the surfactants. They found that AzoPS in the *cis*-PSS have a higher CMC than those in the *trans*-state. This was ascribed to the increased hydrophilicity of the surfactant in the *cis*-form, due to the higher dipole moment upon photoisomerisation. Subsequently, changes in physicochemical properties depending on the isomeric form of the AzoPS, such as conductivity,[155] interfacial tension,[35,50] foamability[156,157] and self-assembly,[46,51,158,159] have been reported. The general trends observed for AzoPS are: (1) a higher CMC in the *cis* form compared to the *trans* form,[26,155,160] with the difference in CMC between isomers varying with the alkyl tail length of the surfactant;[51,153] (2) the change in surface tension between isomers depends strongly on the structure,[50,161] and in particular flexibility,[35] of the AzoPS; (3) different self-assembly behaviour for each isomer,[46,51,158] with reversible disruption and reformation of micelles possible.[159,160] It is clear from all reports that the structure of the AzoPS is crucial to the extent of change observed upon photoisomerisation and careful consideration of the molecular structure (length of pendant tail length, length of spacer, identity of head group; Figure 1.2) is imperative.

The possibility for facile switching between different values for key properties such as CMC, surface tension *etc.*, without the removal or addition of any reagents, means AzoPS can be integrated into a variety of applications[162,163] such as reversible DNA compaction,[30–32,164–168] controlled protein unfolding,[169–171] microfluidics,[29,172,173] foam dyeing[33,174] and actuators for light-mediated transport.[175-178] However, despite the azobenzene motif being relatively easy to synthesise and functionalise,[179] researchers have focused their efforts on investigating the potential applications for the most common AzoPS structures,[154,163,180] rather than on broadening the catalogue of available AzoPS structures[152,154,181–185] or systematically varying the AzoPS structure. In particular, non-ionic AzoPS are much less studied[35,46,186,187] compared to their charged or zwitterionic counterparts. Furthermore, while regular surfactants are known to form WLMs in solution, which offers the possibility of creating fluids with viscoelastic and viscous behaviour, this possibility has not been probed extensively with AzoPS. Given the photo-responsiveness of AzoPS, fluids with light-responsive viscosities could be created;[183] this is the focus of Chapters 3 and 4 of this thesis. The topic of stimuli-responsive rheological fluids has generated significant research interest, the relevant literature of which will be summarised briefly next.

1.2.2 Stimuli-Responsive Fluids formed from Wormlike Micelles

Due to the dynamic and tuneable nature of surfactant self-assembly, the flow behaviour of WLM solutions formed from surfactants is distinctive and interesting. Their rheological properties are fundamental to the interest that WLMs have received in industrial and commercial applications. For example, their transient structural associations and shear-thinning abilities make WLMs excellent candidates as drag reduction fluids in turbulent flows (*e.g.* district heating and cooling).[63,188] It was found that WLMs could drastically reduce the pumping power needed for fluid recirculation.[189] Polymers used for this purpose were found to degrade rapidly with time, while their 'living polymer' WLM counterparts did not suffer from this issue.[189-191] Other areas where WLMs have found use are as fracturing fluids in oil field applications[63,192,193] and in home and personal care applications.[63,194–198]

Zelman *et al.* predicted the thermodynamics and kinetics of WLM solutions using a general theory of phase separation in equilibrium networks.[199] They justified the observation of the "inverse" *cloud-point*, whereby a phase separation is observed for surfactant solutions as the temperature is raised, as arising from the temperature dependence of the spontaneous curvature of the WLM. At low temperatures, the spontaneous curvature is high, favouring long, unbranched micelles. With increasing temperature, the spontaneous curvature decreases, which favours branching and ultimately phase separation. They noted that below a critical temperature, the relaxation time of the WLM is independent of the branching kinetics and depends almost fully on chain breaking and reassembly. Only above a critical temperature did the crucial relaxation mechanism arise from the kinetics of junction formation, with the end-cap energy negligible.

Angelico *et al.* probed the effect of micellar branching on the viscoelasticity of reverse WLMs.[200] They formed reverse WLMs using a lecithin-water solution, with the degree of branching modulated through the addition of an organic solvent. When cyclohexane was used, disconnected WLMs were favoured, while isooctane favoured the formation of branched micelles. A mixed solvent system allowed the degree of branching to be tuned, which was determined using pulsed gradient spin-echo nuclear magnetic resonance spectroscopy. It was observed that when very few branches were present, the viscosity decreased steadily with increasing shear rate. The main effect of increased micellar branching was to shorten the relaxation time of the WLM, supposed to be due to reptation speeding up. A detailed study on topological transitions in aqueous non-ionic WLM solutions can be found in the work of Kwon and Kim,[201] the particulars of which will

not be discussed further here. A detailed review of junctions and end-caps in self-assembled non-ionic WLM has also been written by Dan and Safran.[202]

The dynamic behaviour of WLM solutions is responsible for the attention they have drawn in research. At a fundamental level, the formation of WLMs is a direct result of the preferred packing of the surfactant molecules into long cylinder chains. This self-assembly process is sensitive and can be disrupted through changes to the surfactant structure,[67,203] solution pH,[67,204] temperature[205204] or salinity.[72,206,207] Therefore, it is possible to create stimuli-responsive WLM solutions which can be controlled on-demand *via* changes to their environment. Stimuli-responsive WLMs have attracted considerable interest due to their tuneable rheology. They show potential in a myriad of applications from microfluidic devices[2] to tissue engineering[3] and drag reduction fluids.[188,189,191]

Tsuchiya *et al.* created a redox-responsive WLM system using a mixture of a ferrocenyl surfactant ((11-ferro-cenylundecyl)trimethylammonium bromide) and sodium salicylate.[208] The reduced form of the ferrocenyl group is hydrophobic, while the oxidised form is hydrophilic. This difference disrupts the hydrophobic-hydrophilic balance of the surfactant, resulting in different aggregation behaviour. A viscosity change of 15 to 0.002 Pa s was found between the reduced and oxidised forms, with the high viscosity state also forming a viscoelastic fluid. Davies *et al.* created temperature responsive WLMs by mixing cetyltrimethylammonium bromide (CTAB), with 5-methyl salicylic acid.[205] Above a certain temperature, an entangled network of WLMs was formed. The solution could switch from low-viscosity, Newtonian fluids to viscoelastic, shear-thinning fluids with much larger zero-shear viscosities. Zhao *et al.* formed a triple-stimuli-responsive WLM solution using *N*-cetyl-*N*-methylmorpholinium bromide and *trans*-cinnamic acid.[204] The solution presented different rheological behaviour in response to light, pH and heat. The authors assigned these changes to variations in the packing parameter and degree of entanglement of the micellar network.

It is also possible to control the formation of WLM using light, which offers non-invasive manipulation of the system. There are two main approaches to controlling WLM formation with light. Firstly, by incorporating a light-sensitive additive to a system already known to form WLMs. Secondly, by making the WLMs themselves inherently light-responsive. The former approach has been undertaken more often,[71,142,209,210] while the formation of inherently light-responsive WLM has only been reported twice.[152,211] In 2014, Song *et al.* reported a cationic, gemini AzoPS (sodium-2,20-(diazene-1,2-diylbis(4,1-phenylene))-didodecanoate) which, for the *trans*-isomer, formed a WLM network in aqueous solution.[211] This solution had a viscosity which varied by 4 orders of magnitude upon photoisomerisation of the azobenzene. In 2021, Butler *et al.* reported a

zwitterionic AzoPS (2-(dimethyl(2-(4-((4-(4-methylpentyl) phenyl) diazenyl) phenoxy) ethyl) ammonio) acetate)) which assembled into a WLM network in the *trans*-form but formed ellipsoidal aggregates upon photoisomerisation to the *cis*-isomer.[152] The viscosity decreased by a factor of 16,000 upon isomerisation to the *cis*-isomer. A light-responsive WLM system with an adjustable viscosity has never been reported for a neutral AzoPS.

WLM also show interesting behaviour under shear, with investigation of the self-assembled structure under shear requiring the use of combined techniques such as rheo-SANS. Stellbrink *et al.* investigated the shear-induced structural changes of kinetically frozen diblock copolymer micelles using combined rheology and SANS (rheo-SANS).[212] Their work emphasised the utility of rheo-SANS for probing soft matter systems. For the interested reader, a detailed review on the topic of flow and rheo-SANS applied to soft matter was published by Eberle and Porcar.[213] Rogers *et al.* probed the dynamic response of a dispersion of surfactant WLMs using a novel methodology relying on large-amplitude oscillatory shear and time-resolved SANS.[77] The aim was to investigate the deformation of the surfactant solution and the degree of alignment exhibited before the onset of flow instabilities, such as shear-banding. They found that prior to yielding, the Kuhn segments of the WLM were "over-oriented" compared with the steady-sheared fluid state. Fardin *et al.* found that shear-banding occurs for a range of WLM systems due to flow instabilities, even WLM systems previously reported to not exhibit shear banding.[214] They emphasised that common techniques such 1D velocimetry or global rheology tests cannot determine the presence of flow instabilities. Their work encouraged the use of 2D and 3D images of the flow field to determine the presence of flow instabilities on top of shear-banding.

Calabrese *et al.* investigated the rheology and microstructure of branched WLM under shear.[76] They created WLMs from a mixed cationic-anionic surfactant system (cetyl- trimethylammonium tosylate-sodium dodecyl benzene sulfonate), controlling micellar branching through the addition of sodium tosylate. The degree of branching was determined using cryo-transmission electron microscopy (cryo-TEM), with the rheology and structure monitored using rheology and SANS under flow. They observed that the zero-shear viscosity and relaxation time as a function of micellar branching decreases monotonically. At high degrees of branching, shear thickening behaviour was observed at high shear rates. They also noted from 1-2 plane SANS measurements that shear-banding was not observed when significant branching is present.

While WLMs are an interesting aspect of surfactant self-assembly, further structures continue to be formed with increasing surfactant concentration. In particular, LLC phases are a phenomenon commonly observed for 'regular' surfactants at high concentrations that have not been reported to the same extent for AzoPS.

1.2.3 Lyotropic Liquid Crystal Phases

There are several key behaviours relating to LLC phases which are observed for non-ionic surfactants, photoresponsive or otherwise; these will be outlined in this section. Non-ionic surfactants do not experience long-range electrostatic forces, which means that intra- and inter-micellar head group interactions have a much shorter range. As a result, the non-ionic head groups can pack closely together and often experience strong hydrogen-bonding interactions which facilitate self-assembly and the formation of long-range order. An additional consequence is that non-ionic surfactants tend to have a much lower CMC than their charged counterparts, in part due to their reduced ability to be solubilised in water. Non-photoactive polyethylene oxide-based surfactants (C_nEO_m) have been studied extensively in terms of their ability to form LLC phases. Some key results and trends will be summarised here, to better allow comparison with the potential for LLC phases to be formed by AzoPS, which will be the subject of Chapter 5.

It is difficult to develop a quantitative theory to rationalise inter-micellar repulsions for non-ionic surfactants; electrostatic repulsions tend to be easier to model and describe.[82,215,216] To overcome this, Mitchell *et al.* provide a comprehensive study on the phase behaviour of a series of polyoxyethylene surfactants in water, systematically varying the surfactant structure to assess the contribution of various factors (head-group area, alkyl chain length *etc.*) to mesophase formation.[38] On the basis of optical microscopy images and geometric considerations, they deduced a typical phase diagram which rationalises the phase adopted by a surfactant in terms of the surfactant volume fraction and micelle curvature. (Figure 1.9) Significant trends observed were that large head groups (EO_m where $m > 5$) and lower temperatures favour higher curvature phase, such as cubic and hexagonal phases (Figure 1.10), while lamellar and reversed phases occur for smaller headgroups and higher temperatures. They discuss how intra-micellar contributions determine the micelle shape above the CMC (*i.e.* alkyl chain length), while inter-micellar interactions contribute significantly to aggregate shape at higher concentrations. This work also briefly explored EO surfactants with a phenyl group in the alkyl tail. For these structures, the temperature stability of a given phase is increased relative to its alkyl counterpart, attributed to the aromatic interactions of the phenyl groups. In general, these structures behaved as if smaller than their alkyl counterpart. This is potentially due to both less favourable water-hydrocarbon interactions and attractive interactions between phenyl groups.
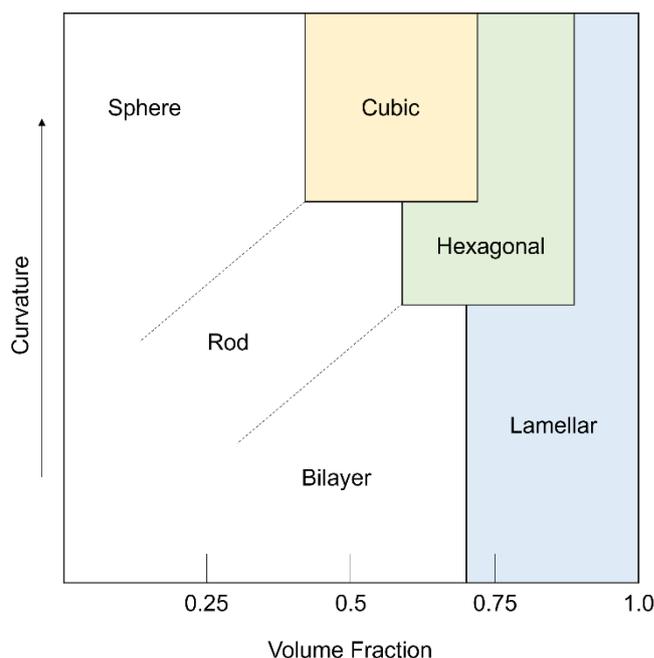
Figure 1.9. Schematic phase diagram of LLC mesophases as a function of surfactant volume fraction and increasing spontaneous curvature. The dotted lines indicate the transitions between micellar shapes. Schematic recreated based on a figure from reference 38.

The work of Mitchell *et al.* proposes that mesophase formation can be rationalised on the basis of packing considerations. Analysis of preferred curvature based on head-group area and stabilisation has the consequence of assuming that increasing alkyl chain length will not change the micelle shape or LLC phase, as the volume contribution should scale accordingly with the increase in chain length. This assumption of alkyl tail length being a non-dependent parameter is also implicit in the packing parameter model.[61] However, in practice it has been reported that varying the length of the alkyl tail has a striking effect on both the self-assembly behaviour[62] and formation of LLC phases. Varade *et al.* reported the phase diagrams for a variety of alkylTAB surfactants, with increasing alkyl tail length.[88] They observed using polarised optical microscopy that all surfactants form L_I, H_I, V_I and L_α phases with increasing surfactant concentration in water. The effect of the increasing alkyl chain length was to increase the extension of the LLC phases in the phase diagram, with a shorter chain having a much smaller LLC region. This behaviour has also been reported for polyoxyethylene surfactants, whereby C_8EO_4 has no LLC mesophases,[38] $C_{10}EO_4$ forms lamellar mesophases,[83] and $C_{12}EO_4$ also forms lamellar phases but over a broader concentration range.[217] Similarly, both $C_{10}EO_4$ and $C_{12}EO_4$ also form hexagonal phases. For the C_{10} surfactant, this phase only occurs up to 4 °C, between 40 and 60 wt%. For the C_{12} surfactant, the hexagonal phase is observed up to about 35 °C for the same concentration range. This leads to the conclusion that increasing tail length increases both the upper temperature limit and concentration range of a given phase, for both trimethylammonium bromide and polyoxyethylene surfactants.
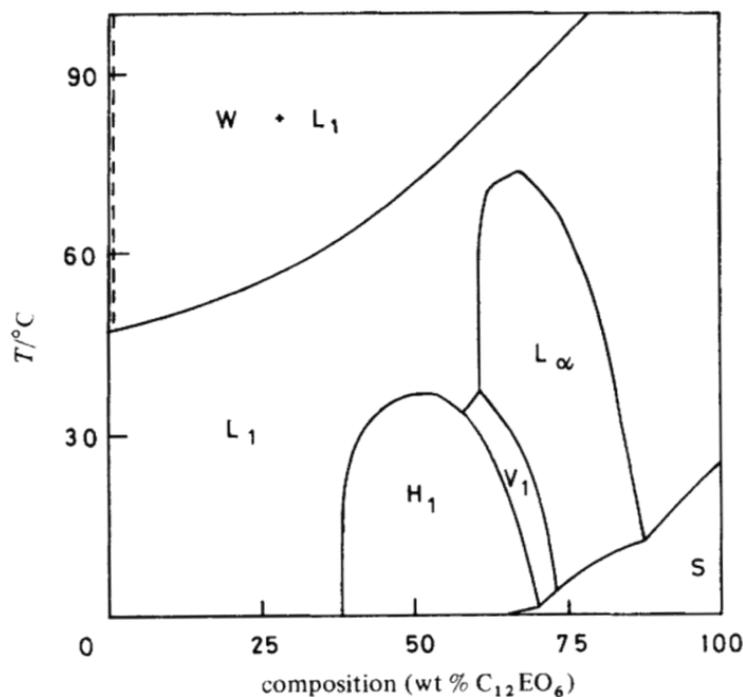
Figure 1.10. Binary concentration-temperature phase diagram of $C_{12}EO_6$ in water. L_1 refers to an aqueous surfactant solution, W is a very dilute surfactant solution, H_1 represents a hexagonal phase, V_1 a cubic phase, L_α a lamellar phase and S indicates solid surfactant. The diagram is taken from reference 38.

Kratzat *et al.* studied surfactants for which the packing parameter, and in some cases physical dimensions, are the same across molecules with different structures, *i.e.* asymmetrically branched EO_m surfactants.[218] They discovered that different structures can be formed from surfactants with the same packing parameter, posited as being due to the tail of the surfactant not approximating a cylinder, instead truncating towards the top or bottom depending on the asymmetry in the branched tail. This emphasises that the simple packing parameter model assumes (1) linear alkyl surfactants with a tail volume that is constant along its length and (2) independence of tail length. The second assumption has been challenged as discussed previously, as well as both assumptions addressed in this study by Kratzat *et al.*[218] They report that a lengthening of the alkyl chain, C_n, leads to a lower wedge angle of the surfactant, causing a decrease in curvature and stabilisation of the lamellar phase. They also introduce a symmetry parameter, *S*, to modify the packing parameter in the case of asymmetric hydrophobic chains.

Lühmann *et al.* further explored this idea of varying the composition and shape of the alkyl tail.[219] They probed the LLC phase behaviour of amphiphilic monomers and polymers containing a hydrophobic, rod-like segment by the incorporation of a biphenyl group to the alkyl tail. They found cubic, hexagonal and lamellar phases formed, with the same general trends of decreasing curvature with increasing concentration or temperature. They reported that when the length of either the flexible hydrophobic unit

or EO$_m$ head group is increased, the extent of the cubic and hexagonal phases, where present, increased in terms of temperature and concentration range. It is sensible that a larger head group can stabilise a lower curvature phase but the variation with flexible tail length is unusual. They also reported that when the flexible hydrophobic length is decreased, there was a strong tendency towards crystallisation and packing into structures with low surface curvature, *i.e.* lamellar phases. This can be rationalised by considering the packing constraints of the biphenyl units in the micelle cores.

Reports of LLC phases for AzoPS are uncommon. In 2014, Peng *et al.* reported LLC phases formed by an oligoethylene glycol-based AzoPS with a five-carbon spacer and four-carbon pendant tail[186] (Figure1.11a). They observed (using POM and SAXS) the presence of a hexagonal LLC phase between 40 and 60 wt% surfactant, and a lamellar LLC phase between 70 and 80 wt% surfactant in water (Figure 1.11b, c). Upon UV irradiation, optical anisotropy was lost, indicating disruption of the LLC phase, which could be recovered with visible light irradiation. Peng *et al.* built upon this initial work by varying the position of the azobenzene group within the molecular structure.[187] When the azobenzene group was directly attached to the head group, only lamellar phases were observed, while when a spacer moiety was included, hexagonal and lamellar LLC phase were found.[186] SAXS data indicated a shift to smaller physical dimensions with both increasing surfactant concentration and temperature. Only the structure with the spacer separating the azobenzene from the head group showed changes upon isomerisation.

Tan *et al.* synthesised a series of amphitropic azobenzene derivatives to probe their thermotropic and lyotropic liquid crystal phase-forming abilities.[220] The structure of the polar groups and number of alkyl chains were varied across the series. Most compounds with only one alkyl chain formed tilted smectic phases, while compounds with two or three alkyl chains formed columnar hexagonal phases. Photoresponsive behaviour was observed for all amphiphiles but not reported in detail.

Yang *et al.* investigated a series of non-ionic AzoPS to create multi-stimuli responsive hydrogels.[221] They synthesised three AzoPS, varying the molecular weight of the hydrophilic polyetheramine head groups for a constant azobenzene-based tail length. It was found all three AzoPS formed gels in aqueous solutions and transitioned between gel and sol states depending on pH, temperature, applied stress or light. One structure, C$_4$-Azo-C$_5$-D$_{400}$ formed LLC phases at certain water contents. Yang *et al.* also reported an azobenzene based super-gelator, 4-chlorocarbonyl-benzoic acid 4'-(4''-octy-loxy-phenylazo)-benzyl ester (C$_8$-Azo-TPC) which formed gels at concentrations as low as 0.08 wt%. Upon UV irradiation, heating or application of shear the gel viscosity dropped rapidly, attributed to the disruption of π-π bonds within the gel network.
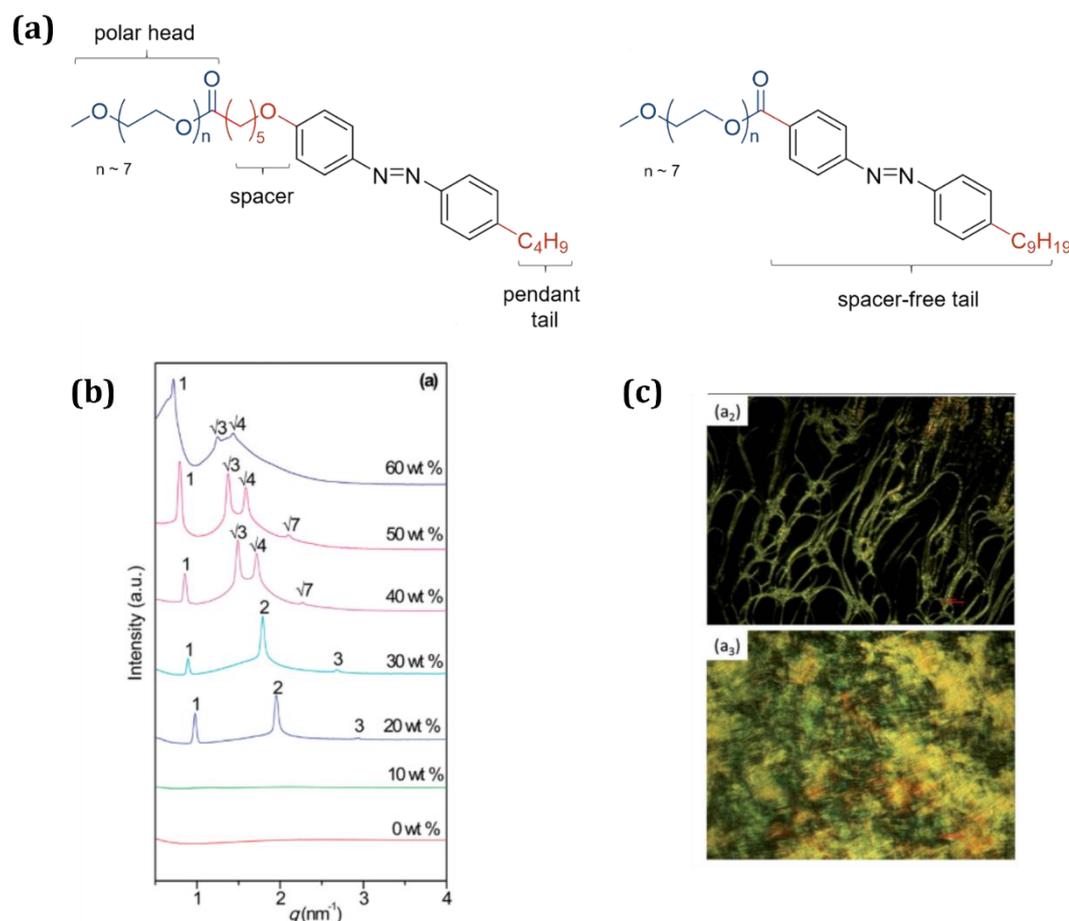
Figure 1.11. (a) Molecular structures of the oligoxyethylene AzoPS with a five-carbon spacer and the spacer-free AzoPS reported to form LLC phases by Peng *et al.*[187] (b) SAXS data of aquoues solutions of the AzoPS with a spacer, wt% corresponds to the weight percent of water in the solution. With increasing water content, a change from a lamellar to hexagonal phase is observed. (c) the lamellar (top) and hexagonal (bottom) phases have distinct birefringent textures when observed using polarised optical microscopy. Figures are adapted from reference 187.

Okano *et al.* reported a novel photoresponsive polymer with a block mesogenic side group containing an azobenzene component. The polymer formed a lamellar liquid crystalline phase which changed its molecular alignment to form a highly aligned structure when irradiated with linearly polarised light. This observation was attributed to the Weigert effect whereby dichroic dye molecules can orient themselves upon photoisomerisation. Related work on photoresponsive liquid crystal polymers based on polymethacrylates with amide-substituted azobenzene mesogens has been reported by Li *et al.* They found through Fourier-transform infrared spectroscopy that presence of the amide group resulted in strong hydrogen bonding interactions which stabilised the formation of smectic C liquid crystal mesopohases.[222] As well as being capable of self-association to form dynamic structures with long-range order, surfactants interact with other species in solution, giving surfactants great potential as structure-directing agents. As this is the subject of Chapter 6, the relevant background literature on using surfactants as templates for the formation of porous nanoparticles will be summarised next.

1.2.4 Surfactants as Templating Agents to Create Porous Metal Oxide Nanoparticles

As previously discussed, surfactants are commonly used as soft templating agents for the synthesis of mesostructured metal oxides.[94-98] This style of soft-templating involves cooperative interactions between the surfactant species and inorganic precursor, driven by non-covalent interactions.[100-102] As these cooperative, equilibrium interactions are dynamic they lend themselves well to modification through manipulation of the external environment. Despite this potential, the use of photosurfactants as templating agents is extremely rare. Generally non-photoactive surfactants, such as CTAB, and block-copolymers are used as templating agents. There are many possible approaches to synthesising mesoporous oxides using surfactant templates, with potential products ranging from spheres[110,116,223] to films.[127,224-226] In this thesis, mesoporous, photocatalytic TiO$_2$ is the metal oxide of interest to demonstrate proof-of-concept for AzoPS as templating agents.. There are several reviews available which discuss different synthetic approaches for the formation of mesoporous titania,[131,227-229] with some of the key highlights summarised here.

Early work on the formation of TiO$_2$ sols was done in 1977 by Matijevic *et al.*[230] They used high temperatures and acidic conditions to create spherical sols of TiO$_2$ with narrow size distributions. Monodisperse titania powders were later produced from by Barringer and Bowen in 1982, who used aqueous alcohol solutions to control hydrolysis of the titania precursor.[231] Mesoporous titania was first produced in 1995 by Antonelli and Ying, who used Ti(isopropoxide) *bis*-acetylacetonate as the precursor in a modified sol-gel process.[232] With an acetylacetonate-based titania precursor and an alkylphosphate surfactant (at 10 wt%), hexagonally packed titania mesostructures were produced. The final products had a narrow pore size distribution and a Brunauer-Emmett-Teller (BET) area of 200 m^2/g.

The morphology and size distribution of the product titania particles results from the interplay of many forces during the sol-gel process (*e.g.* electrostatic, van der Waals, short-range repulsive interactions). Jean and Ring examined the growth rate required to produce monodisperse particles of a certain size by varying the ratio of water to titania precursor.[233] They also investigated the effect of steric stabilisation on the final particle size and morphology, using hydoxypropylcellulose as a steric stabiliser. They found that depending on the rate-limiting step, the size distribution of the product titania will change as the reaction proceeds. If the nucleation period (following supersaturation due to sol formation) is short, then a narrow size distribution is achieved. This is due to supersaturation being relieved and further nucleation does not occur, instead growth occurs until the reaction stops due to equilibrium. Look and Zukoski investigated

changing the surface potential to control particle size.[234] If the surface potential is sufficiently positive or negative, repulsive interactions become strong enough to prevent aggregation under Brownian motion and uniform titania particles can be formed. The surface potential can be tuned through the addition of a salt to the reaction mixture. For example, Eiden-Assman *et al.* investigated the effect of adding various aqueous salt solutions to the sol-gel reaction of titania tetraethoxide in ethanol.[235] Using alkali salts with varying cations (LiCl, NaCl, KCl, CsCl; 0.4 mM) resulted in particles with diameters ranging from ~200 to 2000 nm, respectively. The larger cations resulted in higher zeta potentials, which gave rise to smaller final particle sizes. For the same salt, increasing the concentration resulted in smaller particles, attributed to the increase in zeta potential with higher salt concentrations. At very high ionic strength, no particles were observed; it was proposed this is because the ions bind most of the water in a hydration shell, leaving no water left over for the hydrolysis of the titania precursor. The authors reported that the concentrations of ethanol, water and titania tetraethoxide probed did not affect the particle size significantly, but did affect the particle size distribution.

As well as mesoporous spheres, it is also possible to form porous films using templates. In 1997, Lu *et al.* formed cubic and hexagonal mesoporous films through a sol-gel dip-coating method.[236] Zhao *et al.* synthesised mesoporous titania films using a non-ionic triblock copolymer and a sol-gel method.[237] They systematically varied several synthetic parameters and removed the surfactant template by ethanol extraction. Using an evaporation-induced phase separation method, Nursam *et al.* synthesised anatase titania thin films with both meso- and macropores. The porosity could be tuned by varying the proportion of the polymeric components used as templates. There are several synthetic reviews which detail further advances in porous film formation.[131,227–229,238] While films are interesting, in this thesis submicrometre spheres are the desired product as they offer better surface areas for photocatalysis, are easily recycled and reused, and show promise as good scatterers for optical applications (Figure 1.12).[127,239,240]
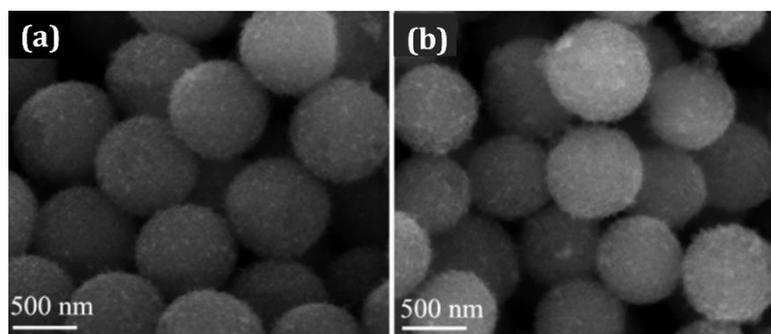
Figure 1.12. SEM images of mesoporous titania beads formed using hexyldecylamine as a template. Image taken from reference 240[240].

In 2014, Deng *et al.* reported a cationic azobenzene photosurfactant (6-4'-ethoxy-4-azophenyl)hexyloxytrimethyl ammonium bromide) for the templated sol-gel synthesis of mesoporous silica nanospheres for the first time.[241] Their work demonstrated that amphiphilic molecules confined in mesostructured nanocomposites could adjust their configuration in response to light. The nanoparticles synthesised under ambient light had irregular morphologies, while those synthesised under UV light has a spherical morphology. This approach has not yet been extended to other metal oxides, such as TiO_2, nor have other AzoPS structures been used for templating purposes. The next closest example of AzoPS being used as structure-directing agent is a report by Zakrevskyy *et al.* showing that photoisomerisation of an AzoTAB embedded within poly(NiPAM)-based organic microgel particles could be used to control swelling.[242] Extending the use of photosurfactants as templating agents is warranted, in particular to create functional materials such as porous TiO_2 and to explore the effect of photoisomerisation on the template function and properties of the nanoparticle product.

1.3 Aims

It is clear that AzoPS can produce photoresponsive micellar structures in solution, with some reports of long-range order and liquid crystal phases. However, their dynamic self-assembly behaviour under photoisomerisation has not been explored in detail. Neither has there been much variety in the type of LLC phase found for AzoPS, and LLC phase-forming AzoPS are seldom used for applications. Light-responsive WLM solutions have been investigated with regards to their controllable flow behaviour, but to date only two single-component formulations has been reported. Furthermore, the use of AzoPS as templating agents has not been examined in detail. In this work, a family of neutral AzoPS will be synthesised and their ability to propagate changes on the molecular level *via* isomerisation to macroscopic properties such as self-assembly and flow behaviour will be investigated. The key experimental procedures and instrumentation is provided in Chapter 2.

Chapter 3 of this thesis will present a combined UV-Vis absorption spectroscopy-small-angle neutron scattering approach, using a model AzoPS. It will become evident that combining these two techniques is a powerful way to track the photoisomerisation process *in situ*, and correlate this to changes in the self-assembled structure of the surfactant. The rheological behaviour of light-responsive wormlike micelles will also be investigated. It will be shown that neutral AzoPS can form highly viscous, shear-thinning, solutions in the *trans*-PSS but transition to low viscosity Newtonian fluids after irradiation with UV light.

Chapter 4 will focus further on the relationship between self-assembled structure and flow behaviour, through detailed rheo-SANS experiments. It will become clear that concentration-dependent effects are crucial to the self-assembly and flow behaviour of AzoPS, with shearing starkly effecting the self-assembled structure.

Chapter 5 describes the creation of photoresponsive LLC phases for all four AzoPS structure, and the effect of molecular structure, isomeric form, concentration and temperature on the LLC phase. Binary concentration-temperature phase diagrams are created for each AzoPS.

In Chapter 6, the use of AzoPS as surface-directing agents to create porous TiO_2 nanoparticles for photocatalytic applications is described, with the product TiO_2 used to degrade a model organic dye. Each of the above results sections will begin by briefly outlining the relevant literature in more detail, allowing the work to be placed in the context of the field. Finally, a conclusions section will summarise the principal findings and outline the future work arising from this research. Some of the results here have been published elsewhere. The relevant publications will be outlined before each Chapter.

1.4 References

1   F. Xu, C. Fu and Y. Yang, *Phys. Rev. Lett.*, 2020, **124**, 38003.

2   C. V. Mora, M. Davison, J. Martin Wild and M. M. Walker, *Nature*, 2004, **432**, 508–511.

3   T. Leucht, *J. Comp. Physiol. A*, 1984, **154**, 865–870.

4   M. Nouvian and C. G. Galizia, *Sci. Rep.*, 2020, **10**, 1–15.

5   T. Newbold, D. P. Tittensor, M. B. J. Harfoot, J. P. W. Scharlemann and D. W. Purves, *Sci. Rep.*, 2020, **10**, 1–10.

6   G. S. Shideler, R. J. Araujo, B. K. Walker, J. Blondeau and J. E. Serafy, *Ecosphere*, , DOI:10.1002/ecs2.1943.

7   W. R. Browne and B. L. Feringa, *Nat. Nanotechnol.*, 2006, **1**, 25–35.

8   Y. Takashima, S. Hatanaka, M. Otsubo, M. Nakahata, T. Kakuta, A. Hashidzume, H. Yamaguchi and A. Harada, *Nat. Commun.*, , DOI:10.1038/ncomms2280.

9   F. Lancia, A. Ryabchun, A. D. Nguindjel, S. Kwangmettatam and N. Katsonis, *Nat. Commun.*, , DOI:10.1038/s41467-019-12786-2.

10   Y. Zhao, Z. Li, Q. Li, L. Yang, H. Liu, R. Yan, L. Xiao, H. Liu, J. Wang, B. Yang and Q. Lin, *Macromol. Rapid Commun.*, 2020, **41**, 1–11.

11   N. Oliva and B. D. Almquist, *Adv. Drug Deliv. Rev.*, 2020, **161**–**162**, 22–41.

12   D. Hua, J. Jiang, L. Kuang, J. Jiang, W. Zheng and H. Liang, *Macromolecules*, 2011, **44**, 1298–1302.

13   S. H. Pham, Y. Choi and J. Choi, *Pharmaceutics*, 2020, **12**, 1–19.

14   J. Wen, K. Yang, Y. Xu, H. Li, F. Liu and S. Sun, *Sci. Rep.*, 2016, **6**, 2–11.

15   T. D. Nguyen, K. C. F. Leung, M. Liong, Y. Liu, J. F. Stoddart and J. I. Zink, *Adv. Funct. Mater.*, 2007, **17**, 2101–2110.

16   P. K. Kundu, D. Samanta, R. Leizrowice, B. Margulis, H. Zhao, M. Börner, T. Udayabhaskararao, D. Manna and R. Klajn, *Nat. Chem.*, 2015, **7**, 646–652.

17   G. S. Kumar and D. C. Neckers, *Chem. Rev.*, 1989, **89**, 1915–1925.

18   Y. Guo, Y. Gong, Y. Gao, J. Xiao, T. Wang and L. Yu, *Langmuir*, 2016, **32**, 9293–9300.

19   R. Yang, G. Dong, Y. Liu, C. Zheng and D. Wang, *Chem. Lett.*, 2017, **46**, 319–322.

20   F. J. M. Hoeben, P. Jonkheijm, E. W. Meijer and A. P. H. J. Schenning, *Chem. Rev.*, 2005, **105**, 1491–1546.

21   V. Balzani, A. Credi, F. Marchioni and J. F. Stoddart, *Chem. Commun.*, 2001, **2**, 1860–1861.

22   S. Palagi, A. G. Mark, S. Y. Reigh, K. Melde, T. Qiu, H. Zeng, C. Parmeggiani, D. Martella, A. Sanchez-castillo, N. Kapernaum, F. Giesselmann, D. S. Wiersma, E. Lauga and P. Fischer, *Nat. Mater.*, 2016, **15**, 647–654.

23   N. Umeki, T. Yoshizawa, Y. Sugimoto, T. Mitsui, K. Wakabayashi and S. Maruta, *J. Biochem.*, 2004, **846**, 839–846.

24   E. M. M. Tan, S. Amirjalayer, S. Smolarek, A. Vdovin, F. Zerbetto and W. J. Buma, *Nat. Commun.*, , DOI:10.1038/ncomms6860.

25   I. K. Lednev, T. Q. Ye, P. Matousek, M. Towrie, P. Foggi, F. V. R. Neuwahl, S. Umapathy, R. E. Hester and J. N. Moore, *Chem. Phys. Lett.*, 1998, **290**, 68–74.

26   S. Shinkai, K. Matsuo, A. Harada and O. Manabe, *J. Chem. Soc. Perkins Trans*, 1982, **2**, 1260–1265.

27   E. Léonard, F. Mangin, C. Villlete, M. Billamboz and C. Len, *Catal. Sci. Technol.*, 2016, **6**, 379–398.

28   A. Diguet, H. Li, N. Queyriaux, Y. Chen and D. Baigl, *Lab Chip*, 2011, **11**, 2666–2669.

29   L. Nurdin, A. Venancio-Marques, S. Rudiuk, M. Morel and D. Baigl, *Comptes Rendus Chim.*, 2015, **19**, 199–206.

30   K. Schille, T. Nylander, M. Cárdenas, K. Schillen, T. Nylander, J. Jansson and B. Lindman, *Phys. Chem. Chem. Phys.*, 2004, **6**, 1603–1607.

31   Y. Zakrevskyy, P. Cywinski, M. Cywinska, J. Paasche, N. Lomadze, O. Reich, H. G. Löhmannsröben and S. Santer, *J. Chem. Phys.*, 2014, **140**, 044907.

32   A. Diguet, N. K. Mani, M. Geoffroy, M. Sollogoub and D. Baigl, *Chem. - A Eur. J.*, 2010, **16**, 11890–11896.

33   S. Chen, W. Zhang, C. Wang and S. Sun, *Green Chem.*, 2016, **18**, 3972–3980.

34   S. Chen, C. Wang, Y. Yin and K. Chen, *RSC Adv.*, 2016, **6**, 60138–60144.

35   T. Shang, K. A. Smith and T. A. Hatton, *Langmuir*, 2003, **19**, 10764–10773.

36   C. T. Lee, K. A. Smith and T. Alan Hatton, *Langmuir*, 2009, **25**, 13784–13794.

37   M. F. Cox, in *Handbook of Applied Surface and Colloid Chemistry*, ed. K. Holmberg, John Wiley & Sons, 2001, pp. 294–309.

38   D. J. Mitchell, G. J. T. Tiddy and L. Waring, *J. Chem. Soc., Faraday Trans. 1*, 1983, **79**, 975.

39   C. D. Adam, J. A. Durrant, M. R. Lowry and G. J. T. Tiddy, *J. Chem. Soc. Faraday Trans. 1 Phys. Chem. Condens. Phases*, 1984, **80**, 789–801.

40   G. Wanka, H. Hoffmann and W. Ulbricht, *Macromolecules*, 1994, **27**, 4145–4159.

41   S. Funari and G. Rapp, *J. Phys Chem. B*, 1997, **101**, 732–739.

42   G. S. Hartley, *Nature*, 1937, **140,** 281–281.

43   G. S. Hartley, *J. Chem. Soc.*, 1938, **113**, 633–642.

44   K. G. Yager and C. J. Barrett, *J. Photochem. Photobiol. A Chem.*, 2006, **182**, 250–261.

45   J. García-Amorós and D. Velasco, *Beilstein J. Org. Chem.*, 2012, **8**, 1003–1017.

46   T. Shang, K. A. Smith and T. A. Hatton, *Langmuir*, 2006, **22**, 1436–1442.

47   H. M. Dhammika Bandara and S. C. Burdette, *Chem. Soc. Rev.*, 2012, **41**, 1809–1825.

48   Z. Wu, R. Xue, M. Xie, X. Wang, Z. Liu, M. Drechsler, J. Huang and Y. Yan, *J. Phys. Chem. Lett.*, 2018, **9**, 163–169.

49   F. Aleotti, A. Nenov, L. Salvigni, M. Bonfanti, M. M. El-Tahawy, A. Giunchi, M. Gentile, C. Spallacci, A. Ventimiglia, G. Cirillo, L. Montali, S. Scurti, M. Garavelli and I. Conti, *J. Phys. Chem. A*, 2020, **124**, 9513–9523.

50   L. Yang, N. Takisawa, T. Hayashita and K. Shirahama, *J. Phys. Chem.*, 1995, **99**, 8799–8803.

51   H. C. Kang, B. M. Lee, J. Yoon and M. Yoon, *J. Colloid Interface Sci.*, 2000, **231**, 255–264.

52   J. Eastoe, M. S. Dominguez, H. Cumber, P. Wyatt and R. K. Heenan, *Langmuir*, 2004, **20**, 1120–1125.

53   P. Arya, J. Jelken, N. Lomadze, S. Santer and M. Bekir, *J. Chem. Phys.*, ,
        DOI:10.1063/1.5135913.

54   A. Patist, in *Handbook of Applied Surface and Colloid Chemistry*, ed. K. Holmberg,
        John Wiley & Sons, 2001, pp. 239–249.

55   D. Lombardo, M. A. Kiselev, S. Magazù and P. Calandra, *Adv. Condens. Matter Phys.*,
        2015, **2015**, 1–22.

56   J. Fuhrhop and W. Helfrich, *Chem. Rev.*, 1993, **93**, 1565–1582.

57   O. G. Us'yarov, *Colloid J.*, 2007, **69**, 95–102.

58   S. Lee Yoon, *Self-Assembly and Nanotechnology: A Force Balance Approach*, Wiley,
        Hoboken, New Jersey, 2008.

59   S. Kozo, T. Yamaguchi and R. Hori, *Bull. Chem. Soc. Jpn.*, 1961, **34**, 237–241.

60   H. Maeda, S. Muroi, M. Shii, R. Kakehashi, H. Kaimoto, T. Nakahara and K.
        Motomura, *J. Colloid Interface Sci.*, 1995, **175**, 497–505.

61   J. N. Israelachvili, D. J. Mitchell and B. W. Ninham, *J. Chem. Soc. Faraday Trans. 2
        Mol. Chem. Phys.*, 1976, **72**, 1525–1568.

62   R. Nagarajan, *Langmuir*, 2002, **18**, 31–38.

63   J. Yang, *Curr. Opin. Colloid Interface Sci.*, 2002, **7**, 276–281.

64   U. Olsson, J. Börjesson, R. Angelico, A. Ceglie and G. Palazzo, *Soft Matter*, 2010, **6**,
        1769–1777.

65   M. E. Cates, *Macromolecules*, 1987, **20**, 2289–2296.

66   P. Schurtenberger, R. Scartazzini and P. L. Luisi, *Rheol. Acta*, 1989, **28**, 372–381.

67   Z. Chu, C. A. Dreiss and Y. Feng, *Chem. Soc. Rev.*, 2013, **42**, 7174.

68   C. A. Dreiss, in *Wormlike Micelles: Advances in Systems,Characterisation and
        Applications*, Royal Society of Chemistry, 2017, pp. 1–8.

69   C. A. Dreiss, *Soft Matter*, 2007, **3**, 956–970.

70   W. R. Chen, P. D. Butler and L. J. Magid, *Langmuir*, 2006, **22**, 6539–6548.

71   A. M. Ketner, R. Kumar, T. S. Davies, P. W. Elder and S. R. Raghavan, *J. Am. Chem.
        Soc.*, 2007, **129**, 1553–1559.

72   J. Yang, Z. Yang, Y. Lu, J. Chen and W. Qin, *J. Dispers. Sci. Technol.*, 2013, **34**, 1124–1129.

73   E. Cappelaere, J. F. Berret, J. P. Decruppe, R. Cressely and P. Lindner, *Phys. Rev. E - Stat. Physics, Plasmas, Fluids, Relat. Interdiscip. Top.*, 1997, **56**, 1869–1878.

74   M. E. Cates and S. J. Candau, *J. Phys. Condens. Matter*, 1990, **2**, 6869–6892.

75   S. R. Raghavan and E. W. Kaler, *Langmuir*, 2001, **17**, 300–306.

76   M. A. Calabrese, S. A. Rogers, R. P. Murphy and N. J. Wagner, *J. Rheol. (N. Y. N. Y).*, 2015, **59**, 1299–1328.

77   S. Rogers, J. Kohlbrecher and M. P. Lettinga, *Soft Matter*, 2012, **8**, 7831–7839.

78   S. T. Hyde, in *Handbook of Applied Surface and Colloid Chemistry*, ed. K. Holmberg, John Wiley & Sons, 2001, pp. 299–332.

79   K. Kratzat, C. Stubenrauch and H. Finkelmann, *Colloid Polym. Sci.*, 1995, **273**, 257–262.

80   P. Alexandridis, U. Olsson and B. Lindman, *Langmuir*, 1998, **14**, 2627–2638.

81   K. Kratzat and H. Finkelmann, *Liq. Cryst.*, 1993, **13**, 691–699.

82   B. Jönsson and H. Wennerstrom, *J. Colloid Interface Sci.*, 1981, **80**, 482–496.

83   C. Stubenrauch, S. Burauer, R. Strey and C. Schmidt, *Liq. Cryst.*, 2004, **31**, 39–53.

84   J. F. Nagle and S. Tristram-Nagle, *Biochim. Biophys. Acta - Rev. Biomembr.*, 2000, **1469**, 159–195.

85   J. Mitchell, G. J. T. Tiddy, L. Waring, T. Bostock and M. P. McDonald, *J. Chem. Soc., Faraday Trans.*, 1983, **79**, 975–1000.

86   Y. Zhao, X. Yue, X. Wang and X. Chen, *J. Colloid Interface Sci.*, 2013, **389**, 199–205.

87   C. Fong, A. Weerawardena, S. M. Sagnella, X. Mulet, L. Waddington, I. Krodkiewska and C. J. Drummond, *Soft Matter*, 2010, **6**, 4727.

88   D. Varade, K. Aramaki and C. Stubenrauch, *Colloids Surfaces A Physicochem. Eng. Asp.*, 2008, **315**, 205–209.

89   L. Feigin and D. Svergun, *Structure Analysis by Small-Angle X-Ray and Neutron Scattering*, Plenum Press, 1987.

90   O. Glatter and O. Kratky, *Small Angle X-ray Scattering*, Academic Press, London, 1982.

91   Z. Qian, X. Yue, S. Yi, Q. Li and X. Chen, *RSC Adv.*, 2015, **5**, 101393–101400.

92   K. Kornmueller, B. Lehofer, G. Leitinger, H. Amenitsch and R. Prassl, *Nano Res.*, 2018, **11**, 913–928.

93   N. D. Tien, S. Sasaki, H. Masunaga, N. Shimizu, N. Igarashi and S. Sakurai, *Polym. J.*, 2014, **55**, 2562–2569.

94   D. Zhao, J. Feng, Q. Huo, N. Melosh, G. H. Fredrickson, B. F. Chmelka and G. D. Stucky, *Science*, 1998, **279**, 548–552.

95   K. M. Mcgrath, D. M. Dabbs, N. Yao, I. A. Aksay and S. M. Gruner, *Science.*, 1997, **277**, 552–555.

96   S. A. Bagshaw, E. Prouzet and T. J. Pinnavaia, *Science*, 1995, **269**, 1242–1244.

97   C. G. Göltner and M. Antonietti, *Adv. Mater.*, 1997, **9**, 431–436.

98   N. Pal and A. Bhaumik, *Adv. Colloid Interface Sci.*, 2013, **189**–**190**, 21–41.

99   C. T. Kresge, M. E. Leonowicz, W. J. Roth, J. C. Vartuli and J. S. Beck, *Nature*, 1992, **359**, 710–712.

100   Y. Wan and D. Zhao, *Chem. Rev.*, 2006, **107**, 2821–2860.

101   W. Li, Z. Wu, J. Wang, A. A. Elzatahry and D. Zhao, *Chem. Mater.*, 2014, **26**, 287–298.

102   D. Gu and F. Schüth, *Chem. Soc. Rev.*, 2014, **43**, 313–344.

103   G. S. Attard, J. C. Glyde and C. G. Göltner, *Nature*, 1995, **378**, 366–368.

104   A. A. Ismail and D. W. Bahnemann, *J. Mater. Chem.*, 2011, **21**, 11686–11707.

105   S.-H. Wu, C.-Y. Mou and H.-P. Lin, *Chem. Soc. Rev.*, 2013, **42**, 3862.

106   N. Pal and A. Bhaumik, *Adv. Colloid Interface Sci.*, 2013, **189**–**190**, 21–41.

107   Y. Boyjoo, M. Wang, V. K. Pareek, J. Liu and M. Jaroniec, *Chem Soc Rev*, 2016, **45**, 6013–6047.

108   J. S. Beck, J. C. Vartuli, W. J. Roth, M. E. Leonowicz, C. T. Kresge, K. D. Schmitt, C. T. W. Chu, D. H. Olson, E. W. Sheppard, S. B. McCullen, J. B. Higgins and J. L.

Schlenker, *J. Am. Chem. Soc.*, 1992, **114**, 10834–10843.

109   W. Yue and W. Zhou, *J. Mater. Chem.*, 2007, **17**, 4947–4952.

110   K. Abitaev, Y. Qawasmi, P. Atanasova, C. Dargel, J. Bill, T. Hellweg and T. Sottmann, *Colloid Polym. Sci.*, 2021, **299**, 243–258.

111   B. Bonelli, S. Esposito and F. S. Freyria, in *Titanium Dioxide*, 2017, pp. 119–142.

112   A. K. Patra, S. K. Das and A. Bhaumik, *J. Mater. Chem.*, 2011, **21**, 3925–3930.

113   A. J. Salinas, S. Shruti, G. Malavasi, L. Menabue and M. Vallet-Regí, *Acta Biomater.*, 2011, **7**, 3452–3458.

114   C.-Y. Liu, C.-F. Chen and J.-P. Leu, *J. Electrochem. Soc.*, 2009, **156**, J16.

115   T. Wagner, S. Haffer, C. Weinberger, D. Klaus and M. Tiemann, *Chem. Soc. Rev.*, 2013, **42**, 4036–4053.

116   M. Colilla, M. Manzano, I. Izquierdo-Barba, M. Vallet-Reg, C. Boissiére and C. Sanchez, *Chem. Mater.*, 2010, **22**, 1821–1830.

117   R. Gomes, S. Dutta and A. Bhaumik, *APL Mater.*, 2014, **2**, 1–7.

118   M. Paul, N. Pal, P. R. Rajamohanan, B. S. Rana, A. K. Sinha and A. Bhaumik, *Phys. Chem. Chem. Phys.*, 2010, **12**, 9389–9394.

119   A. Fujishima, T. N. Rao and D. A. Tryk, *J. Photochem. Photobiol. C Photochem. Rev.*, 2000, **1**, 1–21.

120   S. Z. Alsheheri, *Des. Monomers Polym.*, 2021, **24**, 22–45.

121   H. Ahmari, S. Z. Heris and M. H. Khayyat, *Environ. Technol. (United Kingdom)*, 2018, **39**, 536–547.

122   A. Baharvand, R. Ali, A. M. Yusof, A. N. Ibrahim, S. Chandren and H. Nur, *J. Chinese Chem. Soc.*, 2014, **61**, 1211–1216.

123   C. Byrne, G. Subramanian and S. C. Pillai, *J. Environ. Chem. Eng.*, 2018, **6**, 3531–3555.

124   R. Fagan, D. E. McCormack, D. D. Dionysiou and S. C. Pillai, *Mater. Sci. Semicond. Process.*, 2016, **42**, 2–14.

125   L. Chu, Z. Qin, J. Yang and X. Li, *Sci. Rep.*, 2015, **5**, 1–10.

126   F. Huang, D. Chen, X. L. Zhang, R. A. Caruso and Y.-B. Cheng, *Adv. Funct. Mater.*, 2010, **20**, 1301–1305.

127   F. Sauvage, D. Chen, P. Comte, F. Huang, Ḱ. L. Heiniger, Y. Cheng, R. A. Caruso and M. Graetzel, *ACS Nano*, 2010, **4**, 4420–4425.

128   T. Sreethawong, Y. Suzuki and S. Yoshikawa, *J. Solid State Chem.*, 2005, **178**, 329–338.

129   F. Akira and H. Kenichi, *Nature*, 1972, **238**, 37–38.

130   J. Zhang, P. Zhou, J. Liu and J. Yu, *Phys. Chem. Chem. Phys.*, 2014, **16**, 20382–20386.

131   D. Chen and R. A. Caruso, *Adv. Funct. Mater.*, 2013, **23**, 1356–1374.

132   J. L. Vivero-Escoto, Y. D. Chiang, K. C. Wu and Y. Yamauchi, *Sci. Technol. Adv. Mater.*, 2012, **13**, 013003.

133   Y. Hu, H. L. Tsai and C. L. Huang, *J. Eur. Ceram. Soc.*, 2003, **23**, 691–696.

134   D. A. H. Hanaor and C. C. Sorrell, *J. Mater. Sci.*, 2011, **46**, 855–874.

135   Y. Wang, L. Li, X. Huang, Q. Li and G. Li, *RSC Adv.*, 2015, **5**, 34302–34313.

136   K. (Guy) Vibulyaseak, B. Ohtani and M. Ogawa, *RSC Adv.*, 2020, **10**, 32350–32356.

137   S. Sugapriya, R. Sriram and S. Lakshmi, *Optik (Stuttg).*, 2013, **124**, 4971–4975.

138   L. Feng, K. Y. Wang, G. S. Day and H. C. Zhou, *Chem. Soc. Rev.*, 2019, **48**, 4823–4853.

139   Q. Liang, X. Liu, G. Zeng, Z. Liu, L. Tang, B. Shao, Z. Zeng, W. Zhang, Y. Liu, M. Cheng, W. Tang and S. Gong, *Chem. Eng. J.*, 2019, **372**, 429–451.

140   A. Alagarasi, P. U. Rajalakshmi, K. Shanthi and P. Selvam, *Catal. Today*, 2018, **309**, 202–211.

141   J. Alphas Jebasingh, R. Stanley and S. Manisha Vidyavathy, *Mater. Lett.*, 2020, **279**, 128460.

142   H. Sakai, H. Ebana, K. Sakai, K. Tsuchiya and T. Ohkubo, *J. Colloid Interface Sci.*, 2007, **316**, 1027–1030.

143   H. Y. Lee, K. K. Diehn, K. Sun, T. Chen and S. R. Raghavan, *J. Am. Chem. Soc.*, 2011, **133**, 8461–8463.

144   K. J. Tangso, W. K. Fong, T. Darwish, N. Kirby, B. J. Boyd and T. L. Hanley, *J. Phys.*

Chem. B, 2013, **117**, 10203–10210.

145   J. Eastoe, M. S. Dominguez, P. Wyatt, A. Beeby and R. K. Heenan, *Langmuir*, 2002, **18**, 7837–7844.

146   J. Eastoe, M. S. Dominguez, P. Wyatt, A. J. Orr-Ewing and R. K. Heenan, *Langmuir*, 2004, **20**, 6120–6126.

147   M. Schnurbus, R. A. Campbell, J. Droste, C. Honnigfort, D. Glikman, P. Gutfreund, M. R. Hansen and B. Braunschweig, *J. Phys. Chem. B*, 2020, **124**, 6913–6923.

148   M. A. Gerkman, R. S. L. Gibson, J. Calbo, Y. Shi, M. J. Fuchter and G. G. D. Han, *J. Am. Chem. Soc.*, 2020, **142**, 8688–8695.

149   L. Stricker, E. C. Fritz, M. Peterlechner, N. L. Doltsinis and B. J. Ravoo, *J. Am. Chem. Soc.*, 2016, **138**, 4547–4554.

150   C. T. Lee, K. A. Smith and T. A. Hatton, *Macromolecules*, 2004, **37**, 5397–5405.

151   R. F. Tabor, R. J. Oakley, J. Eastoe, C. F. J. Faul, I. Grillo and R. K. Heenan, *Soft Matter*, 2009, **5**, 78–80.

152   C. S. G. Butler, J. P. King, L. W. Giles, J. B. Marlow, M. L. P. Vidallon, A. Sokolova, L. de Campo, K. L. Tuck and R. F. Tabor, *J. Colloid Interface Sci.*, 2021, **594**, 669–680.

153   C. Blayo, J. E. Houston, S. M. King and R. C. Evans, *Langmuir*, 2018, **34**, 10123–10134.

154   J. Eastoe and A. Vesperinas, *Soft Matter*, 2005, **1**, 338–347.

155   T. Hayashita, T. Kurosawa, T. Miyata, K. Tanaka and M. Igawa, *Colloid Polym. Sci.*, 1994, **272**, 1611–1619.

156   E. Chevallier, C. Monteux, F. Lequeux and C. Tribet, *Langmuir*, 2012, **28**, 2308–2312.

157   E. Chevallier, A. Saint-Jalmes, I. Cantat, F. Lequeux and C. Monteux, *Soft Matter*, 2013, **9**, 7054.

158   C. Blayo, E. A. Kelly, J. E. Houston, N. Khunti, N. P. Cowieson and R. C. Evans, *Soft Matter*, 2020, **16**, 9183–9187.

159   M. Akamatsu, P. A. Fitzgerald, M. Shiina, T. Misono, K. Tsuchiya, K. Sakai, M. Abe, G. G. Warr and H. Sakai, *J. Phys. Chem. B*, 2015, **119**, 5904–5910.

160   Y. Orihara, A. Matsumura, Y. Saito, N. Ogawa, T. Saji, A. Yamaguchi, H. Sakai and M. Abe, *Langmuir*, 2001, **17**, 6072–6076.

161   J. Y. Shin and N. L. Abbott, *Langmuir*, 1999, **15**, 4404–4410.

162   S. Santer, *J. Phys. D. Appl. Phys.*, , DOI:10.1088/1361-6463/aa95ca.

163   S. Chen, R. Costil, F. K. Leung and B. L. Feringa, *Angew. Chemie*, 2021, **133**, 11708–11731.

164   Y. Zakrevskyy, A. Kopyshev, N. Lomadze, E. Morozova, L. Lysyakova, N. Kasyanenko and S. Santer, *Phys. Rev. E - Stat. Nonlinear, Soft Matter Phys.*, 2011, **84**, 1–9.

165   S. Rudiuk, H. Saito, T. Hara, T. Inoue, K. Yoshikawa and D. Baigl, *Biomacromolecules*, 2011, **12**, 3945–3951.

166   M. Sollogoub, S. Guieu, M. Geoffroy, A. Yamada, A. Estevez-Torres, K. Yoshikawa and D. Baigl, *ChemBioChem*, 2008, **9**, 1201–1206.

167   M. Geoffroy, D. Faure, R. Oda, D. M. Bassani and D. Baigl, *ChemBioChem*, 2008, **9**, 2382–2385.

168   H. Schiessel, M. D. Correa-Rodríguez, S. Rudiuk, D. Baigl and K. Yoshikawa, *Soft Matter*, 2012, **8**, 9406.

169   G. Pouliquen and C. Tribet, *Macromolecules*, 2006, **39**, 373–383.

170   J. Sun, J. Ruchmann, A. Pallier, L. Jullien, M. Desmadril and C. Tribet, *Biomacromolecules*, 2012, **13**, 3736–3746.

171   C. T. Lee, K. A. Smith and T. A. Hatton, *Biochemistry*, 2005, **44**, 524–536.

172   D. Baigl, *Lab Chip*, 2012, **12**, 3637–3653.

173   A. Venancio-Marques, F. Barbaud and D. Baigl, *J. Am. Chem. Soc.*, 2013, **135**, 3218–3223.

174   L. Chen, S. Xu, D. McBranc and D. Whitten, *J. Am. Chem. Soc.*, 2000, **122**, 9302–9303.

175   N. Kavokine, M. Anyfantakis, M. Morel, S. Rudiuk, T. Bickel and D. Baigl, *Angew. Chemie - Int. Ed.*, 2016, **55**, 11183–11187.

176   T. Still, P. J. Yunker and A. G. Yodh, *Langmuir*, 2012, **28**, 4984–4988.

177   M. Anyfantakis and D. Baigl, *Angew. Chem. Int. Ed.*, 2014, **53**, 14077–14081.

178   S. N. Varanakkottu, M. Anyfantakis, M. Morel, S. Rudiuk and D. Baigl, *Nano Lett.*, 2016, **16**, 644–650.

179   E. Merino, *Chem. Soc. Rev.*, 2011, **40**, 3835–3853.

180   S. Santer, *J. Phys. D. Appl. Phys.*, 2018, **51**, 013002-.

181   R. Kumar, G. C. Kalur, L. Ziserman, D. Danino and S. R. Raghavan, *Langmuir*, 2007, **23**, 12849–12856.

182   V. T. Kelleppan, J. E. Moore, T. M. McCoy, A. V Sokolova, L. De Campo, B. L. Wilkinson and R. F. Tabor, *Langmuir*, 2018, **34**, 970–977.

183   B. Song, Y. Hu and J. Zhao, *J. Colloid Interface Sci.*, 2009, **333**, 820–822.

184   B. Song, J. Zhao, B. Wang and R. Jiang, *Colloids Surfaces A Physicochem. Eng. Asp.*, 2009, **352**, 24–30.

185   R. Lund, G. Brun, E. Chevallier, T. Narayanan and C. Tribet, *Langmuir*, 2016, **32**, 2539–2548.

186   S. Peng, Q. Guo, T. C. Hughes and P. G. Hartley, *Langmuir*, 2014, **30**, 866–872.

187   S. Peng, Q. Guo, P. G. Hartley and T. C. Hughes, *J. Mater. Chem. C*, 2014, **2**, 8303–8312.

188   I. Harwigsson and M. Hellsten, *J. Am. Oil Chem. Soc.*, 1996, **73**, 921–928.

189   K. Gasljevic and E. F. Matthys, *Energy Build.*, 1993, **20**, 45–56.

190   J. Myska and Z. Chara, *Exp. Fluids*, 2001, **30**, 229–236.

191   D. Ohlendorf, W. Interthal and H. Hoffman, *Rheol. Acta*, 1986, **486**, 468–486.

192   B. Chase, K. Krauss, T. Lantz and J. Plummer, *Oilf. Rev.*, 1997, 20–33.

193   M. Samuel, *Methods of Fracturing Subterranean Formation Patent No. 5964295*, US, 2001.

194   R. Khan, D. Fritter, L. Alcantara, W. Zhang and M. Helmer, *Viscoelastic Cleaning Composition for Drain Opening. Patent No. 5389157*, US, 1995.

195   D. Balzer, *Aqueous Viscoelastic Surfactant Solutions for Hair and Skin Cleaning. Patent No. 5965502*, US, 1995.

196   F. K. Rubin and D. Van Blarcom, *Alkylamidobetaines With Water Soluble Salts. Patent No. 4375421*, US, 1983.

197   M. E. Besse, R. O. Ruhr, G. K. Wichmann and T. A. Gutzmann, *Thickened Hard Surface Cleaner. Patent No. US6268324B1*, US, 1995.

198   R. . Mould, *Dilution Thickening Personal Washing Composition. Patent No. 9416680*, WO, 1999.

199   A. Zilman, S. A. Safran, T. Sottmann and R. Strey, *Langmuir*, 2004, **20**, 2199–2207.

200   R. Angelico, S. Amin, M. Monduzzi, S. Murgia and G. Palazzo, *Soft Matter*, 2012, **8**, 10941–10949.

201   S. Y. Kwon and M. W. Kim, *Phys. Rev. Lett.*, 2002, **89**, 258302/1–4.

202   N. Dan and S. A. Safran, *Adv. Colloid Interface Sci.*, 2006, **123**–**126**, 323–331.

203   B. Song, Y. Hu, Y. Song and J. Zhao, *J. Colloid Interface Sci.*, 2010, **341**, 94–100.

204   M. Zhao, M. Gao, C. Dai, C. Zou, Z. Yang, X. Wu, Y. Liu, Y. Wu, S. Fang and W. Lv, *Langmuir*, 2017, **33**, 4319–4327.

205   T. S. Davies, A. M. Ketner and S. R. Raghavan, *J. Am. Chem. Soc.*, 2006, **128**, 6669–6675.

206   C. Flood, C. A. Dreiss, V. Croce, T. Cosgrove and G. Karlsson, *Langmuir*, 2005, **21**, 7646–7652.

207   V. Croce, T. Cosgrove, C. A. Dreiss, G. Maitland, T. Hughes and G. Karlsson, *Langmuir*, 2004, **20**, 7984–7990.

208   K. Tsuchiya, Y. Orihara, Y. Kondo, N. Yoshino, T. Ohkubo, H. Sakai and M. Abet, *J. Am. Chem. Soc.*, 2004, **126**, 12282–12283.

209   H. Sakai, Y. Orihara, H. Kodashima, A. Matsumura, T. Ohkubo, K. Tsuchiya and M. Abe, *J. Am. Chem. Soc.*, 2005, **127**, 13454–13455.

210   H. Oh, A. M. Ketner, R. Heymann, E. Kesselman, D. Danino, D. E. Falvey and S. R. Raghavan, *Soft Matter*, 2013, **9**, 5025–5033.

211   B. Song, Y. Hu and J. Zhao, *J. Colloid Interface Sci.*, 2009, **333**, 820.

212   J. Stellbrink, B. Lonetti, G. Rother, L. Willner and D. Richter, *J. Phys. Condens. Matter*, 2008, **20**, 404296.

213   A. P. R. Eberle and L. Porcar, *Curr. Opin. Colloid Interface Sci.*, 2012, **17**, 33–43.

214   M.-A. Fardin, L. Casanellas, B. Saint-Michel, S. Manneville and S. Lerouge, *J. Rheol. (N. Y. N. Y).*, 2016, **60**, 917–926.

215   V. A. Parsegian, *J. Theor. Biol.*, 1967, **15**, 70–74.

216   B. Jönsson, H. Wennerström and B. Halle, *J. Chem. Phys.*, 1980, **84**, 2179–2185.

217   R. Strey, *Ber. Bunsenges. Phys. Chem.*, 1996, **100**, 182–189.

218   K. Kratzat and H. Finkelmann, *J. Colloid Interface Sci.*, 1996, **181**, 542–550.

219   B. Lühmann and H. Finkelmann, *Colloid Polym. Sci.*, 1987, **265**, 506–516.

220   X. Tan, R. Zhang, C. Guo, X. Cheng, H. Gao, F. Liu, J. R. Bruckner, F. Giesselmann, M. Prehm and C. Tschierske, *J. Mater. Chem. C*, 2015, **3**, 11202–11211.

221   R. Yang, S. Peng, W. Wan and T. C. Hughes, *J. Mater. Chem. C*, 2014, **2**, 9122–9131.

222   X. Li, L. Fang, L. Hou, L. Zhu, Y. Zhang, B. Zhang and H. Zhang, *Soft Matter*, 2012, **8**, 5532–5542.

223   C. K. Tsung, J. Fan, N. Zheng, Q. Shi, A. J. Forman, J. Wang and G. D. Stucky, *Angew. Chemie - Int. Ed.*, 2008, **47**, 8682–8686.

224   G. J. Soler-Illia and P. Innocenzi, *Chemistry (Easton).*, 2006, **12**, 4478–4494.

225   N. M. Nursam, X. Wang and R. A. Caruso, *J. Mater. Chem. A*, 2015, **3**, 24557–24567.

226   S. Besson, T. Gacoin, C. Ricolleau, C. Jacquiod and J. P. Boilot, *J. Mater. Chem.*, 2003, **13**, 404–409.

227   N. M. Nursam, X. Wang and R. A. Caruso, *ACS Comb. Sci.*, 2015, **17**, 548–569.

228   A. Alagarasi, P. U. Rajalakshmi, K. Shanthi and P. Selvam, *Catal. Today*, 2018, **309**, 202–211.

229   R. Zhang, A. A. Elzatahry, S. S. Al-deyab and D. Zhao, *Nano Today*, 2012, **7**, 344–366.

230   E. Matijević, M. Budnik and L. Meites, *J. Colloid Interface Sci.*, 1977, **61**, 302–311.

231   E. A. Barringer and H. K. Bowen, *J. Am. Ceram. Soc.*, 1982, **65**, C-199-C-201.

232   D. M. Antonelli and J. Y. Ying, *Chem. Mater.*, 1996, **8**, 874–881.

233   J. H. Jean and T. A. Ring, *Langmuir*, 1986, **2**, 251–255.

234   J. L. Look and C. F. Zukoski, *J. Colloid Interface Sci.*, 1992, **153**, 461–482.

235   S. Eiden-Assmann, J. Widoniak and G. Maret, *Chem. Mater.*, 2004, **16**, 6–11.

236   C. V Stimulated, A. Phys, Y. Lu, R. Ganguli and C. A. Drewien, 1997, **389**, 651–655.

237   L. Zhao, Y. Yu, L. Song, M. Ruan, X. Hu and A. Larbot, 2004, **263**, 171–177.

238   S. Johan, F. Herregods, K. Wyns, M. Mertens, R. Kemps, A. Buekenhoudt and V. Meynen, *Thin Solid Films*, 2015, **593**, 17–25.

239   D. Chen, L. Cao, F. Huang, P. Imperial, Y. B. Cheng and R. A. Caruso, *J. Am. Chem. Soc.*, 2010, **132**, 4438–4444.

240   X. Wang, L. Cao, D. Chen and R. A. Caruso, *ACS Appl Mater Interfaces*, 2013, **5**, 9421–9428.

241   J. Wei, Y. Liu, J. Chen, Y. Li, Q. Yue, G. Pan, Y. Yu, Y. Deng and D. Zhao, *Adv Mater*, 2014, **26**, 1782–1787.

242   Y. Zakrevskyy, M. Richter, S. Zakrevska, N. Lomadze, R. von Klitzing and S. Santer, *Adv. Funct. Mater.*, 2012, **22**, 5000–5009.

Chapter 2

Experimental

The AzoPS in this work were first synthesised as part of an M.Sc. thesis entitled "*Investigation of the Structure-Property Relationships of Photoactive Surfactants*", Elaine Kelly, Trinity College Dublin, 2017, which focused on the very low-concentration and surface tension behaviour of AzoPS and the fluorescence-self-assembly behaviour of aggregation-induced emissive surfactants. As such, the materials synthesis and basic characterisation details of AzoPS will be mentioned only briefly here, with the details available in the Appendix.

2.1 Materials

Azobenzene photosurfactants (Figure 2.1) were synthesised according to a procedure adopted from literature. The essential synthesis and characterisation data (^{1}H and ^{13}C nuclear magnetic resonance spectroscopy, mass spectrometry, Fourier-Transform infrared spectroscopy *etc.*) for each AzoPS can be found in the Appendix (Section A.2.1). Four different AzoPS structures ($C_2AzoOC_4E_4$, 4-ethyl-4'-(mono-tetraethylene glycol) butyloxy azobenzene; $C_6AzoOC_4E_4$, 4-hexyl-4'-(mono-tetraethylene glycol) butyloxy azobenzene; $C_8AzoOC_4E_4$, 4-octyl-4'-(mono-tetraethylene glycol) butyloxy azobenzene; $C_8AzoOC_8E_4$, 4-octyl-4'-(mono-tetraethylene glycol) octyloxy azobenzene) will be investigated in this work. Table 2.1 lists the CMCs for each of the isomeric forms. The CMC values are the average of the CMCs determined by dynamic light scattering and surface tensiometry. These individual values can be found in the Appendix (Table A.2.1). These surfactants are named more generally as $C_nAzoC_mE_4$, where n and m correspond to the number of carbons in the pendant tail and spacer group, respectively, and E_4 refers to the tetraethylene glycol head group. The prefix *trans-* or *cis-* is used to indicate the isomeric state of the surfactant.

Deionised water and Millipore water (18.2 mΩ cm) were obtained through an in-house water purification system. Ammonium hydroxide (25%), ethanol (99.8+%), KCl (>99.0%), titanium (IV) isopropoxide (98.0+%) and methyl orange (pure, indicator grade) were obtained from Fisher Scientific.

Table 2.1. CMC values for each AzoPS in the *trans* or *cis* form. Values are obtained from the average across both surface tension and dynamic light scattering measurements. The uncertainty associated with each value is calculated from the standard deviation and given in brackets.

AzoPS	CMC_{trans} (µM)	CMC_{cis} (µM)
$C_2AzoOC_4E_4$	43.5 (6.2)	45.5 (19.2)
$C_6AzoOC_4E_4$	30.0 (7.6)	26.6 (5.3)
$C_8AzoOC_4E_4$	14.6 (2.6)	16.2 (2.2)
$C_8AzoOC_8E_4$	105.7 (34.0)	127.1 (14.0)

2.2 Instrumentation

Full details of the experimental information (*e.g.* sample concentration, precise instrument configurations and parameters) will be given in each of the relevant results chapters. General information related to each of the instruments used is given below.

UV-Vis Absorption Spectroscopy

UV-Vis absorption spectra were recorded on either a Perkin Elmer Lambda 35 spectrometer (slit width 0.5 nm) or an Edinburgh Instruments DS5 dual beam spectrophotometer. Measurements were performed in quartz cells (1 cm path length).

UV-Vis absorption spectra for in-situ SANS measurements were performed using an Ocean Optics FX UV-Vis spectrometer with a preconfigured wavelength range of 200–850 nm, 25 μm slits and lenses for enhanced sensitivity, an Ocean Optics DH-2000-DUV lamp with shutter (190–2500 nm) as the source and Oceanview software.

Diffuse-Reflectance UV-Vis measurements were performed on a Perkin Elmer Lambda 35 spectrometer. Powder samples were mounted on a home-made holder with a quartz front with measurements performed over the range 200–2000 nm.

Light Irradiation

AzoPS Photoisomerisation: Irradiation was performed using either UV (365 nm, 3.7 mW cm^{-2} 4 cm from source) or blue light (465 nm, 1.3 mW cm^{-2} 4 cm from source) LEDs in a custom built light-box. The irradiance values were obtained using a photodiode (area of 1 cm^2) and a Keithley sourcemeter. The measured current was converted to power using the response curve of the photodiode.

Photocatalysis: A MRL-58 multiple ray lamp with a 365 nm bulb (8 W) was used to provide UV light for irradiation of photocatalysis experiments.

Small-Angle Scattering

Small-angle scattering is a key technique in this work. As it is a less common technique, the fundamental principles will be summarised briefly before the Instrumentation is described. Small-angle scattering techniques quantify the deflection of incident radiation, $\textbf{\textit{k}}_i$, elastically scattered through an angle, θ, by a sample in solution.[1] The incident radiation is typically either X-ray or neutron, with the former interacting with the electron density of the sample, and the latter interacting with the strong nuclear force.[2,3] The geometry of elastic scattering is shown in Figure 2.2, where $\textbf{\textit{Q}}$ is the *scattering wave-vector,* which represents the transfer of momentum (Equation 2.1). The magnitude of $\textbf{\textit{Q}}$ is known as q, which can be related to real-space through substitution of Equation 2.1 into Bragg's law to yield the useful reciprocal relation given in Equation 2.2.[3–5]

(a)

(b)
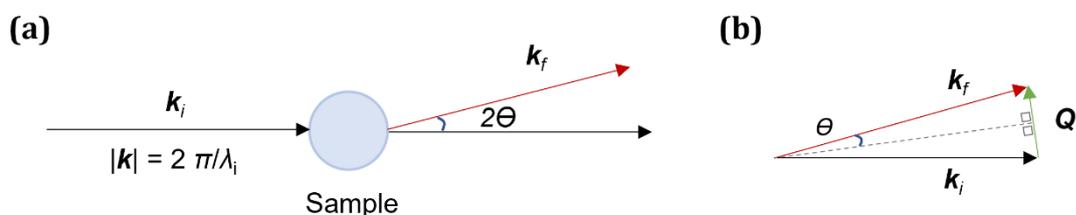
Figure 2.. In SANS incident radiation is elastically scattered off the sample in solution (a) Schematic representation of elastic scattering through an angle of 2θ, where k_i and k_f are the incident and final wave-vectors, respectively. (b) Vector diagram for elastic scattering event, where Q, the scattering wave-vector = $(k_f - k_i)$.

$$|Q| = q = \frac{4\pi sin\theta}{\lambda} \qquad \text{(Eq. 2.1)}$$

$$d = \frac{2\pi}{q} \qquad \text{(Eq. 2.2)}$$

Where d corresponds to the physical distance and λ is the wavelength of the incident radiation. Analysis of the scattering profile can give information on the size, shape and interparticle interactions of the scattering body in solution.[1,2] The key differences between neutron and X-ray scattering are the scattering interactions, the penetration depth and the measurement time. As aforementioned, neutrons are scattered by the strong nuclear force of the atomic nuclei, and are unaffected by the electron density of the sample.[6] This allows neutrons to penetrate further into the bulk of the sample than X-rays. While the degree of X-ray scattering increases with atomic number, the degree of neutron scattering depends on the *neutron scattering length*. This is isotope specific and has a non-linear relationship with atomic number.[7] This means that neutron scattering distinguishes between hydrogen and deuterium, allowing contrast matching (isolation of the scattering contribution from particular parts of the sample through selective deuteration). In general, X-ray scattering measurements tend to be orders of magnitudes faster than neutron scattering measurements (seconds *vs* minutes-hours), so offer advantages for probing kinetics or time-dependent properties of the solution.[1,8]

Small-Angle Neutron Scattering: SANS experiments were performed using the KWS-2 instrument in the Jülich Centre for Neutron Science (JCNS) at the Heinz Maier Leibnitz Zentrum (MLZ) in Garching, Germany.[9] The measurements were performed using sample-to-detector distances of 2, 8 and 20 m and a neutron wavelength of 5 Å ($\Delta\lambda/\lambda$ = 10%), to optimise the q-range of 0.002–0.4 Å^{-1} and the beam flux. These data were converted to absolute scale (cm^{-1}) through reference to the scattering from a secondary standard sample (Plexiglas).

Rheo-SANS: Rheo-SANS measurements were performed at the National Institute for Neutron Science (NIST) Center for Neutron Research in Gaithersburg, Maryland, USA. The measurements were performed using the Very Small-Angle Neutron Scattering

(VSANS) instrument which was fitted with an Anton Paar MCR 501 stress-controlled rheometer.[10,11] Scattering was collected in the q-range of 0.003–0.127 $Å^{-1}$ with sample-to-detector distances of 5 and 17 m, a neutron wavelength of 6 Å and wavelength spread of $\Delta\lambda/\lambda$ of 0.12. The scattering was corrected for empty cell, plexiglass standard and the detector efficiency.

Small-Angle X-ray Scattering: Synchrotron SAXS measurements were performed on the BioSAXS beamline B21, Diamond Light Source, Harwell, United Kingdom.[12] B21 operates in a fixed sample to detector distance (4.014 m) with X-ray beam energy E = 12.4 keV giving a q-range of 0.031–3.8 nm^{-1}. Data were collected using a Pilatus Dectris 2M detector. The background was manually subtracted using ScÅtter.[13]

Form factor models are fitted to the scattering profiles of either SANS or SAXS measurements using SASview,[14] a software package specifically for analysis of small-angle scattering data. The relevant models and their respective equations will be outlined in the Experimental section of the relevant results chapter.

Rheology

Rheology measurements were performed on an Anton Paar MC 301 rheometer. Samples were measured at 25 °C using a cone-plate geometry (50 mm diameter, 1° cone angle, 0.101 mm gap).

Polarised Optical Microscopy

Temperature-controlled POM measurements were carried out at the Jülich Centre for Neutron Science at the Heinz Maier-Leibnitz Zentrum, Garching, Germany by Dr Judith Houston on a Leica DM 6000 Digital Microscope. Samples were imaged with a liquid nitrogen-cooled heating stage.

Transmission Electron Microscopy

TEM measurements were performed on samples dispersed on copper mesh grids and imaged using an FEI Technai F20 transmission electron microscope, with an accelerating voltage of 200 kV, single tilt holder and OneView Camera. TEM measurements were kindly performed by Professor Caterina Ducati and May Ching Lai.

Cryo-TEM

Vitrification was performed using a Thermofisher Vitrobot in a controlled environment. The vitrified specimens were imaged with a ThermoFisher Krios G3i at 300kV acceleration, using a Falcon camera. Cryo-TEM measurements were generously performed by Dr. Giorgio Divitini.

Powder X-ray Diffraction

PXRD measurements were performed on a Bruker D8 Advance instrument with a position-sensitive detector (LynxEye EX). Samples were deposited on a Si zero-background holder and measured using Cu K$_\alpha$ X-ray radiation (λ = 1.5406 Å) across a 2θ range of 10 - 100°, at an increment of 0.02° and dwell time per increment of 0.2 s.

N$_2$ Adsorption

N$_2$ adsorption measurements were kindly performed by Dr David Madden and Dr Ceren Çamur using MicroActive for TriStar II at 77 K.

Differential Scanning Calorimetry

DSC measurements were performed using Perkin Elmer DSC 8000, in the range of 10–80 °C in a nitrogen atmosphere with a heating rate of 5 °C min^{-1}. Samples (<5 mg) were sealed in aluminium crucibles.

Simultaneous Differential Scanning Calorimetry-Thermogravimetric Analysis

SDT measurements were performed on a TA Instruments Q600 SDT instrument. Samples were placed in an aluminium crucible and measured in air across the range 20-650 °C with a heat rate of 5 °C min^{-1}. During Covid-19 restrictions, some measurements were kindly performed by Dr Robert Cornell.

Dynamic Light Scattering

Dynamic Light Scattering measurements were performed using a Malvern Instruments Zetasizer. The instrument is equipped with a He-NE laser (633 nm). The scattering intensity was detected at a backscattering angle of 173° with the choice of appropriate measuring distance and attenuator being automatically selected by the software. The *z*-average value (hydrodynamic diameter, D_H) was obtained through the software, using the Stokes-Einstein equation (Equation 2.3):

$$D_H = \frac{k_B T}{6\pi\eta D}$$ (Eq. 2.3)

where k_B is the Boltzmann constant, T is the solution temperature, η is the solution viscosity and D is the diffusion coefficient. The diffusion coefficient and polydispersity index are obtained *via* Cumulants analysis of the correlation function.

2.3 References

[1]   D. . Sivia, *Elementary Scattering Theory for X- ray and Neutron Users*, Oxford
        University Press, Oxford, 1st edn., 2011.

[2]   L. A. Feigin and D. I. Svergun, *Structure Analysis by Small Angle X-ray and Neutron
        Scattering*, Plenum, New York, 1987.

[3]   O. Glatter and O. Kratky, *Small Angle X-ray Scattering*, Academic Press, London,
        1982.

[4]   H. Schnablegger and Y. Singh, *The SAXS Guide*, Anton Paar GmbH, Graz, Austria,
        3rd edn., 2013.

[5]   A. Guiner and G. Fournet, *Small Angle Scattering of X-rays*, Wiley, 1955.

[6]   J. . Lamarch and A. Barratta, *Introduction to Nuclear Engineering*, Prentice Hall,
        New Jersey, 3rd edn., 2001.

[7]   J. . Dudserstadt and L. . Hamilton, *Nuclear Reactor Analysis*, Wiley, 1976.

[8]   H. B. Stuhrmann, *Prog. Cryst. Growth Charact.*, **1989**, 18, 1–19.

[9]   A. Radulescu, V. Pipich, H. Frielinghaus and M.- Appavou, *J. Phys. Conf. Ser.*, **2012**,
        351, 012026.

[10]   L. Porcar, D. Pozzo, G. Langenbucher, J. Moyer and P. D. Butler, *Rev. Sci. Instrum.*,
        2011, 82, 1–8.

[11]   R. P. Murphy, Z. W. Riedel, M. A. Nakatani, P. F. Salipante, J. S. Weston, S. D. Hudson
        and K. M. Weigandt, *Soft Matter*, **2020**, 16, 6285–6293.

[12]   N. P. Cowieson, C. J. C. Edwards-Gayle, K. Inoue, N. S. Khunti, J. Doutch, E. Williams,
        S. Daniels, G. Preece, N. A. Krumpa, J. P. Sutter, A. D. Tully, N. J. Terrill and R. P.
        Rambo, *J. Synchrotron Radiat.*, **2020**, 27, 1438–1446.

[13]   S. Förster, L. Apostol and W. Bras, *J. Appl. Crystallogr.*, **2010**, 43, 639–646.

[14]   *http://www.sasview.org/*, accessed 10/19.

Chapter 3

Light-Responsive Self-Assembly and Flow Behaviour of AzoPS

3.1 Introduction

As discussed in Chapter 1, AzoPS can isomerise between *cis* and *trans* forms upon illumination with UV and blue light, respectively, with photoisomerisation providing a means to changing the polarity and shape of the surfactant on-demand. The interplay between these properties also affects the self-assembly behaviour of AzoPS, which can have a further domino-effect on the bulk properties of the surfactant solution, such as its rheological behaviour, long-range order and optical anisotropy. In this Chapter, the ability to propagate changes in self-assembly on the molecular level *via* isomerisation to macroscopic properties such as viscosity and flow behaviour will be investigated. First, *in-situ* UV-Vis absorption spectroscopy will be integrated with SANS to determine the extent of AzoPS photoisomerisation in real time. By correlating this knowledge to the scattering profile, an understanding of the dynamic changes in the micellar structure as a result of photoisomerisation can be obtained. The results from this initial exploration will be used to create light-responsive viscoelastic fluids, using the photosurfactants $C_6AzoOC_4E_4$ and $C_8AzoOC_8E_4$ (Figure 3.1), which are characterised in terms of their self-assembly and rheological behaviour. The relevant literature to contextualise this work will be discussed below, before the results are described and discussed.

UV-Vis absorption spectroscopy is a powerful tool to track the photoisomerisation of AzoPS and to characterise the proportion of *cis*- and *trans*-isomers in solution, as each presents a different optical fingerprint.[1,2] As AzoPS become increasingly used in emerging technologies,[3–6] it is crucial that their dynamic self-assembly behaviour under photoisomerisation be understood. However, while the self-assembly behaviour of the *cis*- and *trans*-PSS at equilibrium has been reported for several AzoPS structures,[7–10] few studies follow the isomerisation process and self-assembly changes *in-situ*. Tabor *et al*. used time-resolved (TR)-SANS to track the structural changes of three carbohydrate-based AzoPS over time.[11] They observed that upon UV irradiation, and depending on the concentration regime, either a total loss of micellar structure, a decrease in aggregation number or a change in the micellar dimensions can occur. Lund *et al.* used TR-SAXS to study the kinetics of micelle dissolution and reformation of the cationic AzoPS, AzoTMA, (4-butyl-4′-(3-trimethylammoniumpropoxy)-phenylazobenzene) at concentrations close to the CMC.[12] It was found that AzoTMA could transition between monomers and aggregates in timescales of less than a few seconds, without the formation of premicellar clusters. Neutral AzoPS structures, such as those with a tetraethylene glycol head group, are less investigated compared to their cationic counterparts and have been used in fewer applications.[13,14] In the first part of this chapter, the light-dependent self-assembly of the

neutral AzoPS, $C_8AzoOC_8E_4$, around the CMC of the *trans*-isomer will be investigated through *in-situ* UV-Vis absorption spectroscopy integrated with SANS.

The second part of this chapter focuses on the formation of wormlike micelles by both $C_8AzoOC_8E_4$ and $C_6AzoOC_4E_4$. WLMs often lead to fluids with useful rheological properties, such as high viscosities and viscoelastic behaviour. Most reports of WLMs involve cationic surfactants, such as cetyl trimethyl ammonium bromide (CTAB), with the addition of salts. As mentioned in the Introduction, it is possible to create stimuli-responsive rheological fluids by modifying the environment of the WLM. A review of recent work in this area has been undertaken by Chu *et al.*[15] To create light-responsive rheological fluids, most researchers have taken formulations known to form WLMs (*e.g.* CTAB and salt) and added an additional light-sensitive component (usually azobenzene- or spiropyran-based). This approach has had success but requires the creation of complex, multicomponent formulations.[16–18] For example, Sakai *et al.* added a cationic AzoPS (4-butylazobenzene-4′-(oxyethyl)-trimethylammonium bromide, AZTMA) to a CTAB/sodium salicylate (NaSal) mixture to form a high viscosity, viscoelastic solution.[19] AZTMA did not form WLMs by itself, even with the addition of NaSal. Upon UV irradiation, the viscosity of the ternary solution dropped from 100 to 0.1 Pa·s. This behaviour was attributed the bulkier *cis*-isomer destroying the network structure of the WLMs.

Lee *et al.* created photoresponsive reverse wormlike micelles with controllable viscoelastic behaviour by doping lecithin/sodium deoxycholate reverse micelles with a light-responsive spiropyran molecule.[20] This three-component system formed a viscoelastic fluid initially, attributed to the presence of WLMs. Upon isomerisation of the spiropyran to the open form, the fluid viscosity dropped from 2.5 to 0.2 Pa·s. This system is one of the simplest created to date, in that it is made entirely of commercially available components. However, it is still a ternary system. A single-component formulation is inherently less complex, being simpler to create and understand. Single-component systems are also more desirable for integration with applications as additional components may limit the compatibility of the formulation for a given use. For example, the need for a saline solution could lead to issues with salt deposition, surface fouling and solution salt depletion, depending on the application.

To date, there have been very few reports of a single-component light-responsive WLM solution. Before the publication of this work, only one report existed; Song *et al.* created an azobenzene-based gemini surfactant (sodium-2,20-(diazene-1,2-diylbis(4,1-phenylene))-didodecanoate, C12-azo-C12).[21] An aqueous solution of this surfactant results in a viscous fluid, with a zero-shear viscosity >700 Pa s. This high viscosity was attributed to the presence of the rigid azo-spacer keeping the two hydrophobic tails apart.

According to the authors, this results in a 'pseudo-volume' between the tails, increasing the packing parameter and favouring WLMs. Freeze-fracture-TEM suggested the presence of a densely entangled network. Upon UV irradiation and formation of the *cis*-isomer, the distance between the two ionic head groups is reduced and the entangled network is disrupted. As a result, the zero-shear viscosity dropped by 5 orders of magnitude to ~0.007 Pa·s. The viscosity could be recovered by reverse isomerisation. This year, an additional single-component photorheological fluid was reported by Butler *et al.*[22] They synthesised a zwitterionic betaine AzoPS, AZOB-C6 (2-(dimethyl(2-(4-((4-(4-methylpentyl) phenyl) diazenyl) phenoxy) ethyl) ammonio) acetate) which formed a viscoelastic network of WLM in the *trans*-form and low viscosity ellipsoidal aggregates upon conversion to the *cis*-isomer. Their work emphasised the role of π-π stacking interactions in influencing the aggregate structure and contributing towards micellar rigidity. They also highlighted a five-fold increase in apparent diffusion of particles dispersed in the micellar network, upon UV irradiation and conversion from the WLM network to the ellipsoidal aggregates.

In this work, the ability of light to disrupt the packing of the two AzoPS, $C_8AzoOC_8E_4$ and $C_6AzoOC_4E_4$, and subsequently alter the rheological behaviour on-demand will be investigated here through steady-state and oscillatory rheology measurements. Cryo-TEM and SAXS will also be used to gain insights into the nanostructure of the surfactant solutions. The structures of the two AzoPS which are the focus of this chapter are shown in Figure 3.1.
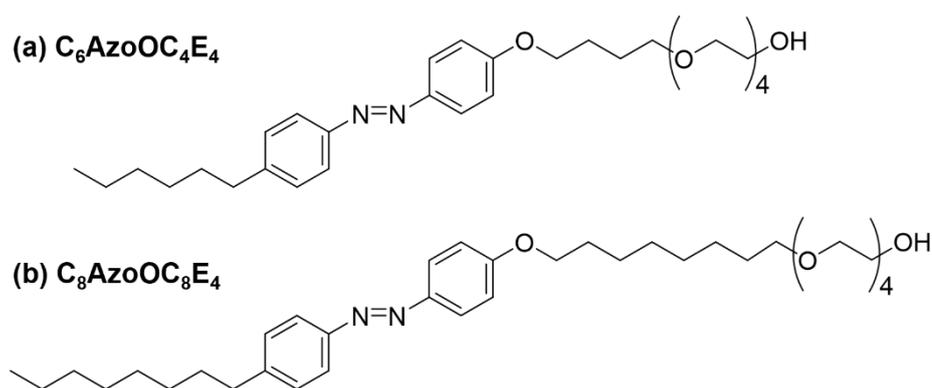
Figure 3.1. Molecular structures of the two neutral AzoPS investigated in this chapter. (a) $C_6AzoOC_4E_4$ with a four-carbon spacer and six carbon pendant tail and (b) $C_8AzoOC_8E_4$ with an eight-carbon spacer and eight-carbon pendant tail. Both photosurfactants have an azobenzene core and a neutral tetraethylene glycol head group.

3.2 Experimental

Materials

Azobenzene photosurfactants were synthesised as outlined in the experimental (Chapter 2). Deionised water and Millipore water (18.2 mΩ cm) were obtained through an in-house water purification system. D_2O was obtained on-site at the Jülich Centre for Neutron Science (JCNS) at the Heinz Maier Leibnitz Zentrum (MLZ) in Garching, Germany.

Instrumentation

UV-Vis Absorption Spectroscopy: Static UV-Vis absorption spectra were recorded on a Perkin Elmer Lambda 35 spectrometer with a slit width of 0.5 nm. Measurements were carried out in quartz cells with a 1 cm path length. All samples were prepared in deionised water. The experimental set-up for simultaneous UV-Vis absorption-SANS measurements is shown in Figure 3.2. The device setup includes an Ocean Optics FX UV-Vis spectrometer with preconfigured wavelength range of 200-850 nm, 25 µm slits and lenses for enhanced sensitivity, an Ocean Optics DH-2000-DUV lamp with shutter (190-2500 nm) and Oceanview software. Fibre optic cables were positioned perpendicular to the direction of the neutron beam. The cell holder was adapted from an Ocean Optics adjustable collimating lens holder. For light irradiation, high power, mounted light-emitting diodes (LEDs), blue (36.4 µW, 450 nm) and ultraviolet (57.7 µW, 365 nm) were purchased from Thorlabs, Inc.

Rheology Measurements: Rheology measurements were performed on an Anton Paar MC 302 rheometer. Samples were measured at 25 °C using a cone-plate geometry (50 mm diameter, 1° cone angle, 0.101 mm gap). An amplitude sweep was performed to ensure that the samples were in the linear response regime. Frequency sweeps to determine the storage (G') and loss moduli (G'') were measured at 1% strain rate. Fits to the Maxwell Model were performed using the software package RepTate.

SANS Measurements: SANS experiments were performed using the KWS-2 instrument in the Jülich Centre for Neutron Science (JCNS) at the Heinz Maier Leibnitz Zentrum (MLZ) in Garching, Germany.[23] The measurements were performed using sample-to-detector distances of 2, 8 and 20 m and a neutron λ of 5 Å ($\Delta\lambda/\lambda$ = 10%), to optimise the q-range of 0.002-0.4 Å^{-1} and the beam flux. These data were converted to absolute scale (cm^{-1}) through reference to the scattering from a secondary standard sample (Plexiglas). Static measurements were performed on each sample before irradiation with UV light, under UV light, and under blue light. The light irradiation setup can be found in Figure 3.2.
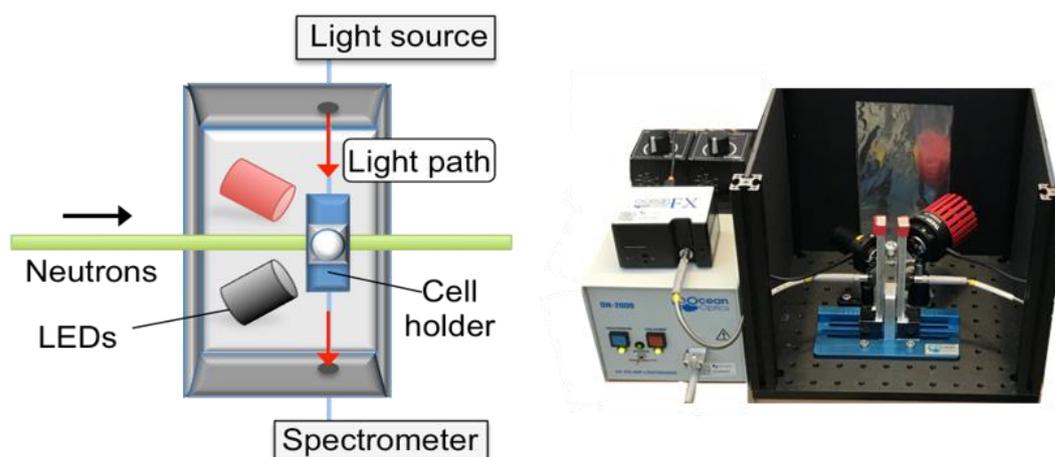
Figure 3.2. Schematic overview and photograph of the setup used for an *in-situ* UV-Vis absorption spectroscopy-SANS experiment with LED (UV or blue) light irradiation**.**

Time-resolved scattering profiles and UV-Vis absorption spectra were collected under irradiation with UV light and blue light for the *trans-cis* and *cis-trans* isomerisation processes, respectively. Each isomerisation took 10-15 min. SANS data were initially recorded over 15 s intervals and combined post-measurement into 60 s intervals. The scattering patterns were averaged over at least 5 cycles to improve statistics. *In-situ* UV-Vis absorption spectra were recorded every second. UV-Vis spectra were compared across each SANS averaging cycle to ensure no deterioration of the sample had occurred. It was found that the final absorption spectrum, after several hours of photoisomerisation cycles, was identical to the initial one (Appendix, Figure A.3.1). Due to the high absorption coefficient of the AzoPS (ε = 12,300 L mol^{-1} cm^{-1}), sample concentrations were limited to 0.2 mM to avoid the occurrence of no light transmission.

SAXS Measurements: Synchrotron SAXS measurements were performed on the BioSAXS beamline B21, at Diamond Light Source, Harwell, United Kingdom. B21 operates with a fixed sample-to-detector distance (4.014 m) with an X-ray beam energy E = 12.4 keV, giving a *q*-range of 0.031–3.8 nm^{-1}.[24] Samples were loaded into polymerase chain reaction well plates in an automated sample changer. Samples (30 µL) were then delivered into a temperature-controlled quartz capillary and exposed for 3 s, collecting 60 frames at 20 °C. Data were collected using a Pilatus Dectris 2M detector. The background was manually subtracted using the ScÅtter software.[25] Laboratory SAXS measurements were performed on the GALAXI beamline at the Jülich Centre for Neutron Science.[26] GALAXI uses a Bruker AXS Metaljet X-ray source working with gallium K$_\alpha$ X-rays (λ = 1.34 Å), and a sample-to-detector distance of 80 cm, resulting in the q-range of 0.1–7.0 nm^{-1}. Data were collected using a Pilatus Dectris 1M detector. Samples (~50 µL) were inserted into borosilicate

glass capillaries (1.0 mm), which were then sealed. The sample-to-detector distance was calibrated using the Bragg reflections from silver behenate.

SAS Models: The scattering function, ($S(q, L, b)$), of a semi-flexible chain with a uniform scattering length density and elliptical cross-section, taking excluded volume effects into account, is used here to fit the scattering profiles of WLM and is given by:[27,28]

$$S(q,L,b) = [1 - w(qR_g)S_{Debye}(q,L,b) + f_{corr}(q)w(qR_g)[1.22(qR_g)^{\frac{-1}{0.585}} +$$

$$0.4288(qR_g)^{-\frac{2}{0.585}} - 1.651(qR_g)^{\frac{-3}{0.585}}] + \frac{Cn_b}{n_b}\{\frac{4}{15} + \frac{7}{15u} - \left(\frac{11}{15} + \frac{7}{15u}\right) \times e^{-u(q,L,b)}\}$$

(Eq. 3.1)

where $w(qR_g)$ is an empirical crossover function, $n_b = L/b$ and $f_{corr}(q)$ is a correction factor added by Chen *et al.* to correct unphysical errors occurring at certain L/b ratios.[28] Further details of $f_{corr}(q)$, $w(qR_g)$, $S_{Debye}(q, L, b)$ and $u(q, L, b)$ can be found in the work of Pederson *et al.*[27] and Chen *et al.*[28] This form factor is normalised by particle volume, averaging over all possible orientations of the flexible cylinder.

Provided that the length scales of L and R_{CS} are well-separated, generally the high q scattering intensity from the cylindrical cross-section of the WLM (in this case, elliptical cylindrical) can be separated from that of the semi-flexible wormlike chain as given by:[29]

$$< P(q,c) >= P_{WC}(q,L(c),b)P_{CS}(q,R_{CS})$$ (Eq. 3.2)

where $<P(q, c)>$ is the full micellar form factor, c is the concentration, P_{WC} is a form factor, in this case, $S(q, L, b)$, used to fit the semi-flexible chain as outlined above in Eq. 1, and P_{CS} is the form factor describing the cross-sectional radius of the WLM. Analysis of the scattering intensity in the high q region can be separated out in this manner as the local cylindrical cross-section is generally unaltered with changing surfactant concentration (WLMs tend to grow 1D along their length) and inter-micellar interactions are also screened on this local level. $P_{CS}(q)$ is described by an elliptical cylinder model in this work, with a scattering intensity given by:[30,31]

$$I(q) = \frac{1}{v}\int d\psi \int d\phi \int d\,\rho(\theta,\phi,\psi)F^2(q,\alpha,\psi)\sin(\theta)\,d\theta$$ (Eq. 3.3)

where:

$$F(q,\alpha,\psi) = 2\frac{J_1(x)\sin(y)}{xy}$$ (Eq. 3.4)

and

$$x = q\sin(\alpha)[r_{major}^2 sin^2(\psi) + r_{minor}^2 \cos(\psi)]^{\frac{1}{2}}\,;y = \frac{L}{2}qcos(\alpha)$$ (Eq. 3.5)

θ and ϕ define the orientation of the axis of the cylinder, ψ and α define the orientation of the major axis of the ellipse with respect to the vector q, J_1 is the Bessel function of first order and r is the cylinder radius.

The scattering from fractal-like aggregates was modelled according the following equation:[32]

$$I(q) = \phi V_{block}(\rho_{block} - \rho_{solvent})^2 P(q)S(q) + bkg \qquad \text{(Eq. 3.6)}$$

where in this case, ϕ represents the volume fraction of the spherical building block particles comprising the fractal-like aggregate, V_{block} is the volume of a single building block, ρ_{block} and $\rho_{solv.}$ are the scattering length densities of the spherical building blocks and solvent, respectively. P(q) and S(q) are the scattering from the randomly distributed spherical blocks and the interference from such blocks arranged in fractal-like aggregates (Equations 3.7-3.9).

$$P(q) = F(qR_0)^2 \qquad \text{(Eq. 3.7)}$$

$$F(qR_0) = 3[\sin(qR_0) - qR_0 cos(qR_0)] \Big/ (qR_0)^3 \qquad \text{(Eq. 3.8)}$$

$$S(q) = 1 + \frac{D_f \Gamma(D_f - 1)}{[1 + \frac{1}{(q\xi)^2}]^{(D_f-1)/2}} \frac{\sin\left[(D_f - 1)\tan^{-1}(q\xi)\right]}{(qR_0)^{D_f}} \qquad \text{(Eq. 3.9)}$$

where ζ is the correlation length, R_0 is the radius of the building block, $\Gamma(x)$ is the gamma function of argument x, and D_F represents the fractal dimension. All model fittings were carried out using either the SASview 4.0.1 or 5.0.3 software.[31]

Cryo-Transmission Electron Microscopy: Vitrification was performed using a Thermofisher Vitrobot in a controlled environment. *Trans* samples were prepared under ambient light, while *cis* samples were irradiated with UV light for 90 min prior to vitrification. A small volume (2.5 µL) of AzoPS solution (0.5 wt% in water) was deposited on a Quantifoil 1.2/1/3 holey carbon film. The sample was blotted for 2.5 s and plunged into liquid ethane to form the vitrified specimens. Specimens were stored in liquid nitrogen (-196 °C) until imaging. The vitrified specimens were imaged with a ThermoFisher Krios G3i at 300kV acceleration, using a Falcon camera. Cryo-TEM measurements were kindly performed by Dr Giorgio Divitini.

Chemical Structure Modelling Engine: Three-dimensional models of chemical structures were created using the PerkinElmer Informatics software Chem3D. The algorithm is based on modified molecular mechanics, which consider bond stretching, angle bending, internal rotation and van der Waals interactions. While this is not a full-scale molecular mechanics engine, it produces a reasonable estimation of the molecular conformation.

3.3 Results

3.3.1. Combined SANS and UV-Vis Absorption Spectroscopy to Investigate the Structure-Self-Assembly Relationship of a Model AzoPS

First, the time-dependent self-assembly of the different photoisomers of $C_8AzoOC_8E_4$ were investigated. Critical to relating the self-assembly behaviour of AzoPS to the extent of photoisomerisation in real-time are the different optical fingerprints of the *cis*- and *trans*-isomers. Figure 3.3 shows the UV-Vis absorption spectra of $C_8AzoOC_8E_4$ (0.065 mM in water, CMC_{trans} = 0.11 mM) in both the *cis*- and *trans*-PSS, and the native *trans*-form. The more thermodynamically stable *trans*-isomer (by ~50 kJ mol^{-1})[33] can be identified from the $\pi \rightarrow \pi^*$ band at 332 nm. Photoisomerisation to the *cis*-isomer upon UV irradiation is confirmed by a change of the $\pi \rightarrow \pi^*$ absorption wavelength from 332 to 308 nm, with a concurrent decrease in intensity, along with the appearance of a new absorption band ($n \rightarrow \pi^*$) at 445 nm.[2] As outlined earlier, rather than an assembly of 100% *cis*-AzoPS being obtained, a photostationary state which consists of a ratio of the two isomers emerges.[8] The *cis*-PSS can be calculated from the ratio of the *cis*-PSS absorbance to 100% *trans*-absorbance, at a given wavelength. This is referred to as the *degree of isomerisation*.[8] The degree of isomerisation from *trans*- to *cis*-$C_8AzoOC_8E_4$ is 61%. The *trans*-isomer can be recovered by irradiation with blue light, yielding an assembly of 90% *trans*-isomers. Further information on the calculation of the PSS can be found in the Appendix (Section A.2.3).
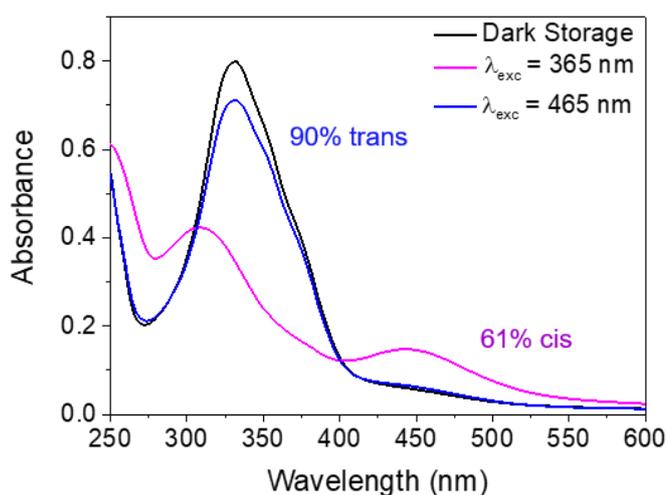
Figure 3.3. UV-Vis absorption spectra of $C_8AzoOC_8E_4$ (0.065 mM in water) for the native *trans*-state (black), *cis*-PSS (pink) and *trans*-PSS (blue). The photostationary states are formed using either UV or blue light, respectively.

SANS is an excellent way to determine the shape and dimensions of micellar aggregates. The scattering profiles and corresponding absorption spectra obtained from combined *in-situ* UV-Vis absorption spectroscopy and SANS measurements of $C_8AzoOC_8E_4$ (0.2 mM) are shown in Figure 3.4. This concentration was chosen to maximise the scattering count rate without exceeding the linear response range of the detector of the spectrometer. This concentration is above the CMC of both the *cis-* and *trans*-states (CMC_{trans} = 0.11 mM; CMC_{cis} = 0.13 mM, Appendix Table A.2.1.) with $C_8AzoOC_8E_4$ appearing fully soluble at this concentration to the naked eye.

SANS data are often interpreted in terms of scaling concepts, which provides information about the aggregate shape and fractal dimension. This can be used to inform the choice of form factor. $C_8AzoOC_8E_4$ initially presents a scattering profile characteristic of wormlike micelles, with varying slopes for the decay in intensity across the entire q range (Figure 3.4a). Such a change in gradient implies the presence of multiple length scales.[29] This assignment of WLMs is supported by the rheological behaviour of the surfactant, which will be discussed further in Section 3.2.2. These asymptotic regions correspond to the different length scales of the physical parameters of the WLM (L_c, L_K, R_{CS}). At low q the scattering profile is distinguished by the self-avoiding random walk of the semi-flexible chain, characterised by a decay of approximately q^{-2}.[27,29] In the mid q-region (~ 0.011 Å^{-1}), where shorter length scales are probed, a decay of q^{-1} can be observed. This correlates to scattering of rods or cylinders, reflecting the local stiffness of the wormlike chain.[27,29] Scattering at higher q corresponds to the cross-sectional radius.

Provided the length scales of L_c and R_{CS} are well separated (as evidenced by the distinct regions here), the scattering from the cross-sectional radius at high q can be separated from that of the bulk chain at lower q.[29] The bottom scattering profile in Figure 3.4a (60 s UV irradiation) is fit in this manner, by deconvoluting the data into two contributions, one from the overall semi-flexible chain of the WLM (flexible elliptical cylinder model fitted from 0.002 – 0.1 Å^{-1}) and one corresponding to the more rigid constituent cylinders (elliptical cylinder model fitted from 0.1 – 0.35 Å^{-1}). This approach could be used for the first three scattering profiles (60–180 s of UV illumination), after which a transition to a fractal-like aggregate was observed (Figure 3.4). With increasing UV irradiation time, the q^{-1} region at ~ 0.011 Å^{-1} diminishes, ultimately resulting in a smooth decrease in scattering intensity that decays as $q^{-2.6}$ in the low- and mid-q regions from 420 seconds onwards. Scalings of q^n with $2 > n > 3$ in this region are commonly ascribed to fractal aggregates.[32] Due to the transitionary nature of these scattering profiles, these fits are cautiously assigned and the physical parameters resulting from them will not be discussed in detail. (see Appendix, Tables A.3.1, A.3.2) The intermediate

scattering profiles at 240 and 300 s could not be well described by either the WLM or fractal model fitting approaches, suggesting that the most significant micellar rearrangements occur within this time-frame.

The observed changes in the micelle structure correspond to changes in the UV-Vis absorption spectra, where the $\pi \rightarrow \pi^*$ band decreases in intensity during the first 180 s of irradiation, blue-shifts during 240–300 s irradiation, before finally maintaining intensity and wavelength from 360 s onwards. This implies that there is no significant lag time and that variations in the aggregate structure arise concurrently with molecular isomerisation. The photoisomerisation reaction follows first-order kinetics (Figure 3.4c, inset) with a rate constant of 8.6×10^{-3} s^{-1}, as commonly observed for azobenzene systems.[3,34,35] This suggests that the AzoPS solution was not so strongly absorbing as to result in diffusion-limited kinetics, as has been reported in some cases.[11]
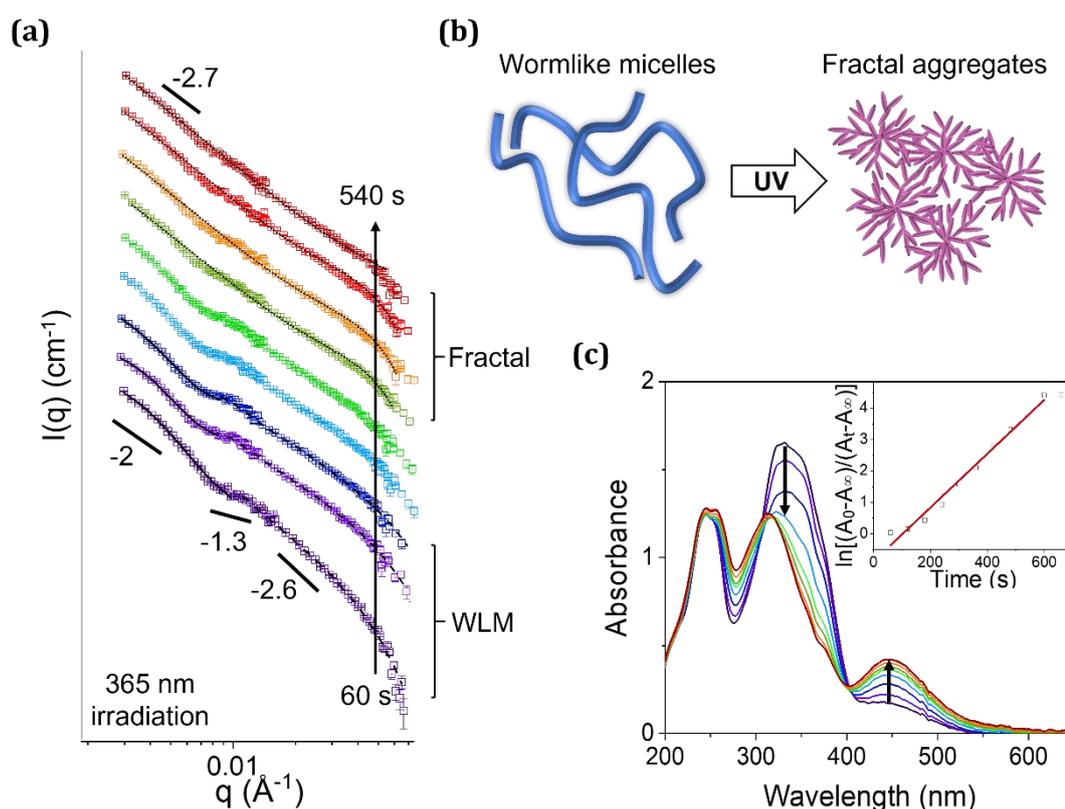
Figure 3.4. Self-assembly behaviour of C$_8$AzoOC$_8$E$_4$ in D$_2$O (0.2 mM) upon *trans-cis* photoisomerisation. (a) SANS scattering profiles as a function of UV irradiation time. C$_8$AzoOC$_8$E$_4$ transitions from wormlike micelles to fractal-like aggregates. Fits to the flexible elliptical cylinder (solid), elliptical cylinder (dashed) and fractal model (dotted) are shown. The scattering curves have been offset for clarity. The solid black lines indicate the slopes in each *q* regime. (b) Schematic representation of the wormlike micelle to fractal aggregate transition. (c) *In-situ* UV-Vis absorption spectra upon UV-irradiation. Inset shows the first order reaction kinetics.

The scattering profiles and corresponding absorption spectra for the reverse isomerisation under blue light are shown in Figure 3.5. $C_8AzoOC_8E_4$ was found to form WLMs in all cases. With increasing irradiation time, $C_8AzoOC_8E_4$ transitions from long ribbon-like WLMs to WLMs consisting of elliptical cylinders of a lower eccentricity. This development is marked by a change in the low q slope from q^{-2} to $q^{-1.8}$ and from 240 s onwards, a return of the plateau at ~0.011 Å^{-1}. As this plateau becomes more pronounced, deconvolution of the scattering profile into fits from two model contributions, as previously outlined, is required. It is apparent that changes to the self-assembled AzoPS structure occur quite rapidly, with variations in the scattering profiles occurring on the same timescale as changes in the UV-Vis absorption spectra. Despite the similarity of the first scattering profile in Figure 3.5 (60 s, blue light) with the final one of Figure 3.4 (540 s, UV light), a flexible elliptical cylinder model was inadequate to describe the former scattering profile (Appendix, Figure A.3.2). This indicates that after only 60 s of illumination with blue light, the majority *cis*-AzoPS solution can be returned to WLMs. The *cis-trans* photoisomerisation reaction also follows first-order kinetics, with a rate constant of 4.7×10^{-3} s^{-1} (Figure 3.5, inset). No further changes to the absorption spectra are observed after 540 s of either UV or blue light irradiation, indicating that the *cis*- and *trans*-PSS are reached. The degree of isomerisation was found to be 58% and 86% for the *cis*- and *trans*-PSS respectively. These values are in good agreement with those obtained previously from static measurements at concentrations below the CMC. (Figure 3.3).

The changes in self-assembled structure upon photoisomerisation are explained by the difference in polarity and geometry between the isomers. *Cis*-azobenzene has a kink in the otherwise linear $C_8AzoOC_8E_4$ structure, disrupting its ability to form WLMs. There are some key similarities between WLMs and fractal aggregates. WLMs are a semi-flexible chain consisting of many locally rigid cylinders. Likewise, fractals comprise many self-similar constituent parts. The packing parameter, P, for $C_8AzoOC_8E_4$ is 0.42 (Appendix Table A.2.3), with values of $1/3 < P < 1/2$ being typical for the formation of cylinders.[36,37] It seems $C_8AzoOC_8E_4$ has a preference to self-assemble into cylindrical aggregates, which, upon incorporation of a "bent" azobenzene core (and associated change in polarity), prefer to manifest as fractals rather than wormlike micelles. This is further supported by the fact that the scattering intensities are on the same order under both illumination conditions. (Appendix, Figure A.3.3). Due to the difference in CMC between *cis*- and *trans*-isomers it would be expected for more monomers to be present for the assemblies formed under UV light compared to under blue light. As the scattering intensity remains roughly similar it can be concluded that the effective size of the scattering bodies is comparable for both the WLM and fractal aggregates.[38]
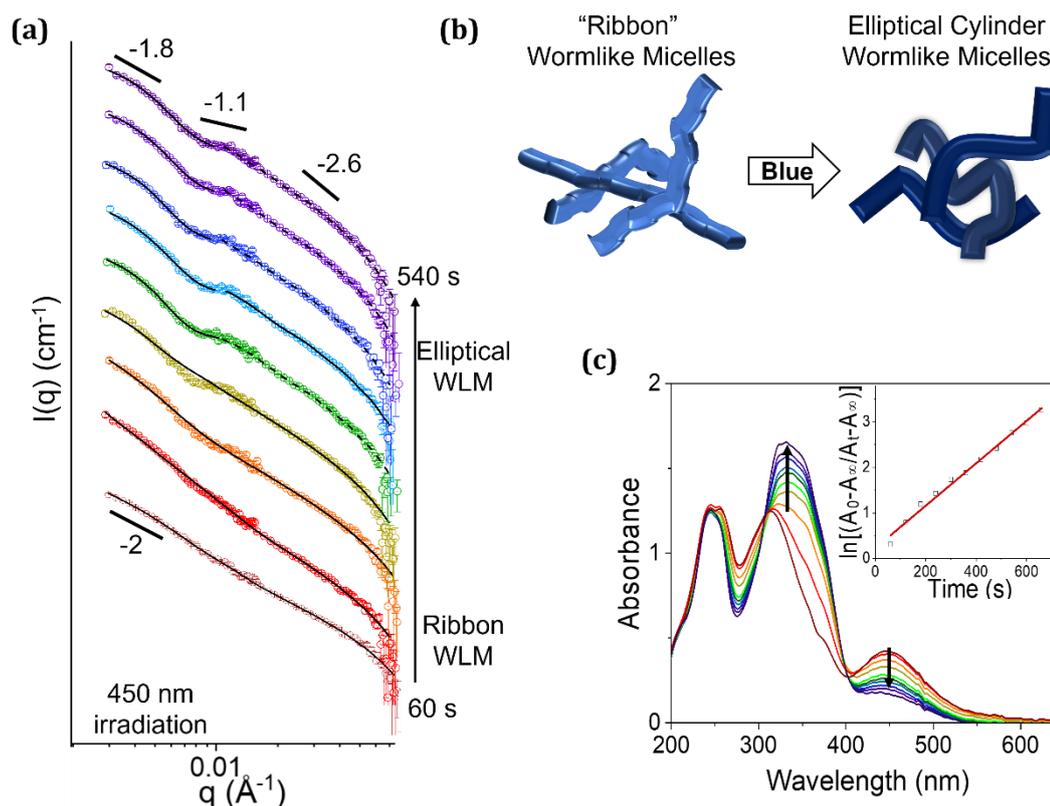
Figure 3.5. Self-assembly behaviour of C8AzoOC8E4 in D2O (0.2 mM) upon cis-trans photoisomerisation. (a) SANS scattering profiles as a function of blue irradiation time. Fits to the flexible elliptical cylinder model (solid) and elliptical cylinder model (dashed) are shown. The scattering curves have been offset for clarity. (b) Schematic representation of the wormlike micelle transition. (c) in-situ UV-Vis absorption spectra upon UV-irradiation. Inset shows that reverse isomerisation also proceeds via first-order reaction kinetics.

The degree of isomerisation can also be used to explain the rapid return to WLM formation. As only 58% *cis*-isomers are formed upon photoisomerisation, it does not take long to return to a majority *trans*-isomer state and preferential WLM formation (60 s blue irradiation, 53% *trans*-isomers.). Similarly, the number of *cis*-monomers in solution would be expected to be quite low compared to a solution with a higher degree of isomerisation. This is striking as photoisomerisation can therefore be considered as only a minor disruption to the AzoPS solution, but also significant enough to completely change the morphology of the micellar aggregates. This highlights the sensitivity of the self-assembly process to changes in the delicate hydrophobic-hydrophilic balance and geometry of the molecule. The trends observed here were found to persist at equilibrium (Appendix, Figure A.3.4) and at higher $C_8AzoOC_8E_4$ concentrations of 1 mM (Appendix, Figure A.3.5) with WLM and fractal aggregates detected for the *trans*- and *cis*-PSS, respectively.

From these experiments it has be shown using a model AzoPS, $C_8AzoOC_8E_4$, that the integration of UV-Vis absorption spectroscopy with SANS measurements can provide

insights to its photoisomerisation and self-assembled structure. Combining these techniques in this way allows the dynamic behaviour of the surfactant, which is often over-looked, to be emphasised. The formation of WLMs here is a promising result as single component photoswitchable wormlike micelle systems are rarely reported, with smart wormlike micelle systems having vast potential as on-demand rheology modifiers.[15,39] This potential will be the topic of the next sub-section.

3.3.2. Photoswitchable Wormlike Micelles and Their Effect on the Flow Behaviour

3.3.2.1. Rheological Behaviour of $C_8AzoOC_8E_4$

Following the discovery of WLM formation, the rheological behaviour of $C_8AzoOC_8E_4$ was investigated to probe any light-responsive flow behaviour. A higher concentration than that used during the *in-situ* UV-Vis-SANS measurements was used, as the concentration limitation imposed by the absorption of the AzoPS is removed and it was anticipated that more pronounced micellar entanglements and more interesting flow behaviour would be observed at higher surfactant concentrations. Figure 3.6 shows the viscosity of *trans*-$C_8AzoOC_8E_4$ (2.5 and 3.5 wt% in H_2O, 25 °C) as a function of increasing shear rate. It is clear that both concentrations of $C_8AzoOC_8E_4$ result in a viscosity much high than that of pure water (0.89 mPa·s).[40] The high value of viscosity for the 3.5 wt% solution at low shear rates suggests the presence of an entangled network.[16,29] This is consistent with the lower concentration solution (2.5 wt%) presenting a lower viscosity, as the result of fewer entanglements. The non-Newtonian shear-thinning behaviour observed for both can be attributed to entangled chains disentangling and aligning themselves with the applied force.[15,29,41] The 2.5 wt% sample could not be measured at shear rates lower than 0.1 s^{-1} due to prohibitively high signal-to-noise ratios.
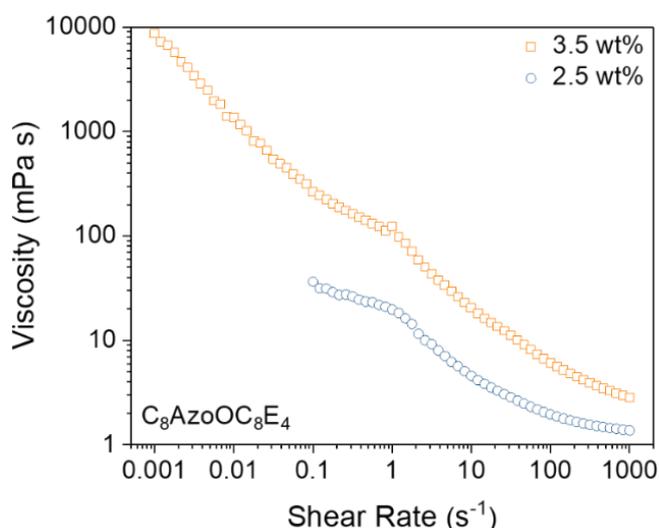
Figure 3.6. Viscosity as a function of shear rate for $C_8AzoOC_8E_4$, at 3.5 wt% (orange) and 2.5 wt% (blue) in H_2O, in the native *trans*-state. Clear shear-thinning behaviour can be observed.

The viscoelastic behaviour of $C_8AzoOC_8E_4$ (3.5 wt%) in the native *trans*-state was probed using oscillatory shear measurements. A sinusoidal deformation was applied to the sample and the response measured. This concentration was chosen as the steady-state rheology results implied a more entangled network than that observed for the 2.5 wt% solution. Figure 3.7 shows the storage (G') and loss (G'') moduli for this sample as a function of applied frequency. As outlined in the Introduction, $G' < G''$ is considered a fluid response, while $G' > G''$ represents a solid response. It is clear that within the frequency range probed here, $C_8AzoOC_8E_4$ only presents an elastic, gel-like response. If a crossover to viscoelastic behaviour does occur, it is outside the observation window of these measurements. Unfortunately, any measurements at frequencies lower than 0.01 s^{-1} were . outside the limit of detection of the instrument. The complex viscosity shows a similar behaviour to that obtained from steady-state measurements, with constant shear-thinning behaviour and no low shear plateau.

Upon isomerisation to the *cis*-form after 3 hours of UV illumination, a watery solution with a red precipitate was formed. This precipitate was insoluble in water and had not been observed for previous photoswitching experiments at lower concentrations. It is thought that this could be due to $C_8AzoOC_8E_4$ forming reverse micelles. Due to the absence of viscoelastic behaviour and the insolubility of the *cis*-isomer, no further rheology measurements were carried out on this AzoPS.
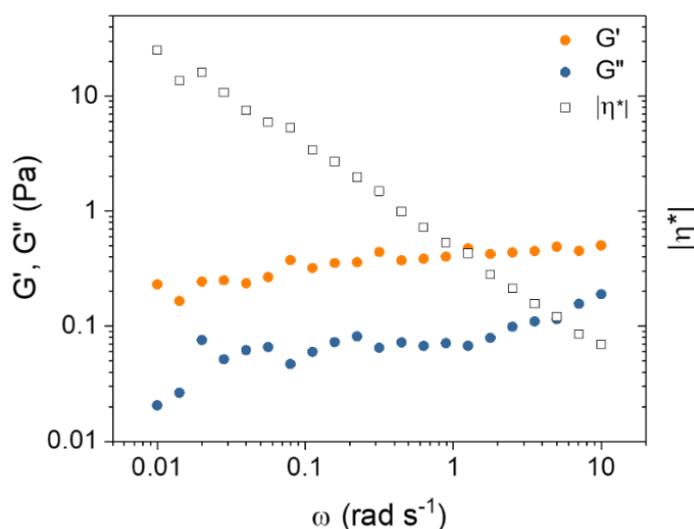
Figure 3.7. Variation of the storage modulus (G', orange circles), loss modulus (G'', blue circles) and complex viscosity (η^*, open squares) as a function of frequency for native-state $C_8AzoOC_8E_4$ (3.5 wt% in H_2O).

3.3.2.2 Rheological Behaviour of $C_6AzoOC_4E_4$

Attention was turned to a different AzoPS of the same family, $C_6AzoOC_4E_4$. This surfactant differs from $C_8AzoOC_8E_4$ in the number of carbon atoms in the spacer and pendant tail (16 *vs.* 10, Figure 3.1). Figure 3.6 shows the UV-Vis absorption spectra for the *trans*- and *cis*-isomers of $C_6AzoOC_4E_4$ (0.065 mM in H_2O, CMC_{trans} = 0.03 mM) at 25 °C. As with $C_8AzoOC_8E_4$, the *trans*-isomer is identified from the wavelength of maximum absorption (λ_{max}) at 332 nm. Isomerisation to the *cis*-isomer occurs upon illumination with UV light, identified by a blue shift in λ_{max} to 320 nm, with a simultaneous decrease in intensity, and the appearance of a new peak at 445 nm (Figure 3.8).[2] This isomerisation occurred within 30 seconds of UV irradiation (365 nm). The solution was irradiated for a further 10 minutes with no change in the absorption spectrum. After UV light illumination, $C_6AzoOC_4E_4$ was found to form an 84% *cis*-PSS, in good agreement with literature values for similar neutral AzoPS (86-89%),[8] and higher than the value obtained for $C_8AzoOC_8E_4$. The *trans*-isomer could be recovered in excellent yield, with a 95% *trans*-PSS obtained after blue light illumination. This value is quite high in comparison to other AzoPS in the literature (72-74%).[42] It was observed by eye that solutions of $C_6AzoOC_4E_4$ formed an extremely viscous, orange solution, making it a prime candidate for study of its rheological properties. It was also found to be strongly flow birefringent in this viscous state (Figure 3.9a). After UV irradiation, a homogenous red, watery solution which flowed easily was formed and birefringence was lost. (Figure 3.9b). Steady shear and oscillatory rheology measurements were performed to quantify these observations.
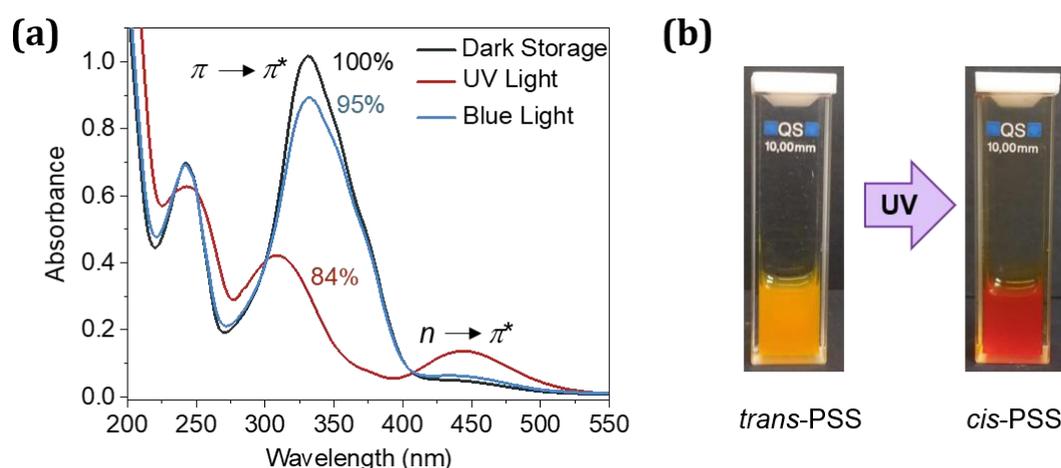
Figure 3.8. $C_6AzoOC_4E_4$ can switch reversibly between majority *trans* and majority *cis* states. (a) UV-Vis absorption spectra of $C_6AzoOC_4E_4$ (0.065 mM in H_2O) after dark storage (black line), 365 nm (red line) and 465 nm (blue line) illumination. Percentages indicate the PSS. (b) photographs of $C_6AzoOC_4E_4$ (48 mM in H_2O) before and after UV illumination. There is an obvious visible change in colour and fluidity of the sample.
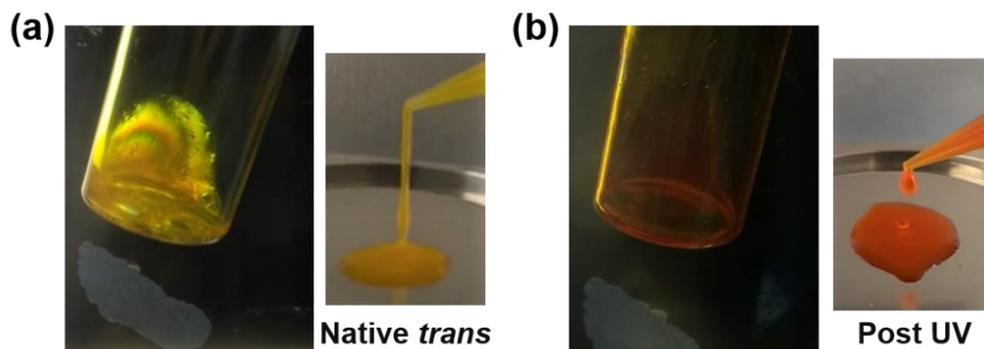
Figure 3.9. Birefringence and flow properties by eye of $C_6AzoOC_4E_4$ (2.5 wt% in H2O) before (a) and after (b) UV irradiation. Birefringence was measured by viewing the sample under cross polarisers.

Figure 3.10 shows the viscosity of *trans*-$C_6AzoOC_4E_4$ (2.5 and 1 wt% in H_2O, 25 °C) as a function of increasing shear rate. The high viscosity at low shear implies the presence of an entangled network.[16,29] The zero-shear viscosity (η_0) can be estimated from this Newtonian regime,[43,44] as in practice the viscosity at extremely low shear rates is extremely difficult to measure. A value of >10,000 mPa·s is obtained here, four orders of magnitude higher than that of pure water at the same temperature (0.89 mPa·s[40]). After a certain critical shear rate (γ_c = 0.02 s^{-1}) the viscosity falls sharply with increasing shear. This non-Newtonian shear-thinning behaviour can be attributed to entangled chains disentangling and aligning themselves with the applied force,[15,29,41] which is consistent with the formation of WLMs.[44,45] The 1 wt% solution also presents shear-thinning behaviour, but in contrast to the 2.5 wt% solution, it eventually becomes independent of viscosity at high shear rates. This is attributed to complete disentanglement of the micellar network.
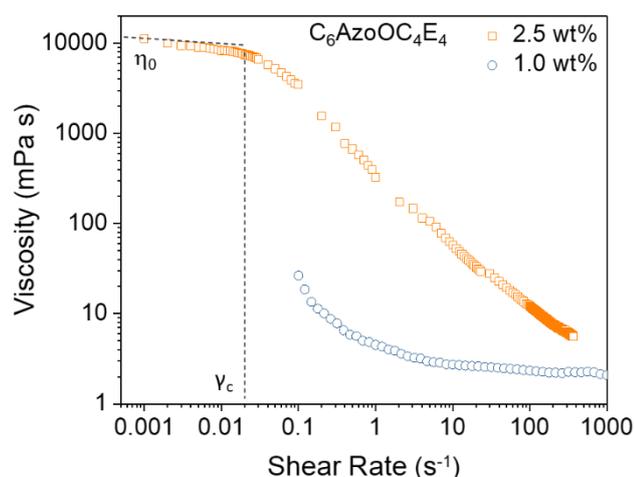
Figure 3.10. Viscosity as a function of shear rate for $C_6AzoOC_4E_4$, 2.5 wt% (orange) and 1.0 wt% (blue) in H_2O, in the native *trans*-state. Shear-thinning behaviour can be clearly observed. Dashed lines indicate the zero-shear viscosity, η_0, and critical shear rate, γ_c.

The viscoelastic behaviour of $C_6AzoOC_4E_4$ (2.5 wt% in water) in the native *trans*-state, was also probed using oscillatory measurements. Figure 3.11 shows a graph of the storage (G') and loss (G'') moduli as a function of frequency. A crossover between the two signifies viscoelastic behaviour and is strongly correlated with the presence of wormlike micelles.[29,44,46,47] This viscoelastic behaviour can be described by a Maxwell model,[29] indicated by the solid lines in Figure 3.11. The deviation of G'' from the model at high frequencies is commonly observed and is generally attributed to fast relaxation processes such as Rousse modes or 'breathing' modes.[29,44,46]

The crossover frequency (ω_c) is inversely related to the relaxation time (τ_R) of the WLM, with a value of ~ 28 s being obtained here. WLMs have two main relaxation mechanisms, reptation (τ_{rep}) and breaking (τ_b). For $\tau_b << \tau_{rep}$, Maxwellian behaviour is also observed and the relaxation times are related by:[29]

$$\tau_R = (\tau_b \tau_{rep})^{\frac{1}{2}} \qquad \text{(Eq. 3.10)}$$

An additional means to confirm the presence of a viscoelastic fluid with Maxwellian behaviour is *via* a Cole-Cole plot (Eq. 3.11). A plot of G' vs G'' should trace a semi-circle with a radius equal to the crossover frequency obtained from oscillatory measurements.[47–49] Such a plot can be seen in the inset of Figure 3.7, with the deviations at high values of G' consistent with those found in the literature, again as a result of additional, fast relaxation processes.[44,46]

$$G''^2 + (G' - \frac{G_0}{2})^2 = (\frac{G_0}{2})^2 \qquad \text{(Eq. 3.11)}$$
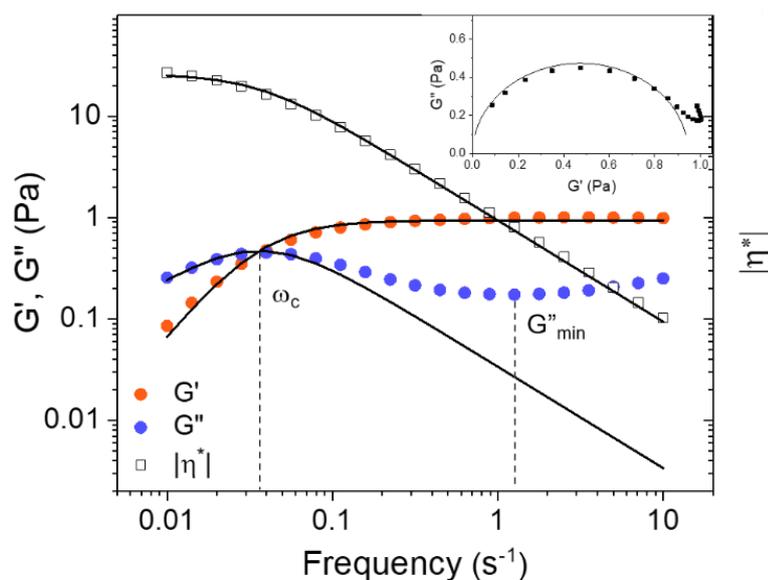
Figure 3.11. Variation of the storage modulus (G', orange circles), loss modulus (G", blue circles) and complex viscosity (η*, open squares) as a function of frequency for native state $C_6AzoOC_4E_4$ (2.5 wt%, H_2O). The black lines are fits to the Maxwell Model. Inset: Cole-Cole plot.

Figure 3.11 also displays the complex viscosity, which, consistent with earlier results, shows shear-thinning behaviour. The complex viscosity is related to the zero-shear viscosity by:

$$|\eta^*| = \frac{\sqrt{G'^2 + G''^2}}{\omega} = \frac{\eta_0}{\sqrt{1 + \omega^2 \tau_R^2}}$$ (Eq. 3.12)

For a Maxwell fluid, the zero-shear viscosity can also be given by:

$$\eta_0 = G_0 \tau_R$$ (Eq. 3.13)

G_0 can be taken from the plateau value of G' at high frequency, here 1 Pa. Using the value for relaxation time obtained early, this results in a zero-shear viscosity of 28 Pa·s. This is in good agreement with the plateau value of η^* in Figure 3.8 and with the value obtained earlier from steady-state measurements.

To observe the impact of photoisomerisation on the rheological behaviour of the surfactant, $C_6AzoOC_4E_4$ was irradiated with UV light for 2.5 hours, until no further changes were observed in the UV-Vis absorption spectrum. The AzoPS solution was visibly different after irradiation (Figure 3.9). Previously, it was a thick, viscous orange solution, after UV illumination it was a thin, watery, red fluid. To quantify this change, viscosity was measured as a function of shear rate (Figure 3.12). It was observed that *cis*-$C_6AzoOC_4E_4$ behaved as a Newtonian fluid with a viscosity independent of shear rate. The viscosity was lower than that observed for *trans*-$C_6AzoOC_4E_4$, (>10,000 mPa·s *vs.* 1.2 mPa·s), closer to that of pure water (0.89 mPa·s).[40] No oscillatory measurements were performed for the *cis* form as there is no indication of micellar entanglement or viscoelasticity. UV-Vis absorption spectra recorded after rheology measurements confirmed the sample remained in the *cis*-PSS for the duration of the experiments (Appendix, Figure A.3.6).
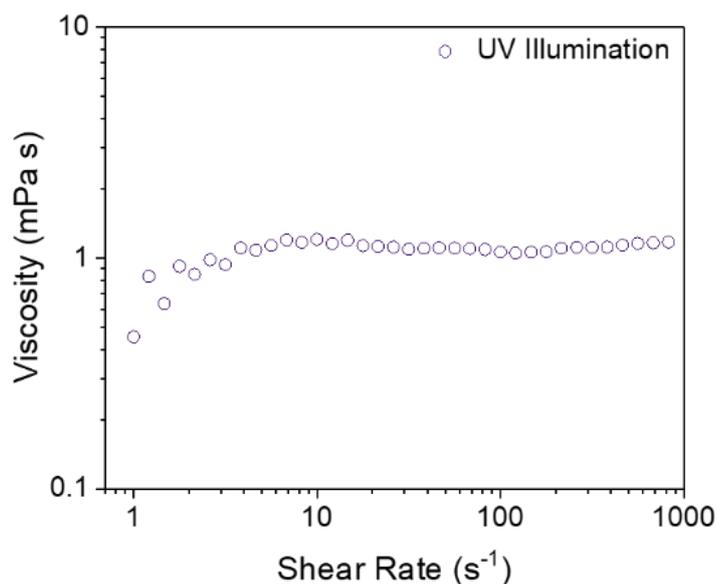
Figure 3.12. Viscosity as a function of shear rate for $C_6AzoOC_4E_4$ (2.5 wt% in H_2O) in the *cis*-PSS.

To probe the possibility of recovering the initial viscoelastic behaviour, *cis*-C$_6$AzoOC$_4$E$_4$ was irradiated with blue light (2 hours) to reverse-isomerise to a *trans*-dominant solution. Oscillatory tests were then repeated. Figure 3.13 presents the variation of *G'*, *G"* and |η*| with frequency. Viscoelastic behaviour can be observed, with *G'* and *G"* behaving similarly to what was observed initially. A Maxwell model describes *G'* and *G"*, with similar deviations in *G"* at high frequency as previously seen for the native *trans*-state. Again, a Cole-Cole plot supports this assignation of viscoelasticity. In this case, the cross-over frequency was found to occur at a higher frequency, indicating a shorter relaxation time of ~ 13 s. The zero-shear viscosity was extrapolated from the complex viscosity as outlined previously, leading to a value of 13 Pa·s. This is lower than but of the same order of magnitude as the value of 28 Pa·s obtained earlier. Figure 3.14 compares the steady-state viscosity between the native *trans*-solution and the AzoPS after UV light irradiation and after blue light irradiation. It is clear that there is a substantial change in viscosity upon photoisomerisation. It was found that it was possible to repeatedly cycle between low and high viscosity states using UV and blue light respectably (Figure 3.14b), in each case with the original viscoelastic behaviour being recoverable with blue light.
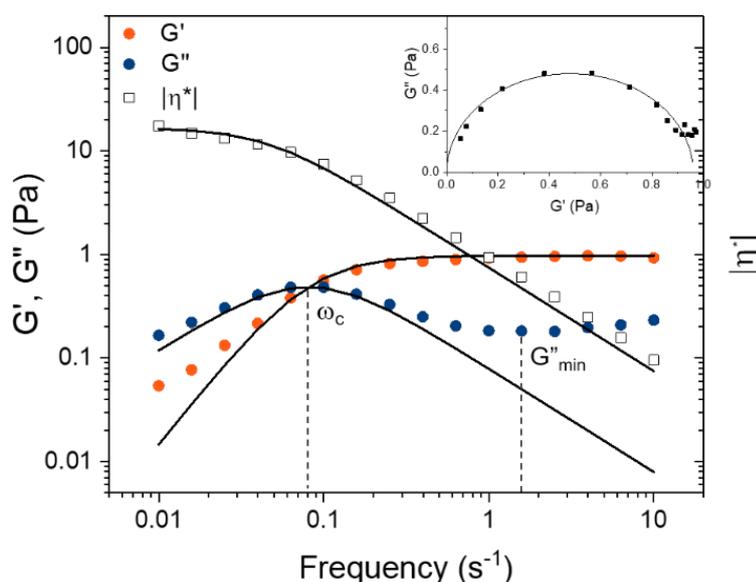
Figure 3.13. Variation of the storage modulus (*G'*, orange circles), loss modulus (*G"*, blue circles) and complex viscosity (η*, open squares) as a function of frequency for C$_6$AzoOC$_4$E$_4$ (2.5 wt%, H$_2$O, 25 °C) in the *trans*-PSS state. The black lines overlaying *G'* and *G"* are fits to the Maxwell Model. Inset shows a Cole-Cole plot.
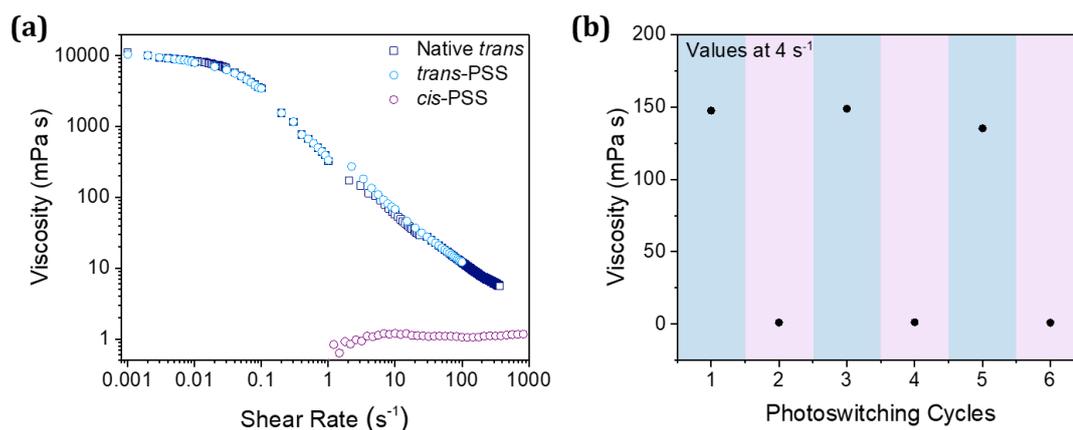
Figure 3.14. (a) Viscosity as a function of shear rate for the native *trans* state (dark blue) after UV illumination (purple) and blue light illumination (light blue). (b) $C_6AzoOC_4E_4$ can cycle reversibly between high and low viscosity solutions. Blue shading indicates blue light illumination while pink shading indicates UV illumination.

As previously discussed, the shape of micelles formed by surfactants can be predicted using the packing parameter, $P = V/a_0 l$, where V is the volume of the hydrophobic surfactant tail, a_0 is the equilibrium area of the surfactant head group and l is the length of the hydrophobic tail.[36] In this case, cylindrical structures are predicted for *trans*-$C_6AzoOC_4E_4$, consistent with the WLMs expected on the basis of previous results (P = 0.4, $1/3 < P < 1/2$ is indicative of cylinder formation, Appendix, Table A.2.3). The packing parameter for *cis*-$C_6AzoOC_4E_4$ is calculated to be 0.46 (Appendix, Table A.2.3), approaching the limit of cylinder formation and onset of vesicle formation ($1/2 > P > 1$). To visualise the formation of any wormlike micelles, cryo-TEM was performed to probe the self-assembled structure of $C_6AzoOC_4E_4$. This is a popular technique for imaging aqueous and soft matter specimens as such materials are normally incompatible with the high vacuum requirements of regular TEM. (Cryo)-TEM is particularly useful for self-assembled structures with dimensions on the order of 10s-100s of nm. As wormlike micelles possess length scales spanning orders of magnitude (from radii on the order of ~5 nm to contour lengths on the order of micrometres), cryo-TEM offers the possibility to visualise these larger dimensions. Later, SAXS will be used to probe the smaller length scales of the self-assembled structures of $C_6AzoOC_4E_4$.

Figure 3.15 shows representative images of $C_6AzoOC_4E_4$ (0.5 wt% in H_2O) before and after 90 min of UV irradiation. Further cryo-TEM images are available in the Appendix (Figure A.3.7). Figure 3.15a supports the formation of a densely entangled WLM network for *trans*-$C_6AzoOC_4E_4$, in line with what would be expected based on the observed high viscosity, viscoelasticity and birefringence.[17,39,44,50] The diameter of the WLMs is estimated to be 47.1 ± 7.2 Å. This value is roughly twice the value of the hydrophobic tail length of $C_6AzoOC_4E_4$ (24.9 Å, Appendix Table A.2.2), indicating that the radius of the WLM is one

surfactant monomer. Due to the high degree of entanglement, the length of the WLM could not be extracted, but is estimated to be on the order of 100s of nm to µm. The darker blobs on the image (indicated by solid white arrows) are attributed to artefacts of the vitrification process, most likely the formation of crystalline ice.[51]

Figure 3.15b shows $C_6AzoOC_4E_4$ after 90 minutes irradiation with UV light. A network with a significantly lower density than that in Figure 3.15a can be observed, with Figure 3.15b presenting looping, branching and vesicle formation. The individual threads here have a diameter of 43.2 ± 9 Å. This reduction in size (~4 Å) cannot be attributed solely to the reduced length of *cis*-azobenzene compared to *trans*-azobenzene (0.55 *vs* 0.9 Å), but rather, reflects a change in the packing behaviour of the surfactant. Reductions in micellar dimensions upon illumination to the *cis*-form have been previously reported.[8,10,11,13] Some circular structures (210 ± 83 Å in diameter) can also be observed, as indicated by empty white arrows in Figure 3.15b. This is likely to be vesicle formation. This mixture of vesicles and dispersed, branched threads were found across many different images. Oh *et al.* also reported vesicle formation for the low viscosity state of their three-component photorheological fluid, based on a cationic surfactant and azobenzene-based additive.[17]
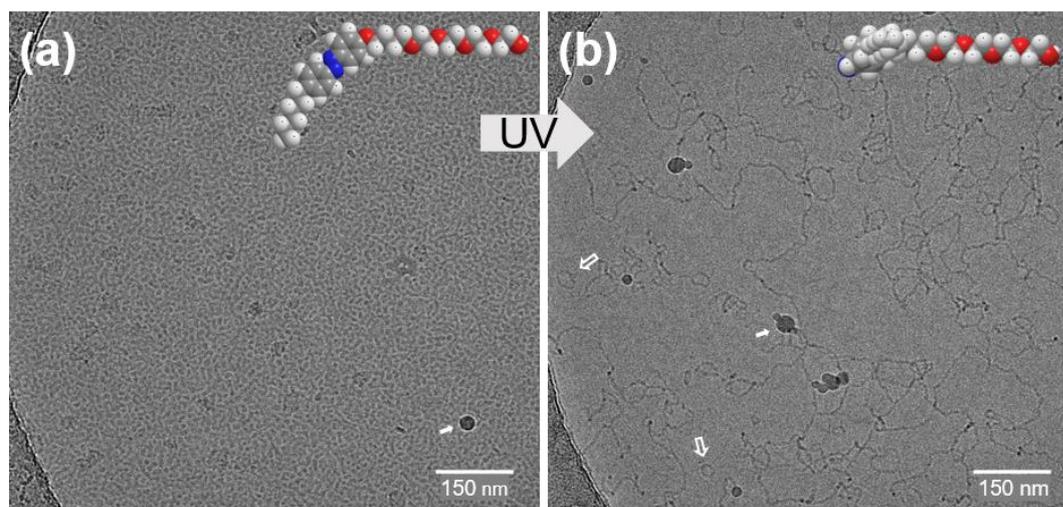
Figure 3.15. Cryo-TEM images of $C_6AzoOC_4E_4$ (0.5 wt% in H_2O) in (a) the native *trans* state and (b) after 90 min. UV irradiation. The scale bar on both images is 150 nm. The dark blobs, indicated by solid white arrows, are artefacts of the vitrification process. The native *trans* specimen (a) shows a densely entangled network while the specimen after UV irradiation (b) shows a lower density network with potential vesicle formation (open arrows). The molecular structure show "3D" space-filled models of *trans*- (a) and *cis*- (b) $C_6AzoOC_4E_4$.

The self-assembled structures formed by *trans*- and *cis*-C$_6$AzoOC$_4$E$_4$ were also investigated using small-angle X-ray scattering (Figure 3.16). The SAXS profiles of native-state C$_6$AzoOC$_4$E$_4$ (0.5 wt%, 2.5 wt%) decay as q^{-1} in the low q region, which indicates that cylindrical scattering bodies are present across this concentration range (Figure 3.13). In general, for small-angle scattering the position of the first scattering minimum is correlated to the radius of the scattering bodies in solution.[52–54] Here, the first minima shift to higher q after UV irradiation (from 0.078 to 0.1 Å^{-1}) indicating that cylinders with a smaller radius are formed. There is no significant difference in the shape of the scattering profiles before and after UV illumination, suggesting that on the length scales probed by SAXS (2 – 200 nm) the shape of the self-assembled structures is similar, with all samples decaying as q^{-1} (Figure 3.16). All scattering profiles could be fitted using cylindrical models, the resulting fitted parameters of which are available in the Appendix (Table A.3.3). *Trans*-C$_6$AzoOC$_4$E$_4$ was best described using a cylinder model (dotted line, Figure 3.13, radius: 55 Å, polydispersity: 0.12) at 0.5 wt% and a flexible cylinder model (solid line, Figure 3.13, radius: 59.5 Å, polydispersity: 0.2; Kuhn length: 677.4 Å, polydispersity: 0.12) at 2.5 wt%. This change from cylinder to flexible cylinder model is consistent with the presence of wormlike micelles, which grow uniaxially along their length with increased concentration.
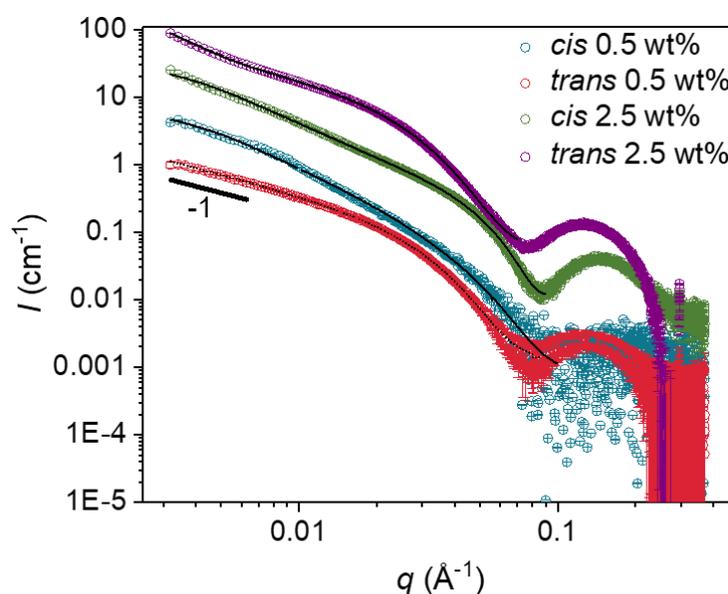
Figure 3.16. SAXS profiles for C$_6$AzoOC$_4$E$_4$ in the native *trans*-state (red, purple) and *cis*-PSS (blue, green) at 0.5 and 2.5 wt%. The fit to a cylindrical model for trans 0.5 wt% is shown with a dotted line, to trans and cis 2.5 wt%, the fit to a flexible cylinder is shown with a solid line and the fit to an elliptical model for cis 2.5 wt% is shown with a dashed line.

After UV irradiation, at 0.5 wt% *cis*-C$_6$AzoOC$_4$E$_4$ could only be described using an elliptical cylinder model (dashed line, Figure 3.16, radius: 28.9 Å, axis ratio: 7.4), which, qualitatively, is not drastically different from a regular cylinder with a distribution for the radius, as found for the *trans*-state at this concentration. At 2.5 wt%, *cis*-C$_6$AzoOC$_4$E$_4$ was described best by a flexible cylinder model, with a smaller radius than the trans-form (solid line, Figure 3.13, radius: 41.5 Å; Kuhn length: 175.7 Å). No model or structure factor contribution was found that considered the interference maxima at ~0.1 Å. Therefore, for clarity, model fittings have only been shown to 0.09 Å. Comparisons of the fits obtained using different cylinder models to the scattering profiles can be found in the Appendix (Figure A.3.8). All structural parameters obtained from model fitting can be found in the Appendix (Table A.3.3). These conclusions can also be reached from examination of the cryo-TEM images, where on the tens of nm scale, the self-assembled structures appear similar (threadlike). The most significant differences between the micellar networks seem to emerge outside the observation window of a SAXS measurement, on the scale of nm–μm (Figure 3.17)

As the nanostructure observed from the cryo-TEM images in Figure 3.15b corresponds to a solution with a viscosity close to that of pure water with no shear-thinning behaviour, and taking into account the packing parameter predictions and SAXS profiles, the change in flow behaviour must be attributed to a change in the degree of entanglement between the wormlike micelles, rather than a dramatic change in the self-assembled structure (*e.g.* a complete WLM to spherical transition). The linear, planar *trans*-isomer can pack effectively, with possible π-π stacking between azobenzene units and H-bonding between the ethylene glycol units of neighbouring head groups. These interactions would favour longer chain lengths and less branching for this more hydrophobic isomer. In fact, the ability of the *trans*-AzoPS to pack effectively has been shown to result in highly-organised structures at high concentrations, such as lyotropic

Entangled Network   **Wormlike Micelle**   **Constituent Cylinders**   **Monomer Assembly**   **Vesicle**
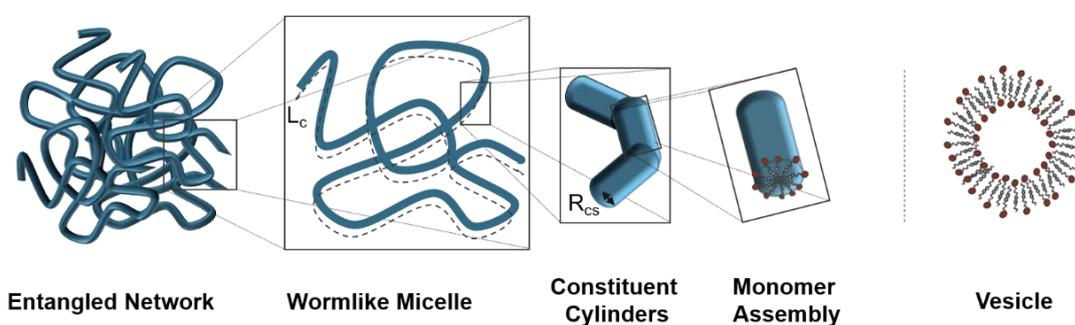
liquid crystal phases.[41,42]

Figure 3.17. Schematic representation of a wormlike micelle and its component parts and of a vesicle.

Upon photoisomerisation to the bent, non-planar, more hydrophilic *cis*-isomer, this packing ability is inhibited. A disruption in packing and self-assembly behaviour upon photoisomerisation has been previously reported for azobenzene derivatives, generally attributed to a change in molecular geometry and polarity.[40–42,61] In this case, the offset in packing ability is expected to lead to an increased number of kinks, twists and branching in the *cis*-dominant solution, as observed in Figure 3.15. The resulting lower-density network allows for greater force dissipation than the extremely entangled network observed for the *trans*-dominant solution. For the *cis*-dominant solution, the presence of vesicles, joints and branching within the micellar network would allow sliding along the WLM length, preventing the formation of the highly entangled network that results in a correspondingly high viscosity and viscoelastic behaviour. Often, the mechanism attributed to responsive, rheological behaviour is a clear change in packing behaviour upon application of a stimulus *e.g.* a wormlike to spherical transition[1,2,43] or a substantial shortening of WLMs and subsequent reduction in relaxation time.[8,31] The results here emphasise that the behaviour of the micellar network on a larger scale (*e.g.* presence of branching, degree of entanglement) is also a key parameter for controlling the rheological behaviour.

3.3.2.3 Comparing the Flow Behaviour of Both AzoPS

It is clear that both $C_8AzoOC_8E_4$ and $C_6AzoOC_4E_4$ form high viscosity solutions with the shear-thinning behaviour typical of entangled networks. However, the dynamic rheology behaviour of these two surfactants differ. $C_8AzoOC_8E_4$ presents gel-like behaviour, which for WLMs is unusual but has previously been observed.[44,50,55,56] The elastic response of $C_8AzoOC_8E_4$ implies that either the sample can be considered a gel, or, it is viscoelastic but has an extremely long relaxation time, with a crossover to viscous behaviour occurring outside the probed frequency range. The steady-state shear-thinning behaviour, consistent with an entangled network, suggests the latter. G' being independent of frequency also supports an extremely long relaxation time. This could be attributed to the long hydrophobic tail of this surfactant disfavouring micellar breaking. Due to the long tail (16 carbons and an azobenzene), micellar breaking, *i.e.* the exchange of monomers with the bulk WLM, would be less favourable than for a surfactant with a shorter carbon tail (*i.e.* $C_6AzoOC_4E_4$). With micellar breaking supressed, reptation would be the predominant relaxation method for the WLM, resulting in 'polymer'-like behaviour. Kumar *et al.* observed similar gel-like behaviour for a 22 carbon-tailed betaine surfactant and reported a value of 10^5 s for the reptation time.[55] In this case, a crossover to the

viscous regime between G' and G'' would then lie at $\sim 1 \times 10^{-5}$ s, a frequency region inaccessible *via* rheology methods. The *cis*-PSS of this surfactant (3.5 wt%) was also found to be insoluble in water. The long hydrophobic tail of this surfactant may also be cause for it potentially forming inverse micelles for the *cis*-isomers at high concentrations. Reverse micelle formation at high concentration is not an unusual occurrence for surfactants,[57-60] but it was decided on this basis not to investigate this surfactant system further.

$C_6AzoOC_4E_4$, on the other hand, presents the high viscosity and viscoelasticity typical of WLMs, with Maxwellian behaviour and a crossover between G' and G'' clearly observable. The packing parameter, P, can be used to rationalise the formation of WLMs; $1/3 < P < 1/2$ is indicative of cylinder formation, with values of 0.4 calculated for *trans*-$C_6AzoOC_4E_4$.[36,37] These cylinders can grow along their length with increased concentration,[29] resulting in the formation of elongated wormlike micelles. The cryo-TEM images of $C_6AzoOC_4E_4$, support this assignation, as long, entwined cylindrical features can be seen. These long features have an average radius of approximately the same value of the length of a surfactant monomer. Upon UV irradiation and photoisomerisation to a majority *cis* solution, the viscosity drops markedly and a switch to Newtonian behaviour occurs. The rheology results give no indication of an entangled viscoelastic network for this isomer. The packing parameter for *cis*-$C_6AzoOC_4E_4$ is calculated to be 0.46, approaching the limit of cylinder formation and onset of vesicle formation ($1/2 > P > 1$). It is likely that the neutral tetraethylene head group is responsible for the lack of dramatic change in structure upon UV isomerisation. In general, the effect of UV irradiation on the surfactant structure is more pronounced for compact AzoPS structures, with short alkyl chains and spacers, and for charged head groups, which typically favour high curvature structures over low curvatures ones. Here, there is little electrostatic repulsion between the non-ionic tetraethylene glycol head groups; they are likely highly solvated and may experience strong intramolecular hydrogen bonding interactions. The influence of surfactant structure on self-assembled structure and flow behaviour will be discussed in more detail in the following Chapter.

3.4 Conclusion

In conclusion, it was found that UV-Vis absorption spectroscopy could be successfully integrated with SANS to study the change in self-assembly of $C_8AzoOC_8E_4$ as a function of the extent of photoisomerisation. Upon irradiation with UV light, $C_8AzoOC_8E_4$ undergoes a wormlike micelle to fractal transition at concentrations above the CMC in D_2O. This is an interesting result as single component photoswitchable wormlike micelle systems are rare. Wormlike micelles could be recovered with as little as 60 s of blue irradiation, with extended illumination times resulting in WLMs of a lower cylindrical eccentricity. It was also found that the AzoPS could reversibly cycle between *cis*- and *trans*-isomers without deterioration over several hours, highlighting the robustness of the azobenzene chromophore.

These initial results have been built upon to demonstrate that a neutral AzoPS, $C_6AzoOC_4E_4$, can be used to create a simple, salt-free, light-responsive fluid, at reasonably low concentrations in water (2.5 wt%), with a viscosity and viscoelasticity that can be reversibly controlled using light. $C_6AzoOC_4E_4$ is the first neutral, single-component fluid capable of a dramatic light-responsive rheological response. Only two other surfactant structures have also been reported to achieve this.[15,22] A viscosity difference of four orders of magnitude is achieved before and after UV irradiation, with the initial high-viscosity state recoverable with blue light illumination. A cycling between high and low viscosity states can be repeated several times, through the application of either UV or blue light. Cryo-TEM images and SAXS data suggest the formation of a densely entangled network of wormlike micelles for the native *trans*-isomer solution, in agreement with the observed birefringence and shear-thinning behaviour. Interestingly, upon UV irradiation the long cylindrical micelles persist (with some vesicle formation), albeit with a different, looser network structure (branching, kinks, twists present). This result can be used to inform the design of further rheological fluids, based on merely disrupting the network structure, rather than drastically changing the self-assembled structure formed by the constituent surfactant molecules. It was also found that $C_8AzoOC_8E_4$ has an extremely high viscosity in the native *trans*-form, consistent with the earlier SANS results.

Such on-demand viscosity changes bring into focus the relationship between molecular structure and macroscopic properties. The formation of 'on' and 'off' states for viscosity and viscoelasticity means $C_6AzoOC_4E_4$ shows promise in applications that require a dramatic switch in flow behaviour e.g. alternating between drag-reduction and efficient heat-transfer capabilities for heating and cooling applications.[61] In particular, applications based on stimuli-responsive materials require that the switch between properties be significant, such as the four order of magnitude difference in viscosity

achieved here. Exciting, future research opportunities lie in integrating simple, photorheological fluids, like $C_6AzoOC_4E_4$ with microfluidic device technology, sensing and controlled-release applications. There is a lot of possibility in exploring the rheology of this material further, particularly in relating the self-assembled structure to the flow-behaviour. This will be the subject of the following chapter.

3.5 References

1   I. K. Lednev, T. Q. Ye, P. Matousek, M. Towrie, P. Foggi, F. V. R. Neuwahl, S. Umapathy, R. E. Hester and J. N. Moore, *Chem. Phys. Lett.*, 1998, **290**, 68–74.

2   H. M. Dhammika Bandara and S. C. Burdette, *Chem. Soc. Rev.*, 2012, **41**, 1809–1825.

3   E. Chevallier, A. Mamane, H. A. Stone, C. Tribet, F. Lequeux and C. Monteux, *Soft Matter*, 2011, **7**, 7866.

4   A. Diguet, R. M. Guillermic, N. Magome, A. Saint-Jalmes, Y. Chen, K. Yoshikawa and D. Baigl, *Angew. Chem. Int. Ed.*, 2009, **48**, 9281–9284.

5   C. T. Lee, K. A. Smith and T. A. Hatton, *Biochemistry*, 2005, **44**, 524–536.

6   S. Chen, W. Zhang, C. Wang and S. Sun, *Green Chem.*, 2016, **18**, 3972–3980.

7   T. Shang, K. A. Smith and T. A. Hatton, *Langmuir*, 2006, **22**, 1436–1442.

8   S. Peng, Q. Guo, P. G. Hartley and T. C. Hughes, *J. Mater. Chem. C*, 2014, **2**, 8303–8312.

9   S. Peng, Q. Guo, T. C. Hughes and P. G. Hartley, *Langmuir*, 2014, **30**, 866–872.

10   C. Blayo, J. E. Houston, S. M. King and R. C. Evans, *Langmuir*, 2018, **34**, 10123–10134.

11   R. F. Tabor, M. J. Pottage, C. J. Garvey and B. L. Wilkinson, *Chem. Commun.*, 2015, **51**, 5509–5512.

12   R. Lund, G. Brun, E. Chevallier, T. Narayanan and C. Tribet, *Langmuir*, 2016, **32**, 2539–2548.

13   J. Eastoe and A. Vesperinas, *Soft Matter*, 2005, **1**, 338–347.

14   S. Santer, *J. Phys. D. Appl. Phys.*, 2018, **51**, 013002-.

15   Z. Chu, C. A. Dreiss and Y. Feng, *Chem. Soc. Rev.*, 2013, **42**, 7174.

16   A. M. Ketner, R. Kumar, T. S. Davies, P. W. Elder and S. R. Raghavan, *J. Am. Chem. Soc.*, 2007, **129**, 1553–1559.

17   H. Oh, A. M. Ketner, R. Heymann, E. Kesselman, D. Danino, D. E. Falvey and S. R. Raghavan, *Soft Matter*, 2013, **9**, 5025–5033.

18   Z. Xia, K. Jia, X. Li and J. Dong, *RSC Adv.*, 2016, **6**, 45673–45680.

19 H. Sakai, Y. Orihara, H. Kodashima, A. Matsumura, T. Ohkubo, K. Tsuchiya and M. Abe, *J. Am. Chem. Soc.*, 2005, **127**, 13454–13455.

20 H. Y. Lee, K. K. Diehn, K. Sun, T. Chen and S. R. Raghavan, *J. Am. Chem. Soc.*, 2011, **133**, 8461–8463.

21 B. Song, Y. Hu and J. Zhao, *J. Colloid Interface Sci.*, 2009, **333**, 820.

22 C. S. G. Butler, J. P. King, L. W. Giles, J. B. Marlow, M. L. P. Vidallon, A. Sokolova, L. de Campo, K. L. Tuck and R. F. Tabor, *J. Colloid Interface Sci.*, 2021, **594**, 669–680.

23 A. Radulescu, V. Pipich, H. Frielinghaus and M.- Appavou, *J. Phys. Conf. Ser.*, 2012, **351**, 012026.

24 N. P. Cowieson, C. J. C. Edwards-Gayle, K. Inoue, N. S. Khunti, J. Doutch, E. Williams, S. Daniels, G. Preece, N. A. Krumpa, J. P. Sutter, A. D. Tully, N. J. Terrill and R. P. Rambo, *J. Synchrotron Radiat.*, 2020, **27**, 1438–1446.

25 S. Förster, L. Apostol and W. Bras, *J. Appl. Crystallogr.*, 2010, **43**, 639–646.

26 E. Kentzinger, M. Krutyeva and U. Rücker, *J. large-scale Res. Facil. JLSRF*, 2016, **2**, 1–5.

27 J. S. Pedersen and P. Schurtenberger, *Macromolecules*, 1996, **29**, 7602–7612.

28 W. R. Chen, P. D. Butler and L. J. Magid, *Langmuir*, 2006, **22**, 6539–6548.

29 C. A. Dreiss, *Soft Matter*, 2007, **3**, 956–970.

30 L. A. Feigin and D. I. Svergun, *Structure Analysis by Small Angle X-ray and Neutron Scattering*, Plenum, New York, 1987.

31 *http://www.sasview.org/*, accessed 10/19.

32 J. Teixeira, *J. Appl. Crystallogr.*, 1988, **21**, 781–785.

33 K. G. Yager and C. J. Barrett, *J. Photochem. Photobiol. A Chem.*, 2006, **182**, 250–261.

34 B. A. Cicciarelli and K. A. Smith, *Langmuir*, 2007, **23**, 4753–4764.

35 T. Shang, K. A. Smith and T. A. Hatton, *Langmuir*, 2003, **19**, 10764–10773.

36 J. N. Israelachvili, D. J. Mitchell and B. W. Ninham, *J. Chem. Soc. Faraday Trans. 2 Mol. Chem. Phys.*, 1976, **72**, 1525–1568.

37 Y. Takahashi, M. Kishimoto and Y. Kondo, *J. Colloid Interface Sci.*, 2016, **470**, 250–

256.

38   C. T. Lee, K. A. Smith and T. Alan Hatton, *Langmuir*, 2009, **25**, 13784–13794.

39   B. Song, Y. Hu and J. Zhao, *J. Colloid Interface Sci.*, 2009, **333**, 820–822.

40   *Viscosity of Ordinary Water. IAPWS, R12-08*, 2018.

41   T. S. Davies, A. M. Ketner and S. R. Raghavan, *J. Am. Chem. Soc.*, 2006, **128**, 6669–6675.

42   H. C. Kang, B. M. Lee, J. Yoon and M. Yoon, *J. Colloid Interface Sci.*, 2000, **231**, 255–264.

43   S. R. Raghavan and E. W. Kaler, *Langmuir*, 2001, **17**, 300–306.

44   J. Wang, Y. Feng, N. R. Agrawal and S. R. Raghavan, *Phys. Chem. Chem. Phys.*, 2017, **19**, 24458–24466.

45   T. M. McCoy, A. Valiakhmetova, M. J. Pottage, C. J. Garvey, L. De Campo, C. Rehm, D. A. Kuryashov and R. F. Tabor, *Langmuir*, 2016, **32**, 12423–12433.

46   D. P. Acharya and H. Kunieda, *Adv. Colloid Interface Sci.*, 2006, **123**–**126**, 401–413.

47   D. Xie, D. You, S. Ying, B. Song and J. Tian, *RSC Adv.*, 2017, **7**, 48120–48126.

48   J. Yang, Z. Yang, Y. Lu, J. Chen and W. Qin, *J. Dispers. Sci. Technol.*, 2013, **34**, 1124–1129.

49   B. Song, Y. Hu, Y. Song and J. Zhao, *J. Colloid Interface Sci.*, 2010, **341**, 94–100.

50   Y. Han, Y. Feng, H. Sun, Z. Li, Y. Han and H. Wang, *J. Phys. Chem. B*, 2011, **115**, 6893–6902.

51   R. F. Thompson, M. Walker, C. A. Siebert, S. P. Muench and N. A. Ranson, *Methods*, 2016, **100**, 3–15.

52   M. J. Derry, O. O. Mykhaylyk and S. P. Armes, *Angew. Chemie*, 2017, **129**, 1772–1776.

53   M. J. Derry, L. A. Fielding, N. J. Warren, C. J. Mable, A. J. Smith, O. O. Mykhaylyk and S. P. Armes, *Chem. Sci.*, 2016, **7**, 5078–5090.

54   C. J. Mable, L. A. Fielding, M. J. Derry, O. O. Mykhaylyk, P. Chambon and S. P. Armes, *Chem. Sci.*, 2018, **9**, 1454–1463.

55   R. Kumar, G. C. Kalur, L. Ziserman, D. Danino and S. R. Raghavan, *Langmuir*, 2007, **23**, 12849–12856.

56   Z. Chu, Y. Feng, X. Su and Y. Han, *Langmuir*, 2010, **26**, 7783–7791.

57   P. Alexandridis, U. Olsson and B. Lindman, *Langmuir*, 1998, **14**, 2627–2638.

58   E. Cabane, X. Zhang, K. Langowska, C. G. Palivan and W. Meier, , DOI:10.1007/s13758-011-0009-3.

59   X. D. Wang, Z. X. Shen, T. Sang, X. Bin Cheng, M. F. Li, L. Y. Chen and Z. S. Wang, *J. Colloid Interface Sci.*, 2010, **341**, 23–29.

60   X. Mulet, B. J. Boyd and C. J. Drummond, *J. Colloid Interface Sci.*, 2013, **393**, 1–20.

61   H. Shi, W. Ge, H. Oh, S. M. Pattison, J. T. Huggins, Y. Talmon, D. J. Hart, S. R. Raghavan and J. L. Zakin, *Langmuir*, 2013, **29**, 102–109.

Chapter 4

Probing the Structure-Flow Relationship of an AzoPS using Rheo-SANS

4.1 Introduction

A more detailed analysis of the combined flow behaviour and self-assembled structure of the light-responsive viscoelastic fluid created using $C_6AzoOC_4E_4$ is possible with rheo-SANS experiments. Here, the most relevant literature on the topic of wormlike micelles and rheo-SANS will be briefly summarised, before the results of rheo-SANS experiments on $C_6AzoOC_4E_4$ and subsequent discussion are presented. In this section, two different concentrations of $C_6AzoOC_4E_4$ will be probed, the 2.5 wt% solution that was the subject of the previous Chapter, along with a 4 wt% solution. Measurements were also performed at higher temperatures and after UV irradiation. The goal of this work is to determine how the dynamic self-assembled WLM system responds to applied shear and gain a deeper insight into how changes in self-assembled structure relates to the measured flow behaviour.

There are several reports of rheo-SANS measurements on polymer and WLM solutions. For the interested reader, earlier studies on the topic of WLMs under shear can be found in the review of flow-SANS and rheo-SANS applied to soft matter, published in 2012 by Eberle *et al.*[1] Along with a summation of the literature, the review outlines typical measurement planes and configurations, as well as standard approaches to data reduction and analysis (*e.g.* annular reduction, sector-averaged reduction, alignment factor). Herein, the results of some studies relevant to this work are briefly described.

In 2011, Takeda *et al.* studied shear-thickening and shear-thinning solutions of rod-like micelles using rheo-SANS.[2] Using CTAB and varying concentrations of sodium *p*-toluene sulfonate, different formulations of rodlike micelles were formed, of varying lengths and physical dimensions. Both shear-thickening and shear-thinning behaviour could be achieved depending on the molar ratio of the salt to the surfactant. Shear-thickening was attributed to either a transition from short rods to long WLM or a connection process between WLM micelles occurring. Shear-thickening behaviour was associated with anisotropic SANS patterns. It was also found the WLM became more elongated and oriented in the flow direction with increasing shear, also giving rise to anisotropic SANS patterns.

In 2017, Kelleppan *et al.* investigated the effect of tail-group structure on WLM formation for a series of five long-chain betaine surfactants.[3] One of the five zwitterionic structures (oleyl amidopropyl betaine, OAPB) was found to form WLMs using regular SANS and was further probed using rheo-SANS. The surfactant displayed strong alignment with increasing shear rate. Another of the five structures formed short rods, rather than WLMs (linoleyl amidopropyl betaine, LAPB), and in that case there was no pronounced alignment of the aggregates under shear. Their key finding was the

importance of surfactant tail structure in promoting favourable self-assembly behaviour for WLMs. In 2018, Moore *et al.* reported on the structure-function relationship and rheology of carbohydrate-based surfactants which form rod-like micelles.[4] They found that when short cylindrical micelles were formed, no shear alignment was observed, implying insufficient micellar entanglements occurred and the cylindrical micelles could freely rotate in solution. For a solution of viscoelastic WLMs, shear alignment was observed and sector averaging from perpendicular angular sectors allowed a more detailed analysis of this anisotropy to be performed. It was observed that the WLMs elongated along the principal scattering axis with increasing shear. In 2019, Iwase *et al.* reported a rheo-SANS study on the relationship between micellar structure and the rheological behaviour of cationic gemini surfactants.[5] They found the scattering bodies formed by the surfactant in solution orientated with the applied flow, with clear scattering anisotropy visible at high shear rates (300-600 s^{-1}). The solution was initially shear-thickening, but presented shear thinning behaviour in the region of 300-600 s^{-1}. A rod model fitted the sector-averaged scattering profiles in the parallel and perpendicular directions, with physical parameters, such as the cylinder radius, extracted. No salt was needed to form WLMs.

Most recently, an AzoPS system studied using rheo-SANS has been reported for the first time. In 2021, Butler *et al.* investigated the structure-flow relationship of an azobenzene-based betaine surfactant.[6] They observed the *trans*-isomer of the zwitterionic structure formed a viscoelastic WLM network, while the *cis*-PSS formed a low viscosity solution of ellipsoids. From UV-Vis absorption spectroscopy and rheo-SANS results, they emphasised the importance of π-π interactions on the packing behaviour of the elliptical WLM formed by the *trans*-isomer.

The aim of this Chapter is to look more deeply at the structure formed by C$_6$AzoOC$_4$E$_4$ during shear. From the previous Chapter, the WLM structures of the 2.5 wt% aqueous solution in the *trans*- and *cis*-PSS at rest were found using SAXS, SANS and cryo-TEM. However, while the rheological behaviour of this solution has been established in terms of characterising the viscoelasticity and the change in viscosity with increasing shear rate, the structural changes of the surfactant solution under shear are still unknown. The knowledge of how self-assembled structure responds to shear will be useful for any future applications involving photorheological fluids, particularly those based on azobenzene surfactants. Potential future avenues include microfluidics, drag-reduction and separation. It is hoped this work will emphasise the utility of rheo-SANS measurements for these types of formulations, as to date only one other report of applying this technique to AzoPS systems exists.

4.2 Experimental

Materials

Azobenzene photosurfactants were synthesised as outlined in the Experimental (Chapter 2). Deionised water and Millipore water (18.2 mΩ cm) were obtained through an in-house water purification system. D_2O was obtained on-site at the National Institute for Neutron Science (NIST) in Gaithersburg, Maryland, USA.

Instrumentation

Rheology Measurements: Rheology measurements were performed on an Anton Paar MCR 301 stress-controlled rheometer. Samples (2.5 wt% or 4 wt% $C_6AzoOC_4E_4$ in water) were measured at 25 °C using a cone-plate geometry (50 mm diameter, 1° cone angle, 0.101 mm gap). An amplitude sweep was performed to determine the linear viscoelastic range (LVR) before oscillatory measurements were performed. (Appendix, Figure A.4.1). A frequency sweep was performed over the angular frequency range 0.01–100 s^{-1} at 1% strain (middle of LVR).

Rheo-SANS Measurements: Rheo-SANS measurements were performed at the National Institute for Neutron Science (NIST) Center for Neutron Research in Gaithersburg, Maryland, USA in February 2020. The measurements were performed using the Very Small-Angle Neutron Scattering (VSANS) instrument which was fitted with an Anton Paar MCR 501 stress-controlled rheometer.[7,8] Shear rates of 0.01–100 s^{-1} were applied. Samples were loaded into a Couette cell and the scattering from the sample (1,3 plane; flow-vorticity) was collected in the *q*-range of 0.003–0.127 $Å^{-1}$ with sample-to-detector distances of 5 and 17 m, a neutron wavelength of 6 Å and wavelength spread of $\Delta\lambda/\lambda$ of 0.12. Measurements in the 1,3 plane are commonly known as radial rheo-SANS measurements. The scattering vector *q* is defined as $q = 4\pi \sin(\theta/2)/\lambda$ where θ is the angle at which the neutron is scattered and λ is the neutron wavelength. For formation of the *cis*-isomer, samples were irradiated with UV light (365 nm) for 2 h before measurement using a Prizmatix UHP-F-LED (1800 mW). UV irradiation was maintained *in-situ* during rheo-SANS measurements. The scattering was corrected for empty cell, plexiglass standard and the detector efficiency. Scattering profiles were reduced using standard National Center for Neutron research protocols with Igor PRO software.[9] The beam-stop and detector edges were masked and the data were integrated over both the full range (360°) and partially integrated in the horizontal (flow plane) and vertical (vorticity plane) directions, for anisotropy analysis. The partial integration was performed on 15 pixel wide, rectangular strips around the beam centre, extending beyond the region in which counts were detected.[10] (Figure 4.1).
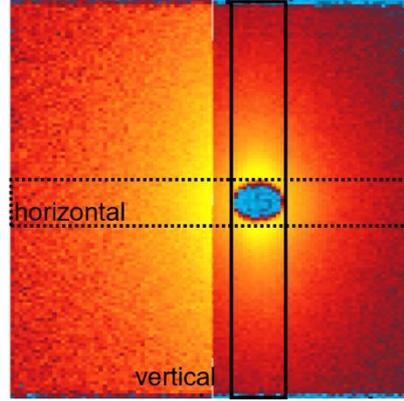
Figure 4.1. Detector image of small-angle scattering from 2.5 wt% solution of $C_6AzoOC_4E_4$ in solution at 10 s^{-1}. Areas over which partial integrations are performed are overlayed by dashed lines for the horizontal direction and solid lines for the vertical direction.

SANS Models: The scattering function, ($S(q, L ,b)$), of a semi-flexible chain with a uniform scattering length density and elliptical cross-section, taking excluded volume effects into account, is used here to fit some of the scattering profiles and is given by:[11,12]

$$S(q, L, b) = [1 - w(qR_g)S_{Debye}(q, L, b) + f_{corr}(q)w(qR_g)[1.22(qR_g)^{\frac{-1}{0.585}} +$$

$$0.4288(qR_g)^{-\frac{2}{0.585}} - 1.651(qR_g)^{\frac{-3}{0.585}}] + \frac{Cn_b}{n_b}\{\frac{4}{15} + \frac{7}{15u} - \left(\frac{11}{15} + \frac{7}{15u}\right) \times e^{-u(q,L,b)}\}$$

$$(Eq. 4.1)$$

where $w(qR_g)$ is an empirical crossover function, $n_b = L/b$ and $f_{corr}(q)$ is a correction factor added by Chen *et al.* to correct unphysical errors occurring at certain L/b ratios.[12] Further details of $f_{corr}(q)$, $w(qR_g)$, $S_{Debye}(q, L, b)$ and $u(q, L, b)$ can be found in the work of Pederson *et al.*[11] and Chen *et al.*[12] This form factor is normalised by particle volume, averaging over all possible orientations of the flexible cylinder.

In some cases an elliptical cylinder model was used, with a scattering intensity given by:[13,14]

$$I(q) = \frac{1}{v} \int d\psi \int d\phi \int d\, \rho(\theta, \phi, \psi) F^2(q, \alpha, \psi) \sin(\theta)\, d\theta \qquad (Eq. 4.2)$$

where:

$$F(q, \alpha, \psi) = 2\frac{J_1(x)\sin(y)}{xy} \qquad (Eq. 4.3)$$

and

$$x = q\sin(\alpha)[r_{major}^2 sin^2(\psi) + r_{minor}^2 \cos(\psi)]^{\frac{1}{2}}\, ; y = \frac{L}{2}q\cos(\alpha) \qquad (Eq. 4.4)$$

where θ and ϕ define the orientation of the axis of the cylinder, ψ and α define the orientation of the major axis of the ellipse with respect to the vector q, J_1 is the Bessel function of first order and r is the cylinder radius.

In some cases a lamellar model was used, with a scattering intensity for dilute, randomly oriented, "infinitely large" sheets given by:[15,16]

$$I(q) = scale \frac{2\pi P(q)}{q^2 \delta} + background \qquad \text{(Eq. 4.5)}$$

where scale is the scale factor or volume fraction, the form factor $P(q)$ is:

$$P(q) = \frac{2\Delta\rho^2}{q^2}(1 - \cos(q\delta)) = \frac{4\Delta\rho^2}{q^2}\sin^2\left(\frac{q\delta}{2}\right) \qquad \text{(Eq 4.6)}$$

δ is the total layer thickness and $\Delta\rho$ is the contrast, or difference in scattering length density.

All model fittings were carried out using the SASview 5.0.3 software.[14]

4.3 Results and Discussion

Building upon the observations discussed in Chapter 3, rheo-SANS measurements were performed on aqueous solutions of $C_6AzoOC_4E_4$ at concentrations of 2.5 and 4 wt%. First, the results from rheo-SANS measurements of the 2.5 wt% solution will be presented. This is the concentration that was found to form a viscoelastic WLM network in the *trans*-form and a low viscosity, open network in the *cis*-form using SAXS, cryo-TEM and rheology measurements (Chapter 3). Here, this solution will be probed in terms of its viscosity and self-assembly behaviour under shear, at room temperature, 40 °C, and after UV irradiation. A higher concentration of 4 wt% will also be discussed, followed by a detailed comparison of the difference in behaviour between the two concentrations.

4.3.1 Viscosity and Scattering Behaviour $C_6AzoOC_4E_4$ (2.5 wt%) under Shear

Figure 4.2 shows the viscosity, η, as a function of shear rate for 2.5 wt% solutions of *trans*-$C_6AzoC_4E_4$ in water. The viscosity values obtained during rheo-SANS measurements are shown in black. These values are the mean taken from each shear rate, as the sample was held at each shear rate for a fixed amount of time (120 s) to allow for sufficient scattering data to be collected. The viscosity shows clear shear-thinning behaviour, with a decrease in viscosity occurring with increasing shear rate on the shear-up ramp. These values reproduce the viscosity behaviour previously observed and discussed in Chapter 3, shown in red. The slight change in slope at 1.5 s $^{-1}$ features on both data sets. Altogether, this indicates the aforementioned non-Newtonian behaviour, due to the alignment of wormlike micelles with the applied shear force.
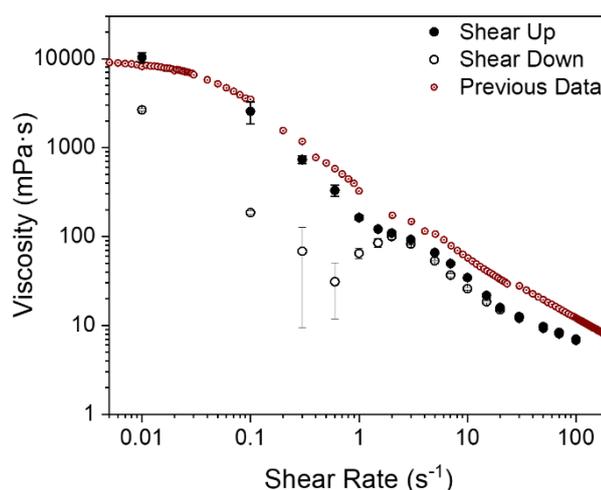
Figure 4.2. Viscosity as a function of shear rate for 2.5 wt% solutions of *trans*-$C_6AzoOC_4E_4$ in water. The average viscosity values taken from the rheo-SANS measurements during the shear-up (filled black circles) and shear-down (open black circles) ramps can be observed. The standard deviations are shown by vertical error bars. The previous shear-up data obtained (open red circles), during earlier off-line rheology measurements (Chapter 3) are in good agreement with the rheo-SANS values.

The viscosity behaviour on the shear-down ramp shows some deviations from full reversibility, particularly in the intermediate shear region, of 0.1–1 s⁻¹. This is the region which a slight change in slope was observed for the shear-up ramp. It is likely that a structural rearrangement occurs here, which is not recovered over the timescales chosen for each shear ramp. Hysteresis is a common feature of viscoelastic systems, which often show time-dependent strain behaviours, with strain not occurring instantaneously and linearly as a result of deformation.[17,18] In particular, WLMs can show long relaxation times on the order of minutes.[19] It is likely that had greater time between shear rates been allowed, within the relaxation time of this system, full recovery of the viscosity would be observed. It is hoped that analysis of the SANS profiles will allow the structure corresponding to this shear-dependent viscosity behaviour to be elucidated.

In order to estimate the relaxation time, a frequency sweep was performed (Figure 4.3). For WLMs and viscoelastic fluids in general, viscous behaviour is characterised by a loss modulus greater than the storage modulus ($G'' > G'$). Similarly, elastic behaviour is characterised by the inverse, $G' > G''$.[20,21] A crossover from viscous to elastic behaviour with increasing shear indicates a viscoelastic fluid, with the crossover frequency inversely related to the relaxation time.[22] In Figure 4.3 the typical high shear trends of G' and G" are observed, indicating elastic behaviour, but the crossover at low shear is not observed. It is possible the crossover may occur at shear rates lower than 0.01 s⁻¹, as G' and G" appear to be trending towards a crossover at low shear. This corresponds to a relaxation time (τ_R) of >100 s⁻¹, as calculated using $\tau_R = 1/\omega_c$ where ω_c is the crossover frequency. This agrees with observation that the viscosity was not recovered during the 120 s intervals allowed for the measurement here (Figure 4.2).
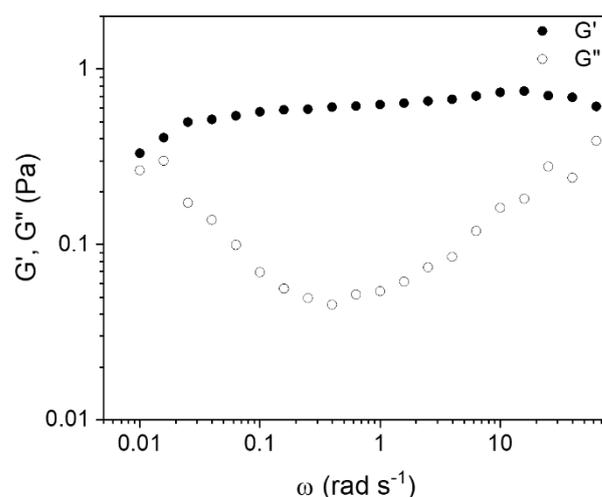
Figure 4.3. A frequency sweep to probe the relaxation time of the 2.5 wt% solution of C₆AzoOC₄E₄ in the native-*trans* form used for rheo-SANS measurements. Storage (G') and loss (G'') moduli are plotted as a function of angular frequency, ω. No crossover value is obtained.

To probe the emergence of anisotropy with shear, the 2D-SANS profiles were annularly reduced, with their intensities plotted against the scattering angle (Figure 4.4a, b). There is a small degree of anisotropy at low shear rates, clear from the peaks centred at ~90 and 270°. This is likely due to increasing alignment of the WLMs along the flow direction upon shearing. These peaks grow dramatically in intensity and anisotropy at a shear rate of 7 s^{-1} (Figure 4.4a). A maximum is observed for 15 s^{-1}, before a steady decrease in peak intensity occurs, in tandem with an increase in the intensity over all angles, up to 100 s^{-1}. For the reverse process, of shearing down 100 – 0.01 s^{-1}, this high intensity over all angles is maintained, with very little anisotropy observed (Figure 4.4b). This is consistent with the long-relaxation times observed from rheology measurements. Isotropic profiles were not observed for any shear rates, with the least anisotropy observed for the highest shear rate of 100 s^{-1}. This behaviour correlates with the trends observed in the viscosity behaviour; a decrease in the viscosity occurs concurrent with an increase in anisotropy. Figure 4.4c shows representative detector patterns with clear anisotropy of scattering at 10 s^{-1}, evidenced by the asymmetric intensity distribution around the central masked area. At 100 s^{-1}, the anisotropy is lower, with a more spherical distribution of intensity observed. It is clear that a structural change is occurring with shear, but at this point the precise details are not clear.
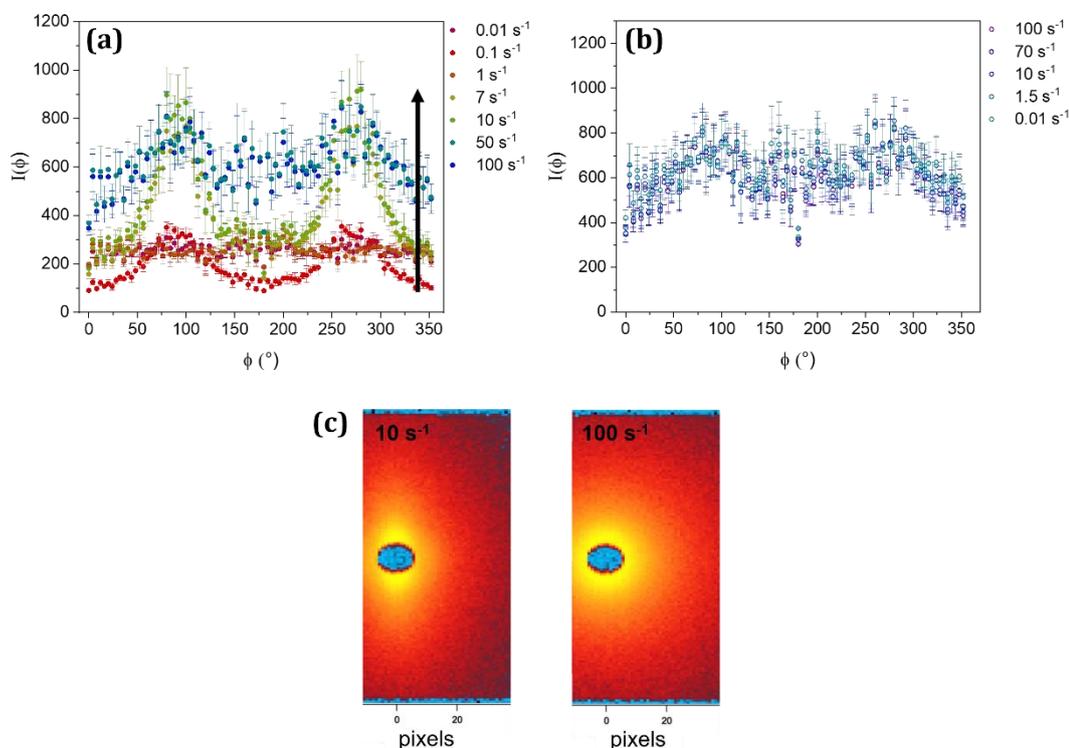
Figure 4.4. Selected annular reductions of 2D detector images for an aqueous 2.5 wt% solution of *trans*-C$_6$AzoOC$_4$E$_4$ for the shear-up (a) and shear-down ramp (b). Arrow indicates change in intensity with shear rate. (c) Detector images showing high (10 s^{-1}) and low (100 s^{-1}) anisotropy of scattered intensity. Higher counts in yellow with lower counts in red. Areas of no scattering are shown in blue, with the central blue region corresponding to the masked beam-stop.

Initially, the scattering patterns were reduced to a 1D form by radially averaging across the full annular range, to determine trends in shape and intensity. Figure 4.5 shows the scattering profiles for 2.5 wt% $C_6AzoOC_4E_4$ in the native *trans*-form for the shear-up and shear-down ramps. For the shear-up ramp, from 0.01–1.5 s^{-1}, the scattering profile decays as q^{-1} at low q, indicating scattering from cylindrical bodies in solution. From 2 s^{-1} there is an abrupt change in the shape of the scattering profiles at low q, with a decay of q^{-2} observed, indicative of scattering from sheet-like structures in solution. This profile remains relatively constant up to 100 s^{-1}. At high q, from 0.3 Å^{-1} onwards, all scattering profiles decay in intensity as $q^{-3.6}$, indicating scattering off the surface of the self-assembled structure. The similarity in scattering profiles at high q also implies that at small length scales, the dimensions of the scattering bodies are similar, *i.e.* for cylindrical bodies in solution, they remain roughly the same radius, independent of shear rate. The most significant changes to the scattering profile occur in the low q region of <0.02 Å^{-1}, which corresponds to changes in self-assembled structure from the length scales of >31 nm. Given that the estimated length of the surfactant molecule is ~3 nm, it is anticipated that these changes in the scattering profile correspond to changes in larger parameters of the scattering bodies in solution (*e.g.,* Kuhn length), as well as shape.

It is interesting to compare the changes in the scattering profiles to the changes in the measured viscosity (Figure 4.2). The transition point of ~1.5–2 s^{-1} is the same point at which a change in scattering profile is observed from SANS and where a large spike in the shear stress was observed in the flow-rate measurements (Appendix, Figure A.4.2.). It indicates that the cylindrical bodies in solution are strongly shear-thinning but at increasing shear, change in structure to scattering bodies more resembling lamellar sheets. These sheet-like structures are still shear-thinning but less strongly so than the cylindrical bodies. It is possible a shear-banding transition is occurring after ~1.5 s^{-1}.
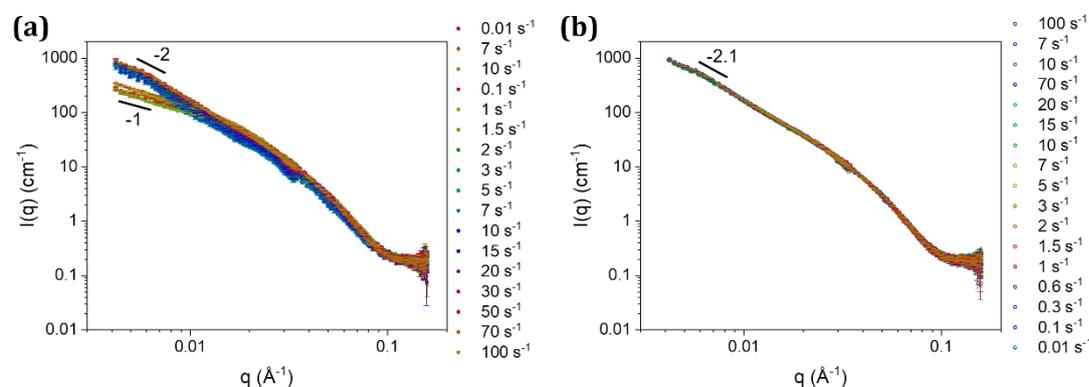
Figure 4.5. Scattering profiles a 2.5 wt% aqueous solution of $C_6AzoOC_4E_4$ in the native trans-form for the shear-up (a) and shear-down (b) ramps. The slope of the decay in scattering intensity at low q is indicated by solid line, with a decay of either -1 or -2 observed, depending on the shear rate and ramp.

In Figure 4.5b, the effect of the long-relaxation time on the self-assembled behaviour is clear. The scattering profiles at low shear do not recover their initial shape, with all profiles on the shear-down ramp retaining the high-shear lamellar structure. It is interesting to note that given the uniformity of the scattering profiles on the shear-down ramp that any recovery in viscosity occurs at all. This highlights the importance of recalling that the SANS profiles capture only a certain window of the scattering bodies in solution in terms of their length scales (3–157 nm here) and changes in entanglements and branching, which would also affect the rheological behaviour, may be occurring outside of this length scale.

4.3.2. Partial Integration in Flow and Vorticity Directions

To obtain information on the self-assembled structure as a function of flow, the scattering patterns were reduced to a 1D form better suited to analyse the data in terms of the structural anisotropy, by partial integration in the horizontal and vertical directions. The horizontal direction (0°) is aligned with the flow, while the vertical direction (90°) is the vorticity plane (Figure 4.1). Figure 4.6 shows the shear dependence of the 1D-SANS profiles, with a clear change in behaviour depending on whether the scattering is averaged parallel or perpendicular to the flow direction. For the horizontal direction on the shear-up ramp (Figure 4.6a), an increase in slope at low q from $q^{-1.2}$ to $q^{-2.2}$ is observed, indicating a change in scattering from a structure with a fractal dimension of a cylinder (q^{-1}) to that of a sheet-like assembly (q^{-2}). Similar behaviour is observed in the parallel direction, although the change in slope is more step-wise than gradual in this case, with a stark change in slope occurring after 1.5 s^{-1}, as was observed for the scattering profiles reduced across the entire annular range (Figure 4.5). For clarity, only selected shear rates are shown here. These data will be shown offset, discussed in more detail and fitted to models presently.

First, the degree to the which the solution becomes aligned with the flow direction will be estimated by defining an alignment factor, A_f, as follows:[23]

$$A_f = \frac{\int_{q_{min}}^{q_{max}} I_V(q)dq - \int_{q_{min}}^{q_{max}} I_H(q)dq}{\int_{q_{min}}^{q_{max}} I_V(q)dq} \qquad \text{(Eq. 4.8)}$$

where $I_V(q)$ and $I_H(q)$ are the scattering intensities perpendicular and parallel to the flow, respectively. Values were determined using $q_{min} = 0.004$ Å^{-1} and $q_{max} = 0.121$ Å^{-1} and are plotted as a function of shear rate in Figure 4.7. The alignment factor was also estimated from the annular reductions to confirm the anisotropy trends with shear rate, with identical behaviour observed using this approach (Appendix, Figure A.4.3). The degree of

alignment is initially small, with a value of 0.06 at 0.01 s^{-1}. This is consistent with the lack of peaks observed in the annularly reduced profiles. The alignment increases rapidly to 0.57 at 0.1 s^{-1}, before decreasing to 0.45 at 0.3 s^{-1}. In the region of 0.6–2 s^{-1}, slightly negative values were obtained (-0.04, -0.08, -0.06, -0.02), indicating that the scattering intensity in the parallel direction was no longer higher than that in the perpendicular direction. This behaviour is also observed in the annularly reduced data, where the intensity between 135° and 225° is on the same order, if not slightly higher, than the intensity of the peaks centred at 90° and 270° (Figure 4.4a). It is also evident in Figure 4.6a, where the scattering profiles at 0.01 and 1 s^{-1} overlap in terms of intensity. This region is also where changes in the viscosity were observed (~1.5 s^{-1}). At higher shear, the alignment begins to increase again, from 0.12 at 3 s^{-1}, increasing steadily to 0.52 at 10 s^{-1}. This is followed by a decrease in alignment before a plateau value of 0.14–0.16 is maintained from 50–70 s^{-1}. For the shear-down ramp, the alignment slowly decreases from 0.17 at 100 s^{-1} to 0.06 at 0.01 s^{-1}, returning to the initial value albeit along a very different path. Due to the long relaxation time outside of the measurement conditions, the shear-down ramp will not be discussed in detail. It is interesting to note that the highest overall alignment occurs at a low shear rate of 0.1 s^{-1}.
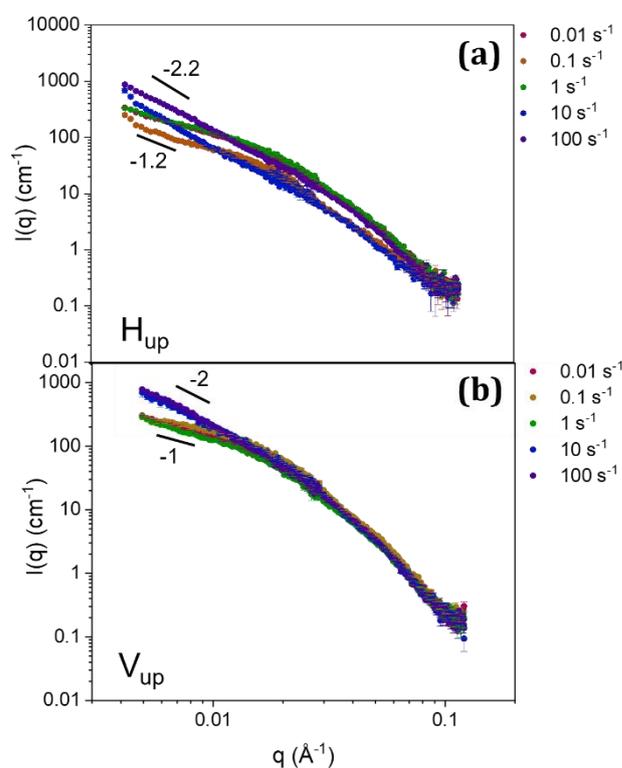
Figure 4.6. Selected 1-D scattering profiles of C$_6$AzoOC$_4$E$_4$ (2.5 wt%) as a function of shear rate in the parallel (H$_{up}$) (a) and perpendicular (V$_{up}$) (b) directions for the shear-up ramp.
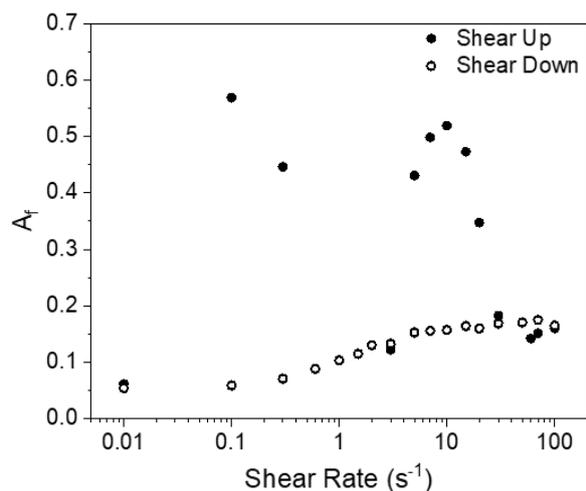
Figure 4.7. Alignment factor as a function of shear rate for 2.5 wt% $C_6AzoOC_4E_4$ in water for the shear-up (0.01–100 s^{-1}, black circles) and shear-down (100–0.01 s^{-1}, open circles) ramps.

To better understand the structural changes occurring with shear, models were fitted to the individual scattering profiles for the vertical and horizontal directions, for the shear-up -down ramps. The choice of model is informed from the shape and slope of the scattering profiles. Figure 4.8 shows selected scattering profiles in the horizontal direction on the shear-up ramp, from 0.01–100 s^{-1}. Individual scattering profiles and fits are available in the Appendix (Figure A.4.4). The scattering profiles from 0.01 to 1.5 s^{-1} were fitted with an elliptical cylinder model. A variety of models were trialled, including various cylindrical models, with an elliptical cylindrical model being the only one to accurately fit the data, providing acceptable χ^2 values ($1 > \chi^2 > 4$) and reasonable physical dimensions. The extracted model parameters are available in the Appendix (Table A.4.1), with examples of attempts to fit other models (Figures A.4.5–6) also shown.

From 2 s^{-1}, scattering profiles have a clear change in shape, with a low q decay of ~q^{-2}. These profiles are fitted using a lamellar model. In the intermediate shear range, particularly at 2 and 3 s^{-1}, there are deviations from the model at low q which are ascribed to it being transitional region where structural reorganisation is occurring. It is likely that something between an elliptical cylinder and a sheet-like structure is emerging, as any attempts to fit the scattering profiles with an elliptical or flexible elliptical cylinder model resulted in a reasonable fit by eye but returned values of 11–12 for the axis ratio, *i.e.* the long axis was 11-12 times the length of the short. (Appendix, Figure A.4.6). In practice, an elliptical cylinder with a major ratio 11–12 times the dimensions of the minor ratio is not qualitatively different from a lamellar sheet. This, and the fact that the lamellar model has fewer variable fitting parameters (thickness, scattering length density) than the elliptical cylinder models (length, Kuhn length, radius, thickness, SLD), is the reason the lamellar model was preferred. At higher shear, the lamellar model describes the scattering profiles increasingly well. All fitting parameters are available in the Appendix (Table A.4.1).
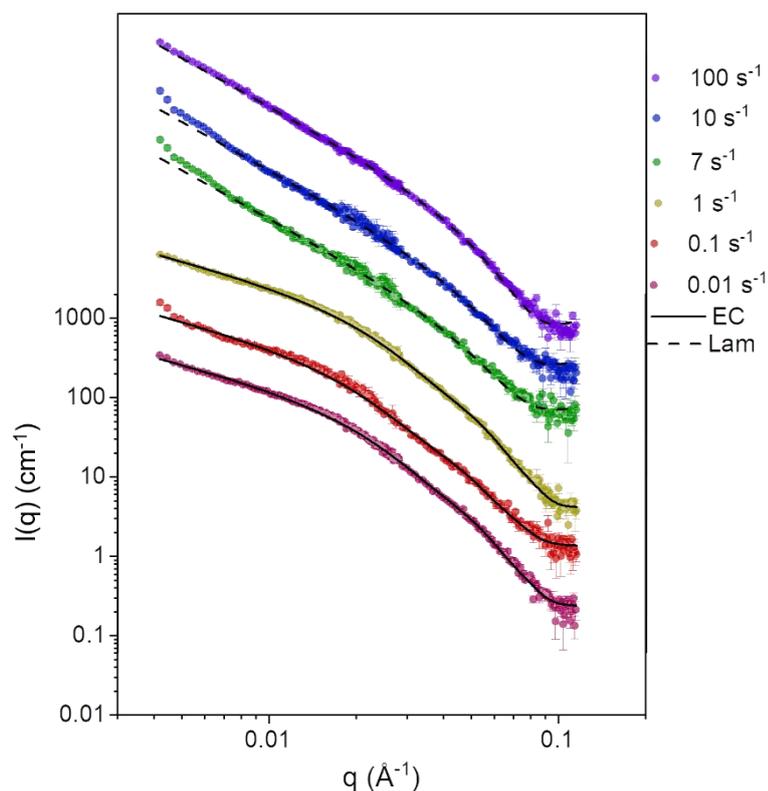
Figure 4.8. Selected scattering profiles of $C_6AzoOC_4E_4$ (2.5 wt%, horizontal direction, shear-up). Models to the elliptical cylinder (EC, solid line) or lamellar model (Lam, dashed line) are shown. Graphs are manually stacked to show the fits clearly. Non-stacked data are shown in Figure 4.6a.

For the vertical direction (vorticity direction) on the shear-up ramp, selected scattering profiles can be observed in Figure 4.9. All scattering profiles and fits are in the Appendix (Figure A.4.7). At very low shear (0.01 s^{-1}) an elliptical cylinder model was fitted to the scattering profile, with a change to a flexible elliptical cylinder model at 0.1 and 0.3 s^{-1}, due to a change in the shape of these two profiles. This change occurs at the same shear rates that the dramatic tenfold increase in alignment factor, from 0.06 to 0.57, occurs. At intermediate shear, from 0.6–1.5 s^{-1}, an elliptical cylinder is again adequate to describe the data, before a return to a flexible elliptical cylinder from 2–100 s^{-1}. The region of 0.6–1.5 s^{-1} is where slightly negative values for alignment factor were obtained, so it is heartening that this region also deviates in terms of its structure. Evidently a shear-induced structural change occurs in the vorticity plane within this shear region. From 2 s^{-1} onwards, the scattering profiles are all similar and correspond to a flexible elliptical cylinder model. The model parameters can be found in the Appendix (Table A.4.2), as well as attempts to fit the scattering profiles to various other models (Figure A.4.8).

All scattering profiles for the shear-down ramp could be fit with lamellar or flexible elliptical cylinder models for the horizontal and vertical directions, respectively. (Appendix, Figures A.4.9–12, Tables A.4.3–4). As discussed, due to the long relaxation times of the WLMs the retention of high-shear behaviour is unsurprising.
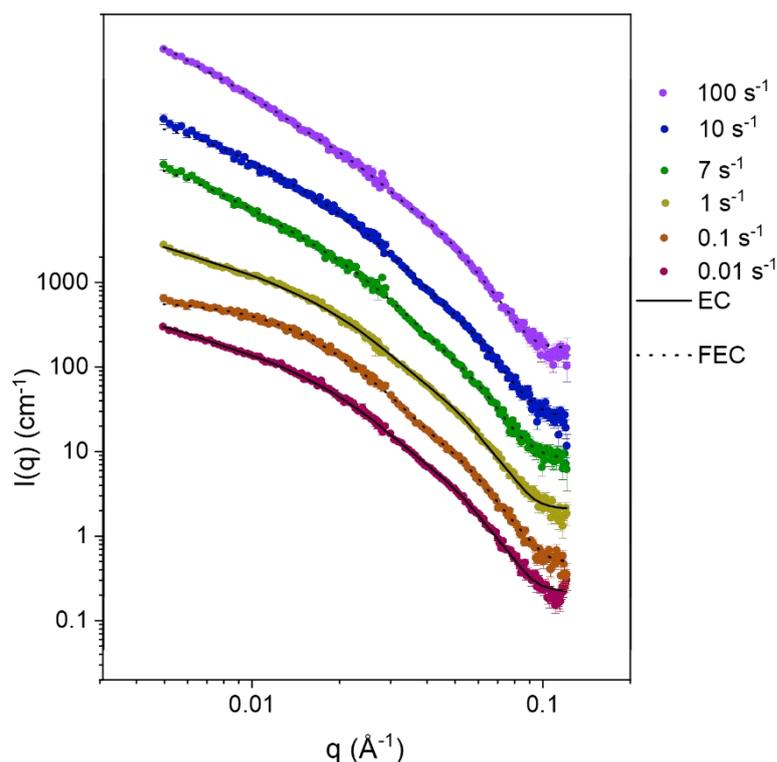
Figure 4.9. Selected scattering profiles of $C_6AzoOC_4E_4$ (2.5 wt%, vertical direction, shear-up). Models to the elliptical (EC, solid line) or flexible elliptical cylinder model (FEC, dotted line) are shown. Graphs are manually stacked to show the fits clearly. Non-stacked data in Figure 4.6b.

The physical parameters from the models are shown as a function of shear rate in Figure 4.10. The values for the minor radius of the elliptical cylinders at low shear rates remain relatively constant, between 32.9 and 34.9 Å (Figure 4.10a). From 2 s^{-1}, the scattering profiles transition towards sheet-like structures, with a lamellar thickness of 59.6 Å initially, before a maximum of 65.4 Å at 10 s^{-1}. At higher shear, the lamellar thickness remains roughly constant, at 64.2–64.5 Å. This is roughly twice the minor radius of the elliptical cylinders, supporting the view that self-assembled structure decreases in curvature with increasing shear, transitioning from a WLM to an increasingly flattened cylinder, ultimately scattering as sheets. (Figure 4.10b). For context, the length of the surfactant tail is estimated at 24.9 Å. Figures 4.10c and d show the model parameters in the vertical direction. Aligned with the flow direction, the minor radius of the elliptical cylinder is estimated to be 33.3 Å initially, before decreasing to 30.9 and 31.2 Å for the flexible elliptical cylinder at 0.1 and 0.3 s^{-1}. This shear range corresponds to the region where a stark increase in alignment factor was observed, indicating that the radii of the WLMs shrink when aligned with the flow. This reduction in radius is not retained at higher shear rates; across the rest of the shear-up ramp, the minor radius fluctuates around the low-shear value. The axis ratio is relatively constant (2.8–3.6) on the shear-up ramp, with the exception of 2 and 3 s^{-1}, where values of 4.7 and 5.2 are found, the same region where a transition to sheet-like assemblies occurs in the horizontal reductions.
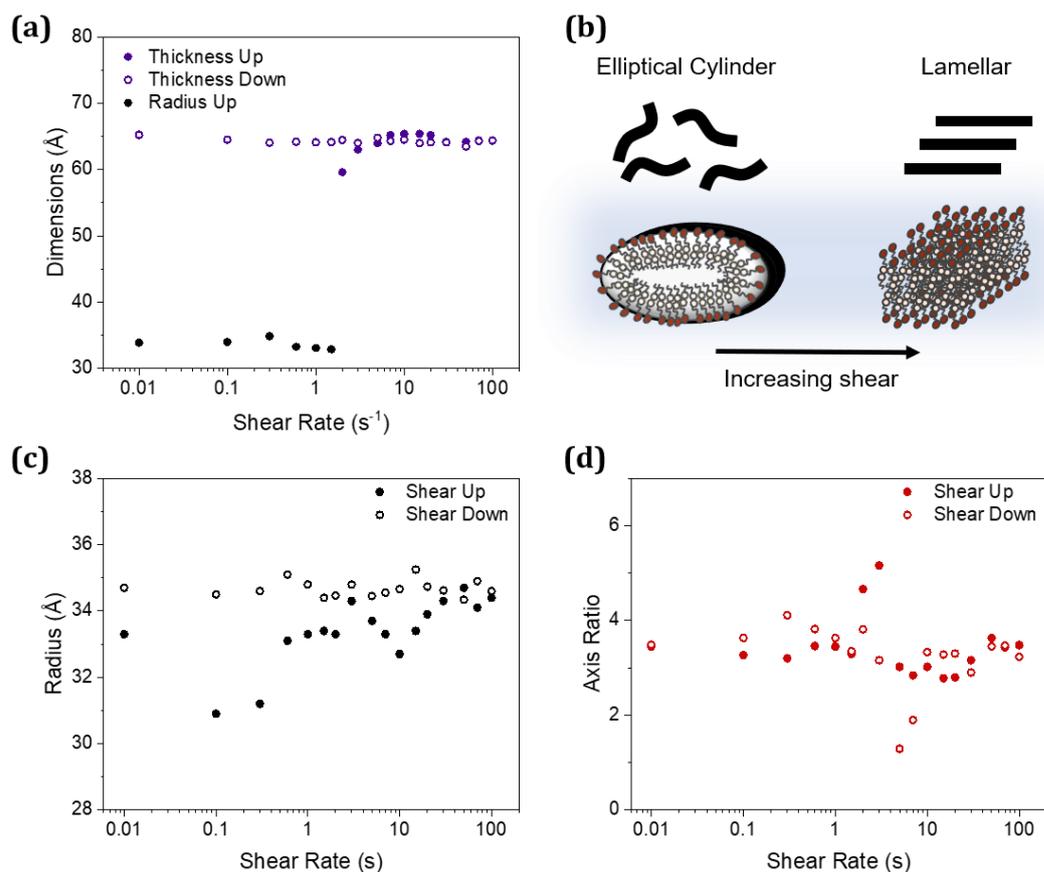
Figure 4.10. Physical parameters from models (elliptical cylinder or lamellar) fitted to the scattering profiles of $C_6AzoOC_4E_4$ (2.5 wt%). (a) Minor radius of elliptical cylinder (black) or lamellar thickness (purple) on the shear-up ramp, in the horizontal direction. Lamellar thickness on the shear-down ramp is given in open circles. (b) Schematic of the self-assembled forms of the elliptical cylinder and lamellar sheet. (c) Minor radius of elliptical cylinder on the shear-up (black) and shear-down (open) ramps and (d) axis ratio of elliptical cylinder on the shear-up (red) and shear-down (open) ramps in the vertical direction.

A comparison between the scattering profiles partially reduced in two perpendicular directions compared with the scattering profile reduced over the full angular range is available in the Appendix (Figure A.4.13). These data mirror the same trend as has been shown through the alignment factor, as they are just a graphical presentation of the intensity difference between the two directions. It may be more intuitive to view the data this way so they are provided for convenience.

To summarise the key findings: clear shear-alignment and time-dependent shear behaviour occurs for this complex fluid. When viewed in the flow direction (horizontal reductions) initially elliptical cylinders are formed which increase in eccentricity to ultimately scatter as sheet-like objects. It is possible that shear-banding is occurring, which would result in 'sheets' which shear at different rates.[24,25] However, the presence or absence of shear-banding cannot be clarified using 1,3 plane rheo-SANS; flow velocimetry or 1,2 plane rheo-SANS is required.[24] When viewed in the vorticity direction (vertical reductions) elliptical cylinders are found across all shear rates. The formation of

elliptical micelles by $C_6AzoOC_4E_4$ seems unusual at first, as surfactants generally self-assemble into isotropic structures as the hydrophobic effect, and other packing considerations, are non-directional. However, AzoPS differ from typical alkyl surfactants due to the conjugated aromatic rings in their tails, which are planar in the *trans*-isomer. Aromatic interactions provide both a directional and solvent-dependent influence on self-assembly.[26,27] Elliptical WLMs have been found for $C_8AzoOC_8E_4$ (Chapter 3) and have been reported for a zwitterionic betaine surfactant.[6] The preferential alignment of the hydrophobic azobenzene results in cylinders with a long major axis and low degree of curvature along the packing direction. As these surfactants have a steric preference to pack as cylinders, there are high curvature sections along the minor radius of the cylinder (Figure 4.10). Surfactant self-assembly is dynamic and small-angle scattering records average properties of scattering bodies in solution, therefore the formation of elliptical WLMs indicates that several favourable radii of curvature are present. Axis ratios of 3.7 have been reported for perylene-based tubular polymersomes,[28] similar to the axis ratios of elliptical WLMs reported here. In fact, the report on polymersomes[28] also investigated the effect of reducing the perylene content (and therefore quantity of aromatic interactions) of the polymers that formed elliptical polymersomes and found elliptical WLMs were formed instead. In view of this, it seems reasonable that azobenzene can influence the packing of surfactants to create eccentric structures. Evidence for π-π stacking interactions is found in the UV-Vis absorption spectra, where the absorption band relating to the π-π* transition is asymmetric above the CMC, due to the blue shift (H-aggregation) that occurs upon aromatic stacking and aggregation (Appendix, Figure A.4.14). It is also possible that the tetraethylene glycol head-group influences anisotropic packing *via* H-bonding interactions (which are also directional).[29,30]

Higher scattering occurs in the vorticity direction where the R_{CS} of the cylinders is observed, whose length scales fall into the observation window (209 - 5 nm). In the flow direction, the key features (length of WLM) are larger than the observation window. The scattering intensity indicates what is aligned and scattering, within a given length scale (determined by the q-range and the detector distance.) Investigating the structures formed in the flow and vorticity directions separately, a transition from elliptical cylinders to sheets occurs in the horizontal direction after 1.5 s^{-1}. The conclusion is that $C_6AzoOC_4E_4$ struggles to maintain a consistent structure under shear, with shear inducing a phase transition. While the viscosity behaviour implies shear-thinning as a result of chain disentanglement, the scattering data indicate that alignment only occurs in certain shear regimes. It appears that $C_6AzoOC_4E_4$ forms elliptical WLMs which scatter as sheet-like objects with increasing shear, which have a relaxation time of >100 s.

4.3.3. Structure and Flow-Behaviour at Higher Temperatures

Rheo-SANS measurements were repeated at 40 °C for 2.5 wt% $C_6AzoOC_4E_4$. For liquids in general, viscosity tends to decrease with increasing temperature, reflecting the increased ability of molecules in solution to overcome intermolecular forces. For surfactant solutions, the effect of temperature can be considered in terms of the underlying thermodynamics, with an added consideration for the dynamic self-assembly behaviour. As self-assembled aggregates result from intramolecular and hydrophobic interactions, it is possible that a consequence of increased thermal energy is the formation of aggregates with different shapes and sizes compared to their room-temperature counterparts, with correspondingly different flow behaviour. *e.g.,* WLMs have different rheologies compared to spherical aggregates.[31,32] For WLMs, the dimensions and branching depend on enthalpic and entropic contributions such as end-cap and scission energy;[21,33–35] it is possible high temperatures will change the flow behaviour.

Figure 4.11 shows the viscosity as a function of shear rate at 40 °C, with strong shear thinning observed. Compared to 25 °C, the viscosity is initially lower at 40 °C, with values of 10323.1 and 3788.3 mPa·s obtained at 0.01 s^{-1} for 25 and 40 °C, respectively. The viscosity plateaus from ~10 s^{-1}, with a value of 22.9 mPa·s, higher than the final value of 6.8 mPa·s at 100 s^{-1} for the room temperature sample. It is likely the viscosity becoming independent of shear-rate is due to WLMs becoming disentangled and aligned with the flow, although the higher final value at 40 °C is interesting. The viscosity is somewhat reversible here; initially the shear-down ramp has the same values as the shear-up ramp, with deviations in the intermediate region. A final value of 618 mPa·s is recovered at 0.01 s^{-1}, compared to an initial value of 3788 mPa·s $^{-1}$. It is likely that due to long relaxation times, the viscosity is not fully recovered over the timescales given for measurement.
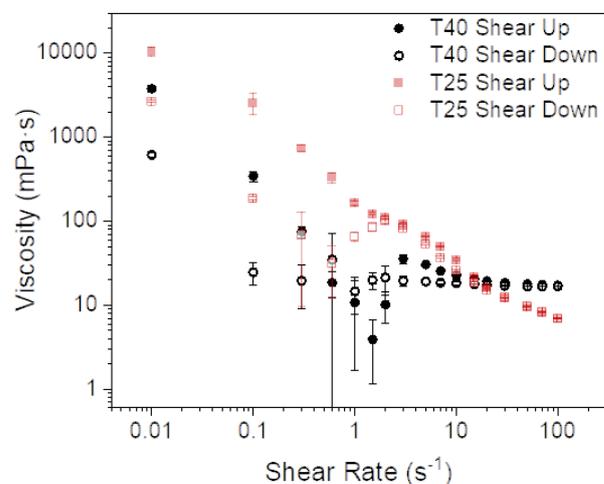
Figure 4.11. Viscosity as a function of shear rate for 2.5 wt% aqueous solutions of $C_6AzoOC_4E_4$ in the native *trans*-state at 40 °C (black) and room temperature (red squares). The shear-up ramps are shown with filled symbols, while the shear-down ramps are shown with open symbols.

Figures 4.12a and b show the annularly-reduced scattering data at 40 °C, for both the shear-up and shear-down ramps. On the shear-up ramp, it is clear the degree of anisotropy varies with shear rate, with some rates having two pronounced peaks at 90° and 270° and others having a flatter profile. The peaks are most obvious between 1 and 3 s^{-1}, with flatter profiles observed at lower and higher shear. To quantify these trends in alignment, the alignment factor was calculated (Figure 4.12c). There is an increase in alignment between 0.01 and 1.5 s^{-1}, corresponding to the shear range with clear shear-thinning behaviour from the viscosity measurements. There is a sharp decrease in alignment between 2 and 10 s^{-1}, the range in which the viscosity increased slightly. The alignment is steady across the high-shear region (10 s^{-1} to 100 s^{-1}). This corresponds to where a viscosity independent of shear rate was observed (Figure 4.11). Interestingly, the alignment at high shear is lower than that observed at low shear. The scattering data were averaged and reduced across the entire angular range (Appendix, Figure A.4.15), with a low q decay of q^{-2} for all shear rates, indicative of lamellar sheets. The general trends observed for 40 °C are similar to those observed at 25 °C; the key difference is the behaviour is simpler here; the alignment factor steadily increases and decreases, with no region where the alignment becomes slightly negative.
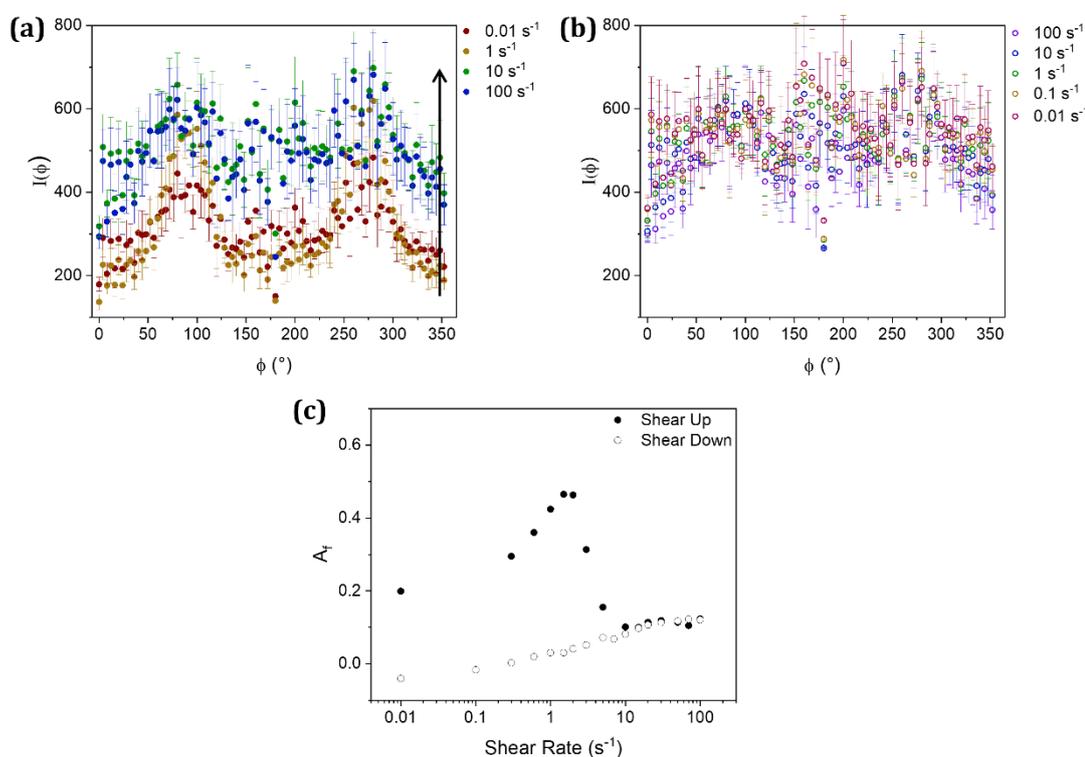
Figure 4.12. Annularly reduced scattering profiles of $C_6AzoOC_4E_4$ (2.5 wt% in water) at 40 °C at different shear rates. (a) Intensity as a function of scattering angle for the shear-up ramp between 0.01 and 100 s^{-1}. (b) Intensity as a function of scattering angle for the shear-down ramp across the same shear range. (c) Alignment factor, A_f, as a function of shear rate for the shear-up (filled symbols) and shear-down (open symbols) ramps.

4.3.4. Rheo-SANS Measurements after UV Irradiation

The 2.5 wt% sample of $C_6AzoOC_4E_4$ in water was irradiated with UV light through the Couette cell for several hours before measurement, with manual mixing of the solution periodically throughout the irradiation time. There was a clear colour change from orange to red, along with a visible change in the fluidity of the solution (Appendix, Figure A.4.16). This solution, now with a large proportion of *cis*-isomers as suggested by the colour change, was measured as previously, with UV irradiation maintained throughout the measurement.

Figure 4.13 shows the viscosity measured for the solution after UV irradiation. The viscosity is lower than the native-*trans* state (3753.7 *vs.* 10323.1 mPa·s at 0.01 s^{-1}, respectively) and retains clear shear-thinning behaviour. As was observed for the high temperature *trans*-sample, there is some shear thinning in the intermediate q regime. In this case the viscosity is fully reversible on the up and down shear ramps, indicating that the relaxation time of the WLMs is within the timescales of the measurement. The viscosity values are about an order of magnitude lower after UV irradiation than for the native *trans*-state, for a given shear rate. However, the viscosity after UV irradiation is different to what was previously observed and reported in Chapter 3. Previously, a Newtonian fluid was found in the *cis*-PSS, with a viscosity of 1.2 mPa·s, independent of shear rate. It is thought that the difference is that the *cis*-PSS is not being formed here. As the UV irradiation was done *in-situ* and without UV-Vis to confirm the formation of the PSS, it is likely that a solution with *cis*-isomers is present, but that it is not yet the final PSS composition. As such, the results here will be limited to a brief discussion of the 1D scattering profiles, but it is still considered useful to observe how the flow behaviour and self-assembled structure is influenced by UV irradiation.
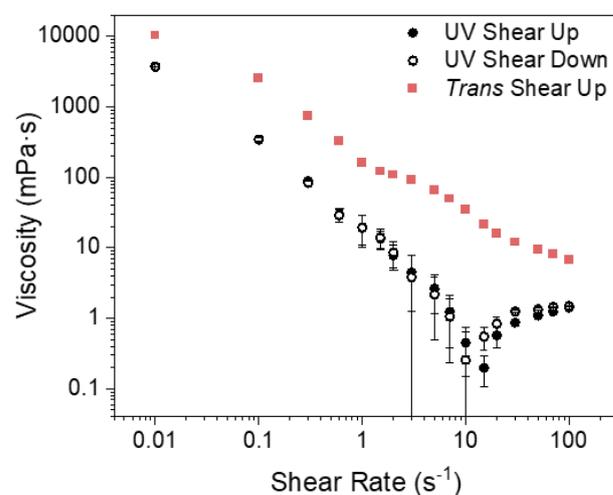
Figure 4.13. Viscosity as a function of shear rate for a 2.5 wt% solution of $C_6AzoOC_4E_4$ in water after, and during, UV irradiation. The shear-up ramp is given by filled black circles while the shear down ramp is given by open circles. The viscosity data from measurements of the native *trans*-state is given by red squares.

Figure 4.14 shows the 1D scattering profiles for 2.5 wt% $C_6AzoOC_4E_4$ after UV irradiation. For the shear-up ramp there is a very slight change in the intensity and shape of the scattering profiles, with an initial low q decay of q^{-1} at low shear and $q^{-1.1}$ at high shear, indicating scattering from cylinders. For the shear-down ramp the reverse trend is observed. From cryo-TEM images reported in the previous chapter, it is known that even in the *cis*-PSS, $C_6AzoOC_4E_4$ retains WLMs in solution, with some vesicles present. The key difference observed previously was the extent of branching of the WLMs, with a much more open, loose network formed for the *cis*-PSS. On the length scales accessible here, not much information about the branching or network can be obtained, so it is not surprising that the scattering profiles retain a decay in intensity indicative of scattering from cylindrical aggregates. The similarity in scattering intensity across the shear rates implies that there is little change in the physical parameters. The scattering profiles after UV irradiation change less with shear rate than those in the native *trans*-state. This relatively fixed local environment with shear could be useful to have, depending on the application.
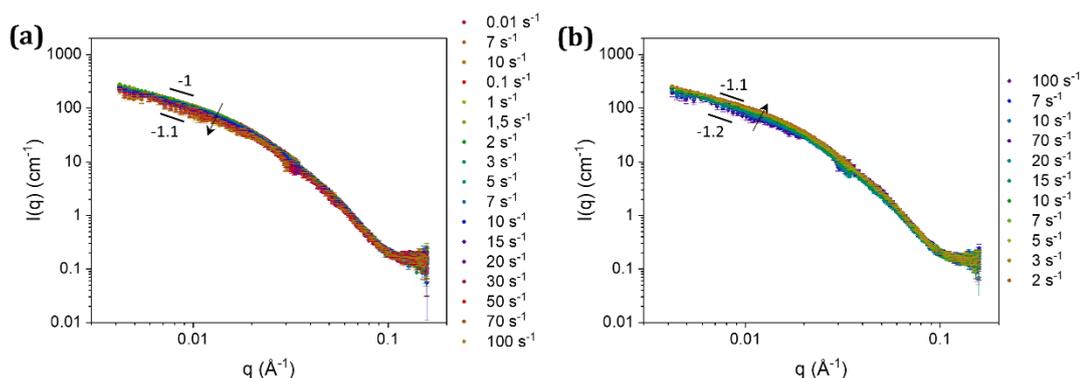
Figure 4.14. 1D Scattering profiles of a 2.5 wt% solution of $C_6AzoOC_4E_4$ in water after UV radiation on the shear-up (a) and shear-down (b) ramps.

4.3.5 Structure and Flow Behaviour at Higher Concentration

Rheo-SANS measurements were repeated on a more concentrated sample as it is likely entanglements and interesting flow behaviour is enhanced at higher concentrations. The solution of 4 wt% $C_6AzoOC_4E_4$ in water was clearly viscous without being too difficult to manipulate, while remaining well below the concentration at which LLC phases were observed (the topic of the following Chapter). The 4 wt% solution of $C_6AzoOC_4E_4$ was measured across the shear range 0.01–100 s^{-1}, at room temperature in the native *trans*-state. Figure 4.15 shows the viscosity, η, as a function of shear rate. There is clear shear-thinning behaviour, even at low shear rates. The shear thinning can be broken into two regimes: strong shear thinning between 0.01 and 2 s^{-1} and less strongly shear-thinning region between 2 and 40 s^{-1}; after 40 s^{-1}, shear-thickening occurs.
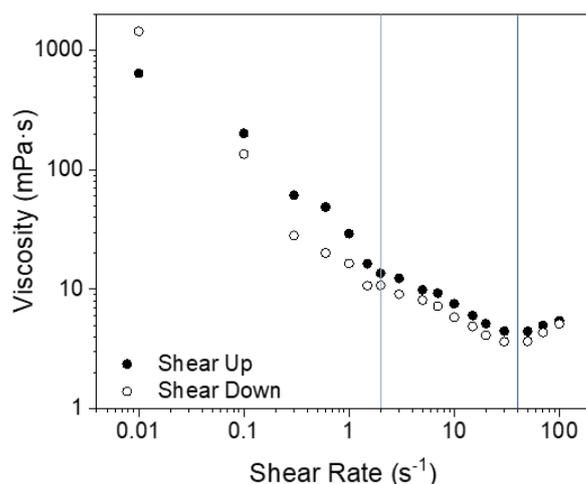
Figure 4.15. Viscosity as a function of shear rate for *trans*-C$_6$AzoOC$_4$E$_4$ (4 wt%). Values from shearing up from 0.01 to 100 s^{-1} are represented by filled circles, while values from shearing back down 100 to 0.01 s^{-1} are represented by open circles.

The shear-thinning behaviour has a break in slope that occurs at the same shear rate as for the 2.5 wt% sample (1.5 s^{-1}). The key difference here is the shear-thickening behaviour at high shear rates. Shear-thickening behaviour has been reported for WLMs upon branching, when new connections are formed between the WLMs.[2,5,36,37] The behaviour while reducing the shear rate loosely mirrors that of the shear-up ramp, with changes in slope occurring at the same shear boundaries. Here, the system almost fully recovers the viscosity values, in stark contrast to the behaviour at 2.5 wt%. This indicates that this solution has a shorter relaxation time than that of the 2.5 wt% sample. A frequency sweep was performed to determine the relaxation time (Figure 4.16). Clear viscoelastic behaviour with a crossover at 0.06 s^{-1} is observed, corresponding to a relaxation time of 16 s^{-1}. This is at least an order of magnitude faster than the 2.5 wt% solution. This is likely due to increased branching of the WLMs with increased concentration.[19]
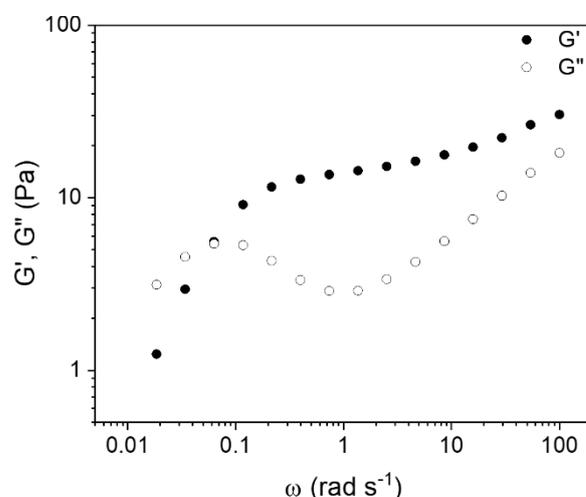
Figure 4.16. Storage (*G'*) and loss (*G''*) moduli *vs.* angular frequency (*ω*) for 4 wt% C$_6$AzoOC$_4$E$_4$. A clear crossover from viscous to elastic behaviour occurs at at shear rate of 0.6 s^{-1}.

The 2D-SANS profiles were annularly reduced (Figure 4.17) with anisotropy present at low shear rates. These peaks mirror the viscosity trend, with three distinct shear regions. They grow in intensity from 0.01 to 1.5 s^{-1}, before reducing (2–20 s^{-1}), and then growing again (30–70 s^{-1}), before a final reduction at 100 s^{-1}. These shear-rate regions mirror those where changes were observed for the viscosity behaviour. For the reverse process, shearing down from 100 to 0.01 s^{-1} causes an increase in peak intensity, across the entire range (Figure 4.17b), indicating structural recovery. Isotropic profiles were not observed for any shear rates, with the least pronounced anisotropy observed for the highest shear rate of 100 s^{-1}.

The scattering intensity was radially reduced across the full angular range to create 1D scattering profiles (Figure 4.18). On the shear-up ramp, a decrease in scattering intensity was observed, accompanied by a change in the slope at low q from $q^{-1.5}$ to q^{-1}. A decay of q^{-1} is indicative of scattering from cylinders in solution, with a reduction in intensity likely due to the alignment of the long cylinder in solution, as the physical dimensions exceed the observation window (209–5 nm) accessible in these measurements. There is also the development of a short plateau or bump at ~0.013 $Å^{-1}$; often the presence of an intensity independent of q can indicate that the dimensions of the scattering bodies are within the observation window probed, and are often seen for spherical objects with a diameter of ~100 nm. However, in this case the plateau does not extend into the entire low q region and there is an uptick in slope below 0.008 $Å^{-1}$. A variation in length scales across the q range is common for WLMs and was observed for $C_8AzoOC_8E_4$ during *in-situ* SANS measurements (Chapter 3). The most likely source for the scattering trends in this case is due to characteristic WLM effects, where well-separated length scales of physical parameters results in variation in the slope across the scattering profiles.[35]
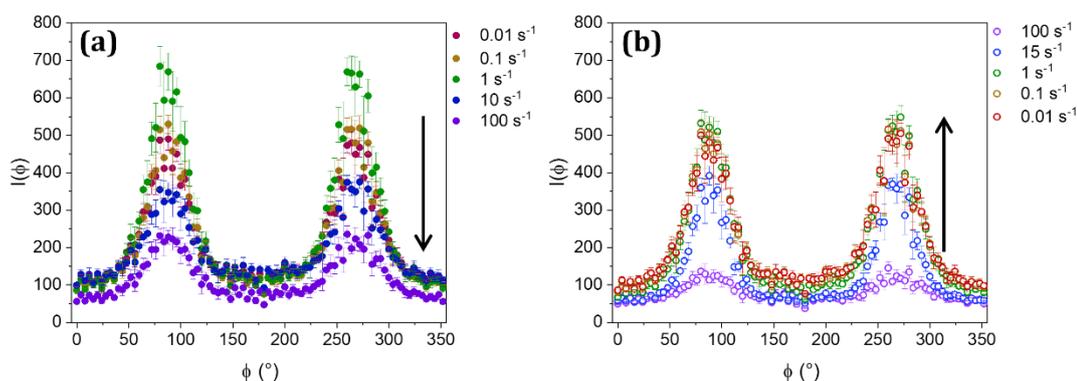
Figure 4.17. Selected annular reductions of the 2D-SANS profiles of a 4 wt% solution of *trans*-$C_6AzoOC_4E_4$ in water at 25 °C. (a) Shearing up from 0.01 to 100 s^{-1} and (b) shearing down from 100 to 0.01 s^{-1}. SANS measurements were performed in the radial configuration.
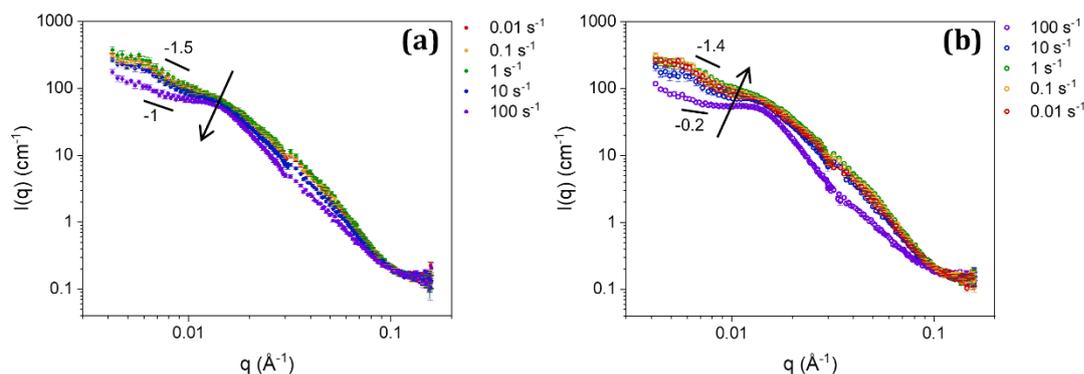
Figure 4.18. Selected scattering profiles of $C_6AzoOC_4E_4$ (4 wt% in water at 25 °C) in the native *trans*-form for the shear-up (a) and shear-down (b) ramps. The slope of the decay in scattering intensity at low q is indicated by solid line. The discontinuities at ~0.01 Å^{-1} are artefacts resulting from the process of merging the scattering intensity from two different detector distances.

From mid q onwards (0.02 Å^{-1}), the shape and slopes of the scattering profiles do not vary significantly with q, particularly at lower shear rates, implying that across this length scale (<30 nm), the scattering bodies in solution do not change in size significantly. For the shear-down ramp, the scattering profile varies with shear rate, in contrast to what was observed for the 2.5 wt% system, and in agreement with the observed recovery of the viscosity and shorter relaxation time. At high shear, the plateau and decrease in slope is even more pronounced that what was observed at 100 s^{-1} at the end of the shear-up ramp (the measurements were recorded in the same run, with 120 s between each shear rate the 100 s^{-1} shear rate was then effectively held for 240 s before shearing back down.). The plateau is lost with increasing shear rate and a low q slope of q^{-1} is recovered. Scattering profiles for the full shear range are available in the Appendix (Figure A.4.17).

4.3.6. Partial Reductions in the Flow and Vorticity Directions

The data were partially integrated in two perpendicular directions, flow and vorticity as before. Figures 4.19a, c show the shear dependence of the 1D-SANS profiles, with a clear change in behaviour depending on whether the scattering is averaged parallel or perpendicular to the flow direction. An example of an anisotropic detector image can be observed in Figure 4.19b, highlighting the utility of integrating with and perpendicular to the flow direction. In the horizontal direction (flow plane), there is increased scattering intensity with shear rate, as observed for the 2.5 wt% solution, which indicates shear-alignment. In this case, there is a strong plateau around 0.01 Å^{-1}, with an upturn at very low q. The scattering is not consistent with lamellar sheets, as noted for the 2.5 wt% solution, here in all cases the scattering profiles indicate WLMs. There is also a growth of structure factor with increasing shear, most obvious at~0.015 Å^{-1} at 100 s^{-1}. This is likely to be due to both the increased concentration, higher shear rates and increased alignment causing increased interparticle interactions. The scattering profile in the vertical

direction (vorticity plane) initially decays with a slope of $q^{-1.2}$, with a decrease in low q slope with increasing shear rate. The slope at high shear decays as $q^{-0.8}$ so it appears the solution is forming WLMs across the entire shear range. Due to the strong variation in slope and intensity across the q-range, as is often characteristic of WLMs, it was not possible to fit these models to form factors. Further efforts to fit these scattering profiles will be the focus of future work, including the development of new models.

From the alignment factor (Figure 4.19d), it is clear there is strong initial alignment at low shear rates, with a value of 0.56 at 0.01 s^{-1} while shearing up. The alignment factor increases before plateauing at 0.67 between 0.6 and 1.5 s^{-1}. This is followed by a strong drop in alignment, to a value of 0.40 between 2 to 15 s^{-1}. This corresponds to the second regime in the viscosity curve, where the initial strong shear thinning levelled off to a weaker shear-thinning behaviour. This is possibly a phase transition, or may indicate the onset of shear-banding.
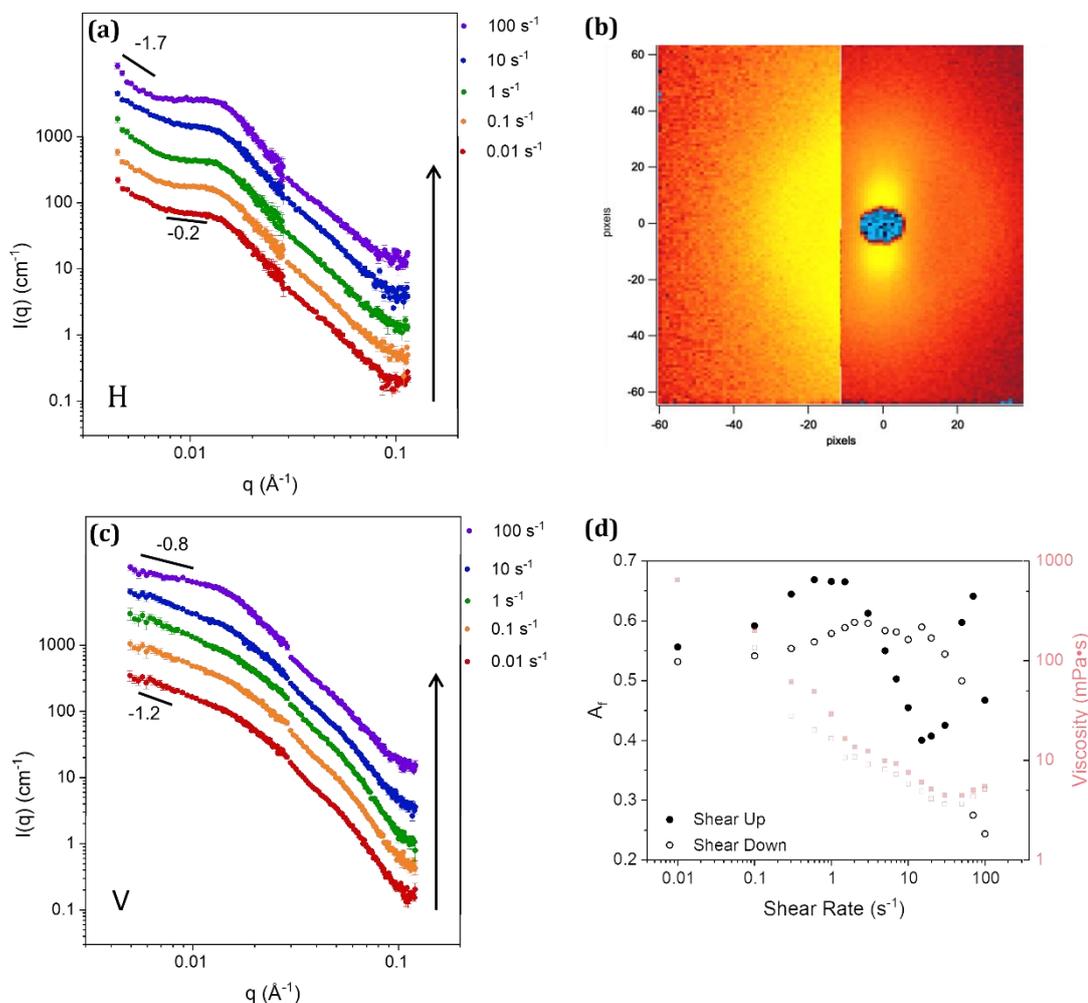
Figure 4.19. 1D scattering profiles of C$_6$AzoOC$_4$E$_4$ (4 wt%) in the (a) horizontal and (c) vertical directions for the shear-up ramp. Arrows indicate increasing shear-rate (b) Detector images at 1.5 s^{-1} (d) Alignment factor for the shear-up (black circles) and down (open circles) ramps. The viscosity is in pale red for comparison.

From 20 to 70 s^{-1} there is an increase in alignment to 0.64, before a second drop to a value of 0.47 at 100 s^{-1}. This region corresponds to the shear thickening observed in the viscosity curve. At first glance it appears as if the solution initially aligns with the shear, holding a maximum value for a short plateau, before loss of alignment and potential disruption of structure in the intermediate shear regime. This may be due to the formation of a new shear-induced structure which itself then temporarily aligns with the shear flow between 20 and 70 s^{-1}, before itself being lost at higher shear values of 100 s^{-1}.

For the reverse process of shearing down, the lowest value of A_f, 0.24, is found at 100 s^{-1}. There is a steady increase in A_f to 0.59 at 15 s^{-1}, at which point there is a step change and slow levelling of the alignment factor, to a final value of 0.53 at 0.01 s^{-1}. This is slightly lower than the initial value, in agreement with the higher viscosity after shear. It can also be observed that while three separate regimes can be observed in the data for viscosity and alignment factor, there is an offset at the shear rates at which the transition between regions occurs. For example, the alignment factor plateaus at a value of 0.67 at 0.6 s^{-1}, while the viscosity doesn't change until 2 s^{-1}. Similarly, the alignment factor begins increasing from 20 s^{-1}, while a change in viscosity isn't observed until 50 s^{-1}. This implies there is a lag time between the formation of a different structure, as indicated by the alignment, and the impact this structure has on the viscosity.

The scattering profiles for the horizontal and vertical partial integrations on shear-down ramp are shown in Figure 4.20. In the horizontal direction, the profiles are very similar to the shear-up ramp. A strong plateau remains at ∼0.01 $Å^{-1}$, even more pronounced in this case. Likewise, in the vertical direction, the reverse trend of the shear-up ramp can be seen, indicating that the structure is recovered, at least over the length scales probed by SANS. This agrees with the viscosity recovery and short relaxation of 16 s. For both shear-up and down ramps in the horizontal direction, very clear WLM profiles are observed, with well-separated length scales. In the vertical direction, smoother scattering profiles are observed, with decays of q^{-1}, characteristic of cylindrical aggregates. In neither case, does sheet-like behaviour emerge, nor is there a clear point at which a phase transition can be assigned. However, as aforementioned, phase transitions and shear-banding may not be evident in the 1,3 plane and further techniques may be required to probe the clear regimes observed in the alignment factor and viscosity.
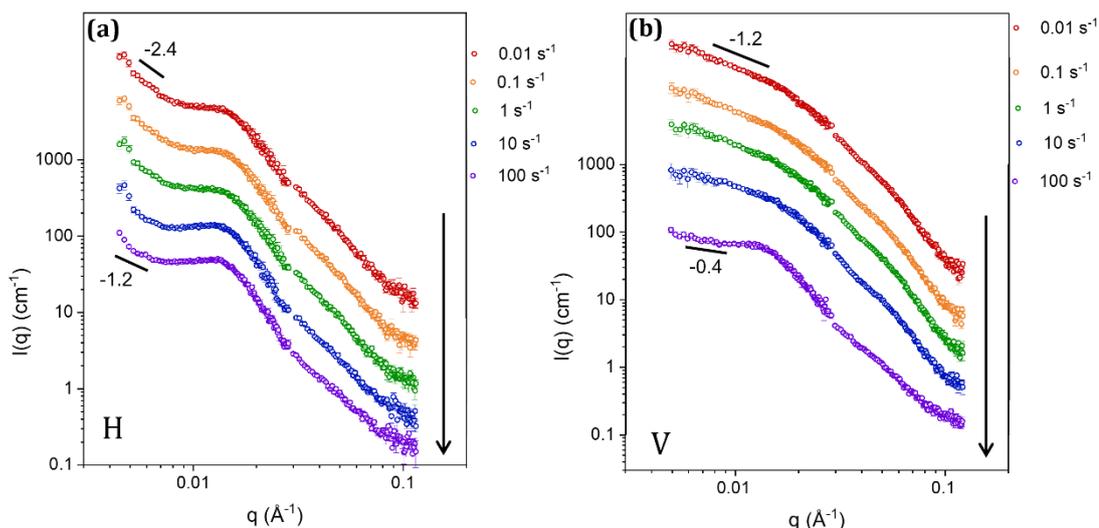
Figure 4.20. 1-D scattering profiles of $C_6AzoOC_4E_4$ (4 wt% in water) as a function of shear rate in the (a) horizontal (vorticity) and (c) vertical (flow) directions for the shear-down ramp. Arrows indicate decreasing shear rate.

4.3.7. Discussion of the 4 wt% Solution and Comparison to 2.5 wt%

The presence of a plateau in the scattering profiles in the low-mid q region (0.006–0.02 Å^{-1}) is typical for WLMs when the length scales of the component parts (contour length, Kuhn length, cross-sectional radius) are well separated.[32,35] This plateau is more pronounced at high shear than low shear, with the shear-dependence being particularly clear for the partial integrations in the vertical direction (vorticity plane). This implies that the length scales of the WLM change with shear rate, becoming either more or less separated. It makes intuitive sense that at higher shear there may be elongation along the principle axis of the WLM (*i.e.,* length) with a concurrent contraction through the radius. Unfortunately it was extremely difficult to fit any models to these scattering profiles, due to their pronounced shapes, plateaus and structure factor; although as the length scales of WLMs tend to be far outside the observation window of SANS, parameters such as contour length cannot be determined through model fitting in any case. It is well-established that the scattering profiles of WLM can be difficult to fit, due to issues in deconvoluting the effect of intermicellar interactions (given by the structure factor) on the scattering.[38–41] An excellent discussion on the topic of fitting the scattering of WLMs is available in a review by Dreiss.[35] It is clear in Figure 4.20 that extensive structure factor is present in these profiles, particularly at higher shear rates in the vorticity plane. The presence of this structure factor also made it difficult to fit the scattering contributions separately as the 'bump' in intensity occurred at the crossover plateau region (*i.e.* fit the high q region using a cylinder model to account for the cross-sectional radius, while fitting a flexible cylinder to the low q region).[35,42] Some efforts have been made to obtain parameterised scattering functions using Monte Carlo techniques.[41,43]

There are two key differences between the 2.5 and 4 wt% samples of $C_6AzoOC_4E_4$ in water. Firstly, the relaxation time. The structure, and viscosity, are both recovered on the shear-down ramp for the 4 wt% sample. The 4 wt% solution seems to have less strongly time-dependent flow behaviour compared to the 2.5 wt% solution, and has a significantly shorter relaxation time, of 16 s compared to over 100 s. The alignment follows a more straightforward dependence on shear rate for the higher concentration solution and does not have any negative or values very close to zero. It is interesting that the 4 wt% fluid is very strongly aligned, even at very low shear, and it is possible this is due to the previously discussed π-π interactions, which give rise to a more rigid WLM which can then align very easily.

It is likely that the increased concentration affects the degree of branching of the micellar network. The 4 wt% solution likely has more branching than the 2.5 wt% solution, resulting in shorter relaxation times, and the recovery of the structure and viscosity within the timescales of the measurement, as observed here. The degree of branching could be investigated as part of any future work using cryo-TEM measurements and NMR self-diffusion. Since an average scattering of the aggregates in solution is obtained with SANS, any differences in branching are difficult to unravel or assign using this technique. Rheology can give hints about the degree of branching, on the basis of viscoelasticity or relaxation time, but again this is indirect evidence to support a supposition, rather than to fully confirm. Previous work has emphasised how different behaviour can occur in different shear regimes, depending on factors such as salt concentration. It is possible to see shear-thinning or shear-thickening behaviour for same material, if only the salt concentration is varied.[2] Here, we highlight that variation of surfactant concentration has similar results.

The key difference in structure between the two concentrations is the clear change to a sheet-like phase which scatters as lamellar aggregates at high shear for the 2.5 wt% sample. After 1.5 s^{-1}, the viscosity, alignment and scattering profiles all transition. It is has been observed that a phase transition to a nematic or shear-banded state can occur for long micelles which disfavour branching and that have long relaxation times.[19,44,45] A nematic phase is an aligned state, such as disentangled WLMs.[44,46] Shear-banding is a broad phenomenon, but in the case of WLMs, it tends to occur at a critical high shear rate where the chains have disentangled with shear-thinning. This aligned, disentangled state has inherently unstable flow and may form a high shear branch, allowing the fluid to phase separate into branches, or bands, of different shear.[44,47] In fact, it is thought shear banding occurs for all WLM solutions but can only be comprehensively probed by 1,2-plane measurements or direct visualisation with a laser.[24,48,49] There can be

variations in turbidity between shear bands due fluctuations in concentration caused by shear,[50,51] meaning that the interface between adjacent bands can be visualised by imaging the flow in the velocity gradient-vorticity plane.[24,52] Investigation into this is outside the scope of the current work but will be the focus of future work.

Such a phase transition is not apparent for the 4 wt% sample for which the scattering profiles are always characteristic of WLMs with well-separated length scales in the horizontal direction and of cylinders in the vertical direction. However, the alignment factor and viscosity possess three clear shear regimes for the 4 wt% sample, with two rates of shear-thinning and shear-thickening observed. The structural changes responsible for these regimes are not evident in the scattering of the 1,3 plane.

4.4 Conclusions

In conclusion, it is clear that aqueous solutions of $C_6AzoOC_4E_4$ can form WLMs with highly concentration-dependent behaviour. These solutions are shear-thinning and viscoelastic, with strong time- and shear-dependent behaviour. Knowledge of these properties is invaluable for any further applications or use of this fluid. From rheo-SANS measurements, it is evident that the structure varies with shear, with structural transitions being most striking for the 2.5 wt% solution. The value of using rheo-SANS as a characterisation tool to study these sorts of surfactant systems is clear. Structural transitions under shear, and in different flow planes, *i.e,.* vorticity and flow, can be probed in a way that is impossible using standard SANS and separate offline rheology measurements. This is only the second report of using rheo-SANS to investigate AzoPS,[6] but given the fascinating behaviour and influence of aromatic interactions on both the structures formed and the degree of alignment, it is hoped that this technique will be more widely integrated with photosurfactant systems.

The concentration of the AzoPS solution strongly affected the rheology and self-assembled structure, offering a way to tune the flow behaviour as required. Higher concentrations seem to result in WLM solutions with significantly more branching, as implied from the shear-thickening behaviour and shorter relaxation time. The lower concentration resulted in a WLM network that appeared to strongly disfavour branching. With increasing shear, a phase transition to a low-viscosity, aligned, sheet-like structure was preferred, over shear-thickening and retention of characteristic WLM scattering.

Preliminary use of UV light to photoisomerise the WLM network resulted in a solution that recovered its viscosity on the shear-up and down ramps, indicating the relaxation time was drastically reduced. Likewise, very few changes in scattering were observed with increasing shear for the UV irradiated solution, in stark contrast to the native *trans*-solution. Following on from the concentration-dependent behaviour observed here, next the AzoPS will be probed in terms of their ability to form lyotropic liquid crystal phases at higher concentrations.

4.5 References

1   A. P. R. Eberle and L. Porcar, *Curr. Opin. Colloid Interface Sci.*, 2012, **17**, 33–43.

2   M. Takeda, T. Kusano, T. Matsunaga, H. Endo, M. Shibayama and T. Shikata, *Langmuir*, 2011, **27**, 1731–1738.

3   V. T. Kelleppan, J. E. Moore, T. M. McCoy, A. V Sokolova, L. De Campo, B. L. Wilkinson and R. F. Tabor, *Langmuir*, 2018, **34**, 970–977.

4   J. E. Moore, T. M. McCoy, L. de Campo, A. V. Sokolova, C. J. Garvey, G. Pearson, B. L. Wilkinson and R. F. Tabor, *J. Colloid Interface Sci.*, 2018, **529**, 464–475.

5   H. Iwase, R. Kawai, K. Morishima, S. ichi Takata, T. Yoshimura and M. Shibayama, *J. Colloid Interface Sci.*, 2019, **538**, 357–366.

6   C. S. G. Butler, J. P. King, L. W. Giles, J. B. Marlow, M. L. P. Vidallon, A. Sokolova, L. de Campo, K. L. Tuck and R. F. Tabor, *J. Colloid Interface Sci.*, 2021, **594**, 669–680.

7   L. Porcar, D. Pozzo, G. Langenbucher, J. Moyer and P. D. Butler, *Rev. Sci. Instrum.*, 2011, **82**, 1–8.

8   R. P. Murphy, Z. W. Riedel, M. A. Nakatani, P. F. Salipante, J. S. Weston, S. D. Hudson and K. M. Weigandt, *Soft Matter*, 2020, **16**, 6285–6293.

9   S. R. Kline, *J. Appl. Crystallogr.*, 2006, **39**, 895–900.

10   E. Törnquist, L. Gentile, S. Prévost, A. Diaz, U. Olsson and H. Isaksson, *Sci. Rep.*, 2020, **10**, 1–11.

11   J. S. Pedersen and P. Schurtenberger, *Macromolecules*, 1996, **29**, 7602–7612.

12   W. R. Chen, P. D. Butler and L. J. Magid, *Langmuir*, 2006, **22**, 6539–6548.

13   L. A. Feigin and D. I. Svergun, *Structure Analysis by Small Angle X-ray and Neutron Scattering*, Plenum, New York, 1987.

14   *http://www.sasview.org/*, accessed 10/19.

15   J. Berghausen, J. Zipfel, P. Lindner and W. Richtering, *J. Phys. Chem. B*, 2001, **105**, 11081–11088.

16   F. Nallet, R. Laversanne and D. Roux, *J. Phys. II*, 1993, **3**, 487–502.

17   S. Basu, U. S. Shivhare and G. S. V. Raghavan, *Int. J. Food Eng.*, , DOI:10.2202/1556-3758.1229.

18   S. Rogers, J. Kohlbrecher and M. P. Lettinga, *Soft Matter*, 2012, **8**, 7831–7839.

19   U. Olsson, J. Börjesson, R. Angelico, A. Ceglie and G. Palazzo, *Soft Matter*, 2010, **6**, 1769–1777.

20   K. Liu and D. Grecov, *Appl. Math. Model.*, 2011, **35**, 1603–1615.

21   M. E. Cates, *Macromolecules*, 1987, **20**, 2289–2296.

22   D. P. Acharya and H. Kunieda, *Adv. Colloid Interface Sci.*, 2006, **123**–**126**, 401–413.

23   H. Iwase, R. Kawai, K. Morishima, S. ichi Takata, T. Yoshimura and M. Shibayama, *J. Colloid Interface Sci.*, 2019, **538**, 357–366.

24   M.-A. Fardin, L. Casanellas, B. Saint-Michel, S. Manneville and S. Lerouge, *J. Rheol. (N. Y. N. Y).*, 2016, **60**, 917–926.

25   J. Y. Lee, G. G. Fuller, N. E. Hudson and X.-F. Yuan, *J. Rheol. (N. Y. N. Y).*, 2005, **49**, 537–550.

26   S. Yagai and A. Kitamura, *Chem. Soc. Rev.*, 2008, **37**, 1520–1529.

27   F. J. M. Hoeben, P. Jonkheijm, E. W. Meijer and A. P. H. J. Schenning, *Chem. Rev.*, 2005, **105**, 1491–1546.

28   C. K. Wong, A. F. Mason, M. H. Stenzel and P. Thordarson, *Nat. Commun.*, 2017, **8**, 1240.

29   N. Liu, K. Yu, B. Smarsly, D. R. Dunphy, Y. B. Jiang and C. J. Brinker, *J. Am. Chem. Soc.*, 2002, **124**, 14540–14541.

30   A. Shahi and E. Arunan, *J. Chem. Sci.*, 2016, **128**, 1571–1577.

31   T. M. McCoy, A. Valiakhmetova, M. J. Pottage, C. J. Garvey, L. De Campo, C. Rehm, D. A. Kuryashov and R. F. Tabor, *Langmuir*, 2016, **32**, 12423–12433.

32   Z. Chu, C. A. Dreiss and Y. Feng, *Chem. Soc. Rev.*, 2013, **42**, 7174.

33   M. E. Cates and S. J. Candau, *J. Phys. Condens. Matter*, 1990, **2**, 6869–6892.

34   C. A. Dreiss, in *Wormlike Micelles: Advances in Systems,Characterisation and Applications*, Royal Society of Chemistry, 2017, pp. 1–8.

35   C. A. Dreiss, *Soft Matter*, 2007, **3**, 956–970.

36   D. Danino, Y. Talmon and R. Zana, *Langmuir*, 1995, **11**, 1448–1456.

37   M. A. Calabrese, S. A. Rogers, R. P. Murphy and N. J. Wagner, *J. Rheol. (N. Y. N. Y).*, 2015, **59**, 1299–1328.

38   L. Arleth, M. Bergström and J. S. Pedersen, *Langmuir*, 2002, **18**, 5343–5353.

39   F. Baldelli Bombelli, D. Berti, U. Keiderling and P. Baglioni, *J. Phys. Chem. B*, 2002, **106**, 11613–11621.

40   G. Jerke, J. S. Pedersen, S. U. Egelhaaf and P. Schurtenberger, *Langmuir*, 1998, **14**, 6013–6024.

41   L. Cannavacciuolo, J. S. Pedersen and P. Schurtenberger, *Langmuir*, 2002, **18**, 2922–2932.

42   P. Schurtenberger, G. Jerke and C. Cavaco, *J. Appl. Crystallogr.*, 1996, **12**, 2433–2440.

43   C. Svaneborg and J. S. Pedersen, *Curr. Opin. Colloid Interface Sci.*, 2004, **8**, 507–514.

44   E. Fischer and P. T. Callaghan, *Phys. Rev. E - Stat. Physics, Plasmas, Fluids, Relat. Interdiscip. Top.*, 2001, **64**, 15.

45   R. Angelico, S. Amin, M. Monduzzi, S. Murgia and G. Palazzo, *Soft Matter*, 2012, **8**, 10941–10949.

46   R. Angelico, U. Olsson, K. Mortensen, L. Ambrosone, G. Palazzo and A. Ceglie, *J. Phys. Chem. B*, 2002, **106**, 2426–2428.

47   M. M. Britton and P. T. Callaghan, *Eur. Phys. J. B*, 1999, **7**, 237–249.

48   R. Angelico, C. O. Rossi, L. Ambrosone, G. Palazzo, K. Mortensen and U. Olsson, *Phys. Chem. Chem. Phys.*, 2010, **12**, 8856–8862.

49   B. Arenas-Gómez, C. Garza, Y. Liu and R. Castillo, *J. Colloid Interface Sci.*, 2020, **560**, 618–625.

50   E. Helfand and G. H. Fredrickson, *Phys. Rev. Lett.*, 1989, 62, 2468.

51   I. A. Kadoma and J. W. van Egmond, *Phys. Rev. Lett.*, 1996, **76**, 4432–4435.

52   S. Lerouge, M. Argentina and J. P. Decruppe, *Phys. Rev. Lett.*, 2006, **96**, 1–4.

Chapter 5

Formation of Light-Responsive Lyotropic Liquid Crystal Phases

Some of the work presented in this Chapter has appeared elsewhere:

1. *Multimodal Control of Liquid Crystalline Mesophases from Surfactants with Photoswitchable Tails,* Judith E. Houston, Elaine A. Kelly, Margarita Kruteva, Kiriaki Chrissopoulou, Nathan Cowieson and Rachel C. Evans, *J. Mater. Chem. C*, **2019**, 7, 10945-10952

2. *Light-Responsive Self-Assembly of a Cationic Azobenzene Surfactant at High Concentration,* Camille Blayo, Elaine A. Kelly, Judith E. Houston, Nikul Khunti, Nathan P. Cowieson, Rachel C. Evans, *Soft Matter*, **2020**, 16, 9183-9187

5.1 Introduction

Up to this point, the self-assembly behaviour of two AzoPS, $C_8AzoOC_8E_4$ and $C_6AzoOC_4E_4$ have been probed at relatively low concentrations, with both the effect of self-assembled structure on flow behaviour and the effect of shear on self-assembled structure examined. In this chapter, the self-assembly behaviour of these AzoPS and two related structures, $C_2AzoOC_4E_4$ and $C_8AzoOC_4E_4$, will be investigated at higher concentrations. Characterising these surfactant systems is important as dynamic structures based on non-covalent interactions offer significant benefits such as reversibility and responsiveness to stimuli.[1–3] Of particular interest are simple, single-component systems with well-defined dimensions and morphologies and a rapid response to the stimulus, which can potentially be created using AzoPS. Applications of light-responsive structures based on non-covalent interactions include controlled uptake and release,[4–6] gelation,[7–9] drug delivery,[10,11] and catalysis.[12]

Lyotropic liquid crystalline phases are an example of dynamic structures based on non-covalent interactions and are often observed for surfactants at high concentrations. LLC phases show long-range periodicity and present a wide variety of structures, the mesoscale organisation of which depends strongly on factors such as the molecular structure of the surfactant, the local packing, as well as solvent and temperature.[13] Further details regarding the fundamentals of LLC phases are available in the Introduction (Section 1.2.3). The design of LLC assemblies that integrate additional functionality, either as an intrinsic property, such as conductivity,[14] or as a response to an external stimulus, such as light,[15,16] magnetic fields[17] or temperature,[18] offers particular potential for novel applications. Understanding the structure-packing relationships of novel surfactants is critical to accessing LLC mesophases with tailored dimensions. As outlined extensively before, light offers many advantages as a stimulus as it can be applied remotely with spatial and temporal control. As a result, light-responsive LLC phases offer the possibility to create structured materials with well-defined dimensions and morphology with various potential uses, such as optical modulators[19] or soft templates for the construction of porous materials[20–22] (the subject of Chapter 6). However, reports of light-responsive LLC phases are quite rare. A brief summary of the key literature in this area will first be presented before the results are described and discussed.

Photoresponsive LLCs have been prepared through the addition of additives, such gold nanoparticles to facilitate photothermal heating,[23–25] or photoactive molecules such as spiropyran[26,27] or photodestructible surfactants,[28] forming a composite system. In contrast, light-responsive LLC mesophases formed from surfactants with chromophores as part of their molecular structure are far less common. While conventional surfactants

self-assemble into a variety of LLC polymorphs at concentrations significantly above the CMC, reports of LLC phase formation in pure AzoPS systems are still rare. Peng *et al.* studied the effect that the position of the azobenzene group within the hydrophobic tail had on LLC phase formation.[29] An oligoxyethylene-based AzoPS with a five-carbon spacer and four carbon pendant tail was chosen for analysis and compared to its spacer-free counterpart ($C_{4+x}AzoC_yE_7$, where $x = 0$, $y = 5$ or $x = 5$, $y = 0$.) Using polarised optical microscopy, small angle X-ray scattering and differential scanning calorimetry it was found that the AzoPS with a spacer moiety could form more than one LLC phase depending on the surfactant concentration and temperature. For the spacer-free AzoPS, only one LLC phase was formed at any temperature and concentration, and this was lost upon photoisomerisation. Peng *et al.* also showed that AzoPS could reversibly gel and de-gel in an aqueous solution.[16] The above AzoPS structure, with a spacer moiety, was found to reversibly transition from a viscous solid-like LLC phase to a lower viscosity liquid-like non-LLC phase upon irradiation with UV light.

Tan *et al.* synthesised a series of amphotropic azobenzene derivatives to probe their thermotropic and lyotropic liquid crystal phase-forming abilities.[30] The structure of the polar groups and number of alkyl chains were varied across the series. Most compounds with one alkyl chain formed tilted smectic phases, while compounds with two or three alkyl chains formed columnar hexagonal phases. Photoresponsive behaviour was observed for all amphiphiles but not reported in detail. Yang *et al.* investigated a series of non-ionic polyetheramine-based AzoPS for creating multi-stimuli responsive hydrogels.[31] They synthesised three AzoPS, varying the molecular weight of the hydrophilic polyetheramine head groups for a constant azobenzene-based tail length. It was found that all three AzoPS could form gels in aqueous solutions and transition between gel and sol states depending on pH, temperature, and applied stress or light. One of these structures, C_4-Azo-C_5-D_{400}, was observed to form LLC phases at certain water contents.

Here, a series of neutral azobenzene photosurfactants with different alkyl tails and spacer lengths have been investigated to assess their LLC phase-forming ability at concentrations significantly above their CMCs. The family of neutral AzoPS discussed thus far ($C_6AzoOC_4E_4$, $C_8AzoOC_8E_4$) will be expanded to include the shorter-tailed $C_2AzoOC_4E_4$ and intermediate length $C_8AzoOC_4E_4$. Molecular structures with different head-to-tail volumes are targeted, to probe the possibility of forming a range of mesophases of varying curvatures. Using SAXS, POM and DSC, these AzoPS will be investigated over a range of concentrations, temperatures and isomerisation conditions to probe their formation of photo-responsive LLC phases. The lowest concentration investigated (10 wt%) is ~1,000 times greater than the CMCs of the AzoPS (Appendix, Table A.2.1). Initially, the room

temperature behaviour of the AzoPS will be investigated, with the presence of LLC phases assigned on the basis of SAXS and POM data. The behaviour of the LLC phases with temperature will also be explored, using the above techniques and DSC, with the ultimate goal of constructing a binary temperature-concentration LLC phase diagram for each AzoPS. The UV response of the LLC phases at room temperature will also be examined, to see the extent to which the formation of LLC phase is disrupted or altered upon photoisomerisation to the *cis*-PSS.

5.2 Experimental

Materials: All AzoPS were synthesised as outlined previously. Millipore water was obtained from an in-house filtration system (18.2 mΩ).

Light Irradiation: Irradiation was performed using either UV (365 nm, 3.7 mW cm^{-2} at 4 cm from source) or blue (465 nm, 1.3 mW cm^{-2} at 4 cm from source) LEDs in a custom built light-box. Conversion to the *cis-* or *trans*-PSS was confirmed using UV-Vis absorption spectroscopy.

Polarised Optical Microscopy: Temperature-controlled POM measurements were carried out at the Jülich Centre for Neutron Science at the Heinz Maier-Leibnitz Zentrum, Garching, Germany by Dr Judith Houston on a Leica DM 6000 Digital Microscope. A series of highly concentrated AzoPS samples (10–100 wt%) were prepared and deposited between two glass cover slips. These samples were imaged using a polarised optical microscope, with a liquid nitrogen-cooled heating stage, to probe the LLC phases formed over a range of temperatures. Each sample was slowly heated and cooled between 5 and 100 °C, at a heating rate of 10 °C min^{-1}. At temperatures where significant phase transitions were recorded repeat measurements were performed at 1 °C intervals, with a slower heating rate of 1 °C min^{-1}. Photoisomerisation of the AzoPS samples was achieved *via* 10 min of irradiation with a UV light-emitting diode (λ = 365 nm) for the *trans–cis* isomerisation and a blue light-emitting diode (λ = 465 nm) for the reverse *cis–trans* isomerisation. Control experiments were performed to ensure that no photoisomerisation would be triggered as a result of the halogen lamp in the optical microscope. A number of *cis*-isomers were left on the light stage for ~2 h and no change in texture of the image was observed in this time.

Small-Angle X-ray Scattering: Synchrotron SAXS measurements were performed on the BioSAXS beamline B21, Diamond Light Source, Harwell, United Kingdom.[32] B21 operates in a fixed sample to detector distance (4.014 m) with X-ray beam energy E = 12.4 keV giving a q-range of 0.031-3.8 nm^{-1}. Samples were loaded into PCR well plates in an automated sample changer. Samples (30 µL) were then delivered into a temperature-controlled quartz capillary and exposed for 3 s, collecting 60 frames at 20 °C. Data were collected using a Pilatus Dectris 2M detector. The background was manually subtracted using ScÅtter.[33] Additional laboratory SAXS measurements were performed by Dr Judith Houston on the GALAXI beamline at the Jülich Centre of Neutron Science (JCNS).[34] GALAXI uses a Bruker AXS Metaljet X-ray source working with gallium K_α X-rays (λ = 1.34 Å), and a sample-to-detector distance of 80 cm, resulting in the q-range 0.1-7.0 nm^{-1}. Data were

collected using a Pilatus Dectris 1M detector. Samples (~50 μL) were inserted into borosilicate glass capillaries (1.0 mm), which were then sealed. The sample-to-detector distance was calibrated using the Bragg reflections from silver behenate.

Differential Scanning Calorimetry: Highly concentrated AzoPS solutions in water were freshly prepared in a glass vial, weighed (4–5 mg) and sealed in aluminium crucibles. DSC measurements were performed using Perkin Elmer DSC 8000, in the range of 10–80 °C in a nitrogen atmosphere with a heat rate of 5 °C min^{-1}. The calculation of the enthalpy of any phase transitions was performed using the Pyris software by integrating the area of the endothermic peak, where present, and the calibrated baseline.

Construction of Phase Diagram: A binary concentration phase diagram was constructed on the basis of SAXS profiles, POM images and DSC thermograms. The POM and SAXS data were used to assign the phase, while DSC informed the position at which order-order mesophase transitions or melting transitions occurred.

5.3 Results

5.3.1 LLC Phases at Room Temperature

Concentrated samples (10–100 wt% in water) of all four AzoPS were prepared and analysed using SAXS and POM at various temperatures, with and without prior UV irradiation to photoisomerise to the *cis*-PSS. The results of these experiments will be discussed for each AzoPS in the native *trans*-state at ambient temperature in turn, starting with the AzoPS of the shortest tail length and lowest curvature and working up to the surfactant of longest tail length and highest curvature. The packing parameter calculated for each AzoPS can be found in the Appendix (Table A.2.3). In general, LLC phases are assigned from POM images on the basis of areas of brightness and coloured textures.[35] These textures and brightness arise from the optical anisotropy of the LLC phase and different phases tend to give different characteristic textures. For example, a lamellar phase presents as streaked, stringy textures or Maltese crosses,[16,29,35,36] while a hexagonal phase presents a conic fan or non-geometric smoke-like texture.[29,35,37,38] A cubic phase is optically anisotropic and will appear dark under POM.[35] SAXS can also be used to assign LLC phases. The long-range order of the LLC phase results in Bragg peaks, the repetition and peak spacing of which varies depending on the symmetry of the LLC phase. For example, a lamellar LLC phase will show peak repetitions at positions that are integer multiples of the first interference peak,[39-41] while a hexagonal LLC phase will show peak repetitions that occur at position in multiples of $1:\sqrt{3}:2$.[39,42]

Figure 5.1 presents POM images for $C_2AzoOC_4E_4$ at room temperature, at various concentrations in water. All POM images show areas of brightness, but defined textures only emerge from 30 wt%. The 10 and 20 wt% samples have suggestions of bright streaks in the background but are assigned here as isotropic; considering the low concentration it is likely that any LLC phase has not fully developed and lacks long-range order. With increasing concentration, the suggestion of optical anisotropy observed at lower concentrations becomes confirmed as defined textures emerge. At 30 and 40 wt%, bright streaked textures can be observed, characteristic of a lamellar phase, with a Maltese cross also visible at 30 wt%. At 50 and 60 wt%, these streaks become long strings of brightness, maintaining a lamellar phase. At higher concentrations of 70–90 wt%, the POM images are mostly dark, with small domains of brightness. This indicates an isotropic phase which could potentially be a cubic phase, normal or reverse. It is also possible no phase is formed at all and the aggregates in solution could represent small insoluble crystallites. These crystallite domains are much more evident as domains of brightness at 100 wt%. It is possible these areas of brightness are merely aggregates of ordered AzoPS in a disordered bulk surfactant solution.
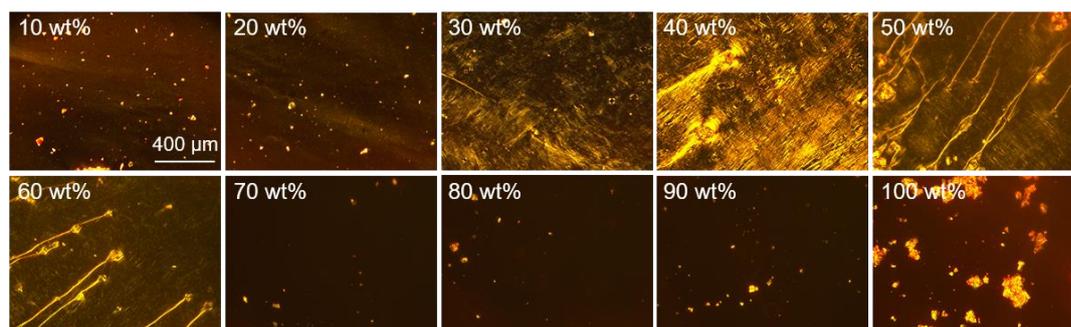
Figure 5.1. Optically anisotropic LLC phases can be assigned on the basis of the brightness and texture of their POM images. POM images of $C_2AzoOC_4E_4$ in the native *trans*-state at varying concentrations in water, measured at a temperature of 25 °C. The long features and stringy textures here indicate a lamellar phase. Scale bar indicates 400 µm.

Figure 5.2 shows the SAXS profiles of $C_2AzoOC_4E_4$ in the native *trans*-state at varying concentrations in water. The growth of interference peaks due to long-range order in the sample can be observed from 15 wt% onwards, with pronounced peaks evident from 20 wt%. This is consistent with the development of optically anisotropic textures in the POM images. The SAXS profiles from 30 to 50 wt% show regular peaks at 2.1 and 4.2 nm^{-1}. LLC phases are typically assigned from SAXS scattering profiles from the ratio of peak positions; with lamellar phases, peaks occur at integer multiples of the first peak *i.e.* 1:2:3:4.[43,44] Due to issues with high viscosities, SAXS measurements could not be performed at concentrations above 50 wt%. The peaks develop with increasing concentration; at 15 wt%, a shoulder emerges at ~0.45 nm^{-1}, which persists at 20 wt% along with the growth of further peaks at 0.25 and 2.14 nm^{-1}. At 30 wt%, it appears the shoulder at ~0.45 nm^{-1} has almost merged with the low q peak, resulting in a double peak centred at 0.37 and 0.44 nm^{-1}. It is possible that before this point, there are varying values for the periodicity of the emerging lamellar phase.[45] This is in agreement with the POM images which showed some brightness at 10 and 20 wt% but did not show clear textures until 30 wt% onwards. The initial low q peak shifts to higher q values with increasing concentration, from 0.25 nm^{-1} at 20 wt% to 0.7 nm^{-1} at 50 wt%, indicating that the repeat distance decreases with increasing surfactant concentration. This is a well-known dilution observation, where $q \propto \phi$, where ϕ is volume fraction.[46] This shift of q_0 with concentration is due to the reduction of the volume of water, resulting in contraction of the lamellar sheets. Using the relation $q_0 = 2\pi/d$, it was found that the periodicity, d, of the lamellar sheets decreases by almost a third, from 25 nm at 20 wt% to 8.85 nm at 50 wt% (Figure 5.2). This implies the water channels between the bilayers vary in thickness from 21 to 5 nm. It is interesting that the higher order reflections are relatively invariant with concentration, while the low q peak varies significantly.
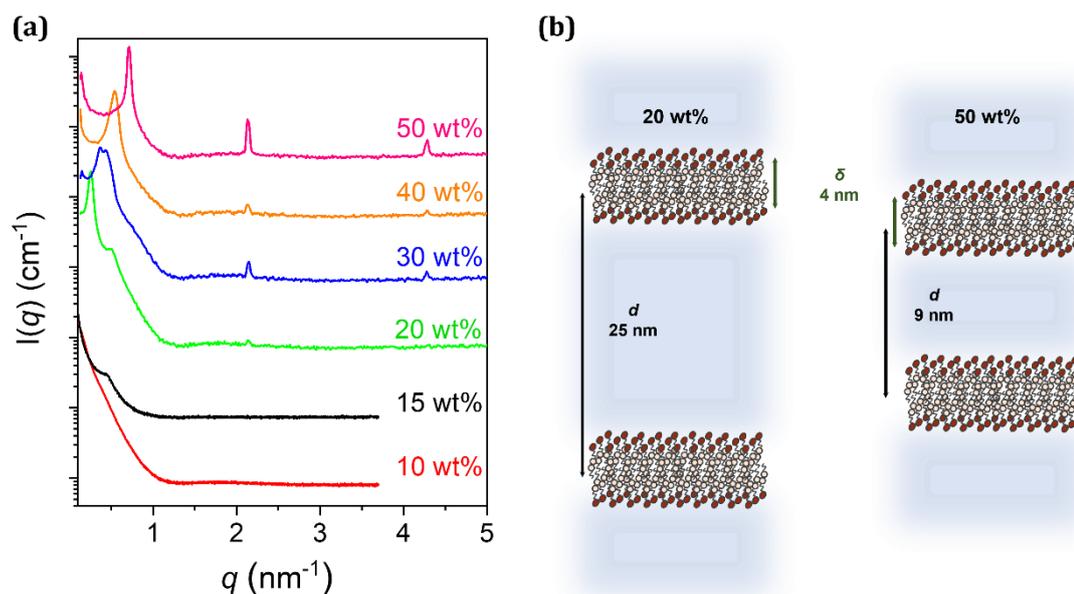
Figure 5.2. SAXS profiles indicate the presence and identity of long-range order, such as lamellar LLC phases. (a) SAXS profiles of $C_2AzoOC_4E_4$ in the native *trans*-state at varying concentrations in water at 20 °C. The q ranges vary as measurements were performed on two different instruments. (b) Schematic representation of the lamellar phase with periodicity, d, and bilayer thickness, δ.

The thickness of the bilayer layer, δ, is normally invariant with dilution and so can be determined from the slope of a plot of q_0 *vs.* concentration[41,46] (Appendix, A.5.1). It is expected that the thickness of the lipid portion of the lamellar sheet is roughly twice the length of the surfactant tail. Using the Tanford equation (Appendix, Table A.2.2) the length of the tail of the AzoPS is estimated to be 2.1 nm, implying that the lipid bilayer thickness is ~4.2 nm. 4.13 nm was found for δ, (Appendix, Figure A.5.1) confirming that the bilayer consists of surfactants arranged tail-to-tail, with little overlap between the tails.

Focus will now turn to the next structure in the series, $C_6AzoOC_4E_4$, which differs from the previous $C_2AzoCO_4E_4$ by having a longer pendant tail. In Figure 5.3, the POM images for $C_6AzoOC_4E_4$ in the native *trans*-state can be observed. A series of bright, textured images can be seen across most concentrations, indicating that this surfactant forms anisotropic LLC phases. The nature of the phases are assigned on the basis of the characteristic textures. 10 wt% has only a suggestion of brightness and so a definite texture cannot be assigned. At 20 wt%, a smoke-like texture with narrow streaks emerges, while at 30 wt%, a mosaic-like texture is observed. These textures are characteristic of hexagonal phases. At 40 wt% a bright, streaked image is observed, very similar to that noted by Peng *et al.* for a hexagonal phase.[16] At 50 wt%, the texture changes to long strings, now suggesting a lamellar phase. This change persists, with 60–80 wt% all presenting long string-like textures characteristic of a lamellar phase. The phase sequence of hexagonal to lamellar phase is not uncommon, in fact the work of Peng *et al*. shows transitions between similar textures.[16,29]
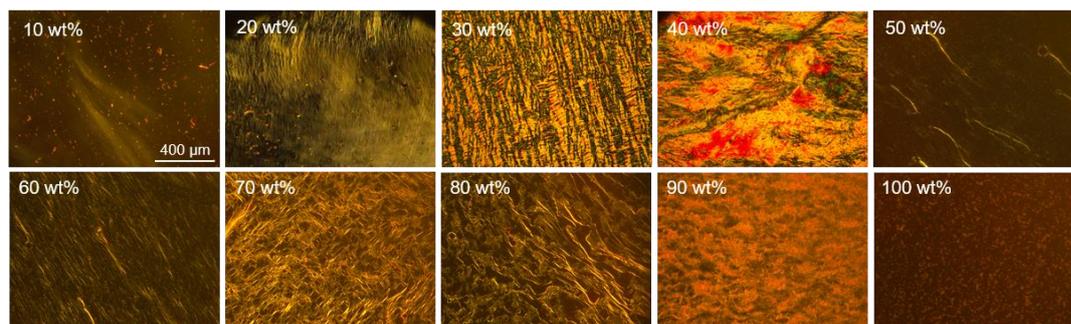
Figure 5.3. Optically anisotropic LLC phases can be assigned on the basis of the brightness and texture of their POM images. POM images of $C_6AzoO_4E_4$ in the native *trans*-state at varying concentration (10–100 wt%) in water at 25 °C. The smoky or streaked textures at 20-40 wt% indicate a hexagonal phase, while the long, stringy textures at higher concentrations indicate a lamellar phase. The scale bar represents 400 μm.

The hexagonal to lamellar phase transition can be rationalised as follows: at higher water contents there is an increase of the effective area of the polar head group favouring the formation of a higher curvature phase. Inversely, as the water concentration decreases, it is preferable to tend towards a lamellar from a hexagonal phase. At 90 wt% the texture returns to a more smoke-like one, which may be an inverse hexagonal phase. Inverse phases are common at very high concentrations, arising as the water content drops low enough to favour curvature in the opposing direction.[35] A small amount of brightness persists at 100 wt%, but the lack of a defined texture prevents any solid conclusions from being drawn.

Figure 5.4 presents the SAXS profiles of $C_6AzoOC_4E_4$ in water, in the native *trans*-form. In this case, a constant peak at 2.96 nm^{-1} is observed for all scattering profiles, even before the emergence of more pronounced peaks. This is similar to the behaviour that was observed for $C_2AzoOC_4E_4$ and suggests strong interparticle interactions. This peak corresponds to a physical distance of $d = 2$ nm and implies organisation on smaller dimensions occurs before organisation at a larger scale, at least as far as can be probed by SAXS. From the optical anisotropy and birefringence in the POM images, it is clear there is organisation from 20 wt% onwards. It is possible that the interference peaks may not be apparent from SAXS due to swelling of the liquid crystal phase or because of the nature of the measurements; POM involves depositing the samples on a substrate with a cover slip above, while SAXS probes the solution behaviour. As a result, there could be surface-ordering or anchoring effects at play in POM which may contribute to the formation of ordered phases. From 20 wt% on, it can be seen that further peaks begin to emerge around 0.25 nm^{-1}, with an additional peak at 1.38 nm^{-1} for 30 wt%. At 40 wt%, four clear peaks emerge at 40 wt%. These peaks have a ratio in their positions of 1:2:3:3.7, indicative of a lamellar phase. It is interesting to note that the POM textures do not look lamellar until 50 wt%, while SAXS ratios indicate a lamellar arrangement at 40 wt%.
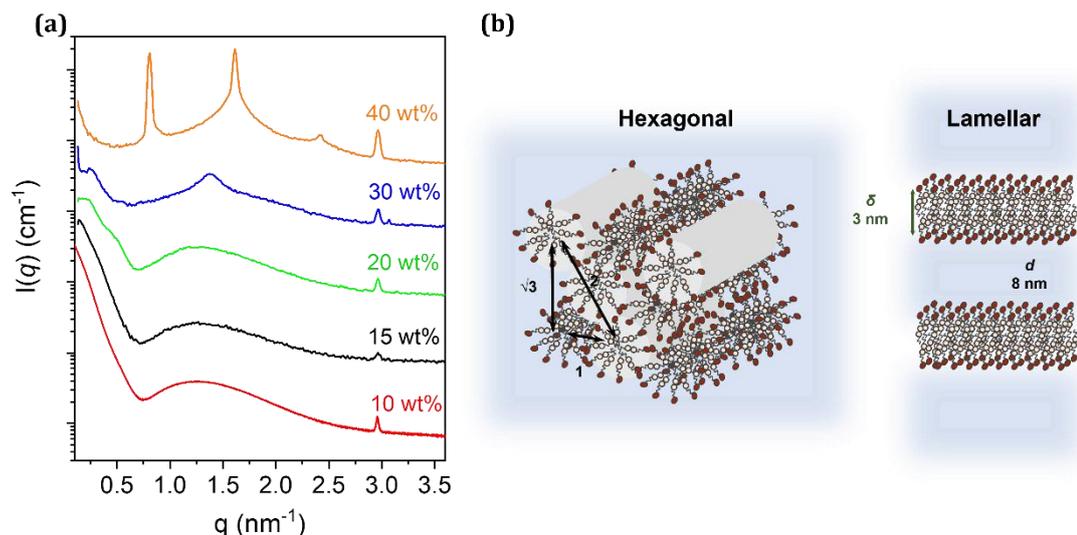
Figure 5.4. SAXS profiles can indicate the presence and identity of long-range order, such as lamellar LLC phases, in the surfactant solution (a) SAXS profiles of $C_6AzoOC_4E_4$ in the native *trans*-state at varying concentrations in water at 20 °C. (b) Schematic representation of the hexagonal phase and the lamellar phase.

It is likely that the hexagonal-lamellar phase transition occurs between these concentrations and that the difference between the two techniques (solution-based *vs.* on a substrate) mean that slightly different areas of the phase boundary are probed. There is also a slight temperature difference (5 °C) between the two measurements, which may also be responsible for the slight shift in transition concentration. For the 40 wt% sample, a value of periodicity of 8 nm was determined from q_0. As the lamellar phase was observed for only one concentration, it was not possible to plot q_0 against concentration to determine the bilayer thickness. The value was estimated for the 40 wt% scattering profile directly from the relation $q_0 = 2\pi\phi/\delta$, with δ estimated to be 3 nm. This implies the thickness of the water channels between the bilayers is approximately 5 nm.

There is no clear hexagonal phase observed for the 20 and 30 wt% samples using SAXS, despite these samples showing clear hexagonal textures using POM. However, the scattering profile at 30 wt% is not lamellar, as it lacks the integer peak spacings required. There is also the suggestion of some peaks at low q for the 20 wt% sample. It is possible that the lack of clear peaks does not mean that no ordered phase is present, but rather that the peak repetition was not easily measurable using SAXS *e.g.* the high water content could result in swollen LLC phases. $C_6AzoOC_4E_4$ is known to produce extremely viscous samples (and was subsequently the subject of the rheology measurements as outlined in Chapters 2 and 3.) As a result, it was not possible to measure concentrations higher than 40 wt% as they could not be loaded into the instrument. The hexagonal-lamellar transition observed here at 40-50 wt% can be probed further by increasing the temperature. As the expulsion of water due to higher temperatures would mimic higher effective concentrations, it would be anticipated that the transition will shift to lower

concentrations with temperature *e.g.* 30 wt% at higher temperatures to look closer to 40 wt% at lower temperature *etc.* This will be investigated in Section 5.3.2.

To summarise the results so far, $C_2AzoOC_4E_4$ appears to form almost exclusively lamellar phases, and $C_6AzoOC_4E_4$ forms lamellar phases above 40 wt%. The only structural difference between these AzoPS is the addition of a further 4 -CH_2- on the pendant tail of $C_6AzoOC_4E_4$. Hyperswollen lamellar phases have previously been reported for neutral, non-photoactive surfactants when a critical alkyl chain (C_m)/ethylene glycol (E_n) ratio is reached (2.4–4).[47] Within this range, the length of the surfactant's headgroup and tail are almost equal, which is expected to favour the formation of packed sheets. The calculated values are 3 for $C_2AzoOC_4E_4$ and 4 for $C_6AzoOC_4E_4$, falling into the required range; this suggests that this basic model could be enough to predict the LLC phase in this case. On the other hand, the packing parameter predicts the formation of the same cylindrical micellar structure for all four of these AzoPS ($1/3 > P > 1/2$ for all, Appendix Table A.2.3). At low concentrations, it has been well-established that $C_6AzoOC_4E_4$ does form cylindrical wormlike micelles (Chapters 2 and 3). It appears that these pack favourably into a hexagonal phase initially, from the textures on the POM images. In general, when the hexagonal packing fraction is reached, the formation of lamellar sheets becomes more likely, both in terms of decreasing curvature with increasing surfactant concentration and increased packing efficiency. The hexagonal packing fraction for cylinders is 0.74 but realistically this packing limit will be reached at a much lower value, closer to 75% of the close-packing limit.[35,48,49] This estimate implies a phase change from the hexagonal to the lamellar phase would be expected to occur at ~50 wt%. This is in heartening agreement with what is observed here for $C_6AzoOC_4E_4$. It is also worth recalling that these AzoPS differ from the alkyl surfactants typically under consideration with the standard models of amphiphile packing, in that they have a bulky aromatic azobenzene core. This azobenzene core likely experiences π-π stacking interactions, as discussed in Chapter 3 and as evident from the UV-Vis absorption spectra having asymmetric absorption bands. Aromatic stacking interactions would favour low curvature structures,[50,51] allowing the π-π interactions to persist along the packing direction. It is thought this is why $C_6AzoOC_4E_4$ forms elliptical, rather than circular, cylinders and by the same logic, the formation of a lamellar LLC phase would be highly favourable, as the π-π stacking could occur over long distances, perpendicular to the lamellar domains.[52,53] To better probe any π-π interactions, Grazing-Incidence Wide-Angle Scattering measurements would be required.

The next structure to be probed, $C_8AzoOC_4E_4$, differs from the previous two in that it has an even longer pendant tail but still maintains the same spacer length and head group. Figure 5.5 presents POM images for $C_8AzoOC_4E_4$ in the native *trans*-state at room temperature (T = 25 °C). Well-defined textures do not emerge until 30 wt%, similar to the behaviour observed for the previous two AzoPS. At 30 wt% a smoky texture is present, indicating a hexagonal phase. The textures at 40 wt% and 50 wt% are difficult to assign but indicate an anisotropic phase. The 60 and 70 wt% samples appear to be lamellar, and are quite similar to the textures reported by Peng *et al*.[16,29] At 80 wt% a lamellar phase is evident from the long stringy texture. This is lost at higher concentration, with a clear lack of both brightness and texture evident at 90 and 100 wt%. It is possible that there are cubic phases being formed, but it is also possible that no LLC phase occurs at these concentrations.

Figure 5.6 shows the corresponding SAXS patterns for $C_8AzoOC_4E_4$. It was the only AzoPS to exhibit three sharp SAXS maxima with q repetitions of $1:\sqrt{3}:2$ at 50 wt%, indicative of hexagonally-packed cylinders, most likely the H_I phase. There are additional peaks present in the scattering profile at 50 wt%, at a ratio of 1:2, suggesting a mixed phase system is formed, with some lamellar phase present. This agrees with the ambiguous POM textures observed for this concentration. Unfortunately, scattering profiles could not be measured above 50 wt% due to the high viscosity of these samples. However, as lamellar peaks are present at 50 wt%, this implies that higher concentrations are likely to also be lamellar, as a hexagonal to lamellar transition is common and can be rationalised as discussed previously. A lamellar to hexagonal transition upon increasing concentration is very uncommon, unless the hexagonal phase is a reverse phase, this typically only occurs are very high concentrations and is unlikely to be the case here as a lamellar texture is clear at 80 wt%. This reasoning is supported by the POM images at 60–70 wt% which also suggest a lamellar phase. The intercylinder distance, a, of the hexagonal phase can be taken from q_{0H} according to $a = 4\pi/(\sqrt{3}q_{0H})$.[54] In this case q_{0H} is 0.82 nm^{-1}, with a value of 9 nm obtained here for a. The periodicity of the lamellar contribution was found to be 11 nm, from a q_{0L} value 0.56 nm^{-1}, with a value of 6 nm found for sheet thickness. This is larger than the value found for $C_2AzoOC_4E_4$ and $C_6AzoOC_4E_4$, in agreement with the increased length of the alkyl tail resulting in a thicker bilayer (Figure 5.6).
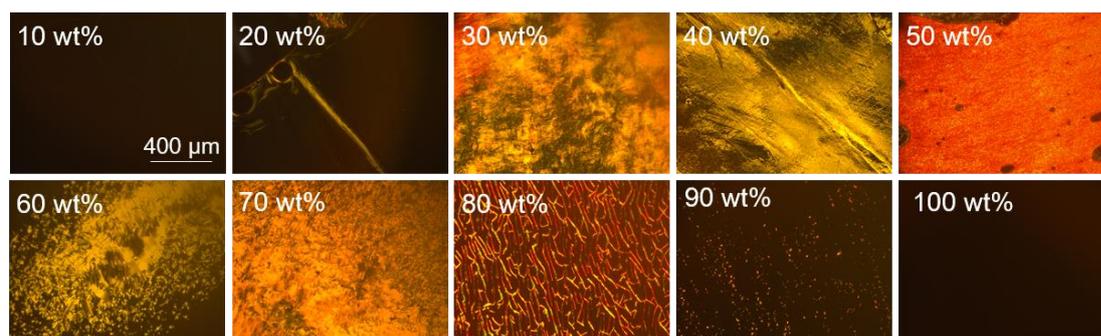
Figure 5.5. POM images of $C_8AzoOC_4E_4$ in the native *trans*-state at varying concentrations in water at 25 °C. A smoky texture indicates a hexagonal phase (*e.g.* 30 wt%) while a stringy texture indicates a lamellar phase (*e.g.* 80 wt%). Scale bar represents 400 μm.

There is a trend between molecular structure and LLC phase emerging; for $C_2AzoOC_4E_4$ only lamellar phases were observed. Upon increasing the alkyl tail length to $C_6AzoOC_4E_4$, hexagonal textures occur up to 40 wt% from POM images, with lamellar phases observed after this point. The SAXS profiles suggest a lamellar phase at 20 °C from 40 wt%. With a further increase of the alkyl tail length to $C_8AzoOC_4E_4$, hexagonal phases are observed up to 30 wt% using POM, and at 50 wt% SAXS indicates a mixed lamellar/hexagonal system. As both the spacer and head group remain unchanged, it is clear the length of the pendant tail effects the packing and LLC phase formed. Small variations in the tail length shift the hexagonal-lamellar transition, or remove it altogether. This supports results reported for alkylTAB surfactants, whereby a longer tail length favoured a greater variety of LLC phases,[39] and for bulky ethylene glycol surfactants, which formed micelles with low surface curvature when the length of flexible alkyl moieties were decreased.[55] Synthetically, adjusting the tail length of the surfactant is trivial, making this a useful way to tune the phase diagram as required.
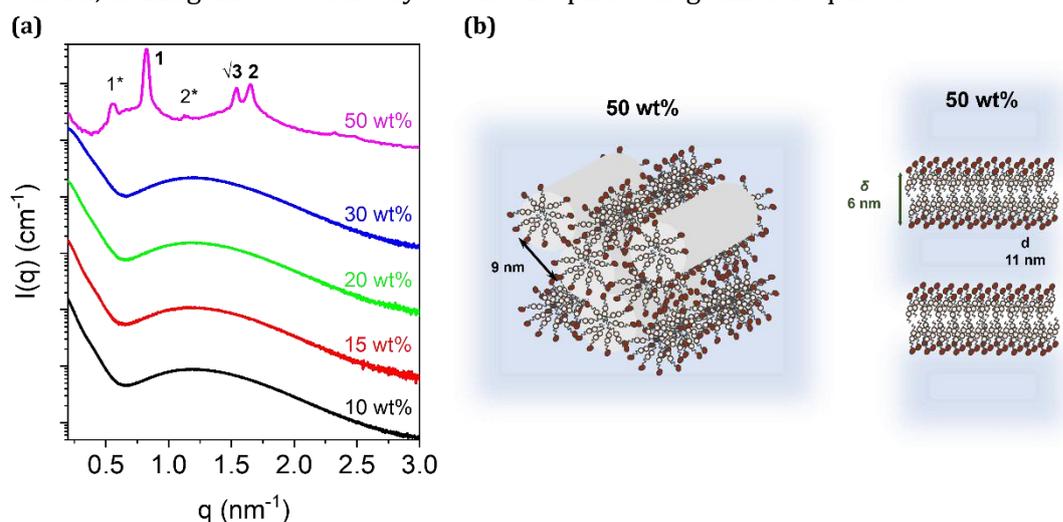
Figure 5.6. (a) SAXS profiles of $C_8AzoOC_4E_4$ in the native *trans*-state at varying concentrations in water at 20 °C. (b) Schematic representation of the hexagonal phase and the lamellar phase that co-occur at 50 wt%.

The final AzoPS, $C_8AzoOC_8E_4$, has the same pendant tail length of $C_8AzoOC_4E_4$, but it has a longer spacer length, of 4 -CH_2- than all three of the AzoPS discussed so far. was relatively insoluble at the concentrations and temperatures investigated and appeared crystalline by POM (Figure 5.7). This may be a result of its high hydrophobicity, due to its long alkyl tail length.[56] At 10 wt% small domains of brightness can be observed; from 30 wt% onwards the sample is quite clearly crystalline, presenting very bright, ordered domains, up to 100 wt%. The SAXS profiles for this AzoPS show strong peaks even at 10 wt%, with clear lamellar peak repetitions occurring at 0.85, 1.69, 2.55 and 3.39 nm^{-1}. These peaks do not vary significantly in their position with increasing concentration, suggesting there is no change in the aggregate dimensions with decreasing water content, as was clearly observed for the other AzoPS. The fixed position of q also implies that the bilayer thickness, if there is indeed a lamellar phase, is invariant with concentration. The value of q_0 found for all concentrations here corresponds to a physical distance of 7.39 nm. These results suggest that the AzoPS was not soluble at these concentrations and so the anticipated self-assembly behaviour did not occur.

It is also possible that this is the gel lamellar phase, L_β. The L_β phase has a gel-like rheology, characterised by a very high viscosity, in contrast to the L_α phase which typically has a low viscosity. The L_β phase is not an actual multiphase system, in the sense that a colloid or polymer gel is. It can be further distinguished from the L_α phase in that the tails in the bilayer are rigid and often tilted, rather than fluid-like. This difference in bilayer fluidity *vs.* rigidity is assigned on the basis of a wide-angle Bragg reflection of either 4.5 Å for the former or 4.2 Å for the latter. As a result, the L_β phase tends to have a thicker bilayer (up to twice the alkyl tail length) compared to L_α. Given the presence of the azobenzene moiety and possibility for π-π stacking, the formation of the less common L_β must be considered for all these AzoPS. L_β phases are also characterised by very large melting transitions, typically 25-75% of the crystalline melting transition can be observed. This will be probed using DSC in the following section.
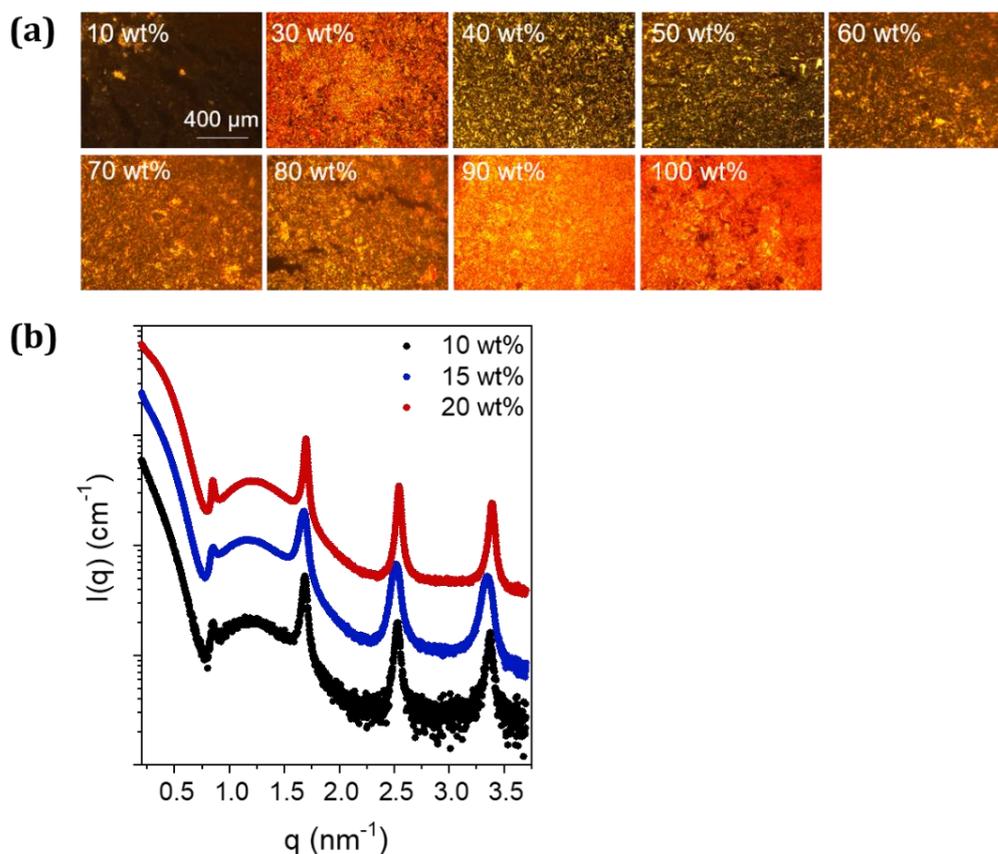
Figure 5.7. Long-range order can be assigned on the basis of optical anisotropy in POM images or peaks present in the SAXS profile. In this case, the long-range order is assigned to insoluble crystalline phases. (a) POM images for solutions of $C_8AzoOC_8E_4$ in the native *trans*-state in water at 25 °C. (b) SAXS profiles of $C_8AzoOC_8E_4$ in the native *trans*-state at varying concentrations in water at 20 °C.

5.3.2 Variation of LLC Phases with Temperature

The temperature-dependence of the AzoPS LLC phases were also investigated using DSC in conjunction with SAXS and POM. For POM measurements, each sample was slowly heated to 70 °C (1 °C min^{-1}), or until a dark image was observed, and then cooled to 20 °C at the same rate. The SAXS measurements performed at 25 °C were repeated at elevated temperatures (50 °C). The aim was to observe any phase changes that occurred and to construct a phase diagram for each AzoPS. In this section, each surfactant will again be presented in turn, with its LLC-phase forming behaviour discussed as a function of both concentration and temperature. Typically, only small changes to the LLC structure were observed upon heating, with the most common transition observed being H_I to L_α This order–order transition is most likely due to the selectivity of water for the hydrophilic oxyethylene units decreasing as the temperature is increased.[31,48,57] A similar phase transition was also reported in the literature for the neutral AzoPS, $C_4AzoC_5E_7$, (50 wt% in water).[31] For all AzoPS solutions, a temperature was reached at which any birefringence previously attributed to the formation of anisotropic LLC phase was lost

with birefringence recovered upon cooling. (Appendix Figure A.5.2-A.5.5) On occasion the texture of the cooled sample was slightly different to the initial texture, attributed to the anchoring or organisation-inducing effect of the glass cover-slips.[58] However, gentle agitation of the glass slides recovered the original textures.

In Figure 5.8 the SAXS profiles for aqueous solutions of $C_2AzoOC_4E_4$ (20 and 40 wt%) at 50 °C can be seen. Pronounced interference peaks are present and the positions are not significantly changed compared to the measurements at 20 °C (Figure 5.2). With increased temperature, there is no shift of peak positions for the 40 wt% sample compared to the 20 °C sample, while for the 20 wt% sample, the two low q peaks have moved closer together, with the initial peak shifting from 0.25 nm^{-1} at 20 °C to 0.37 nm^{-1} at 50 °C while the second peak moves only slightly from 0.45 nm^{-1} to 0.43 nm^{-1}. For the first peak, this represents a decrease in intersheet spacing from 25 nm to 17 nm with increasing temperature from 20 to 50 °C, likely due to the expulsion of water and contraction of the bilayers. Together, it is apparent that not only are LLC phases stable to temperature at these concentrations, but the mesophases are more pronounced, likely due to the effective increase in local concentration upon the expulsion of water.
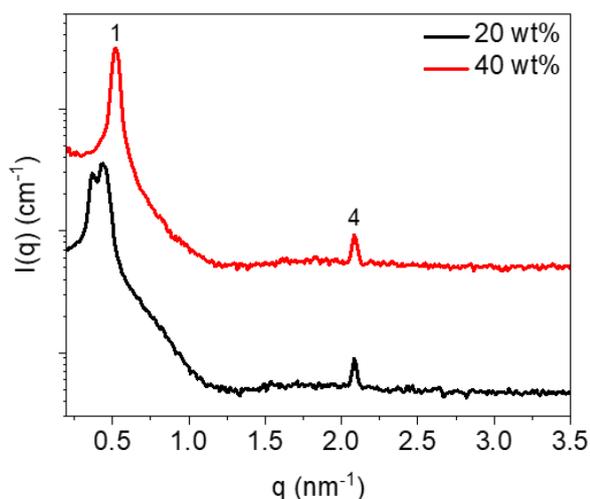
Figure 5.8. SAXS profiles of $C_2AzoOC_4E_4$ at 20 wt% (black) and 40 wt% (red) in water at a temperature of 50 °C. The integer peak repetitions indicate a lamellar phase

POM images were taken for each concentration across a range of temperatures, (Figure 5.9) with DSC measurements also performed. Any order-order transitions or melting of the LLC phases would be expected to appear as endothermic peaks on the DSC thermograms, due to the increased entropy and slight increase in molecular disorder of the higher temperature state. The change in enthalpy is smaller than what would be observed for a full melting transition, typically <10%.[36] At 20 wt%, there is not a significant change in POM images with temperature. The bright streaks visible at 25 °C seem to fade slightly but no clear texture emerges up to 45 °C. Small peaks appear on the DSC thermograms for 20 wt% at 34 and 47 °C, with a larger peak at 66 °C (Figure 5.10) This peak at 66 °C is most likely a melting point, where the LLC phases are lost.[29] The smaller peaks could indicate transitions to and from LLC phases but this cannot be clearly assigned on the basis of the POM images. For the 30 wt% sample, the brightness and distinctive lamellar texture remains in the POM images until 45 °C, at which point the texture and brightness fades; by 55 °C almost all brightness is lost. The DSC thermogram indicates that the lamellar phase is stable up to 66 °C, at which a large peak is observed, most likely corresponding to the melt or loss of the LLC phase. This is a higher melting temperature than indicated by POM, but it is possible that the nature of POM measurements (a small volume of sample between two glass slides) slightly alters the transition points of this dynamic water/surfactant system.

For the 40 wt% sample, the lamellar texture persists in the POM images at 45 °C but has faded significantly by 55 °C. This is in agreement with the SAXS profiles showing a lamellar phase stable to 50 °C. There is a large peak in the DSC thermogram at 71 °C for this sample, again higher than the temperature at which the brightness is lost in the POM images. In general, a similar trend is observed for the higher concentration samples, with the lamellar phase remaining stable to high temperatures. For the 50 wt% sample, a loss of texture doesn't occur in the POM images until 65 °C. In this case, the melting peak is not clear on DSC thermogram, and can only partially be observed at 79 °C. For the 60 wt%, sample a loss of brightness and lamellar texture occurs at 40 °C in the POM images, with a feature in the DSC thermogram at 46 °C and an exothermic peak at 57 °C. In this case, no clear melting peak is observed in the DSC thermogram. It is interesting to note that the large endothermic peak in the DSC thermograms, attributed to the melting of the lamellar phase, shifts to higher temperatures with increasing surfactant concentration. If this trend continues, it is possible the melting peak occurs above 80 °C for the 60 wt% sample and so is outside of the measured range.

The 70-100 wt% samples of $C_2AzoOC_4E_4$ were isotropic and so were not probed in detail in terms of their temperature dependence. For the 90 and 100 wt% samples, the small crystals visible in the POM images reduce in size and number with increasing temperature but no emergence of texture or additional brightness occurs. The POM images shown in Figure 5.9 are reported in 10 °C increments but in practice images were taken in 5 °C increments or less. The phase diagram is assigned taking the full range of POM images into account. It was often the case that the brightness and texture was lost in a POM image at a lower temperature than an endothermic peak was observed in the DSC thermograms. In this case, the intermediate region is shaded in grey. Further POM images are available in the Appendix. (Figure A.5.2)
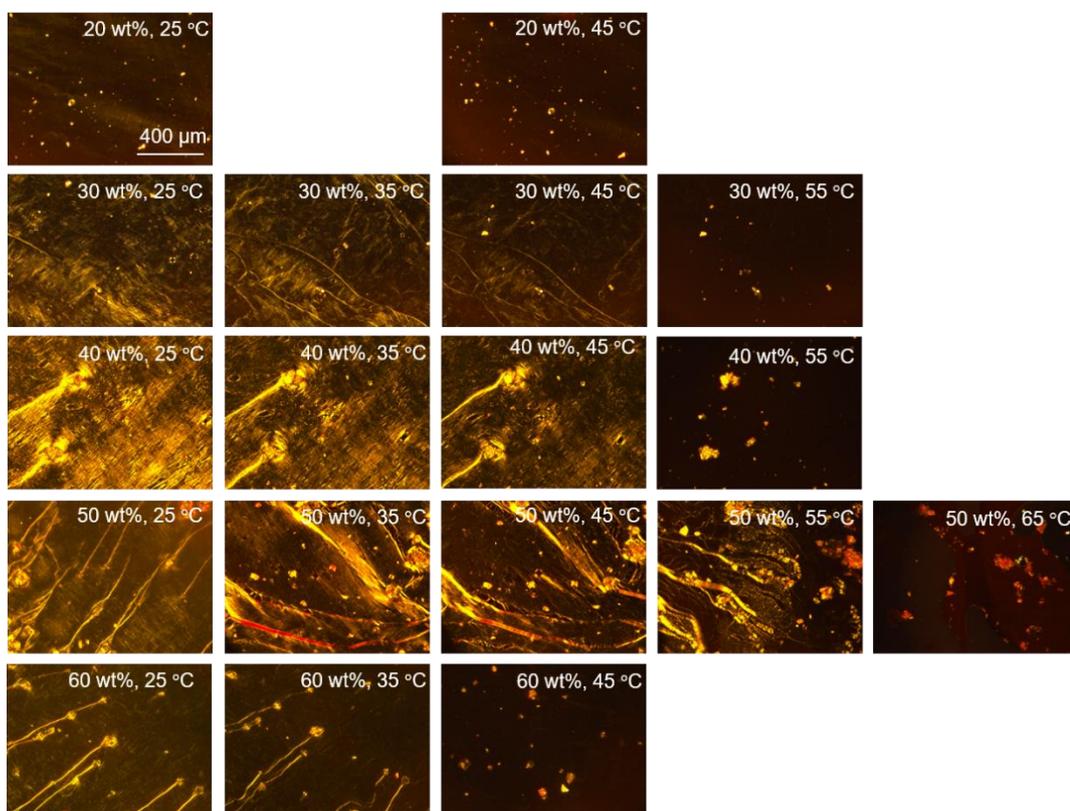
Figure 5.9. POM images of aqueous solutions of $C_2AzoOC_4E_4$ in the native *trans*-state at concentrations of 20-60 wt% with varying temperature. Lamellar textures are lost at increased temperature, indicated by the loss of brightness and texture in the POM images. Scale bar indicates 400 μm.
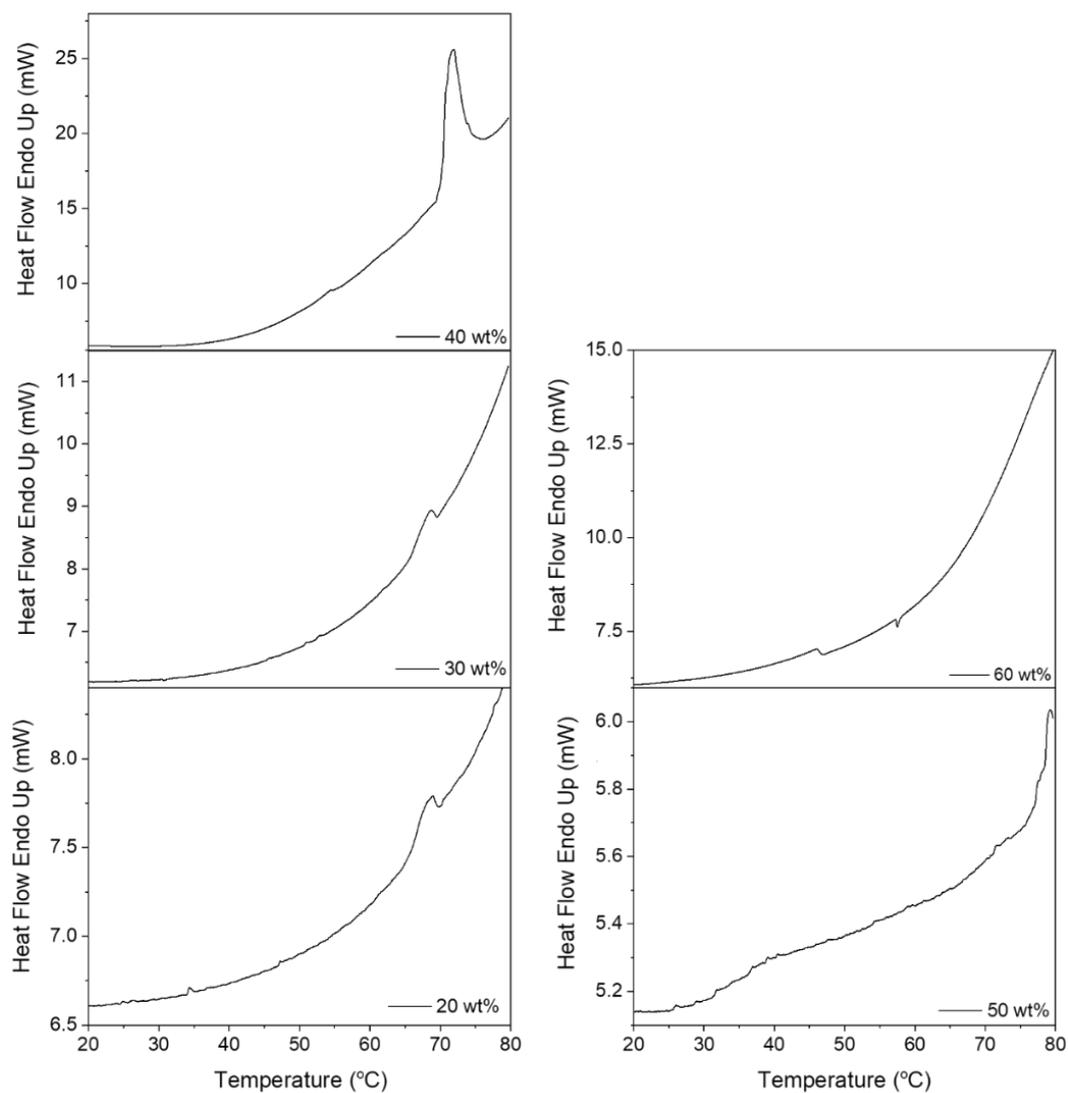
Figure 5.10. DSC thermograms for aqueous solutions of $C_2AzoOC_4E_4$ at 20-50 wt% in water. The endothermic peaks at high temperature indicate melting or dissolution of the lamellar phase
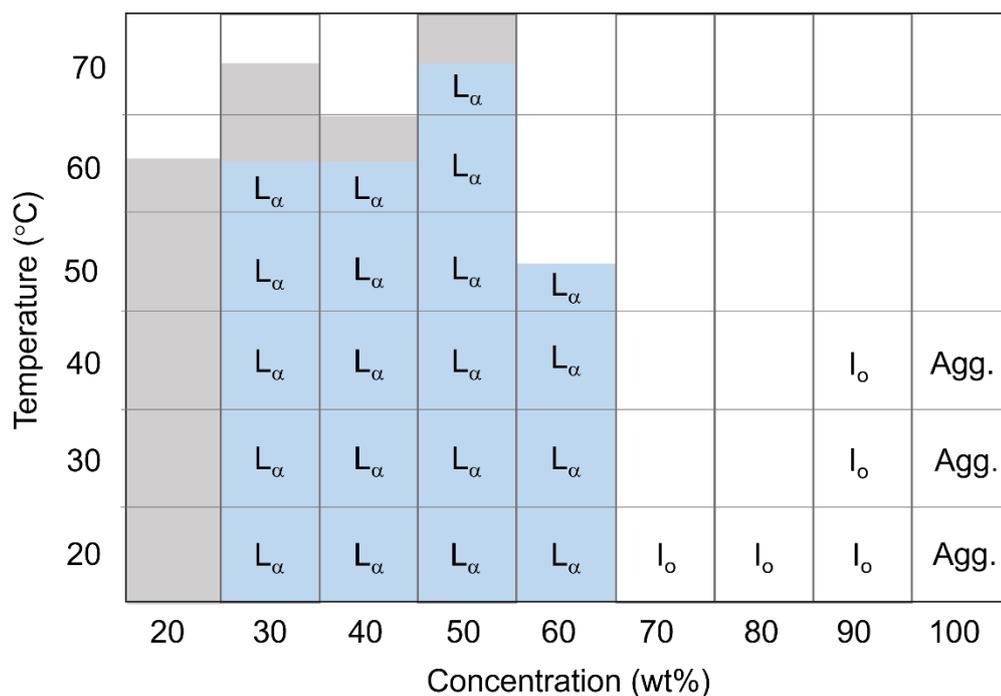
Figure 5.11. Binary concentration-temperature phase diagram for $C_2AzoOC_2E_4$ in the native *trans*-form, constructed on the basis of the SAXS, POM and DSC data. I_o and L_α represent an isotropic and a lamellar LLC phase, respectively. The grey areas represent where an LLC phase is likely present but could not be identified either due to lack of clear textures in POM images or a discrepancy between the loss of brightness in a POM image and the position of the peak in the DSC data. Agg. refers to large aggregates present in an otherwise isotropic POM image.

Figure 5.12 presents the SAXS profiles for aqueous solutions of $C_6AzoOC_4E_4$ (30 and 40 wt%) at 50 °C. The positions of the peaks have not changed significantly for the 40 wt% sample, compared to the 20 °C measurement, with each peak only slightly shifted towards lower q, while still maintaining a peak spacing consistent with a lamellar phase (1:2:3:3.8). The third peak is lower in intensity than the others, even at 20 °C, and maintains this characteristic at elevated temperatures. The scattering profiles for the 30 wt% solution show much more pronounced peaks at 50 °C than at 20 °C, similar to the observations noted for $C_2AzoOC_4E_4$. This supports the explanation for the discrepancy noted earlier, whereby samples that showed clear textures and anisotropy under POM did not have any peaks in their scattering profiles. It is likely this scattering occurs from swollen LLC phases, due to the high water content. As the temperature increases, a lower effective concentration is mimicked, as the water is expelled from the LLC phases. This allows the long-range order to be captured more clearly using SAXS, as evidenced by the interference peaks. At 20 °C, a lamellar phase was not observed at 30 wt%, with no clear repetition emerging from the peaks. Here, a lamellar peak repetition can be observed (1:2:3:3.8), although the third peak is diminished, as was observed for 40 wt%. The initial peak position is 0.74 nm^{-1} at 30 wt% and 0.76 nm^{-1} at 40 wt%, at 50 °C, compared to 0.81 nm^{-1} for the 40 wt% sample at 20 °C. This correspond to a periodicity of 9 nm for

40 wt% at elevated temperature, an increase of almost 7% compared to the room temperature sample. The bilayer thickness was estimated as previously, using the q_0 values for 30 and 40 wt%, and found to be 3.2 nm, very similar to the estimation of 3.1 nm for the room temperature sample. It seems sensible that bilayer thickness is relatively invariant with temperature, as it is for concentration. The most pronounced effect of both parameters is a change in the interlayer spacing, or periodicity, rather than the bilayer itself.

The formation of the lamellar phase here at 30 wt% is not unsurprising. At room temperature, a transition from a hexagonal to a lamellar phase in the region of 40-50 wt% is observed. At elevated temperature, as water is expelled from the head groups of the LLC phase, it is expected that the lower curvature phase, typically observed at higher AzoPS concentrations, would occur at lower concentrations than for room temperature.[48] It is also noteworthy that the peaks at elevated temperature are asymmetric. It is possible the shoulders emerging at 40 °C will continue to deconvolute into two separate peaks with increasing temperature, or gradually shift to higher q values as the headgroups dehydrate and the lamellar spacing decreases.
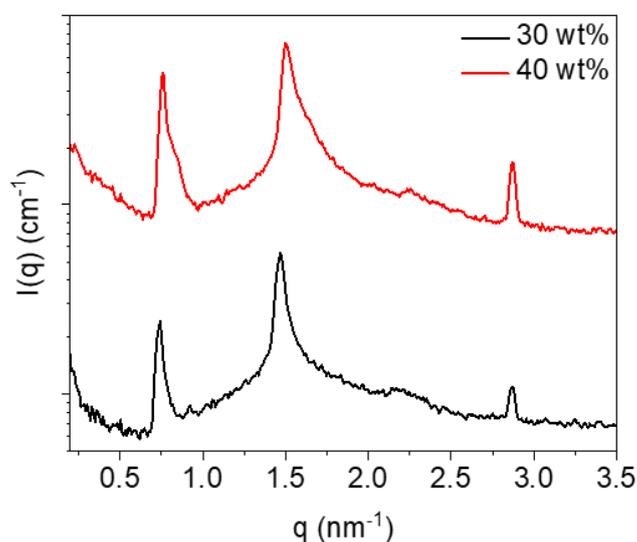
Figure 5.12. SAXS profiles of $C_6AzoOC_4E_4$ in the native *trans*-state at 30 wt% (black) and 40 wt% (red) in water at a temperature of 50 °C. Integer peak repetitions indicate a lamellar phase.

The POM images of aqueous solutions of $C_6AzoOC_4E_4$ at elevated temperatures are shown in Figure 5.13. At 30 wt%, the POM image shows a streaky mosaic texture at 25 °C, assigned as a hexagonal phase, which begins to lose brightness and appears ambiguous in texture at 35 °C. At 45 °C a stringy texture emerges, consistent with a lamellar phase. DSC thermograms show a sharp endothermic peak at 44 °C (0.233 J g^{-1} or 0.12 kJ mol^{-1}), likely corresponding to this H_I-L_α order-order transition (Figure 5.14). The lamellar texture remains and brightness returns with increasing temperature. This brightness begins to fade at 65 °C but no loss of texture is observed. Over the range scanned using DSC, no further transitions were found. This implies that the lamellar phase is stable to at least 80 °C. At 40 wt%, the bright, streaked texture is maintained at 30 °C but fades abruptly at 31 °C. This corresponds to a peak onset of 32 °C in the DSC thermogram, with a second peak at 50 °C also observed in the DSC. This is likely a transition from a hexagonal to a lamellar phase, occurring at lower temperatures for this more concentrated sample. The origin of the two peaks in the DSC data is not clear, it may be that an intermediate phase is formed between the hexagonal and lamellar phases. It is not uncommon for cubic phases to form in between hexagonal and lamellar phases, as the concentration is increased.[59,60] Cubic phases are optically anisotropic, so would result in dark POM images, as appears to be the case here at 31°C. From the room temperature measurements, it is known that there is a transition in the concentration regime of 40-50 wt% from hexagonal to lamellar. It seems sensible that higher temperatures would shift this transition to lower concentrations. Unfortunately, no POM images were recorded above 31°C so the emergence of lamellar texture cannot be observed.

As expected, the POM images remain lamellar from 50–80 wt% with increasing temperature. In several cases, the brightness and optical anisotropy builds with increasing temperature; this is particularly visible for the 50 and 60 wt% samples (Figure 5.13). The 50 wt% sample is remarkably stable, with POM images consistent with a lamellar phase clearly visible with no loss of texture up to 70 °C, the highest temperature probed. The DSC thermograms are relatively featureless from 60-80 wt%, indicating that the lamellar phases formed are stable across the entire temperature range to at least 80 °C. For the 90 wt% sample, a smoke-like texture was observed at room temperature that was tentatively assigned as an inverse hexagonal phase, H_{II}. At 35 °C, a lamellar phase can clearly be observed from the POM image, with a long stringy texture evident. The DSC thermogram for this concentration shows small endothermic peaks at 33 and 42 °C, indicating it is possible that at room temperature a reverse hexagonal phase is formed, that transitions to a lamellar phase at 33 °C. The second peak may be similar to what was

observed for 40 wt%, with a two-stage transition between hexagonal and lamellar phases. A phase diagram was constructed for $C_6AzoOC_4E_4$ and can be observed in Figure 5.15. Further POM images can be found in the Appendix (Figure A.5.3)

It remains clear from the temperature-dependent data that there is a strong tendency for $C_2AzoOC_4E_4$ and $C_6AzoOC_4E_4$ to form lamellar phases. In cases where hexagonal phases were initially formed for $C_6AzoOC_4E_4$, a transition to a lamellar phase was observed at relatively low temperatures (30-40 °C). The lamellar phases themselves are quite stable, in most cases to at least 50 °C and often above 80 °C. In general, the melting temperature was of the lamellar phase was higher for $C_6AzoOC_4E_4$ than for $C_2AzoOC_4E_4$. This is likely a consequence of the increased hydrophobicity and decreased solubility of this longer-tailed surfactant.
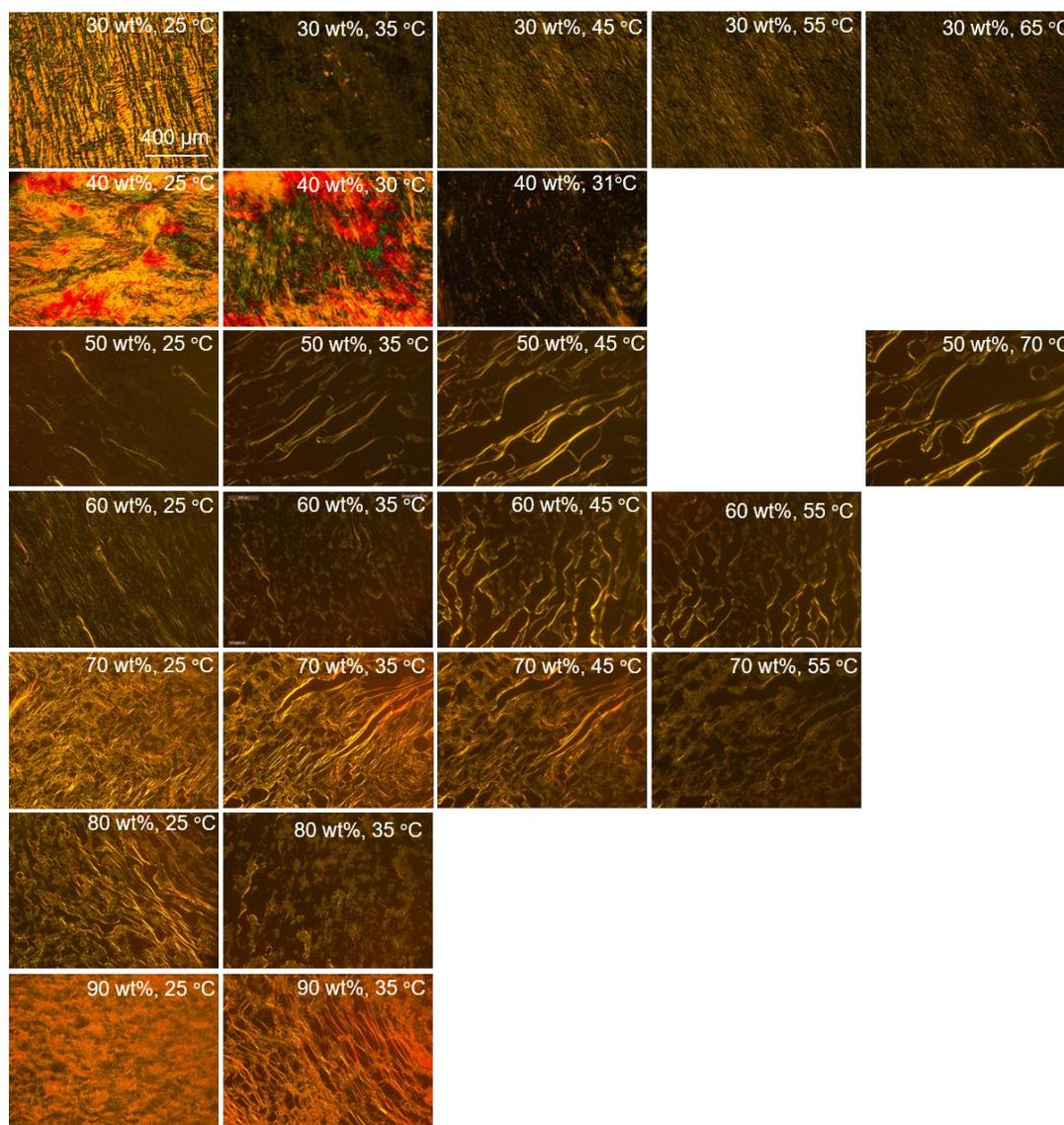
Figure 5.13. POM images of aqueous solutions of $C_6AzoOC_4E_4$ in the native *trans*-state at concentrations of 30-90 wt% with varying temperature. At lower concentrations, the hexagonal textures are lost at increased temperature, indicated by the change in texture in the POM images. The lamellar phases remain stable to elevated temperature. Scale bar indicates 400 μm.
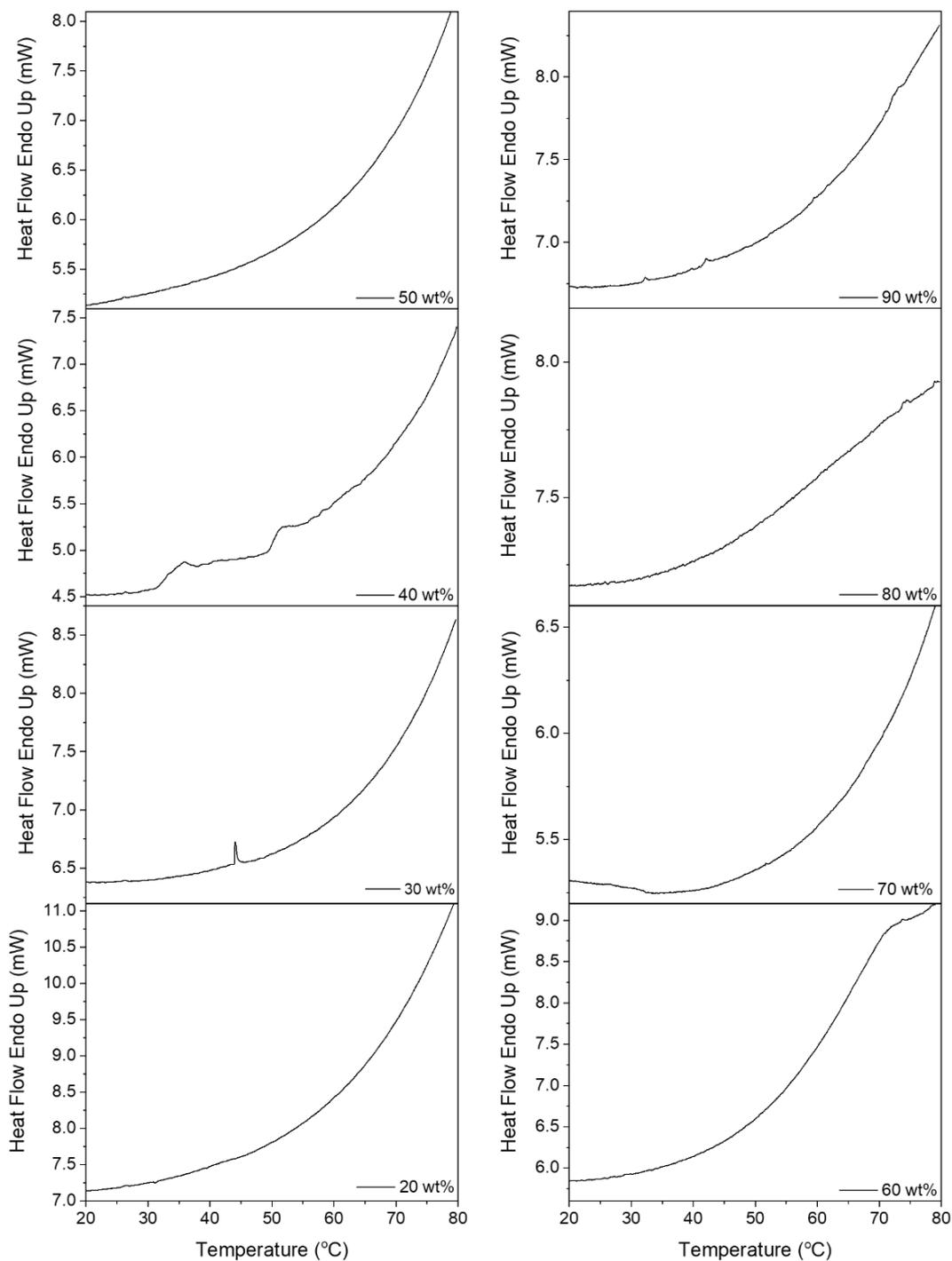
Figure 5.14. DSC thermograms for aqueous solutions of $C_6AzoOC_4E_4$ in the native *trans*-state at concentrations of 20-90 wt%. Endothermic peaks indicate order-order transitions from the hexagonal to lamellar phase. The absence of peaks implies no mesophase transitions or melts occur over the temperature range scanned.

Temperature (°C)	20	30	40	50	60	70	80	90	100
70	H_I	L_α	L_α	L_α	L_α	L_α	L_α	L_α	
60	H_I	L_α	L_α	L_α	L_α	L_α	L_α	L_α	
50	H_I	L_α / H_I	Int.	L_α	L_α	L_α	L_α	L_α	
40	H_I	H_I	Int. / H_I	L_α	L_α	L_α	L_α	L_α	
30	H_I	H_I	H_I	L_α	L_α	L_α	L_α	L_α	
20	H_I	H_I	H_I	L_α	L_α	L_α	L_α	H_{II}/L_α	I_o
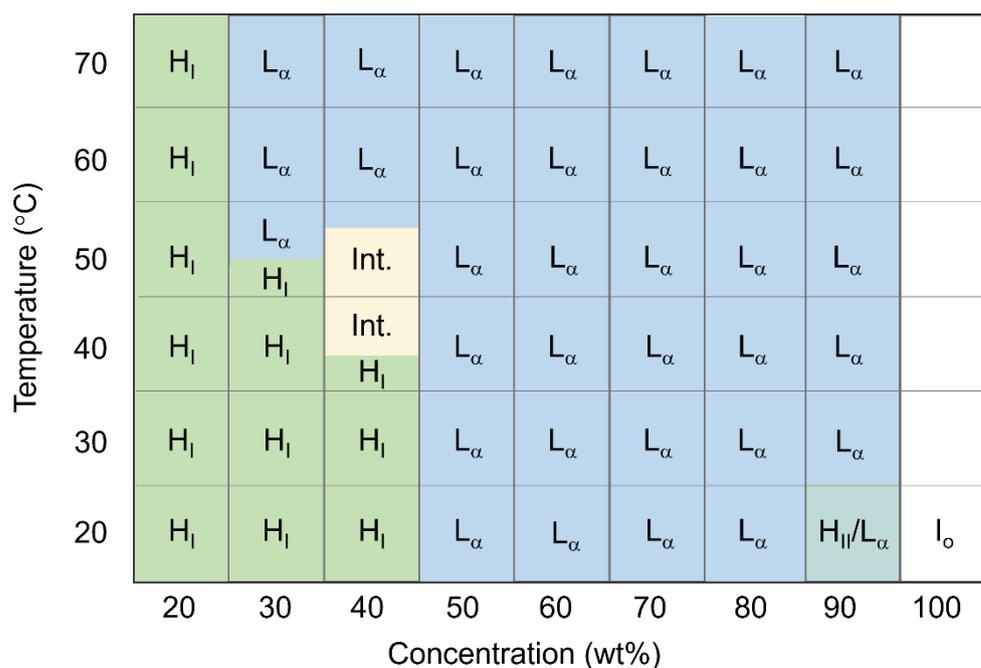
Concentration (wt%)

Figure 5.15. Binary concentration-temperature phase diagram for $C_6AzoOC_4E_4$ in the native *trans*-state. H_I indicates a normal hexagonal phase, I_o indicates an isotropic phase, L_α indicates an isotropic phase, Int. indicates an intermediate phase, likely cubic, and H_{II} indicates a reverse hexagonal phase.

Figure 5.16 presents the SAXS profiles for 50 wt% aqueous solutions of $C_8AzoOC_4E_4$ at 20 and 50 °C. As previously discussed, at 20 °C both lamellar and hexagonal LLC phases are observed. At 50 °C, only peaks corresponding to a lamellar phase are observed; the third peak ($q = 2.3$ nm^{-1}) is significantly lower in intensity compared to the first two, as was noted for $C_6AzoOC_4E_4$. This follows the same trend as was discussed for $C_2AzoOC_4E_4$ and $C_6AzoOC_4E_4$, where a lamellar phase is favoured over a hexagonal phase at higher temperatures. In this case, the periodicity of the lamellar phase, determined from q_0, decreases from 11.22 nm at 20 °C to 8.29 nm at 50 °C. This can be observed qualitatively from q_0 shifting to higher q with temperature.

The temperature-dependent behaviour of $C_8AzoOC_4E_4$ was probed using DSC and POM (Figure 5.17, 5.18). At 20 °C, % no peaks were observed below 50 wt in the SAXS profiles, with POM images indicating a hexagonal phase at 30 and 40 wt% and lamellar phases favoured at 60 wt% and above. Some of the POM textures for this sample were ambiguous and difficult to assign, especially considering the lack of peaks in the SAXS profiles. At 20 wt%, the brightness and optical anisotropy in the POM images increases with temperature, indicating the development of long-range order, appearing lamellar at 60 °C. The DSC thermogram has an endothermic peak at 66 and 69 °C, along with a larger peak at 78 °C. This is similar behaviour to what was observed for the other AzoPS, with order-order transitions occurring at intermediate temperature, with a melting of the final LLC phase, generally lamellar, at high temperatures.
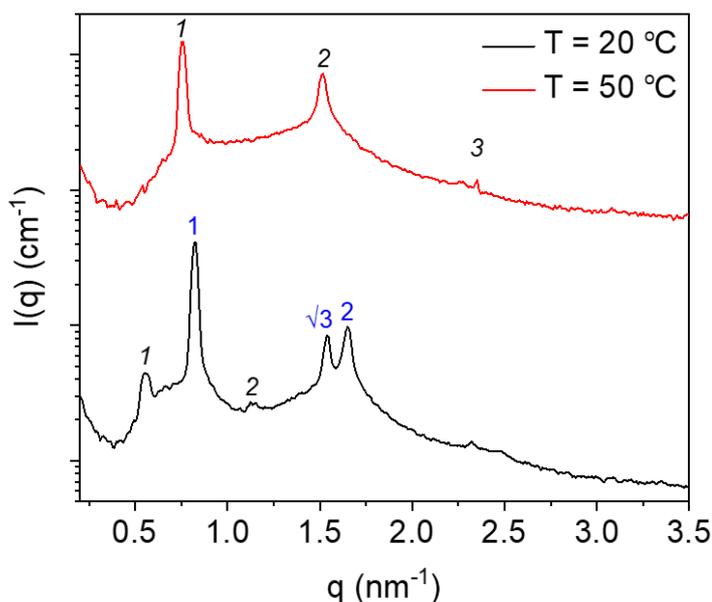
Figure 5.16. SAXS profiles of $C_8AzoOC_4E_4$ at 50 wt% in water at 20 °C (black) and 50 °C (red). Integer peak spacing indicates a lamellar phase, while peak repetitions of 1:√3:2 indicate a hexagonal phase.

At 30 wt%, a distinctive streaked texture with vivid colours can be observed, similar to $C_6AzoOC_4E_4$ at 40 wt%. This texture, assigned as a hexagonal phase, begins to lose brightness at 40 °C, and develops a slightly more stringy texture. The DSC thermogram has endothermic peaks at 53 °C and 62 °C, with the suggestion of a high temperature peak at 80 °C. It is possible that, similar to previous AzoPS, a transition to a lamellar phase occurs in two stages, with an intermediate phase formed, before a melting of the final supposed lamellar mesophase at 80 °C. This intermediate phase is most likely cubic, rationalised on the basis of packing considerations and similar trends observed for non-photoactive ethylene glycol surfactants,[59–61] however there is not enough experimental evidence to support this assignation firmly. An increase in melting temperature with increasing temperature was also observed for $C_2AzoOC_4E_4$. The room temperature POM image at 40 wt% was difficult to assign, displaying characteristics of both a hexagonal and a lamellar phase. With increasing temperature, the texture of the POM images changed, concurrent with endothermic peaks in the DSC thermogram at 32 and 47 °C. It is most likely that this is a transition from a hexagonal to a lamellar phase, similar to what was observed for $C_6AzoOC_4E_4$.

At 50 wt%, the SAXS profiles suggest a mixture of lamellar and hexagonal phases. The POM images for this temperature are accordingly difficult to assign. They are clearly bright but the texture is not clear, with the image appearing "molten". With increasing temperature, the phase does not become more obvious and by 45 °C the image is quite dark. From the SAXS profile (Figure 5.16) there is a clear lamellar phase at 50 wt%. The

DSC data show small peaks in the region of 36–41 °C, indicating that the transition from a mixture of hexagonal to lamellar phases occurs over this temperature region. For the 60 wt% sample, the POM images initially appear lamellar. The texture and brightness are lost at 30 °C, implying a phase change occurs within this region. The DSC thermogram for this concentration shows two small endothermic bumps at 32–35 °C, in agreement with the POM images. There is a much larger endothermic peak at 69 °C, repeating the trend that has been observed so far, whereby a mesophase change occurs at intermediate temperatures followed by a melting of the mesophase at high temperatures. This behaviour is repeated at 70 wt%, with a loss of the texture at 30 °C, accompanied by bumps in the DSC thermogram. There is no further high temperature transition in this case, implying that the second mesophase is stable to above 80 °C. The formation of dark POM images here suggests the formation of a cubic phase or an isotropic surfactant solution. Given the high surfactant concentrations and viscosities, it was not possible to perform SAXS measurements on these samples to investigate further.

At 80 wt%, the stringy texture of the POM image at 20 °C strongly suggests a lamellar phase. The texture fades with heating, as observed for 60 and 70 wt%. In this case, the mesophase is slightly more stable to temperature, with a dark image not obtained until 35 °C. However this is a markedly lower stability of the lamellar phase compared to that observed for the other two AzoPS, whereby the lamellar phase was often stable to over 70 °C . For this concentration, the DSC thermograms, has some small peaks throughout the temperature range, at 34 °C, 64 °C and 72 °C. It is possible a cubic phase is formed above 30 °C for 60-80 wt%, which would be isotropic when imaged using POM. At 90 wt%, the DSC thermograms appear relatively featureless. On the basis of these results, a binary temperature-concentration phase diagram was constructed for $C_8AzoOC_4E_4$ (Figure 5.19). Further POM images are available in the Appendix (Figure A.5.4)
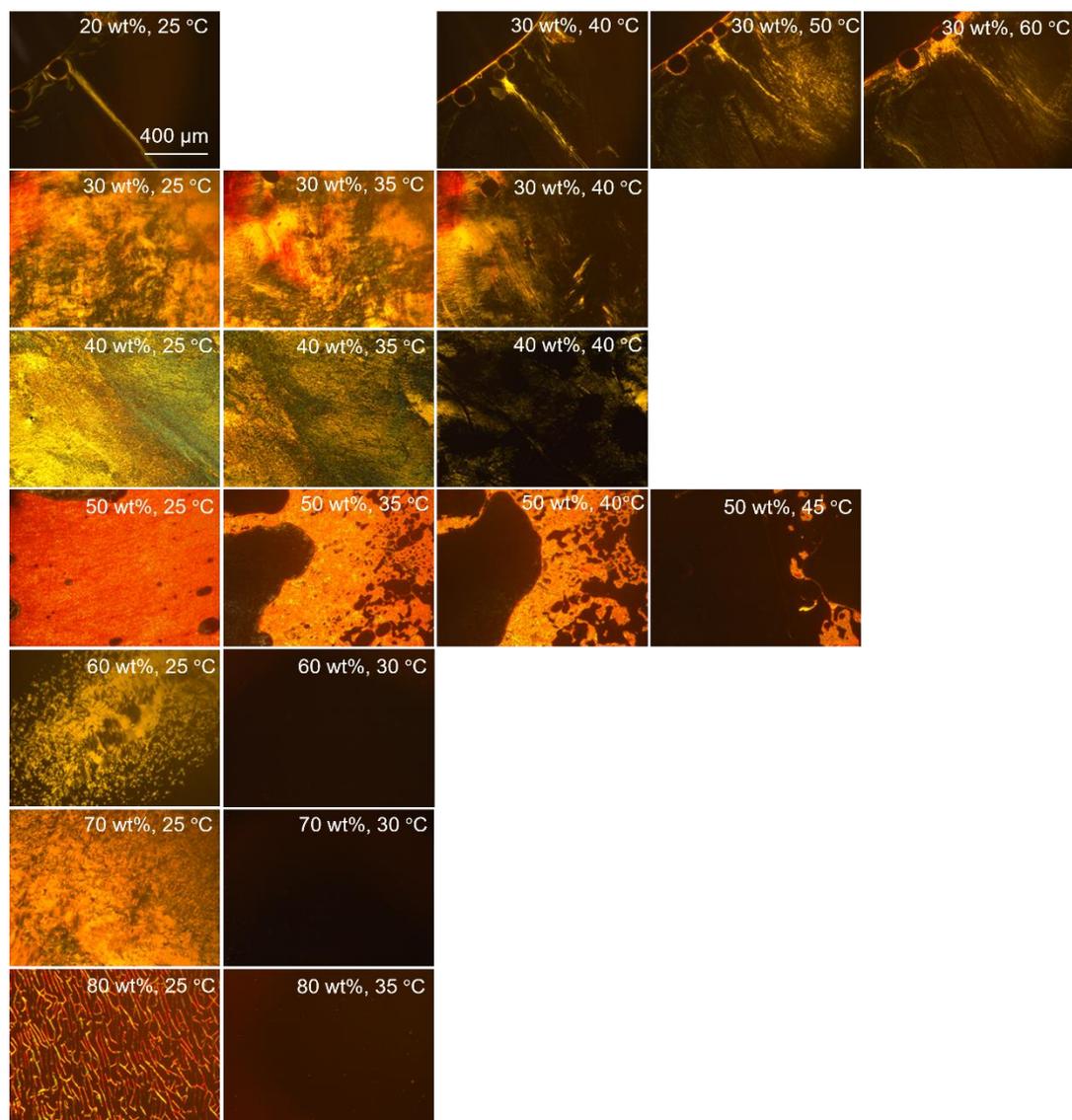
Figure 5.17. POM images of aqueous solutions of $C_8AzoOC_4E_4$ in the native *trans*-state at concentrations of 20–80 wt% with varying temperature. Both hexagonal and lamellar textures are lost at increased temperature, indicated by the loss of brightness and texture in the POM images. Scale bar indicates 400 µm.
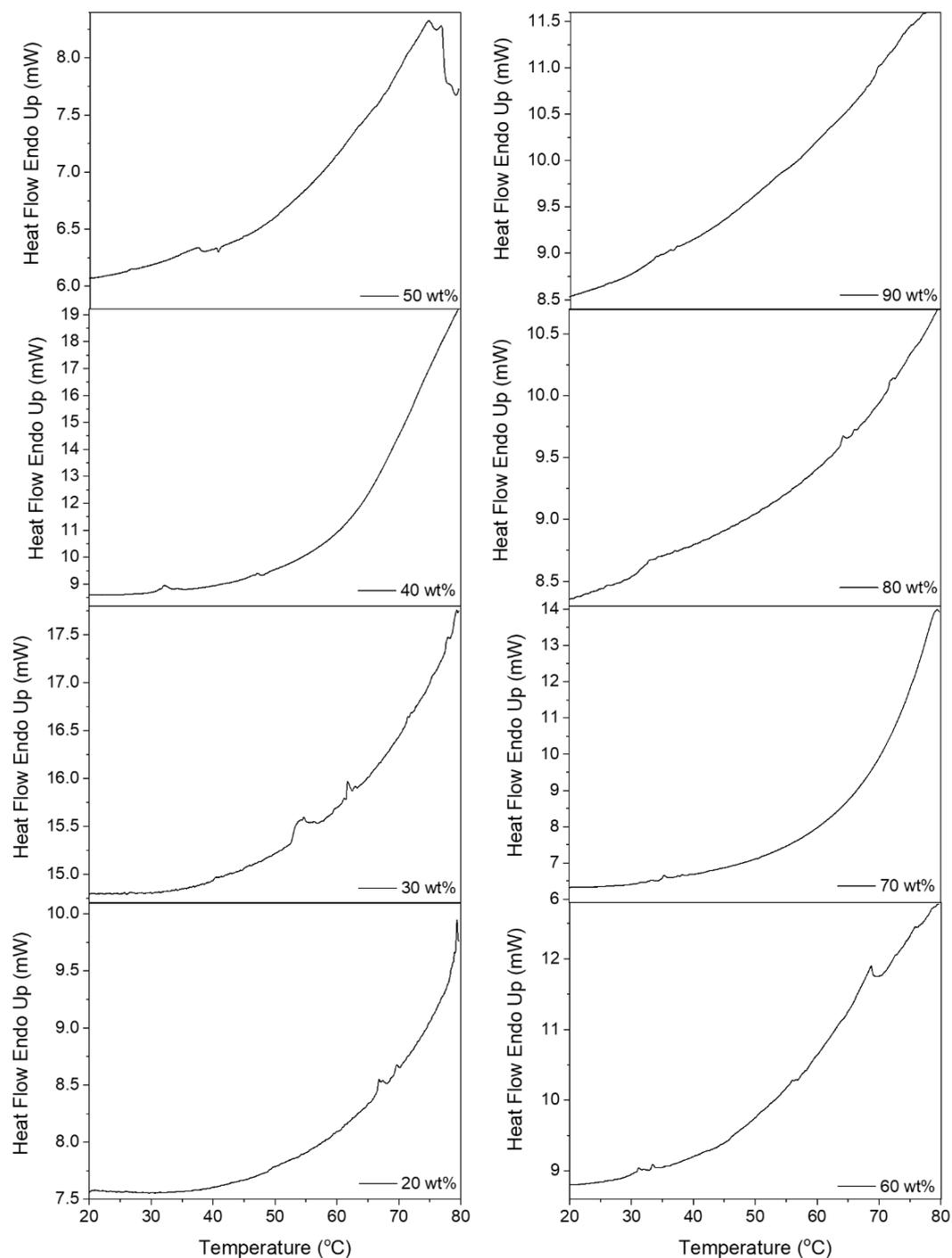
Figure 5.18. DSC thermograms for aqueous solutions of $C_8AzoOC_4E_4$ in the native *trans*-state at 20–90 wt%. Endothermic peaks indicates order-order transitions between mesophases, while large peaks at elevated temperature indicate melting or total loss of the ordered phase.
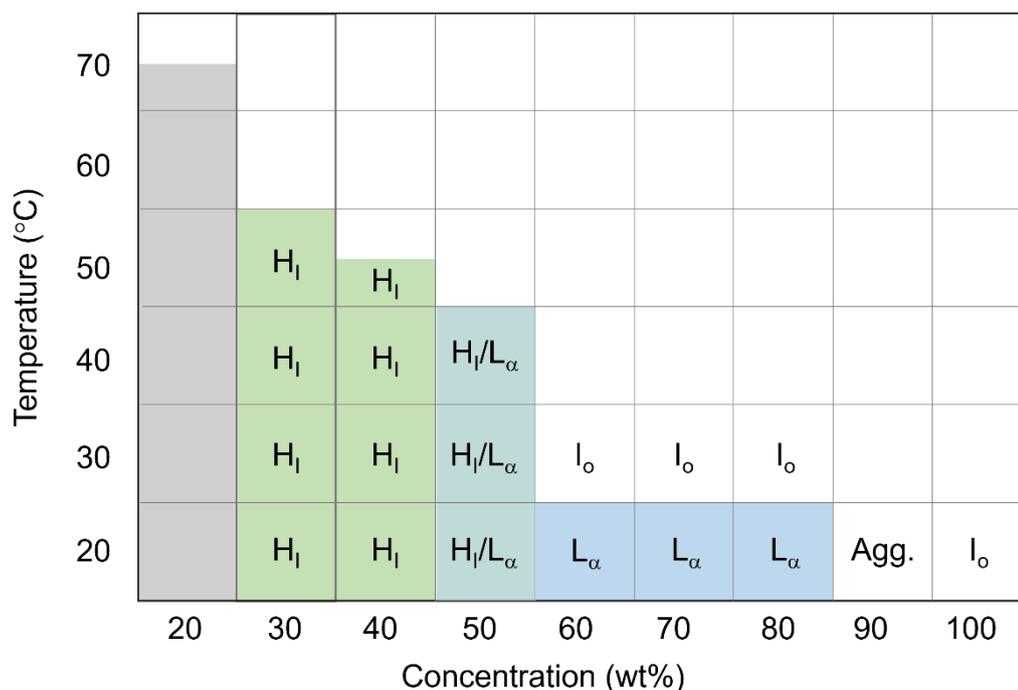
Figure 5.19. Binary concentration-temperature phase diagram for $C_8AzoOC_4E_4$ in the native *trans*-state. H_1 indicates a normal hexagonal phase, I_o indicates an isotropic phase and L_α indicates an isotropic phase.

As previously discussed, for aqueous solutions of $C_8AzoOC_8E_4$, all concentrations appeared crystalline by POM at 20 °C and pronounced interference peaks with integer repetitions of peak positions were observed in the SAXS profiles, even as low as 10 wt%. With increasing temperature, the same trend is observed for all concentrations whereby a loss of the crystallinity occurs until the POM images appear fully dark. This loss of brightness and crystallinity was accompanied by very large endothermic peaks in DSC, significantly higher in magnitude than the peaks observed for the other AzoPS, indicating that this was a transition with a higher enthalpy. This is consistent with the melting or dissolution of a crystalline phase, rather than an order-order transition or melt of a mesophase.[36]

At 30 wt%, the POM images have regions of darkness at 30 °C and are almost fully dark by 35 °C, with a large endothermic peak (10.5 J g^{-1}) observed at 24 °C in the DSC thermograms. For the 40 wt% sample, the same behaviour occurs, with a loss of brightness at 30 °C, but in this case a texture similar to an LLC phase is apparent at 35 °C. It is possible this is an intermediate molten phase with some long-range order, rather than a true LLC phase. By 40 °C at 40 wt%, all brightness and textures is lost from the POM image. The DSC thermograms for this sample has a smaller endothermic peak at 24 °C (3.2 J g^{-1}) and a much larger one at 37.5 °C (37.5 J g^{-1}). In general, the DSC thermograms show very similar behaviour for all concentrations, with a large endothermic peak present at 30-40 °C. This is in agreement with the POM images which show a loss of

crystallinity and brightness from 30 °C onwards. The behaviour of the 100 wt% sample is interesting, as it indicates that the surfactant behaves similarly, even in the absence of solvent. In this case a loss of crystallinity and brightness is observed at 30 °C, with only small domains of birefringence remaining at 35 and 40 °C. For the 40, 70 and 90 wt% sample, some of the POM images at elevated temperatures appear less crystalline and more like LLC or molten phases. It is possible an LLC phase is formed in a narrow region at these higher temperature. Potential future work would be to allow the sample to equilibrate at an elevated temperature of 30-35 °C and then repeat the SAXS measurement to see if a mesophase has established. This is supported by the phase diagram of the long chain, alkyl surfactant, $C_{12}E_4$, which only forms LLC phases at some concentrations above 31 °C.[49] Further POM images for $C_8AzoOC_8E_4$ as a function of temperature are available in the Appendix (Figure A.5.5). For all concentrations, the original crystalline texture was recovered upon cooling (Appendix Figure A.5.2–A.5.5)
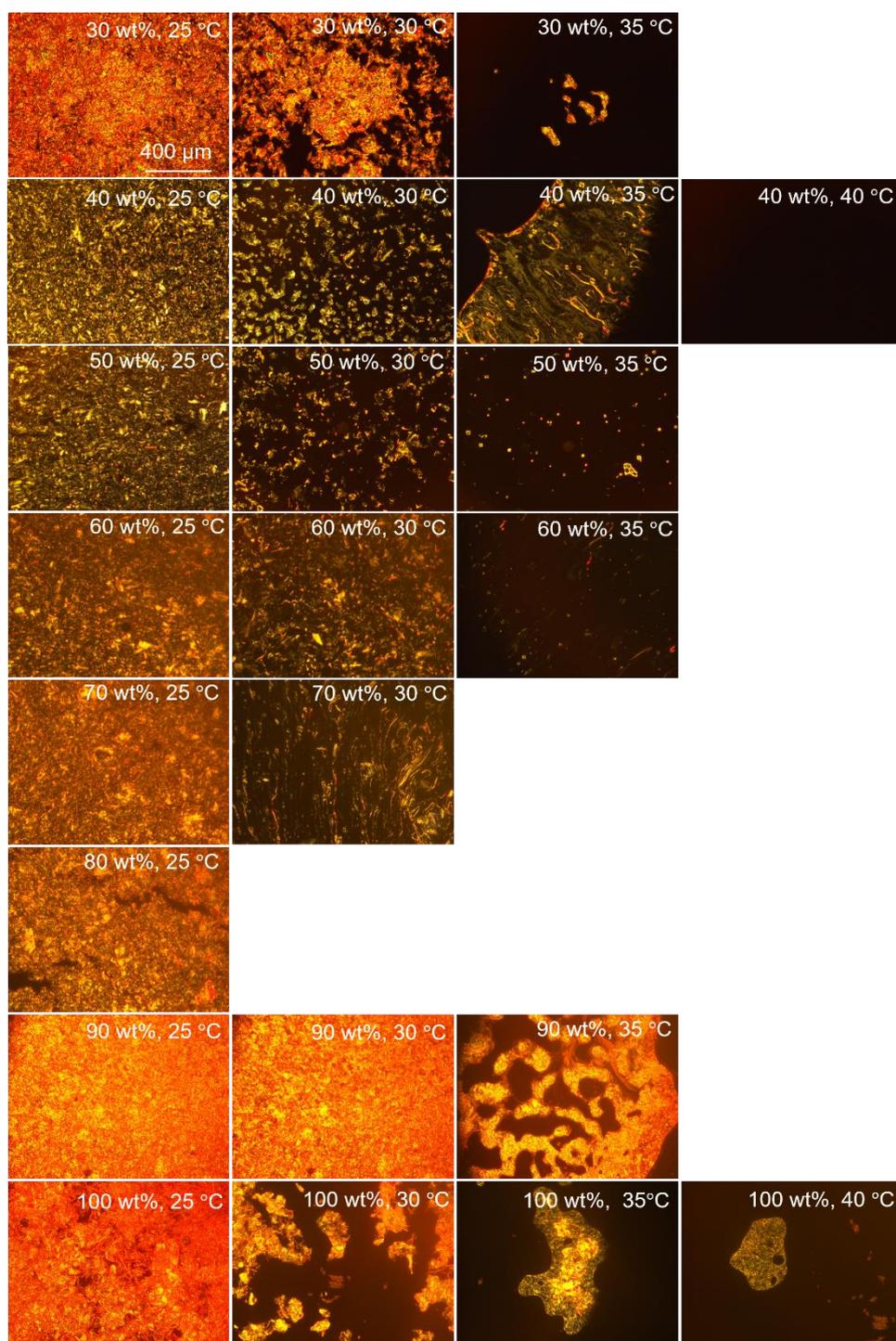
Figure 5.20. POM images of $C_8AzoOC_8E_4$ in aqueous solutions at concentrations of 30–100 wt% at increasing temperature. At 25 °C, insoluble crystals can be observed which lose brightness and texture upon dissolution at elevated temperatures.
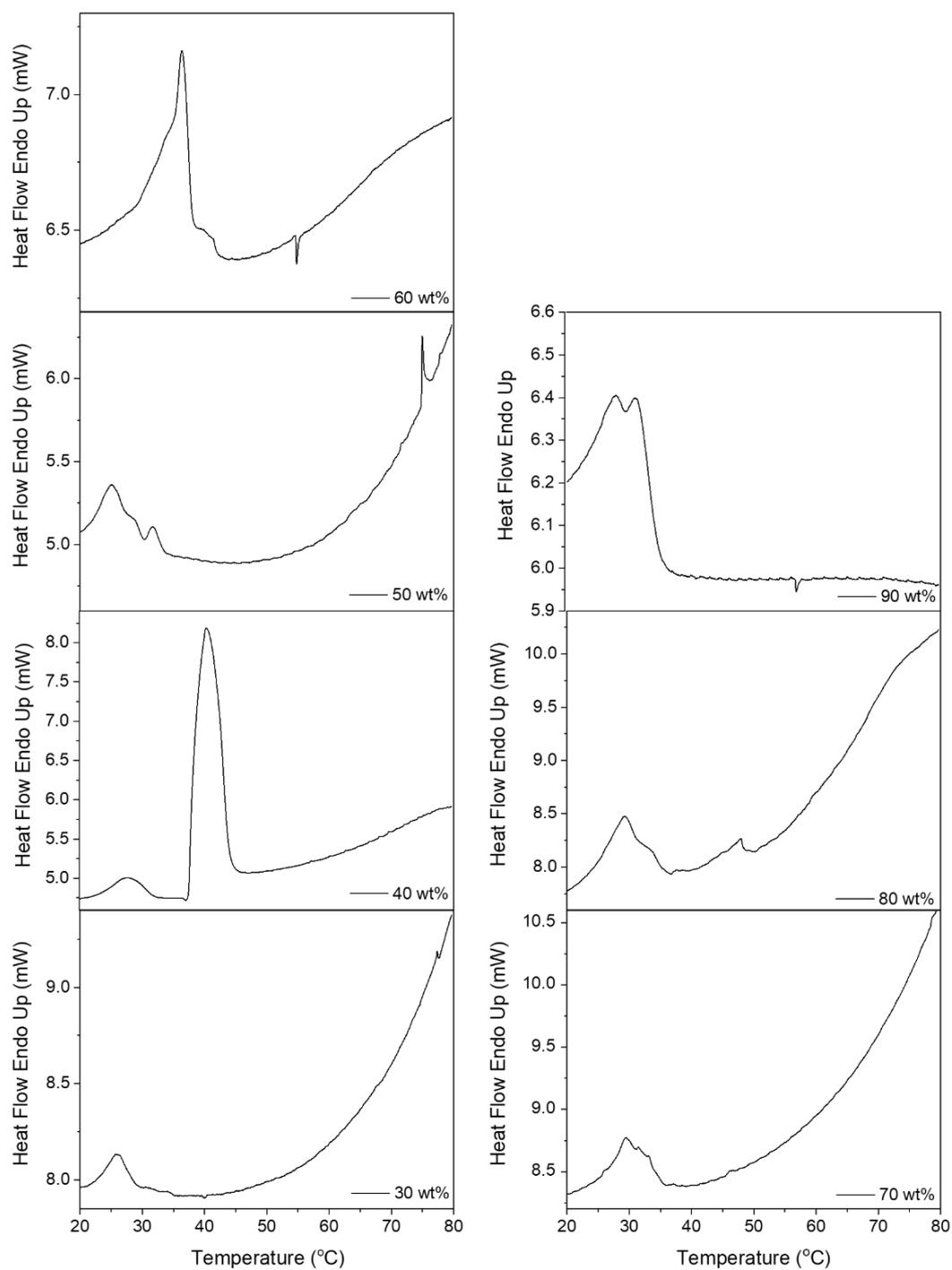
Figure 5.21. DSC thermograms of aqueous solutions of $C_8AzoOC_8E_4$ in the native *trans*-state at concentrations of 30–90 wt%. Large endothermic peaks indicate the melting or loss of the poorly soluble crystals.

5.3.3. Effect of Photoisomerisation on LLC Phases

The effect of UV irradiation (λ = 365 nm) on the LLC phases was probed using POM. Figure 5.22 presents POM images for each AzoPS at varying concentrations in water, before and after UV irradiation. Further POM images showing each AzoPS before and after irradiation across a broader variety of concentrations are available in in the Appendix (Figure A.5.6-A.5.9). In all cases, after UV irradiation the brightness of the POM images is significantly decreased and the anisotropic textures are lost. In some cases, small points of light remain, which are most likely small aggregates. As it is not possible to form a 100% *cis*-photostationary state, any remaining brightness could be due to small domains of the *trans*-isomer. The textures of the *trans*-isomers before UV irradiation reaffirm the phases assigned previously, with textures characteristic with either a hexagonal or lamellar phase occurring at the same concentrations as was previously observed for $C_6AzoOC_4E_4$ and $C_8AzoOC_4E_4$ (Section 5.3.1). Unfortunately, it was not possible to perform SAXS measurements of the AzoPS in their *cis*-forms as irradiating with the X-ray beam appeared to accelerate the reverse isomerisation process to the *trans*-dominant form, as shown in the UV-Vis absorption spectra of two *cis*-samples measured before and directly after SAXS measurements (Appendix, Figure A.5.10) Any conclusions about the structure of the *cis*-isomeric phases can only be drawn from the loss of birefringence in the POM measurements, which indicates either a total loss of the LLC phase or the formation of a cubic LLC phase, which is optically isotropic.

In the case of $C_8AzoOC_8E_4$, it is particularly interesting to note the complete lack of brightness after UV irradiation. The starkness of the effect of isomerisation is most apparent when a mask is used to only partially disrupt the sample. In Figure 5.23 there is an obvious horizontal boundary between the UV irradiated and masked areas, for all AzoPS probed. It can be clearly seen that the bottom, masked section retains the brightness and texture of either the LLC or crystalline phase, while the top, exposed section has become dark and lost texture. This indicates that it is possible to only partially deform the LLC phase.
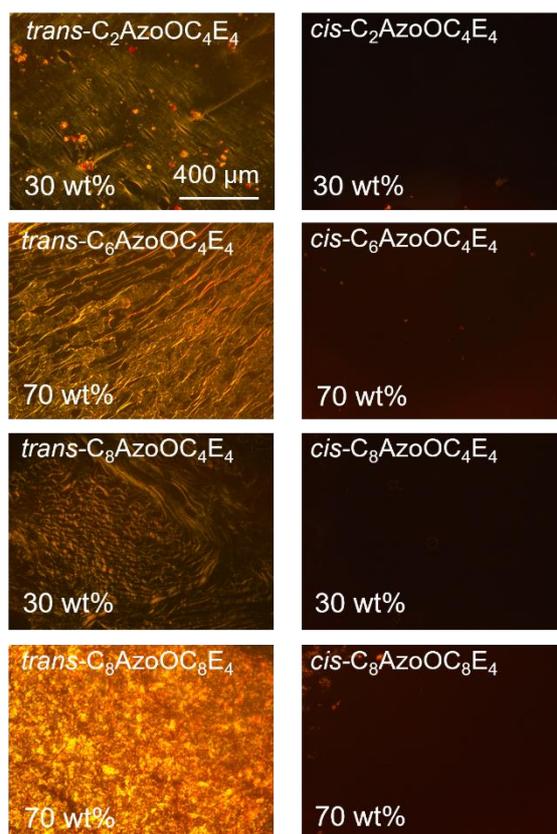
Figure 5.22. LLC phases formed by the native *trans*-isomer are lost upon UV isomerisation and formation of the *cis*-PSS. POM images of lamellar phases (30 wt% $C_2AzoOC_4E_4$, 70 wt% $C_6AzoOC_4E_4$), hexagonal phases (30 wt% $C_8AzoOC_4E_4$) and insoluble crystallites (70 wt% $C_8AzoOC_8E_4$) all lose brightness and texture upon UV irradiations. Scale bar indicates 400 μm.
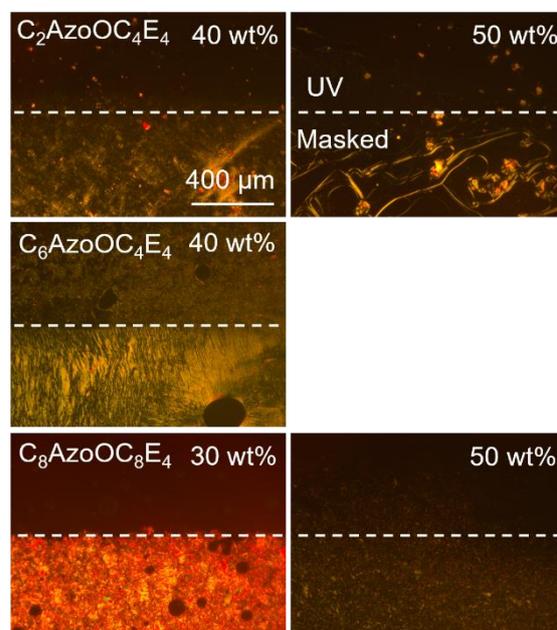
Figure 5.23. The self-assembled structure formed by each AzoPS can be selectively disrupted through the use of a mask. The top section only (above the dotted line) of each sample was irradiated with UV light while the bottom portion was masked. In each case the texture and brightness is significantly disrupted or lost entirely upon UV irradiation. Scale bar indicates 400 μm.

5.4 Discussion

The key findings and trends of the results presented in this Chapter will be discussed below. The fundamental behaviour of EO surfactants and their phase diagrams and typical trends have been previously outlined in the Introduction and will be briefly referred to again here. First, the expected behaviour of each AzoPS on the basis of packing considerations will be discussed. The size of the tetraethylene glycol head group is calculated to be 0.426 nm^2, from X-ray data.[62]   For each AzoPS in order of increasing tail length, the calculated tail lengths are 2.24, 2.75, 3.00 and 3.50 nm, for $C_2AzoCO_4E_4$, $C_6AzoOC_4E_4$, $C_8AzoOC_4E_4$ and $C_8AzoCO_8E_4$, respectively. The values are determined using the Tanford equations; further details can be found in the Appendix (Table A.2.2). Using geometric considerations, it is possible to work out the critical size of the surfactant head group needed, for a given tail length, to stabilise a certain shape. For example, for these AzoPS, in order to stabilise a spherical packing arrangement, the head group would need to be at least 0.538-0.574 nm^2, depending on the tail length. To stabilise a cylinder, the head group would need to be >0.359-0.389 nm^2, while for a lamellar sheet, the headgroup required would be >0.180-0.191 nm^2. This means the E_4 head group (0.426 nm^2) can stabilise either a cylindrical or sheet-like packing arrangement, for each tail length used here. It is entropically favourable for the smallest aggregate to be adopted, so cylinders will generally be formed ahead of sheets.[36,62]   The same conclusion can be reached by directly calculating the packing parameter of these AzoPS, with all here falling into the range required for cylinders.[63] On the basis of these packing considerations, it is expected that all four AzoPS will form cylindrical micelles and so would be expected with increasing concentration to transition from a hexagonal LLC phase to a lamellar phase, when the packing fraction of the cylinders is reached.[36,49,62] With increasing temperature and dehydration of the head groups, a transition to a lower curvature phase, such as a lamellar or even reversed phase, would also be expected.[48]

For the *cis*-isomers, the packing parameter is estimated to be 0.46 for all structures, again predicting cylindrical micelles, although now very close to the boundary with sheet-like packing (P = 0.5). The packing parameter suggests therefore that no change in micellar shape, and consequently mesophase, is expected upon photoisomerisation. It is clear from the results shown thus far these packing considerations are insufficient to fully describe the behaviour of the AzoPS, as cylindrical phases were observed for only two of the four structures ($C_6AzoOC_4E_4$ and $C_8AzoOC_4E_4$) and there was a clear disruption of the mesophase for the *cis*-isomer. There are some useful trends observed for EO surfactants in general, on the basis of the packing fraction and packing parameter. Typically, with increased concentration the sequence of

hexagonal → cubic → lamellar is observed, although the precise transitions and their extent depends on the surfactant and the micelle shape formed at low concentrations.[59–61] This general trend is in agreement with what was observed here. The key findings for each structure will now be summarised and discussed in more detail.

$C_2AzoOC_4E_4$ was found to form only lamellar sheets, with no evidence of any hexagonal phase formed. POM images and SAXS profiles consistent with a L_α phase were found between 20-50 wt% , across a temperature range of 20-85 °C. It is thought that the rigid azobenzene core likely dominates the packing interactions for this surfactant. The short tail length will result in a more rigid structure, compared to the longer-tailed AzoPS, with π-π stacking interactions occurring between neighbouring molecules, favouring self-assembly along the perpendicular direction, which would lead to the formation of low-curvature lamellar sheets. This behaviour has been observed previously for biphenyl surfactants[55,64] and polymersomes.[50] Based on the packing parameter considerations, it is theoretically possible for the E_4 head group to stabilise a lower curvature structure, such as cylinders. Typically the smallest possible aggregate would be favoured, that can be stabilised by a given head group, but in this case it appears the enthalpic gain from the π-π stacking interactions dominates over any entropic gain of having an increased number of smaller aggregates in solution.

At low concentrations (0.1, 0.5, 1 wt%) this AzoPS was also found to form lamellar sheets. (Appendix, Figure A.5.11) so it is to be expected that this low-curvature packing trend would continue through to the LLC phase. These lamellar phases are stable to over 65 °C, with the melting temperature shifting to higher values with increased concentration, from 20 to 50 wt%. This behaviour is not uncommon, with lamellar phases often stable to 75 °C.[42,65] The lamellar phase boundary often appears "egg-shaped", in that the intermediate concentrations have very high temperature stabilities, with lower melting temperatures occurring on either side. The increase in temperature here is expected only to result in a melting of the lamellar phases. Dehydration of the surfactant head groups favours the formation of lower curvature phases[48] but in this case, no lower curvature, or inverse phase, is likely. The short, rigid tail lengths of $C_2AzoOC_4E_4$ are unlikely to be able to pack in such a way as to form the continuous medium. Inverse phases are more likely for AzoPS with longer, floppier alkyl chains.[55,62,66] In general it has been reported that the shorter the alkyl chain of a surfactant, the shorter the extension of its LLC region,[39,55] so given the short chain of $C_2AzoOC_4E_4$ it is unsurprising that the lamellar phase does not persist across large concentrations and that only one LLC phase is observed. The onset of LLC phases occurring as low as 20 wt% is unusual. For conventional EO surfactants, LLC phases do not emerge until ~50 wt%. This presence of

the azobenzene moiety is likely responsible for the formation of LLC phases at low-concentrations, as this facilitates self-association through attractive intermolecular forces, rather than just the hydrophobic effect.[36]

At low concentration, it has been established that $C_6AzoOC_4E_4$ forms cylindrical, wormlike micelles, consistent with the packing parameter prediction (Chapters 3 and 4). The key difference between this structure and $C_2AzoCO_4E_4$ is the introduction of length to the pendant alkyl tail, decreasing the rigidity of the tail. It appears that across this increase of 2 to 6 carbons in the pendant tail, the azobenzene core and its associated π-π stacking interactions no longer dominate over the more typical packing interactions. As discussed in previous sections, the π-π interaction still do influence the packing in that elliptical, rather than cylindrical, micelles are formed for this AzoPS.[50,51] Given the formation of cylindrical micelles at low concentration, it is unsurprising that hexagonal LLC phases are formed initially for this structure. From 40 wt% onward, lamellar phases begin to form at room-temperature, implying that the packing fraction of the hexagonal phase has been reached. This follows the typical trend of decreasing curvature with increasing surfactant concentration.

With increasing temperature, the hexagonal-lamellar transition begins to shift to lower concentrations, as expected up dehydration of the head groups and preference for a lower curvature phase.[59] At some concentrations (40 wt%), there is evidence that an intermediate, potentially cubic, phase is formed between the hexagonal and lamellar phases, as two peaks emerge on the DSC thermograms, with correspondingly dark POM images. It is not uncommon for a small intermediate or cubic region to exist on the phase diagram for EO surfactants.[59-61] The lamellar phases, when formed, show high-temperature stability, particularly at increased concentrations. This AzoPS behaves quite typically, showing a wide variety of LLC phases across a wide range of temperatures and concentrations, in the sequence that would be predicted based on packing constraints.

$C_8AzoOC_4E_4$ was found to behave very similarly to $C_6AzoOC_4E_4$, forming hexagonal phases at low concentration, which transitioned to lamellar phases with both increased temperature and concentration. The main difference in this case is that the transitions occurred at lower temperatures. This AzoPS also showed a loss of texture and formation of dark POM images at low temperatures (30, 35 °C) for 70, 80 and 90 wt% samples. It is possible that this structure also has intermediate or cubic regions as part of its phase diagram. These would require further investigation by SAXS, however sample loading would be difficult owing to the high viscosity associated with both highly concentrated samples and cubic phases.

$C_8AzoOC_8E_4$ was crystalline across all concentrations at room temperature, as clear from the POM images and pronounced SAXS peaks that were invariant with concentration. While the insolubility of this AzoPS in the *trans*-form was initially disappointing, the stark effect of UV irradiation makes this AzoPS quite interesting. There is a pronounced change in phase, from a crystalline structure to an optically anisotropic solution which could be useful for applications relying on on-demand or controlled release, such as microfluidic devices. There is a strong endothermic energy contribution associated with this phase change and photoisomerisation, which could also have useful applications in solar thermal fuels and phase-change materials.[56,67–69]

For all AzoPS, global irradiation of the sample with UV light results in a loss of brightness in the POM image. This indicates that the *cis*-isomers do not form anisotropic LLC phases. It is possible all AzoPS form a cubic phase upon irradiation but considering the variety of tail lengths, concentrations and temperatures probed, this is considered unlikely. More likely is that the introduction of the bent, less-polar, non-planar *cis*-form inhibits the ability of the AzoPS to form LLC phases. A similar order–disorder transition was observed for the neutral AzoPS, $C_4AzoC_5E_7$, which formed an ordered H_I phase at 50 wt% before UV-irradiation but transitioned to an isotropic state upon UV irradiation.[29] The ordered phases formed by the *trans*-isomers are likely to be disrupted by a change in molecular geometry (rod-like to ''bent'') upon photoisomerisation, which would also inhibit π-π stacking interactions along the packing direction. The *cis*-AzoPS do self-assemble, in that they have a clear CMC and have neutron scattering profiles at lower concentrations (Appendix, Figure A.5.12), but it appears that the micelles do not interact to become LLC mesophases. It has also been established that LLC mesophases form more easily with pure, monodisperse materials, rather than polydisperse solutes, due to the free energy change from the loss of entropy in forming an ordered solution being less than the gain in free energy from dissolving more solute.[36] As photoisomerisation results in a *cis*-PSS, not an assembly of 100% *cis*-isomers, this polydispersity may be the reason LLC phase do not appear to form readily. The lack of optically anisotropic LLC phases upon photoisomerisation may also be a consequence of the difference in hydrophobicity of the two isomers, with the trans-isomer being considerably more hydrophobic than the *cis*-form (dipole moments of 0 and 3 D, respectively for pure azobenzene[70,71]). As a result, $C_8AzoOC_8E_4$, which has the longest tail, appears crystalline in the *trans*-state at high concentration, but dissolves upon photoisomerisation to the *cis*-PSS. Unfortunately, it was not possible to perform SAXS measurements on the *cis*-isomers to characterise their structure, due to their inherent instability under the intense X-ray beam, resulting in reverse isomerisation of the AzoPS to its *trans*-state.

5.5 Conclusion

In this Chapter it has been shown that all four AzoPS investigated can form LLC phases in the native *trans*-form. It is observed that while packing considerations and the packing parameter model can be useful to rationalise the observed behaviour in some cases, in general it is insufficient to confidently predict the behaviour of these surfactants, likely due to it neglecting the effect of the azobenzene core on both the shape of the hydrophobic tail and the additional aromatic interactions the azobenzene moiety facilitates. It is possible to access different LLC phases, through variation of either molecular structure, concentration or temperature. Irradiation with UV light results in destruction of the LLC phase due to photoisomerisation to the *cis*-PSS. This change is not predicted by any of the typical packing considerations, suggesting that the simple packing parameter model cannot take into account the dramatic volume change associated with the *trans*–*cis* photoisomerisation of the azobenzene, as well as the corresponding change photoisomerisation induces in the physicochemical properties.

Future work lies in creating dispersions of these LLC phases to form cubosomes or hexosomes; droplets which retain the long-range order and structure of the parent LLC phase, but are dispersed in an aqueous solution to reduce the viscosity and improve the applicability of these solutions. This work is already underway in the Photoactive Materials group. The potential to use $C_8AzoOC_8E_4$ as a phase-change material is also very interesting and warrants further study. Having observed that these surfactants form LLC phases at high concentrations and can become isotropic on-demand with photoisomerisation, initial studies on the use of AzoPS as photodeformable templates for the formation of mesoporous titania have been performed and will be the subject of the following Chapter.

5.6 References

1　　T. Yan, F. Li, S. Qi, J. Tian, R. Tian, J. Hou, Q. Luo, Z. Dong, J. Xu and J. Liu, *Chem. Commun.*, 2019, **56**, 149–152.

2　　J. Lee, K. H. Ku, J. Kim, Y. J. Lee, S. G. Jang and B. J. Kim, *J. Am. Chem. Soc.*, 2019, **141**, 15348–15355.

3　　X. Xie, L. Wang, X. Liu, Z. Du, Y. Li, B. Li, L. Wu and W. Li, *Chem. Commun.*, 2020, **56**, 1867–1870.

4　　M. Villa, G. Bergamini, P. Ceroni and M. Baroncini, *Chem. Commun.*, 2019, **55**, 11860–11863.

5　　T. Kunitake, Y. Okahata, M. Shimomura, S. ichiro Yasunami and K. Takarabe, *J. Am. Chem. Soc.*, 1981, **103**, 5401–5413.

6　　L. Stricker, E. C. Fritz, M. Peterlechner, N. L. Doltsinis and B. J. Ravoo, *J. Am. Chem. Soc.*, 2016, **138**, 4547–4554.

7　　F. G. Downs, D. J. Lunn, M. J. Booth, J. B. Sauer, W. J. Ramsay, R. G. Klemperer, C. J. Hawker and H. Bayley, *Nat. Chem.*, 2020, **12**, 363–371.

8　　B. K. Das, B. Pramanik, S. Chowdhuri, O. A. Scherman and D. Das, *Chem. Commun.*, 2020, **56**, 3393–3396.

9　　J. Baillet, A. Gaubert, D. M. Bassani, J. Verget, L. Latxague and P. Barthélémy, *Chem. Commun.*, 2020, **56**, 3397–3400.

10　　T. Yan, F. Li, S. Qi, J. Tian, R. Tian, J. Hou, Q. Luo, Z. Dong, J. Xu and J. Liu, *Chem. Commun.*, 2019, **56**, 149–152.

11　　F. Huang, W. C. Liao, Y. S. Sohn, R. Nechushtai, C. H. Lu and I. Willner, *J. Am. Chem. Soc.*, 2016, **138**, 8936–8945.

12　　O. Rifaie-Graham, S. Ulrich, N. F. B. Galensowske, S. Balog, M. Chami, D. Rentsch, J. R. Hemmer, J. Read De Alaniz, L. F. Boesel and N. Bruns, *J. Am. Chem. Soc.*, 2018, **140**, 8027–8036.

13　　Y. Huang and S. Gui, *RSC Adv.*, 2018, **8**, 6978–6987.

14　　A. Klaiber and S. Polarz, *ACS Nano*, 2016, **10**, 10041–10048.

15　　M. A. C. Stuart, W. T. S. Huck, J. Genzer, M. Müller, C. Ober, M. Stamm, G. B.

Sukhorukov, I. Szleifer, V. V. Tsukruk, M. Urban, F. Winnik, S. Zauscher, I. Luzinov and S. Minko, *Nat. Mater.*, 2010, **9**, 101–113.

16   S. Peng, Q. Guo, T. C. Hughes and P. G. Hartley, *Langmuir*, 2014, **30**, 866–872.

17   J. J. Vallooran, S. Bolisetty and R. Mezzenga, *Adv. Mater.*, 2011, **23**, 3932–3937.

18   W. K. Fong, T. Hanley and B. J. Boyd, *J. Control. Release*, 2009, **135**, 218–226.

19   E. Tunkara, C. Albayrak, E. O. Polat, C. Kocabas and Ö. Dag, *ACS Nano*, 2014, **8**, 11007–11012.

20   S. Besson, T. Gacoin, C. Ricolleau, C. Jacquiod and J. P. Boilot, *J. Mater. Chem.*, 2003, **13**, 404–409.

21   J. Jennings, B. Green, T. J. Mann, C. A. Guymon and M. K. Mahanthappa, *Chem. Mater.*, 2018, **30**, 185–196.

22   S. Akbar, J. M. Elliott, M. Rittman and A. M. Squires, *Adv. Mater.*, 2013, **25**, 1160–1164.

23   W. K. Fong, T. L. Hanley, B. Thierry, A. Hawley, B. J. Boyd and C. B. Landersdorfer, *J. Control. Release*, 2016, **228**, 67–73.

24   X. Liu, G. Qi, A. M. G. Park, A. Rodriguez-Gonzalez, A. Enotiadis, W. Pan, V. Kosma, G. D. Fuchs, B. J. Kirby and E. P. Giannelis, *Small*, 2019, **15**, 1–8.

25   S. Saliba, C. Mingotaud, M. L. Kahn and J. D. Marty, *Nanoscale*, 2013, **5**, 6641–6661.

26   W. K. Fong, N. Malic, R. A. Evans, A. Hawley, B. J. Boyd and T. L. Hanley, *Biointerphases*, 2012, **7**, 3–8.

27   W. Fong, S. Antoni, F. G. Ortelli, W. Sun and B. J. Boyd, *RSC Adv.*, 2017, **7**, 4368–4377.

28   A. Zou, J. Eastoe, K. Mutch, P. Wyatt, G. Scherf, O. Glatter and I. Grillo, *J. Colloid Interface Sci.*, 2008, **322**, 611–616.

29   S. Peng, Q. Guo, P. G. Hartley and T. C. Hughes, *J. Mater. Chem. C*, 2014, **2**, 8303–8312.

30   X. Tan, R. Zhang, C. Guo, X. Cheng, H. Gao, F. Liu, J. R. Bruckner, F. Giesselmann, M. Prehm and C. Tschierske, *J. Mater. Chem. C*, 2015, **3**, 11202–11211.

31   R. Yang, S. Peng, W. Wan and T. C. Hughes, *J. Mater. Chem. C*, 2014, **2**, 9122–9131.

32   N. P. Cowieson, C. J. C. Edwards-Gayle, K. Inoue, N. S. Khunti, J. Doutch, E. Williams, S. Daniels, G. Preece, N. A. Krumpa, J. P. Sutter, A. D. Tully, N. J. Terrill and R. P. Rambo, *J. Synchrotron Radiat.*, 2020, **27**, 1438–1446.

33   S. Förster, L. Apostol and W. Bras, *J. Appl. Crystallogr.*, 2010, **43**, 639–646.

34   E. Kentzinger, M. Krutyeva and U. Rücker, *J. large-scale Res. Facil. JLSRF*, 2016, **2**, 1–5.

35   S. T. Hyde, in *Handbook of Applied Surface and Colloid Chemistry*, ed. K. Holmberg, John Wiley & Sons, 2001, pp. 299–332.

36   S. Hassan, W. Rowe and G. J. T. Tiddy, *Surfactant Liquid Crystals*, 2001.

37   F. B. Rosevear, *J. Am. Oil Chem. Soc.*, 1954, **31**, 628–639.

38   S. Hassan, W. Rowe and G. J. T. Tiddy, *Surfactant liquid crystals*, 2001.

39   D. Varade, K. Aramaki and C. Stubenrauch, *Colloids Surfaces A Physicochem. Eng. Asp.*, 2008, **315**, 205–209.

40   Y. Kobayashi and K. Fukada, *Biochim. Biophys. Acta*, 1998, 363–370.

41   M. Skouri, J. Marignan and R. May, *Colloid Polym. Sci.*, 1991, **269**, 929–937.

42   M. Nishizawa, K. Saito and M. Sorai, *J.Phys.Chem.B*, 2001, **105**, 2987–2992.

43   N. D. Tien, S. Sasaki, H. Masunaga, N. Shimizu, N. Igarashi and S. Sakurai, *Polym. J.*, 2014, **55**, 2562–2569.

44   K. Kornmueller, B. Lehofer, G. Leitinger, H. Amenitsch and R. Prassl, *Nano Res.*, 2018, **11**, 913–928.

45   J. Bahadur, A. Das and D. Sen, *J. Appl. Crystallogr.*, 2019, **52**, 1169–1175.

46   F. Nallet, R. Laversanne and D. Roux, *J. Phys. II*, 1993, **3**, 487–502.

47   Y. Uchida, T. Nishizawa, T. Omiya, Y. Hirota and N. Nishiyama, *J. Am. Chem. Soc.*, 2016, **138**, 1103–1105.

48   L. Thompson, J. M. Walsh and G. J. T. Tiddy, *Colloids Surfaces A Physicochem. Eng. Asp.*, 1996, **106**, 223–235.

49   D. J. Mitchell, G. J. T. Tiddy and L. Waring, *J. Chem. Soc., Faraday Trans. 1*, 1983, **79**, 975.

50   C. K. Wong, A. F. Mason, M. H. Stenzel and P. Thordarson, *Nat. Commun.*, 2017, **8**, 1240.

51   C. S. G. Butler, J. P. King, L. W. Giles, J. B. Marlow, M. L. P. Vidallon, A. Sokolova, L. de Campo, K. L. Tuck and R. F. Tabor, *J. Colloid Interface Sci.*, 2021, **594**, 669–680.

52   Y. H. Lin, K. G. Yager, B. Stewart and R. Verduzco, *Soft Matter*, 2014, **10**, 3817–3825.

53   T. Wang, A. J. Pearson, A. D. F. Dunbar, P. A. Staniec, D. C. Watters, D. Coles, H. Yi, A. Iraqi, D. G. Lidzey and R. A. L. Jones, *Eur. Phys. J. E*, 2012, **35**, 2–7.

54   E. P. Dos Santos, M. S. Tokumoto, G. Surendran, H. Remita, C. Bourgaux, P. Dieudonné, E. Prouzet and L. Ramos, *Langmuir*, 2005, **21**, 4362–4369.

55   B. Lühmann and H. Finkelmann, *Colloid Polym. Sci.*, 1987, **265**, 506–516.

56   Y. Shi, M. A. Gerkman, Q. Qiu, S. Zhang and G. G. D. Han, *J. Mater. Chem. A*, 2021, **9**, 9798–9808.

57   T. P. Lodge, B. Pudil and K. J. Hanley, *Macromolecules*, 2002, **35**, 4707–4717.

58   T. Ichikawa, T. Kato and H. Ohno, *J. Am. Chem. Soc.*, 2012, **134**, 11354–11357.

59   J. Corcoran, S. Fuller, A. Rahman, N. Shinde, G. J. T. Tiddy and G. S. Attard, *J. Mater. Chem*, 1992, **2**, 695–702.

60   S. Funari and G. Rapp, *J. Phys Chem. B*, 1997, **101**, 732–739.

61   K. Rendall, G. J. T. Tiddy and M. A. Trevethan, *J. Chem. Soc. Faraday Trans. 1 Phys. Chem. Condens. Phases*, 1983, **79**, 637–649.

62   J. M. Walsh and G. J. T. Tiddy, *Langmuir*, 2003, **19**, 5586–5594.

63   J. N. Israelachvili, D. J. Mitchell and B. W. Ninham, *J. Chem. Soc. Faraday Trans. 2 Mol. Chem. Phys.*, 1976, **72**, 1525–1568.

64   B. Lühmann and H. Finkelmann, *Colloid Polym. Sci.*, 1986, **264**, 189–192.

65   R. Strey, *Curr. Opin. Colloid Interface Sci.*, 1996, **1**, 402–410.

66   J. Mitchell, G. J. T. Tiddy, L. Waring, T. Bostock and M. P. McDonald, *J. Chem. Soc., Faraday Trans.*, 1983, **79**, 975–1000.

67   K. Masutani, M. A. Morikawa and N. Kimizuka, *Chem. Commun.*, 2014, **50**, 15803–15806.

68   Z. Y. Zhang, Y. He, Z. Wang, J. Xu, M. Xie, P. Tao, D. Ji, K. Moth-Poulsen and T. Li, *J. Am. Chem. Soc.*, 2020, **142**, 12256–12264.

69   G. G. D. Han, H. Li and J. C. Grossman, *Nat. Commun.*, , DOI:10.1038/s41467-017-01608-y.

70   K. G. Yager and C. J. Barrett, *J. Photochem. Photobiol. A Chem.*, 2006, **182**, 250–261.

71   G. S. Hartley, *J. Chem. Soc.*, 1938, 633–642.

Chapter 6

AzoPS as Templating Agents for Photocatalytic Titania

6.1 Introduction

To this point, the primary research focus has been on the properties and behaviour of the azobenzene photosurfactants themselves, principally in terms of their structure, photoisomerisation and self-assembly behaviour. The effect of these parameters on macroscopic properties such as flow behaviour and liquid crystal formation have been investigated and discussed in Chapters 3 and 4. In this Chapter, the focus will shift to the possibility of using these AzoPS as templates to create porous titania particles for photocatalytic applications. The fundamentals of titania (TiO$_2$) - its function, key properties and applications - have already been presented in the initial Introduction (Section 1.2.4). In this section, the literature specific to surfactant-assisted templating of titania will be introduced, to provide context for the ensuing results.

Photocatalytic activity arises from the creation, and separation, of election-hole pairs, the reductive and oxidative potential of which can be used for the degradation of organic pollutants (usually *via* the formation of hydroxyl radicals or superoxide in aqueous solution).[1] To create titania for photocatalytic applications, the key requirements are: (1) a high surface area, to both maximise contact of the substrate with the photocatalytic surface and to create a high density of localised states which can act as trapping sites for the photogenerated charge carriers; (2) a high porosity, to allow easy diffusion of the substrate through the catalyst and (3) the formation of crystalline titania, ideally anatase phase, which shows the highest photocatalytic ability.[1–3] Titania formed as sub-micrometre mesoporous spheres are particularly interesting because of their effective light absorbance and easy separation for reuse, compared to nanometre-sized titania.[4] They also have a relatively high refractive index and comparable size to optical wavelengths.[5] This makes submicron, mesoporous, spherical titania a good candidate for applications relying on interactions with photons, such as dye-sensitised solar cells, in addition to photocatalysis. [6–8]

However, creating mesoporous titania spheres can be challenging as it can be difficult to obtain uniformity. A variety of reviews are available which discuss different synthetic approaches for the formation of mesoporous titania.[9–11] It has been shown that sol-gel chemistry can be used to create titania spheres, with template assistance to allow control over the dimensions and porosity of the material.[9,11,12] The typical approach to forming titania for photocatalytic applications is to initially create amorphous, porous titania which is then converted to a crystalline phase in the furnace *via* high temperature calcination. The temperature chosen will determine the crystalline phase formed. As outlined in the Introduction, rutile titania is the most thermodynamically stable phase but is photocatalytically less active than anatase titania.[3] Rutile is usually the phase formed

from calcination above 700 °C at ambient pressure, depending on the synthetic approach. Brookite titania can also be formed but is historically difficult to form the pure phase.[13] The anatase phase tends to be formed at temperatures between 350–700 °C.[14,15] The crystallinity, as well as the phase itself, strongly influences the photocatalytic activity of titania; highly crystalline materials have fewer defects which enhances charge transfer across the material and decreases the rate of electron-hole pair recombination. However, formation of and conversion between phases at high temperatures leads to decreased surface area and pore collapse.[6,16,17] Therefore, there is a careful balancing act between forming high crystallinity anatase phase titania and maintaining high surface areas and porosity within the particle. Combined with synthetic challenges, such as the high chemical reactivity of the titania precursor, it can be difficult to obtain the required product.

Surfactant-templated synthesis offers the possibility to create mesoporous titania. To date, there has been a strong focus on optimising synthetic techniques and understanding particle - and crystal - formation and growth. The variety of templates used to form mesoporous titania has not been particularly broad. Initial work focused on phosphate surfactants[18] and alkylTAB surfactants,[19-21] with later work preferring amines[22] such as hexadecylamine (HDA).[8,17,19-21] There has been some research exploring block copolymers, but in general the choice of surfactant has not been widely explored. In particular, the use of photosurfactants to template titania has never been reported. There is only one report of an trimethylammonium bromide azobenzene photosurfactant used to template silica.[23] The surfactant used, AZTMA (6-(4′-ethoxy-4-azophenyl)hexyloxytrimethyl ammonium bromide) was initially irradiated with UV light, with tetraethyl orthosilicate then added to form spherical, porous silica *via* a template-assisted sol-gel reaction. The analogous synthesis performed under ambient light resulted in silica with an irregular morphology. This initial work highlights the possibility of AzoPS to be used as a templating agent, with tunable properties depening on the irradiation conditions. The focus of the work presented in this Chapter will be on building upon the optimised synthetic sol-gel parameters developed by others for standard surfactant templates, the relevant literature of which will be outlined briefly in the following paragraphs, in order to effectively probe the influence of the photoresponsive template in terms of its size, shape and isomeric form on the morphology, surface area and photocatalytic performance of the product titania.

Titania precursors are highly reactive and can hydrolyse and precipitate rapidly, resulting in large, inhomogeneous structures. Controlling the hydrolysis process by limiting the quantity of water available is crucial to forming well-defined, monodisperse

products. The literature in general has attempted to do this by using alcohol-based syntheses with small volumes of water or aqueous salts and acids. Several other approaches are also possible. For example, Kluson *et al.* used reverse Triton X-100 micelles in cyclohexane with titanium isopropoxide (TTIP) to limit the volume of water available for hydrolysis.[24] They formed an amorphous gel which transformed to rutile or anatase titania upon heating. Another, more common method to control the hydrolysis rate of the titania precursor is through evaporation-induced self-assembly (EISA). This method was first reported in the late nineties for the formation of a variety of metal oxides, including titania.[25,26] The general approach is to begin with a homogenous solution of the titania precursor and surfactant in ethanol and water, with the concentration of the surfactant below the CMC or concentration desired. This solution is placed in an open dish, where evaporation of the ethanol concentrates the deposited solution, driving the self-assembly of the surfactant micelles and coordinated metal species to build an inorganic network around the surfactant liquid crystal phase. (Scheme 6.1) The mesophase passes through a tuneable steady state before condensation, the length of which depends on the relative humidity.[27] The final result is the formation of mesophases that are highly oriented with well-defined morphologies.

As previously said, it is a well-known obstacle that it is difficult to form both crystalline titania and retain the porosity/high surface areas after calcination of the hydrolysed titania. Many reported synthesis suffer from collapse of the pore structure at temperatures above 350 °C.[6,16,28,29] Higher temperatures than this are required to fully remove the surfactant template and to crystallise the amorphous titania. Post-synthetic treatments have been developed to try and improve the thermal stability of the titania network, the most widely adopted of which has been a basic ammonia treatment. Initial work of Barringer and Bowen[30] involved dispersing the titania product in a basic solution but many reports in the intervening years did not employ this step. In 2004, Cassiers *et al.* developed an aqueous ammonia treatment to control the transformation of amorphous titania walls into crystalline walls after calcination, while retaining porosity.[31] They used either HDA or cetyltrimethylammonium bromide (CTAB) to template the mesoporous titania formed from TTIP using the EISA method. The recovered powder was then refluxed in a basic ammonia solution for 48 hours. Beyers *et al*. also investigated the effect of an ammonia treatment on the final titania product, synthesised using the EISA method with TTIP under both acidic and basic conditions and with either CTAB or HDA as surfactant templates.[21] They proposed that the use of an ammonia treatment (48 h reflux in aqueous ammonia) increases the thermal stability of the titania product, preventing pore collapse upon calcination. They reported that in certain cases, a small amount of

anatase phase can be formed before calcination. This supports additional reports of the presence of crystallinity before calcination for EISA process.[25] Zimney *et al.*, also investigated the EISA method with an ammonia treatment.[32,33] They found that high BET areas (>180 m^2/g) were retained after calcination when an ammonia treatment was applied.

Non-EISA approaches have also found success in mediating good crystallinity with porosity. A combined sol-gel solvothermal method was developed by the Caruso group. Caruso and coworkers reported mesoporous anatase titania beads with diameters and pore sizes than can be tuned through the reaction conditions.[8,17,34] Using this approach, TTIP was hydrolysed using a sol-gel synthesis in ethanolic solution with aqueous KCl and HDA as a surfactant template.[17] The initial product was then solvothermally treated in an ethanol, water and ammonia solution at 160 °C for 16 hours. After the initial sol-gel step, monodisperse, amorphous, non-porous beads were obtained. Following the solvothermal ammonia treatment and calcination, monodisperse beads of ~800 nm in size were formed, with a BET area of 89 m^2/g and an average pore size of 18-22 nm. When the ammonia was excluded from the solvothermal treatment, higher surface areas (108 m^2/g), smaller pores (14 nm) and smaller anatase crystals were formed. The effect of calcination temperature and time was also probed,[8] with furnace temperatures of 500-800 °C and calcination times of 2-24 h explored. The photocatalytic properties of the resulting titania beads were investigated in terms of their ability to degrade methylene blue, an organic dye that is commonly used as a model organic pollutant. Higher temperatures improved crystallinity at the expense of porosity, and *vice versa* for low temperatures. This work emphasised the importance of balancing crystallinity, porosity and surface area. The titania beads made using this method were incorporated as the seminconductor layer in dye-sensitised solar cells, achieving efficiencies of 8-10%.[4,35]

On the basis of this literature review, it was decided to probe both: (1) the non-evaporative sol-gel method reported by the Caruso group, which seems to produce monodisperse, well-defined titania beads with high crystallinity and surface areas, using KCl as a means to control the ionic strength and particle size; and (2) the EISA method, due to the presence of a tuneable steady-state during the evaporation and condensation process, which could potentially be exploited for i*n-situ* UV light irradiation of the photoresponsive AzoPS template. An ammonia treatment would be employed in both cases, to improve the thermal stability of the titania product to calcination, in the hopes of better retaining the templated pore structure. The aim is to use AzoPS as templates in both the native *trans*-state and in the *cis*-PSS. It would be expected that the *cis*-PSS would relax back to the *trans*-isomer over the time scale of the synthesis, with the intention that

this will impart additional porosity or morphology changes to the product particle. The titania particles will be characterised in terms of their key parameters (crystal phase, crystallinity, surface area) and assessed in terms of their photocatalytic performance, to determine if AzoPS can be used as effective templates for the formation of mesoporous titania and whether any additional advantages are imparted through the use of a photosurfactant as the templating agent.

6.2 Experimental

Materials

Ammonium hydroxide (25%), ethanol (99.8+%), KCl (>99.0%), titanium (IV) isopropoxide (98.0+%) and methyl orange (pure, indicator grade) were obtained from Fisher Scientific. All reagents were used as received. Deionised water and Millipore water (18.2 mΩ cm) were obtained through an in-house water purification system. Azobenzene photosurfactants were synthesised as outlined in Chapter 2.

Methods

Non-Evaporative Sol-Gel Method: AzoPS (3.3 mmol, ~1.5-2 g depending on the AzoPS used) was dissolved in EtOH (80 mL) and aqueous KCl added (0.32 mL, 0.1 M). The solution was stirred until homogenous and TTIP (6.2 mmol, 1.84 mL) added dropwise with vigorous stirring. The vessel was left to age at 25 °C for 24 h and the product particles collect *via* centrifugation (Sorvall Legend Micro 17 Microcentrifuge, 4 min, $14 \times g$) and washed with ethanol. The eluent was retained to recover the AzoPS. The collected particles were placed in an flask with ethanol (25 mL), water (12.5 mL) and ammonium hydroxide (0.75 mL, 25%) and refluxed for 24 h. The particles were recovered via centrifugation and washed with EtOH. The particles were characterised at this stage and after calcination in air (450 °C, 2 h). The temperature was selected from the phase transition observed using differential scanning calorimetry (DSC).

The above procedure uses the AzoPS in the native-*trans* state. For syntheses using the *cis*-isomer as the template, the surfactant-ethanol solution was first irradiated with UV light (365 nm) to form the *cis*-PSS. This process was tracked using UV-Vis absorption spectroscopy, with UV irradiation continued for several hours until no further changes were observed in the absorption spectrum, establishing a *cis*-PSS that was 63% *cis*-isomers. (Appendix, Figure A.5.1). KCl was then added to the surfactant-ethanol solution, followed by TTIP, and the rest of the synthesis proceeded as above. At the end of the hydrolysis step, after the particles were recovered by centrifugation and ~24 h since the UV irradiation, the UV-Vis absorption spectrum of the AzoPS-ethanol solution was measured again to quantify the extent of reverse isomerisation that occurred during the synthesis. The proportion of AzoPS in the *cis*-isomer after the synthesis was found to be 29% for $C_6AzoOC_4E_4$, a decrease from the *cis*-PSS in ethanol of 63% (Figure A.6.2).

For all syntheses, after hydrolysis and initial particle formation, any ethanol supernatant recovered (coloured orange/red) was retained for recovery of the AzoPS surfactant. The ethanol was removed *via* rotary evaporation and the surfactant was washed several times in DCM/water to react any remaining TTIP and remove salt by-

products. The solvent was removed using rotary evaporation and the recovered AzoPS was confirmed using NMR spectroscopy. This means the AzoPS has the potential to be re-used as a templating agent for future titania syntheses.

Evaporation-Induced Self-Assembly Approach: The surfactant (1.84 mmol, 1.03 g) was dissolved in water (0.3 mL) and ethanol (29.3 mL). The solution was stirred until homogenous and TTIP (5.58 mmol, 1.66 mL) added dropwise with stirring. The solution was aged in a sealed vessel overnight and then poured into an open Petri dish and left to evaporate for 7 days. The product was recovered and placed in an RBF with water (50 mL) and ammonia (25%, 0.04 mL). The resulting solution was refluxed for 24 h and the titania product recovered *via* centrifugation and washed with ethanol. The particles were then calcined in air at 450 °C for 2 h.

For the EISA syntheses using the *cis*-isomer as a template, the surfactant solution was irradiated with UV light for several hours when first poured into the evaporating dish, after aging overnight. A distinct colour change from yellow to orange was observed over the course of the irradiation (Appendix, Figure A.6.2). The syntheses then proceeded as above. Owing to the evaporation of the solvent, the proportion of the *cis*-isomer was not tracked as the synthesis proceeded but it is expected that the reverse isomerisation occurred with the same rate as for the non-evaporative approach, with the reverse isomerisation leaving ~30% *cis*-isomer after 2 h, and with this value decaying further over the course of the evaporation.

An outline of both synthetic approaches can be found in Scheme 6.1.

Simultaneous Differential Scanning Calorimetry-Thermogravimetric Analysis (SDT): SDT measurements were performed on a TA Instruments Q600 SDT instrument. Samples were placed in an aluminium crucible and measured in air across the range 20-650 °C with a heat rate of 5 °C min^{-1}. During Covid-19 restrictions, some measurements were kindly performed by Dr Robert Cornell.

Powder X-Ray Diffraction (PXRD): PXRD measurements were performed on a Bruker D8 Advance instrument with a position-sensitive detector (LynxEye EX). Samples were deposited on a Si zero-background holder and measured using Cu Kα X-ray radiation (λ = 1.5406 Å) across a 2θ range of 10 - 100°, at an increment of 0.02 and dwell time per increment of 0.2 s. The data were simulated as fixed slits using DIFFRAC.EVA. The phase was fitted with EXPO2014[36] using the LeBail method with Pearson peak fitting.[37] The average crystallite size was estimated using the Scherrer equation.

N₂ Adsorption: N_2 adsorption measurements were kindly performed by Dr David Madden and Dr Ceren Çamur using MicroActive for TriStar II at 77 K. BET analysis was performed on the resulting isotherms to estimate the internal surface area of the titania particles. The pore size distributions were estimated from density functional theory, using a cylindrical pore Tarazona model.

Dynamic Light Scattering (DLS): Dynamic Light Scattering measurements were performed using a Malvern Instruments Zetasizer. The instrument is equipped with a He-NE laser (633 nm). The scattering intensity was detected at a backscattering angle of 173° with the choice of appropriate measuring distance and attenuator being automatically selected by the software. Samples were dispersed in triple-filtered Millipore water at concentrations of less than 1 mg mL^{-1}. Results were obtained from an average of three runs, each running being ∼14-20 measurements. The z-average value (hydrodynamic diameter, D_H) was obtained through the software, using the Stokes-Einstein equation (Eq. 6.1)

$$D_H = \frac{k_B T}{6\pi\eta D}$$
(Eq. 6.1)

where k_B is the Boltzmann constant, T is the solution temperature, η is the solution viscosity and D is the diffusion coefficient. The diffusion coefficient and polydispersity index are obtained *via* Cumulants analysis of the correlation function.

Transmission Electron Microscopy (TEM): TEM measurements were performed on samples dispersed on copper mesh grids and imaged using an FEI Technai F20 transmission electron microscope, with an accelarating voltage of 200 kV, single tilt holder and OneView Camera. TEM measurements were kindly performed by Professor Caterina Ducati and May Ching Lai.

UV-Vis Absorption Spectroscopy: UV-Vis absorption spectra were performed on either a Perkin Elmer Lambda 35 spectrometer or an Edinburgh Instruments DS5 dual beam spectrophotometer. Measurements were carried out in quartz cells with a 10 mm path length. All samples were prepared in deionised water.

Diffuse-Reflectance UV-Vis (DRUV): Diffuse-Reflectance UV-Vis measurements were performed on a Perkin Elmer Lambda 35 spectrometer. Powder samples were mounted on a home-made holder with a quartz front with measurements performed over the range 200-2000 nm. The reflectance values, R, were used to determine the Kubelk-Munk function, k/s, (Eq. 6.2)

$$\frac{k}{s} = \frac{(1-R)^2}{2R}$$ (Eq. 6.2)

The band-gap for the indirect transition was then determined from a Tauc plot,[38,39] by plotting $((k/s)*hv)^2$ against hv and taking the x-intercept or background (if present) as the band-gap value.

Photocatalytic Measurements: A MRL-58 multiple ray lamp with a 365 nm bulb (8 W) was used to provide UV light. The lamp illuminated a quartz beaker containing an aqueous methyl orange solution (20 ppm, 0.061 mM) with 0.5 mg mL^{-1} of AzoPS-templated titania. The titania-dye solution was stirred for 1 h in the dark to establish an absorption-desorption equilibrium. After 1 h, the UV lamp was switched on and the titania-dye solution was irradiated for >2 h, with aliquots being withdrawn every 15-20 min. These aliquots were centrifuged to separate the titania and the UV-Vis absorption spectrum of the supernatant measured to determine changes to the dye concentration.
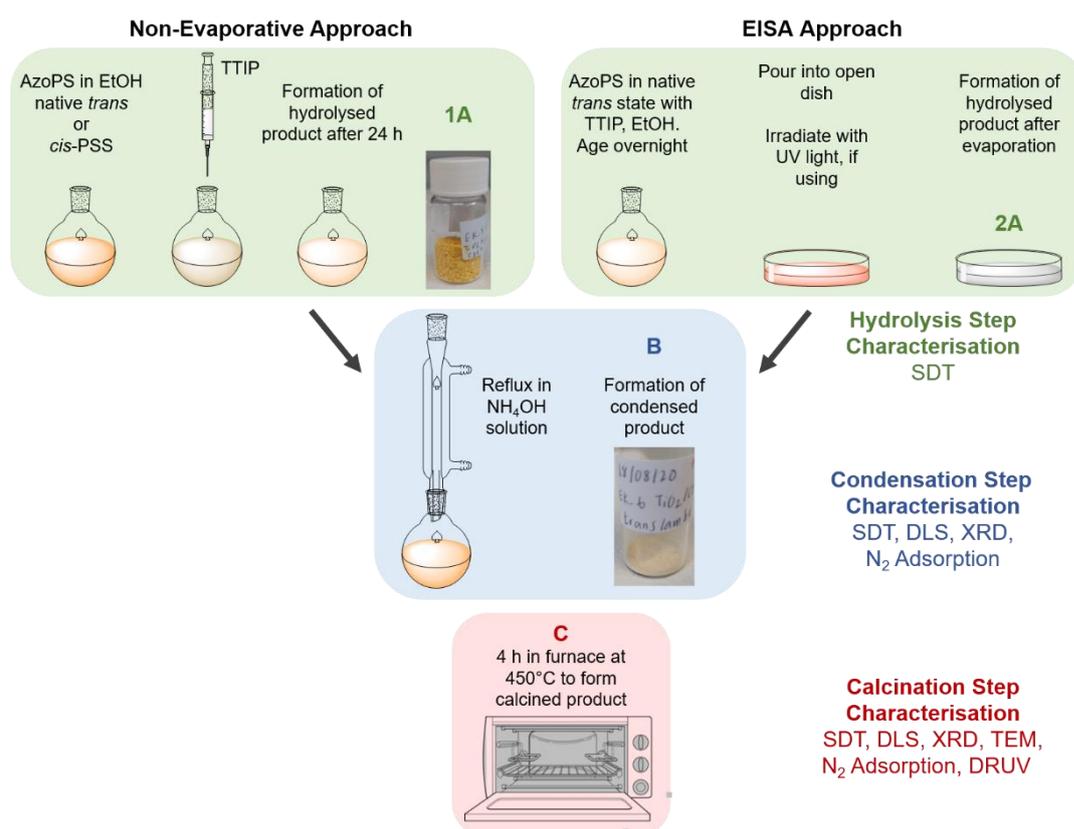
Scheme 6.1. Experimental approach taken to synthesise templated titania using AzoPS. Either a non-evaporative or EISA synthetic method was used. In both cases, the AzoPS was used in both the native *trans*-state and the *cis*-PSS, following UV irradiation The initial hydrolysed product (green box) was characterised using SDT. The condensed product was formed following an ammonia treatment (blue box) and was characterised using SDT, DLS, XRD and N$_2$ Adsorption. The final product (red box) was obtained after calcination to remove all traces of AzoPS and form crystalline titania. The final product was characterised using SDT, DLS, XRD, TEM, N$_2$ Adsorption, DR-UV and used for photocatalytic experiments.

6.3 Results

6.3.1 AzoPS-Templated Titania using the Non-Evaporative Sol-Gel Method

Titania was initially synthesised using the non-evaporative sol-gel method based upon a method reported by the Caruso group,[5,8,17,34] consisting of a static hydrolysis step in an aqueous ethanolic solution, followed by an overnight ammonia reflux to fully condense the titania network and improve thermal stability (Scheme 6.1). The samples are named as follows: TiO_2-"AzoPS", with UV at the end of the sample name if the AzoPS was irradiated with UV light and converted to the *cis*-PSS prior to the initial hydrolysis step, *e.g.*, TiO2-$C_8C_4E_4$-UV is the titania synthesised with the AzoPS $C_8AzoOC_4E_4$ in the *cis*-PSS, while TiO2- $C_8C_4E_4$ is the titania synthesised with the AzoPS $C_8AzoOC_4E_4$ in the native *trans* state. The characterisation, which focused on probing the sample size, crystallinity and porosity, will be reported below for all templated titania samples, before trends and observations are discussed in more detail. Finally, the possibility of using these titania as photocatalysts will be reported and the photocatalytic performance analysed in terms of the synthesis and characterisation.

6.3.1.1 Size and Morphology

The hydrodynamic diameters of the calcined titania particles were determined using DLS and ranged from 314.1 ± 4.1 to 414.4 ± 4.1 nm. The particles were monodisperse, with polydispersity indices from 0.07 to 0.34. (Table 6.1). There is no significant trend between the size of the titania particles and the surfactant or irradiation conditions used to create them. The hydrodynamic diameters before calcination were also measured and found to be slightly larger, in the region of 400-520 nm. Particle shrinkage as a result of calcination is expected and will likely have consequences for the pore size and BET area of the final particles. TEM was used to image the particles and gain insight about the size, shape and morphology. Representative TEM images for TiO_2-$C_8C_4E_4$ and TiO_2-$C_8C_4E_4$-UV are given in Figures 6.1 and 6.2.

Table 6.1. Hydrodynamic diameters (D_H) and polydispersity indices (PDI) of final titania particles synthesised using AzoPS with the Non-Evaporative Sol-Gel method. The error associated with each value is given in parentheses.

Sample	D_H (nm)	PDI
TiO_2-$C_8C_4E_4$	314.1 (4.1)	0.14 (0.08)
TiO_2-$C_8C_4E_4$-UV	414.4 (4.1)	0.13 (0.03)
TiO_2-$C_6C_4E_4$	397.6 (1.9)	0.11 (0.06)
TiO_2-$C_6C_4E_4$-UV	334.0 (8.3)	0.34 (0.03)
TiO_2-$C_8C_8E_4$	341.2 (5.1)	0.07 (0.04)
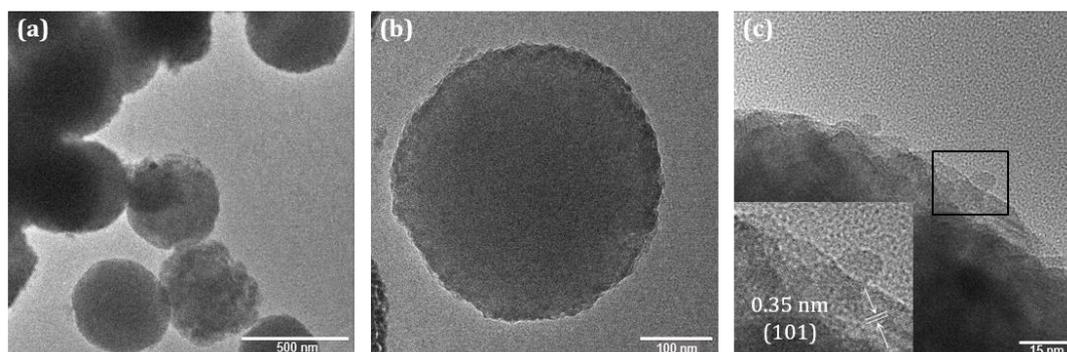
Figure 6.1. TEM images of TiO$_2$-C$_8$C$_4$E$_4$ after calcination show spherical particles roughly 460 nm in diameter. The particles are comprised of smaller crystalline domains of ~10 nm. The (101) planes of the anatase phase can be observed in the crystalline domains.

It can be seen in Figure 6.1 that TiO$_2$-C$_8$C$_4$E$_4$ forms spherical nanoparticles, approximately 460 nm in diameter. The particles appear monodisperse with relatively smooth surfaces. Further corroborating TEM images are available in the Appendix (Figure A.6.3). There are visible crystal domains which appear to be approximately 10 nm in width, a parameter which will be later confirmed by applying the Scherrer Equation to the X-ray diffraction peaks of the sample. It is expected that the porosity will arise from the spaces between the crystallite domains, with the pore sizes therefore likely to be <10 nm. Further information about the crystal can be found from the spacing of the lattice fringes visible within these crystal domains. Through taking a Fourier Transform of the TEM image, a value of 0.35 nm was found for the lattice spacings. This value was confirmed by measuring the variation in grey-scale values with perpendicular distance across the fringes in the image itself. This spacing of 0.35 nm corresponds to the (101) reflection of the anatase phase, expected to occur at 25.5° in the diffraction pattern.

For titania synthesised using the AzoPS in the *cis*-PSS (Figure 6.2), a wider variety of morphologies can be observed. For TiO$_2$-C$_8$C$_4$E$_4$-UV, most of the titania still forms spherical particles, but this time they appear larger (~650 nm). The crystal domains in this case are elongated, appearing more rectangular than square along their sides, along with having larger dimensions of ~12 nm (Figure 6.2d). The (101) reflections of the anatase phase can also be observed in these crystal domains. Along with the spherical particles, more unusual morphologies can be observed, including flower-like crystals (Figure 6.2c, 6.2f) and long, fibrous structures (Figure 6.2b and 6.2e). The common trait amongst these morphologies is their aspect ratio, in each case there is a significant deviation between length and width of the structures. Further TEM images of the different morphologies of TiO$_2$-C$_8$C$_4$E$_4$-UV are available in the Appendix (Figure A.6.4).
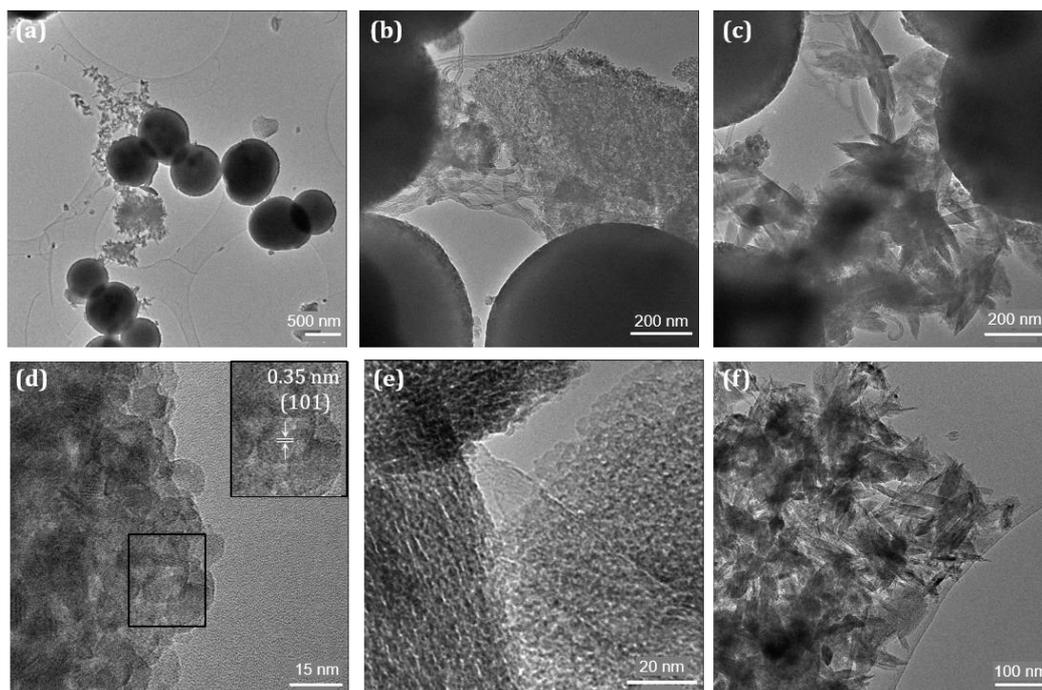
Figure 6.2. TEM images of TiO$_2$-C$_8$C$_4$E$_4$-UV after calcination show a variety of morphologies including (a, b, c) spherical particles (~650 nm), long ribbons (b, e) and flower-like crystals (a, c, f). The spherical particles have crystalline domains of ~12 nm. The (101) planes of the anatase phase can be observed in these domains.

6.3.1.2 Crystal Properties

The titania particles were measured using simultaneous differential scanning calorimetry and thermogravimetric analysis after the hydrolysis and condensation steps, to estimate the extent of AzoPS incorporation and determine the optimum temperature for calcination. Figure 6.3a shows the TGA data, measured after condensation but before calcination, for all five TiO$_2$ samples templated with AzoPS, as well as a control sample templated with the non-photoactive surfactant Brij L4. The final weight percent of the pre-calcination particles varies from 64–78 wt%. The titania synthesised using C$_6$AzoOC$_4$E$_4$ (TiO$_2$-C$_6$C$_4$E$_4$, TiO$_2$C$_6$C$_4$E$_4$-UV) show higher final values (78, 71 wt%) than those made using the other two AzoPS. A higher final wt% implies that less surfactant was incorporated into the titania particle compared to a lower final wt%; it is suspected these values give an insight into the porosity and surface area of the titania particles, as these are key parameters controlled by the template. Generally, the titania synthesised with AzoPS have a lower final wt% than those synthesised with Brij L4; it is hoped this will translate into an improved surface area and porosity. Figure 3b shows the TGA data for TiO$_2$-C$_8$C$_4$E$_4$ after the hydrolysis, condensation and calcination steps. The weight loss step <100 °C corresponds to adsorbed solvent, while weight loss at higher temperatures corresponds to the decomposition of the template. These data confirm that no AzoPS remains in the titania after the calcination step.
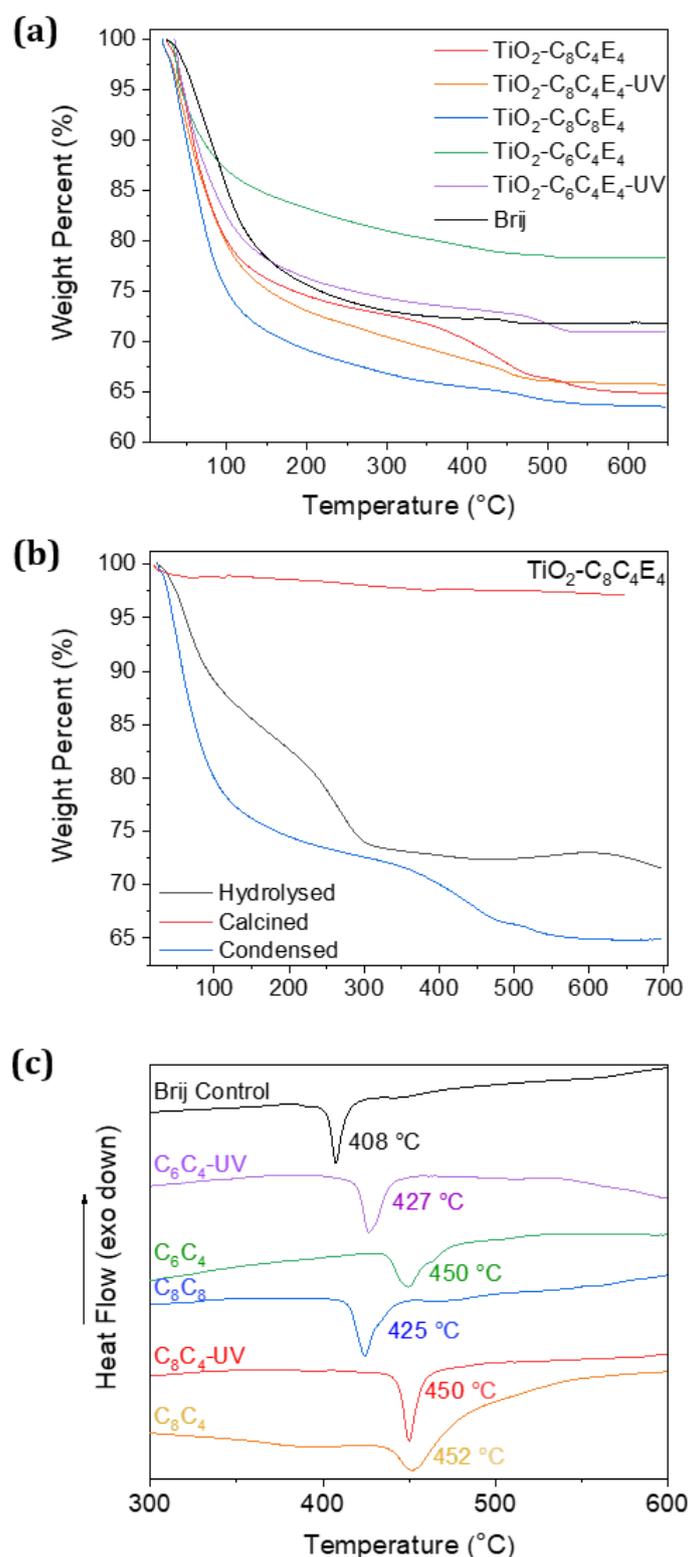
Figure 6.3. Characterisation of the thermal properties of titania prepared using the Non-Evaporative Sol-Gel Method. Weight percent as a function of temperature for (a) all pre-calcination titania templated with AzoPS and Brij L4 and (b) TiO2 templated with C8C4E4 under ambient light after hydrolysis (black), condensation (blue) and calcination (red) steps. (c) Heat flow as a function of temperature for all pre-calcination titania templated with AzoPS and Brij L4. The exothermic peaks correspond to the crystallisation temperature for the amorphous-anatase transition. Data have been offset and rescaled for ease of viewing.

Figure 6.3c shows the heat flow as function of temperature for all five TiO_2 samples, plus the Brij L4 control. These data have been offset and rescaled for ease of viewing the crystallisation transitions; the full individual graphs are available in Appendix (Figure A.6.5). The temperature at which crystallisation occurs varies as either ~425 or 450 °C between the different AzoPS, with all titania-templated AzoPS having higher crystallisation temperature (T_c) than the titania templated with Brij L4.

The crystallinity of the titania product was probed before and after calcination using powder X-ray diffraction. The crystal phase is vital for photocatalytic activity, with anatase phase titania generally found to result in a higher photocatalytic activity than rutile or brookite titania.[40,41] It is important that crystalline titania is not formed until after the surfactant has completed its function as a template, otherwise it is likely the surfactant will be degraded upon UV irradiation of the crystalline titania, due to the photocatalytic effect. Formation of crystalline titania too early in the synthetic process limits the potential for UV light to be applied *in-situ.* In later sections, it will be demonstrated that in some cases crystalline titania can be formed prior to the calcination step. Figure 6.4a and 6.4b show the XRD diffractograms before and after calcination at 450 °C, respectively, with Figure 6.4a showing amorphous titania, with no diffraction peaks observed. Figure 6.4b displays the diffractograms for all five samples after calcination, with clearly resolved diffraction peaks consistent with the anatase phase observed for all. Comparison with the Crystallographic Information File (CIF) for anatase titania[42] indicates that the titania after calcination is phase pure, forming exclusively the anatase phase. This was confirmed by fitting the powder diffractograms using the LeBail method with Pearson peak fitting to a tetragonal model.[36,37] The unit cell parameters are summarised in Table 6.2 for all AzoPS used and a full peak list and fitted diffractograms can be found in the Appendix (Table A.6.1, Figure A.6.6).
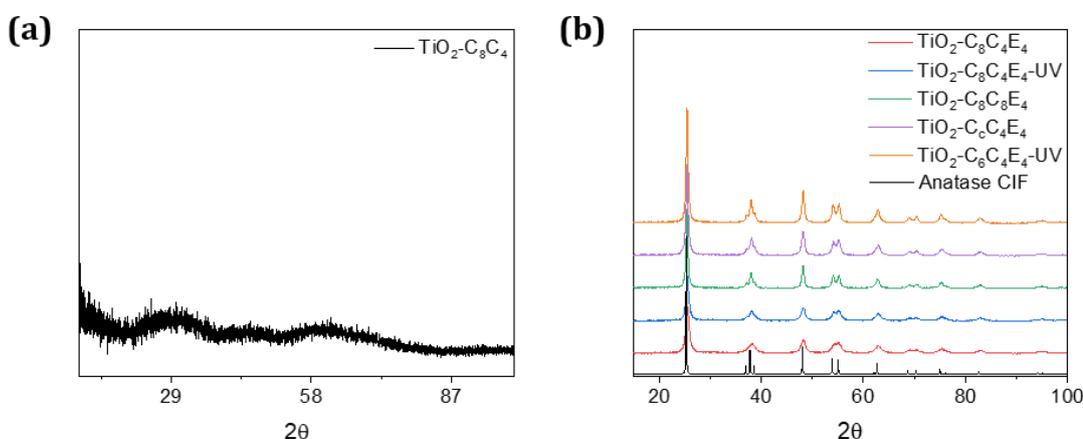
Figure 6.4: X-ray diffractograms of (a) TiO_2-$C_8C_4E_4$ before calcination showing amorphous titania and (b) TiO_2-$C_8C_4E_4$ (red), TiO_2-$C_8C_4E_4$-UV (blue), TiO_2-$C_8C_8E_4$ (green), TiO_2-$C_6C_4E_4$ (purple) and TiO_2-$C_6C_4E_4$-UV (orange) after calcination at 450 °C for 2 hours. The crystallographic information framework file for anatase titania is shown in black.[42]

Table 6.2: Structural parameters obtained from XRD data for TiO_2 samples synthesised with AzoPS. The crystallite size is the value estimated through the Scherrer Equation, a and c are the lattice constants for the tetragonal model.

Sample	a (Å)	c (Å)	Crystallite size (nm)	Relative Crystallinity
TiO_2-$C_8C_4E_4$	3.77	9.44	9.4	0.56
TiO_2-$C_8C_4E_4$-UV	3.78	9.47	11.2	0.66
TiO_2-$C_6C_4E_4$	3.79	9.49	14.6	0.87
TiO_2-$C_6C_4E_4$-UV	3.79	9.52	15.8	0.94
TiO_2-$C_8C_8E_4$	3.79	9.50	16.8	1.00

The c cell parameter is slightly larger for each UV synthesis, compared to its non-UV counterpart, for example 9.44 Å for Tio2-$C_8C_4E_4$ compared to 9.47 Å for TiO_2-$C_8C_4E_4$-UV. It is thought this may link back to the observations of increased length along one axis observed in the TEM images, where the sample synthesised with UV light generally had crystallite domains with a higher aspect ratio. The average crystallite size, τ, was estimated from the full-width half-maximum of the (101) peak at 25.5° using the Scherrer equation:

$$\tau = \frac{K\lambda}{\beta cos\theta} \hspace{3cm} \text{(Eq. 6.2)}$$

where K is the dimensionless size factor, taken to be 0.94,[43] λ is the X-ray wavelength in Å (λ = 1.5406 Å) β is the full-width half-maximum and θ the Bragg angle of the peak in question, with all angles in radians.

For all titania samples synthesised under ambient light (*trans*-AzoPS), an increase in crystallite size was observed from 9.41 nm for TiO_2-$C_8C_4E_4$ to 16.75 nm for TiO_2-$C_8C_8E_4$. It is possible that the increase in crystal size correlates with the amorphous-crystalline phase transition temperature. On the DSC curve (Figure 6.3c), this transition occurs at a higher temperature for $C_8AzoOC_4E_4$ (452 °C) than for $C_8AzoC_8E_4$ (425 °C). As a result, the calcination temperature of 450 °C is much further above the transition temperature for TiO_2-$C_8C_8E_4$ than for TiO_2-$C_8C_4E_4$. It has been well-established that higher temperature result in larger crystal sizes and a greater degree of crystallinity.[8] However this reasoning does not account for the difference in crystallite size observed between samples synthesised under ambient *vs*. UV light. The samples synthesised without UV light have a crystallite size that is 84 or 92% that of their UV counterparts, with crystallite size increasing from 9.41 to 11.16 nm for TiO_2-$C_8C_4E_4$-UV and from 14.61 to 15.79 nm for TiO_2-$C_6C_4E_4$-UV, respectively. This agrees with the observations of larger and more asymmetric crystal domains in the TEM images, indicating that synthesis with the AzoPS in the *cis*-PSS results in anatase titania with a slightly elongated unit cell and larger crystallite sizes,

compared to synthesis with *trans*-AzoPS. High crystallinity is a key parameter for good photocatalytic activity, as recombination is reduced when the charge-transfer of the electron-hole pairs is promoted.[2,44] It is expected that the samples with higher crystallite sizes are likely to have higher photocatalytic activity.

6.3.1.3 Surface Area and Optical Properties

The pore size distribution and surface areas of the titania particles were measured using N_2 adsorption and analysed using BET theory and density-functional theory (DFT). Figure 6.5 shows the adsorption-desorption isotherms of N_2 at 77 K for the titania samples before (6.5a, 6.5b) and after (6.5c, 6.5d) calcination. Before calcination, a Type 1 isotherm can be observed, characteristic of a microporous materials;[45] the steepness and shape of the isotherm at low P/P_o can give a qualitative understanding of the pore size. For example, the isotherms of TiO_2-$C_8C_8E_4$ and TiO_2-$C_8C_4E_4$-UV are anticipated to have similar BET areas, yet it would be expected that the pores are slightly smaller in TiO_2-$C_8C_8E_4$ owing to the steeper curve at low values of P/P_o. It is anticipated from the 'knee' beginning at ~0.3 P/P_o that these pores will be on the micropore-mesopore boundary of ~2 nm. To determine this more quantitatively, the pore size distributions were estimated from DFT, using a cylindrical pore Tarazona model (Figure 6.5b). It can be observed that most samples show a bimodal distribution, with a sharp peak at <1 nm and a second broader distribution between ~2–3 nm. The exception is TiO_2-$C_6C_4E_4$, which shows a wide distribution from 0.5–4 nm. High surface areas are crucial for efficient photocatalysis, as higher surface areas will allow greater adsorption of organic species to the titania and positively influence the rate of photocatalytic degradation. The surface areas of the titania particles were estimated by applying BET theory to the isotherms. The parameters obtained from these analyses can be found in Table 6.3. All samples show a reasonably high BET area before calcination, with TiO_2-$C_8C_4E_4$ showing the highest value of 462 m^2 g^{-1} and TiO_2-$C_6C_4E_4$ the lowest, with 279 m^2 g^{-1}. As expected from their similar plateau values, TiO_2-$C_8C_4E_4$-UV and TiO_2-$C_8C_8E_4$ show very similar values, of 3,700 and 409 m^2 g^{-1}, respectively. All individual graphs are available in the Appendix (A.6.7)

The N_2 adsorption experiments were repeated after calcination of all samples at 450 °C for 2 hours. The N_2 adsorption-desorption isotherms (Figure 6.5c) now show Type IV isotherms, with hysteresis loops characteristic of mesopores (2-50 nm).[17,45] These hysteresis loops arise due to capillary condensation; the pores are now of an intermediate size such that vapour condensation can occur below the saturation vapour pressure, due to the increased intermolecular interactions within the confines of the capillary. The less steep increase in adsorption at low pressures compared to the pre-calcination isotherms

also indicates larger pores are formed after calcination. The plateaus also occur at lower values of N_2 adsorbed, implying lower surface areas in this case. A loss of surface area, with concurrent pore collapse, is to be expected upon calcination, and highlights one of the key issues in the field – maintaining a balance between good porosity and favourable crystalline properties for efficient photocatalysis. The highest BET value is now 115 m^2 g^{-1} for TiO_2-$C_8C_8E_4$, a decrease of 72%, followed by similar values for $C_6C_4E_4$ and TiO_2-$C_8C_4E_4$, of 66 and 59 m^2 g^{-1}, respectively, representing decreases of 76 and 87%. The BET area for TiO_2-$C_8C_4E_4$-UV dropped significantly, by 90% to 36 m^2 g^{-1}. TiO_2-$C_6C_4E_4$ had the lowest BET area of all, with a value of 28 m^2 g^{-1} determined after calcination. The pore size distribution after calcination has shifted to large pore widths, with most samples having pores ranging from 2-10 nm. TiO_2-$C_8C_8E_4$ has noticeably larger pores than the other samples, with pores in the 20-40 nm range. This could be the reason for its high BET area. Other attempts to synthesise titania using this surfactant-assisted non-evaporative method report values of ~89 – 108 m^2 g^{-1} for BET area,[17,34] indicating that the BET areas in this case are reasonable.
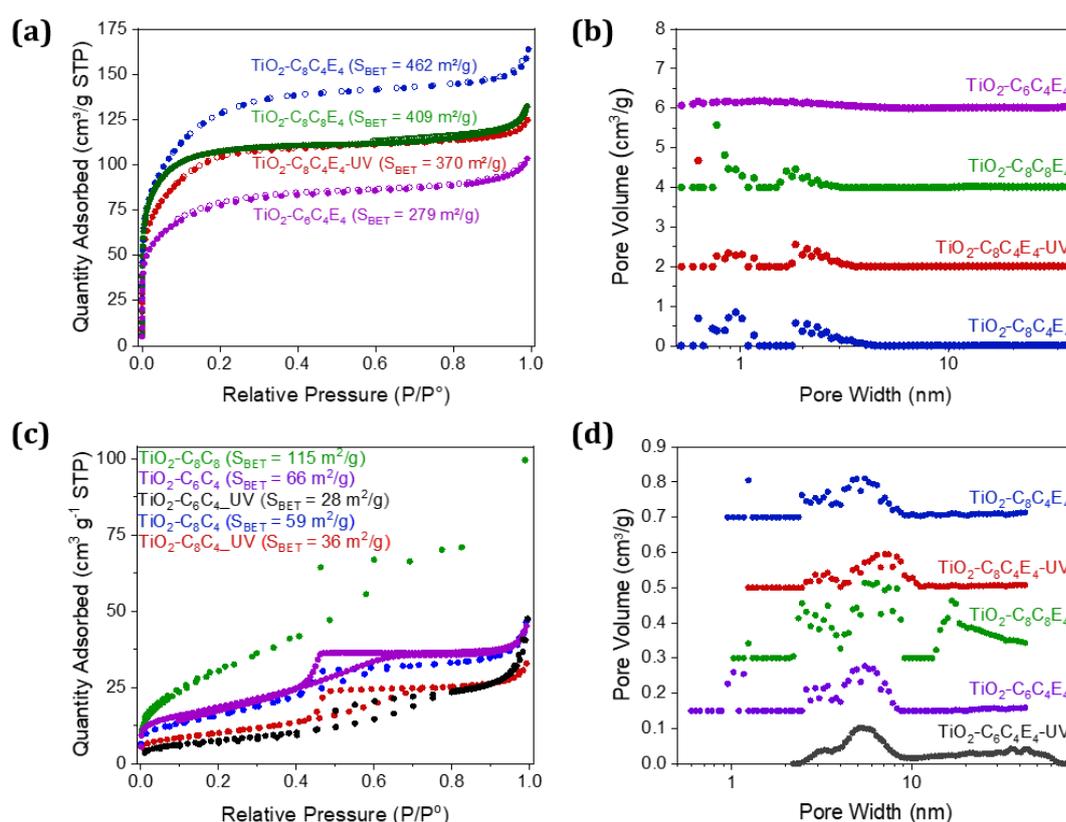
Figure 6.5. The BET area and pore-size distribution were determined through N_2 adsorption measurements. N_2 adsorption isotherms (a, c) and pore size distributions (b, c) for all five titania samples, before (a, b) and after (c, d) calcination. (b) has been offset by a factor of 2. (d) has been offset by a factor of 0.5.

Table 6.3. BET area and pore size distributions extracted from N_2 adsorption isotherms before and after calcination.

Sample	Before Calcination		After Calcination	
	BET area ($m^2 g^{-1}$)	PSD (nm)	BET area ($m^2 g^{-1}$)	PSD (nm)
TiO_2_$C_8C_4E_4$	462	0.9, 2-4	59	2-8
TiO_2-C_8C_4-UV	370	0.6, 2-3	36	3-10
TiO_2-$C_6C_4E_4$	279	0.5-4	66	2-8
TiO_2-$C_6C_4E_4$-UV	-	-	28	2-9, 20-60
TiO_2_C_8C_8	409	0.8-3	115	2-9, 11-13

The optical properties of the titania nanoparticles TiO_2-$C_8C_4E_4$ and TiO_2-$C_8C_4E_4$-UV were probed using diffuse UV-Vis reflectance spectroscopy (Figure 6.6a) to determine the band-gaps of the indirect transition for the anatase phase using a Tauc plot. (Figure 6.6b). The values were extrapolated from the intersection of the straight-line portion of $(F(R)h\nu)^2$ *vs* $h\nu$, where *F(R)* is the Kubelka-Munk function, with either the x-axis or the background. The particles showed strong absorption in the UV region, with a value for the indirect bandgap of 3.35 eV, or 370 nm, obtained for both samples. The bandgap for commercial anatase phase titania is 3.2 eV[2,46] with reports of anatase phase titania in the literature ranging from 3-3.4 eV.[6,47] An increase in the bandgap compared to commercial titania is generally attributed to quantum size effects which occur when the semi-conductor domains are less than ~10 nm, as the confinement is on the same order as the de Broglie wavelength of the charge carriers.[3]
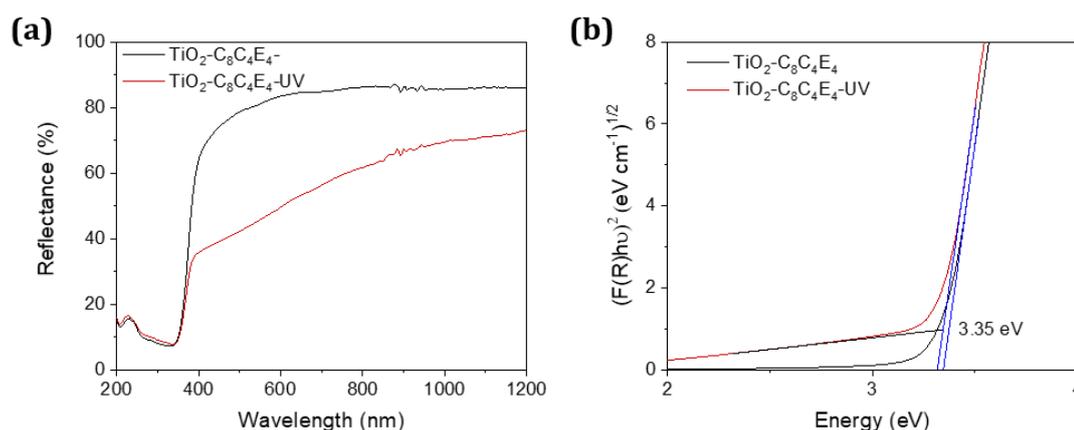
Figure 6.6. (a) Diffuse Reflectance UV-Vis spectra of TiO_2-$C_8C_4E_4$ (black) and TiO_2-$C_8C_4E_4$-UV (red) and their corresponding Tauc plots (b) showing the band-gap values for the indirect band-gap transition. The band gap has been taken from the intercept of the vertical decay with either the x-axis (TiO_2) or the background (TiO_2-UV). In both cases, the intercept is 3.35 eV.

From the characterisation techniques used so far, some trends and observations can be noted. These will be briefly summarised before the photocatalytic ability of the titania spheres is investigated in the following section. It was observed from SDT measurements that samples with the lowest final wt% after heating to 650 °C had the most N_2 adsorption and highest BET areas (*e.g.*, 64 wt% and BET area of 115 m^2 g^{-1} for TiO_2-$C_8C_8E_4$) and *vice versa* in that the samples with the highest final wt% had lower BET areas (71 wt% TiO_2 and BET area of 28 m^2 g^{-1} for TiO_2-$C_6C_4E_4$-UV). This indicates TGA could be used as a preliminary screening step as part of the procedure for determining surface area. As N_2 adsorption experiments are time-consuming and expensive, it is useful to have a means of gauging an approximate idea of which samples are worth pursuing with more involved techniques. It is also noted that the crystallisation peak for amorphous to anatase occurs at either 425 or 450 °C for the titania templated with the AzoPS, with the titania templated using Brij L4 having a transition at a lower temperature again (408 °C). The significance of this is as of yet unknown but considered worth remarking upon in case it is useful in determining mechanistic differences or trends in thermal stability in the future.

From the N_2 adsorption isotherms of the titania formed using the AzoPS in the native *trans*-state, it appears that the titania with the largest crystallite domains experienced the least pore collapse upon calcination and crystallisation. For example, TiO_2-$C_8C_8E_4$ has a crystallite size of 16.8 nm and experienced a reduction in BET area upon calcination of 72%, from 409 to 115 m^2 g^{-1}, while TiO_2-$C_6C_4E_4$ had a crystallite size of 14.6 nm and a reduction in BET area of 76%, from 280 to 66 m^2 g^{-1}; finally TiO_2-$C_8C_4E_4$ had the smallest crystallite size, of 9.4 nm, and experienced the greatest reduction in BET area of 87%, from 462 to 59 m^2 g^{-1}. This is somewhat counterintuitive as it seems more logical to expect that the formation of large crystallite domains would be at the expense of the porosity or surface area. The trend observed here implies that the factors required to create high crystallinity are the same as, or at least strongly linked to, those responsible for thermal stability and retention of porosity. This behaviour could arise from the self-assembly behaviour of the surfactant, as it has already been shown that $C_8AzoOC_8E_4$ and $C_6AzoOC_4E_4$ have similar self-assembly behaviour to each other, while $C_8AzoOC_4E_4$ does not.

There is also a change in crystallite size and dimensions depending on whether the AzoPS was used in the *cis*-PSS following irradiation with UV light, or in the native *trans*-state. The syntheses that used the AzoPS in the *cis*-PSS had larger crystallite sizes, by about 2 nm, with larger and more asymmetric crystal domains visible in the TEM images (Figure 6.2). However, the trend between larger crystallite size and retention of

BET area upon calcination was not observed here. The titania templated using the AzoPS in the *cis*-PSS show the lowest BET areas, of 36 m^2 g^{-1} for TiO$_2$-C$_8$C$_4$-E$_4$-UV and 28 m^2 g^{-1} for TiO$_2$-C$_6$C$_4$E$_4$-UV.   Here, it becomes important to take into account that the titania synthesised with the *cis*-PSS had multiple morphologies and did not form only spherical particles, as was observed for the titania synthesised with the AzoPS in the native *trans*-state. A wide variety of morphologies were observed; as well as spheres, there are flower-like crystals and long fibrils. It is likely that some of these morphologies, particularly the flower-like crystals, may be non-porous and not contribute towards the BET area.

6.3.1.4 Photocatalytic Activity

The photocatalytic activity of the titania particles was investigated by monitoring the degradation of an organic dye, methyl orange. The particles were soaked in an aqueous methyl orange solution (20 ppm) for 1 hour in the dark to allow for an adsorption-desorption equilibrium. The solution was then irradiated with UV light, with continuous stirring to promote good aeration. The dye concentration was monitored every 15-20 minutes using UV-Vis absorption spectroscopy, starting from before UV irradiation began. Aliquots were removed from the reaction vessel, centrifuged to remove any particles and the absorption spectrum of the supernatant measured to determine the concentration of methyl orange. The degradation followed *pseudo*-first order kinetics, with a rate equation of $\ln(C_0/C_t) = -kt$, where C_0 is the initial dye concentration, C_t is the concentration after time, t, and k is the first-order rate constant (Figure 6.7). All absorption spectra can be found in the Appendix (A.6.8) with the associated rate constants available in Table 4.
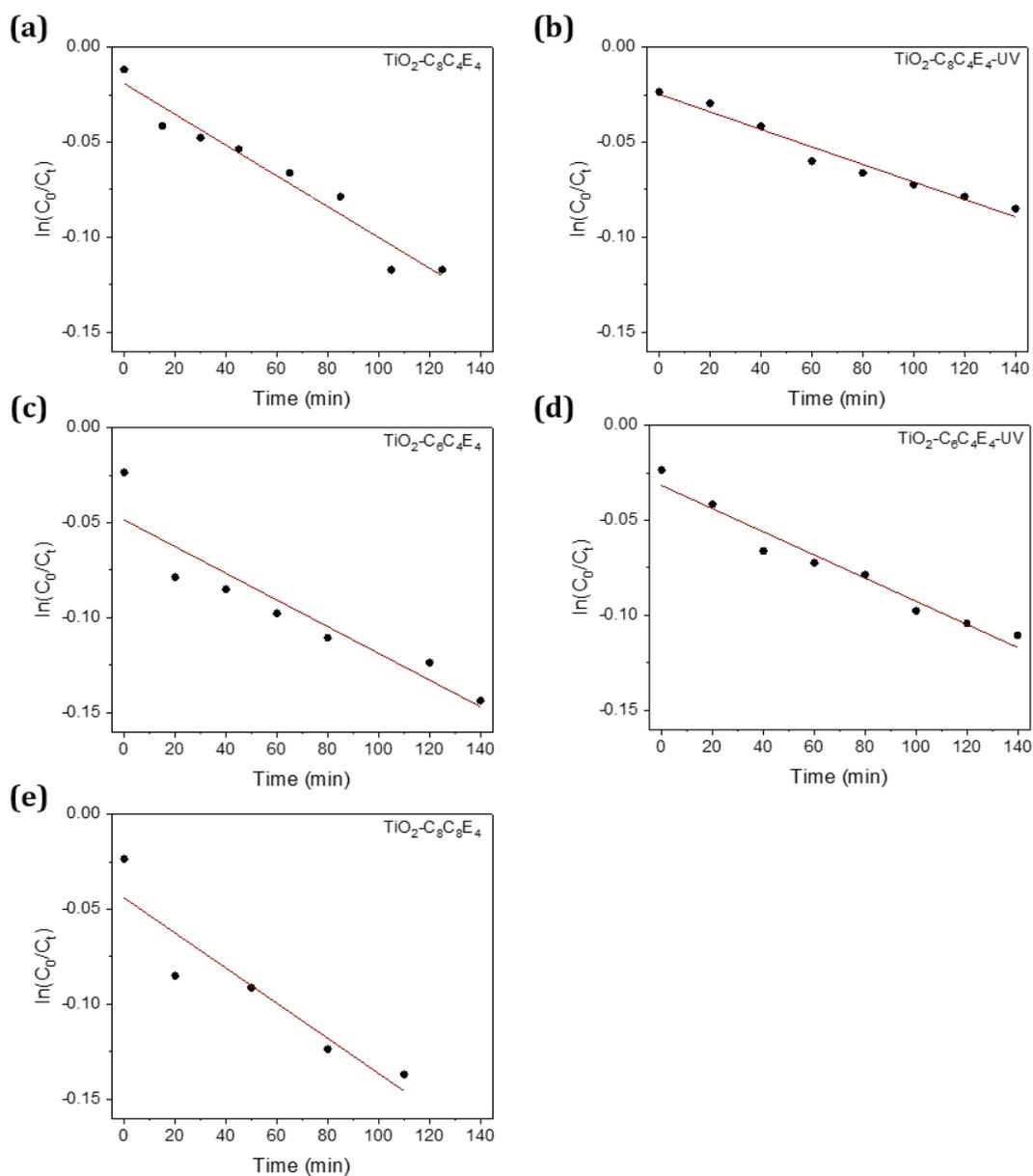
Figure 6.7. The degradation of methyl orange by the porous anatase-phase titania templated using the AzoPS. (a) *trans*-$C_8AzoOC_4E_4$ (b) *cis*-PSS $C_8AzoOC_4E_4$ (c) *trans*-$C_6AzoOC_4E_4$ (d) *cis*-PSS $C_6AzoOC_4E_4$ (e) *trans*-$C_8AzoOC_8E_4$ followed *pseudo*-first order kinetics.

Table 6.4. *Pseudo*-first order rate constant, k, and key physical properties (crystallite size, BET area) for all five titania samples synthesised with AzoPS.

Sample	k (s^{-1})	Crystallite Size (nm)	BET area (m^2 g^{-1})
TiO$_2$-C$_8$C$_4$E$_4$	0.81 $\times$ 10^{-3}	9.4	59
TiO$_2$-C$_8$C$_4$E$_4$-UV	0.46 $\times$ 10^{-3}	11.2	36
TiO$_2$-C$_6$C$_4$E$_4$	0.72 $\times$ 10^{-3}	14.6	66
TiO$_2$-C$_6$C$_4$E$_4$-UV	0.60 $\times$ 10^{-3}	15.8	28
TiO$_2$-C$_8$C$_8$E$_4$	0.95 $\times$ 10^{-3}	16.8	115

The observations for the titania synthesised using the AzoPS in the native *trans*-state will be discussed first. The highest rate constant of 0.95 $\times$ 10^{-3} s^{-1} was found for TiO$_2$-C$_8$C$_8$E$_4$, with a decrease to 0.81 $\times$ 10^{-3} and 0.72 $\times$ 10^{-3} s^{-1} observed to TiO$_2$-C$_8$C$_4$E$_4$ and TiO$_2$-C$_6$C$_4$E$_4$, respectively. It is unsurprising that the top performing titania samples had both the highest crystallite size and the highest BET area, given that these are the key parameters required for effective photocatalytic performance. For TiO$_2$-C$_8$C$_4$E$_4$, it is odd that it had a slightly higher rate constant compared to TiO$_2$-C$_6$C$_4$E$_4$, given that it had a smaller crystallite size, with the BET areas being very similar. The pore-size distribution of TiO$_2$-C$_6$C$_4$E$_4$ is unusual compared to the other samples before calcination, it has a very low broad distribution. However, after calcination the pore-size distribution is very similar to TiO$_2$-C$_8$C$_4$E$_4$.

In all cases, the rate constant for the titania synthesised using the AzoPS in the *cis*-PSS is lower than that synthesised with using its native *trans*-state counterpart. For example, the rate constant decreases from 0.81 $\times$ 10^{-3} s^{-1} to 0.46 $\times$ 10^{-3} s^{-1} for TiO$_2$-C$_8$C$_4$E$_4$ and TiO$_2$-C$_8$C$_4$E$_4$-UV, respectively and from 0.72 $\times$10^{-3} s^{-1} to 0.60 $\times$ 10^{-3} s^{-1} for TiO$_2$-C$_6$C$_4$E$_4$ and TiO$_2$-C$_6$C$_4$E$_4$-UV, respectively. This is despite the syntheses using the *cis*-PSS having larger anatase crystallite sizes than their native *trans*-state counterparts, emphasising the key role that high BET areas has for good photocatalysis. In the case of titania made using the *cis*-PSS, BET areas are low, likely due to the presence of a variety of morphologies, not just mesoporous spheres.

It is clear that AzoPS can be used to template titania using the Non-Evaporative Sol-Gel Method and can form monodisperse, mesoporous spherical particles. UV irradiation and formation of the *cis*-PSS so far does not seem to improve photocatalytic performance, despite increasing the size of the anatase crystallite domains within the titania. The formation of a variety of morphologies, rather than exclusively spheres, seems to reduce the BET area and hinder the photocatalytic performance. Next, an additional synthesis method will be trialled using an evaporation-induced self-assembly approach.

6.3.2 AzoPS-Templated Titania using the EISA Method

The EISA method was also trialled to synthesise titania using AzoPS as templates. Briefly, TTIP was added to a homogenous solution of ethanol, water and surfactant which was then aged overnight. This solution was poured into an open Petri dish and left to evaporate for 7 days (Scheme 6.1). For the syntheses using the AzoPS in the *cis*-PSS, the Petri dish was irradiated with light for several hours, with a distinctive orange-red colour change taking place. As it was anticipated that some crystallinity may occur before calcination due to the increased alignment the evaporation induces, this method was first trialled using a non-photoresponsive surfactant, Brij L4, as an analogue, to determine at which point it would be possible to irradiate the AzoPS without destroying the surfactant network through undesired photocatalysis.

6.3.2.1 Control Measurements with Brij L4

The XRD data for the titania synthesised using the non-photoresponsive surfactant, Brij L4, and the EISA method indicate that that titania was initially formed crystalline, after the ammonia treatment but before calcination (Figure 6.8a). Both anatase and brookite phase were present, with the most obvious peak corresponding to the brookite phase visible at ~32°. Following calcination at 400 °C for 2 h, the crystallinity of the sample improved, but the presence of two phases persisted. From the SDT analysis, the sample retained >80% wt% titania after heating, which may imply a reduced porosity and surface area compared to the titania that has been examined so far (Figure 6.8b). The DSC is also now more complex than previously observed for the non-evaporative process, with two broad peaks present, centred at 200 and 380 °C. It is thought that these peaks refer to crystallisation of both the brookite and anatase phase, despite some crystalline domains being present before calcination, a conversion from amorphous to crystalline would still occur for any outstanding amorphous domains, as well as growth of the as-formed domains.

Following this initial trial, the EISA method was repeated using one AzoPS, $C_8AzoOC_4E_4$. XRD was performed to investigate if this system would be suitable for UV irradiation – the presence of crystallinity, particularly the anatase phase, would limit the possibility to use UV irradiation for templating, as the photosurfactant template would likely be destroyed or damaged through the photocatalytic ability of the titania. As such, it is not yet known is the EISA approach will be compatible with photosurfactants.

(a) **(b)**
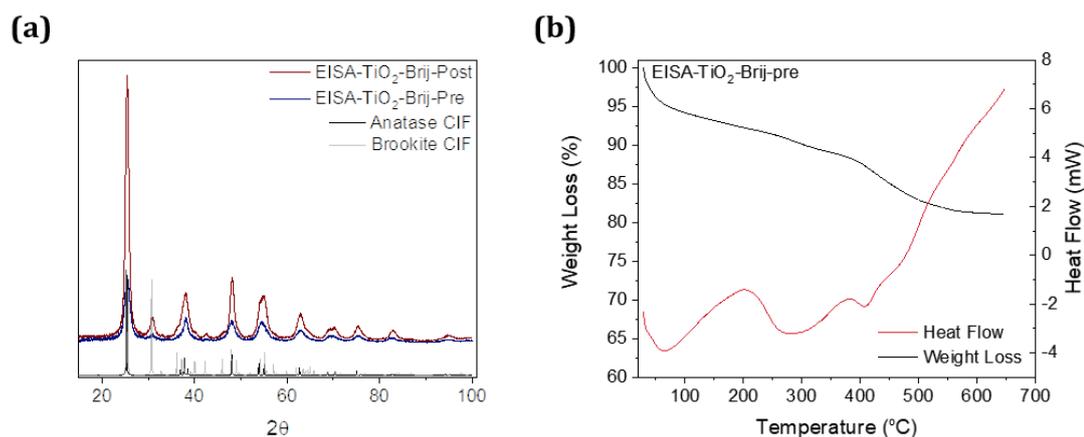
Figure 6.8. Characterisation of the non photoactive surfactant Brij L4, to compare with the AzoPS. (a) SDT data showing weight loss and heat flow as a function of temperature for titania synthesised using Brij L4 and (b) X-ray diffraction patterns. The diffraction patterns are offset by a factor of 2. The CIF files for anatase[42] (black) and brookite (grey)[48] are given for comparison.

6.3.2.2 Morphology and Size

DLS was used to obtain the hydrodynamic diameter of the EISA-titania particles. It was found before condensation that these particles were 873.5 ± 68.3 and 810.1 ± 20.5 nm in diameter for the non-UV and UV syntheses, respectively. After calcination this value shrunk to 825.5 ± 83.5 and 374.5 ± 13.5 nm, respectively with polydispersity indices of 0.46 and 0.28, respectively. These values can also be found in Table 6.5. The particles synthesised using the EISA method in the native *trans*-state have a diameter approximately twice as large as those synthesised using the non-evaporative method (D_H varied between ~300–400 nm). There appears to be a significant amount of shrinkage after calcination for the EISA approach using the AzoPS in the *cis*-PSS, with a reduction in diameter of roughly 50% after calcination at 450 °C for 2 h. Size is a crucial parameter for some applications of titania, particularly those that rely on interaction and scattering of light, such as DSSC, or for those that benefit of easy separation of particles from a liquid, such as water purification and environmental remediation.

Table 6.5. Hydrodynamic diameters (D_H), polydispersity indices (PDI) of titania particles synthesised using AzoPS EISA method, before (grey) and after (white) calcination. The error associated with each value is given in parentheses

Sample	Before Calcination		After Calcination	
	D_H (nm)	PDI	D_H (nm)	PDI
EISA-TiO$_2$- C$_8$C$_4$E$_4$	873.5 (68.3)	0.38 (0.08)	825.5 (83.5)	0.45 (0.05)
EISA-TiO$_2$-C$_8$C$_4$E$_4$-UV	810.1 (20.5)	0.40 (0.05)	374.5 (13.5)	0.28 (0.01)

TEM was used to image the particles and gain insight into their size, shape and morphology. Representative TEM images for EISA-TiO$_2$-C$_8$C$_4$E$_4$ and EISA-TiO$_2$-C$_8$C$_4$E$_4$-UV are given in Figures 6.9 and 6.10. It can be seen in Figure 6.9 that EISA-TiO$_2$-C$_8$C$_4$E$_4$ forms spherical nanoparticles, ranging from 400–600 nm in diameter. The particles are comprised of crystallite domains, with dimensions of roughly 15 nm. Further TEM images are available in the Appendix (Figure A.6.9). Once again, taking a Fourier Transform of the TEM images results in a value of 0.35 nm for the lattice spacings, which corresponds to the (101) reflection of the anatase phase, expected to occur at 25.5° in the diffraction pattern. The images recorded here appear very similar in morphology to those of the titania synthesised using the non-evaporative method. They key difference here appears to be the tendency of the spherical particles to agglomerate on the substrate (Figure 6.9a, Figure A.6.8). This is in agreement with the large PDI of 0.45 reported from DLS measurements.

For titania synthesised using the AzoPS in the *cis*-PSS (Figure 6.10), spherical particles ranging from 350–500 nm can be observed, consistent with the hydrodynamic diameter obtained from DLS measurements. In this case, a single morphology occurs, with no flower-like crystals or long fibrils, as was observed for the non-evaporative method using UV light. In this case, the particles appear very similar to those synthesised under ambient light, with crystallite domains in the region of 15 nm observable. Further images of EISA-TiO$_2$-C$_8$C$_4$E$_4$-UV are available in the Appendix (A.6.10)
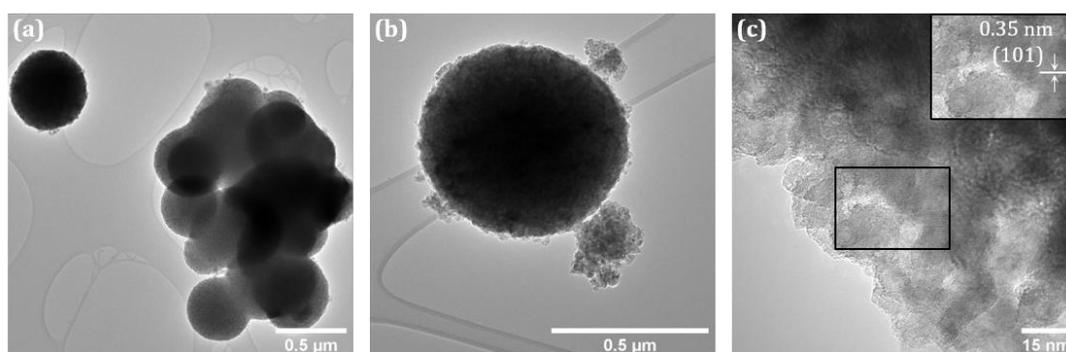
Figure 6.9. TEM images of titania synthesised using *trans*-C$_8$AzoOC$_4$E$_4$ and the EISA method. Spherical particles ranging from 400-600 nm in diameter can be observed. These particles are crystalline, with crystallite domains in the region of 15 nm observable. The lattice fringes corresponding to the (101) can be clearly seen.
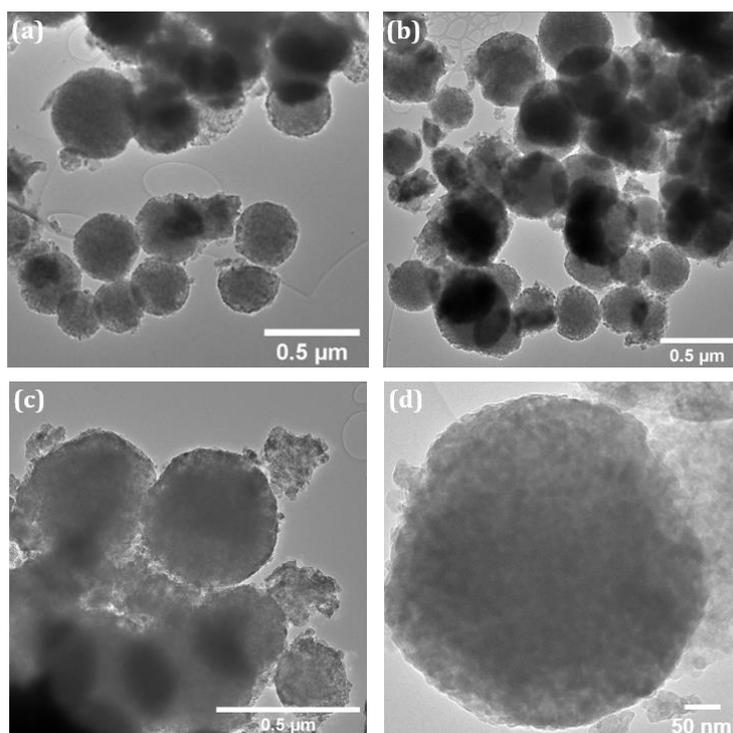
Figure 6.10. TEM images of titania synthesised using $C_8AzoOC_4E_4$ after UV irradiation, using the EISA method. Spherical particles ranging from 400–600 nm in diameter can be observed.

6.3.2.3 Crystal Properties

The temperature required for the formation of the crystalline phase, as well as the quantity of surfactant incorporated to the titania particles, were investigated using SDT. Figure 6.11a shows the heat flow *vs.* temperature for all titania synthesised using $C_8AzoC_4E_4$ before calcination, comparing the non-evaporative and EISA methods. It is clear that the synthesis route does not affect the crystallisation temperature, with all samples having an exothermic crystallisation peak ~450 °C. The extent of surfactant incorporation was estimated from the graph of weight loss *vs.* temperature (Figure 6.11b), with final values of 69 and 73 wt% for the surfactant in the *cis*-PSS and native *trans*-isomer, respectively. These values are slightly higher than those of the counterpart titania obtained using the non-evaporative method (65 and 66 wt%) and may reflect a reduced internal surface area.

The crystallinity and phase of the titania formed using the EISA procedure was investigated using XRD. Unlike titania templated with Brij, before calcination the titania templated using AzoPS was amorphous (Figure 6.12a). The lack of crystallinity before calcination indicates that UV light could be applied *in-situ*, without degrading the surfactant template through unwanted photocatalysis. After calcination in air at 450 °C for 2 h, only anatase phase titania was formed (Figure 6.12b). This represents a significant improvement compared to using Brij L4, a non-photoresponsive analogue, which formed mixed brookite and anatase phases both before and after calcination (Figure 6.8).
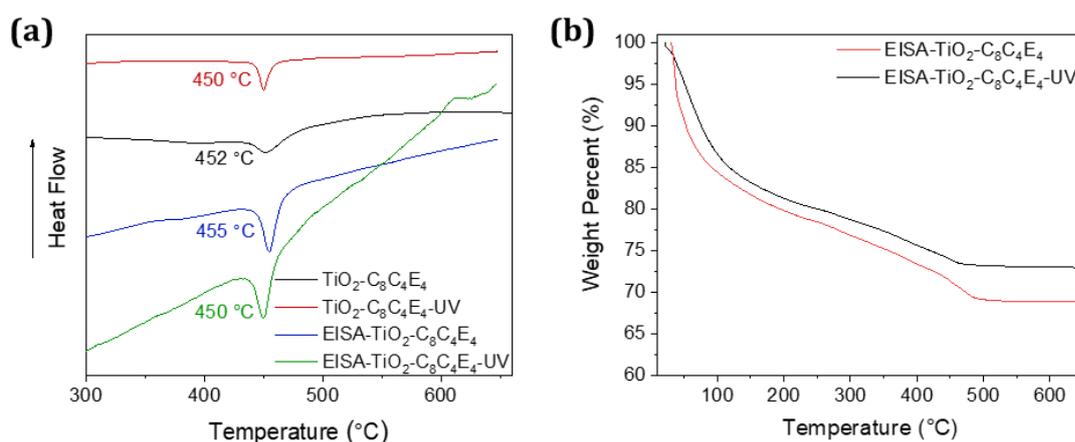
Figure 6.11. Heat flow as a function of temperature for titania synthesised using $C_8AzoOC_4E_4$ and the non-evaporative method in the *cis*-PSS (red) and native *trans* state (black) and using the EISA method in the *cis*-PSS (green) and native *trans* state (blue). Data have been offset and rescaled for ease of viewing peaks. (b) Weight percent as a function of temperature for titania synthesised using the EISA method and $C_8C_4E_4$ as a template in the *trans*-PSS (red) and *cis*-PSS (black).
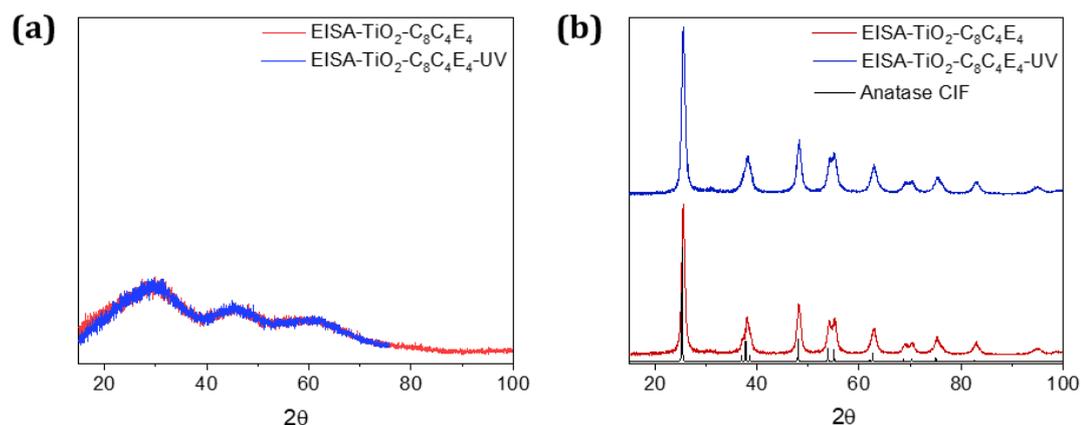
Figure 6.12. X-ray diffractograms of TiO_2 templated with $C_8AzoCO_4E_4$ in the native trans state (red) or the *cis*-PSS (blue) using the EISA method before (a) and after (b) calcination. The Crystallographic Information File for anatase titania is given in black.[42]

The diffraction peaks were fitted to the anatase CIF file[42] using the LeBail method with Pearson peak fitting.[37] The unit cell parameters are summarised in Table 6.6 and a full peak list and fitted diffractograms can be found in the Appendix (Table A.6.2, Figure A.6.11). The Scherrer equation (Equation 6.2) was applied to the (101) diffraction peak at 25.5° to estimate the size of the crystallite domains. These values can also be found in Table 6.6. The crystallite size was estimated to be 12 nm for EISA-TiO_2-$C_8C_4E_4$ and 11.2 nm for EISA-TiO_2-$C_8C_4E_4$-UV. Interestingly, the crystallite size is now slightly larger for the non-UV synthesis than for the UV synthesis, the opposite trend to that observed for the non-evaporative synthesis, although it is worth noting that the values obtained are very similar and are likely within error of each other. For the non-evaporative synthesis, the crystallite size was estimated to be 9.4 nm for the non-UV synthesis, while the value was 11.2 nm for the UV synthesis. These values are in agreement with the size of the crystallite domains observed using TEM.

Table 6.6. Unit cell parameters for anatase titania determined from XRD using a tetragonal model, and average crystallite size, τ, as estimated from the Scherrer Equation.

Sample	a (Å)	c (Å)	τ (nm)
EISA-TiO_2-$C_8C_4E_4$	3.78	9.47	12.0
EISA-TiO_2-$C_8C_4E_4$-UV	3.78	9.45	11.2

6.3.2.4 Surface Area and Optical Properties

The BET area and pore size distribution of the titania samples synthesised using the EISA method were obtained from the N_2 adsorption isotherm (Figure 6.13). The isotherms show Type IV behaviour, with hysteresis loops characteristic of mesoporosity.[17,45] After calcination, BET areas of 43 and 62 $m^2 g^{-1}$ were calculated for the samples templated using the AzoPS in the native *trans*-state and *cis*-PSS, respectively. This is an interesting change from that observed from the non-evaporative synthesis, with the AzoPS in the *cis*-PSS now providing a higher BET area than that in the native *trans*-state. For the non-evaporative approach, BET areas of 59 and 36 $m^2 g^{-1}$ were found for titania templated using the native *trans*-state and *cis*-PSS, respectively. Changing the synthesis approach seems to cause a slight decrease (-27%) in the BET area for titania formed with the native *trans*-state and a large increase (+72%) in the BET area of the titania formed with the *cis*-PSS.

In Figure 6.13b it can be observed that the pore size distribution begins at lower pore widths for EISA-TiO$_2$-C$_8$C$_4$E$_4$-UV than for EISA-TiO$_2$-C$_8$C$_4$E$_4$, with a peak a maximum in pore volume occurring at 3.8 nm for the former and 5.2 nm for the latter. Interestingly, both samples have a low, broad distribution at ~8-60 nm. This was absent for their counterparts synthesised using the non-evaporative method. It is likely that the increase BET area for the titania synthesised using the *cis*-PSS is due to the lack of non-porous morphologies in this case. From the TEM images, (Figure 6.10) exclusively spherical particles can be observed for the EISA synthesis, while an array of different morphologies (flower-like crystals, long fibrils) were seen for the non-evaporative synthesis.
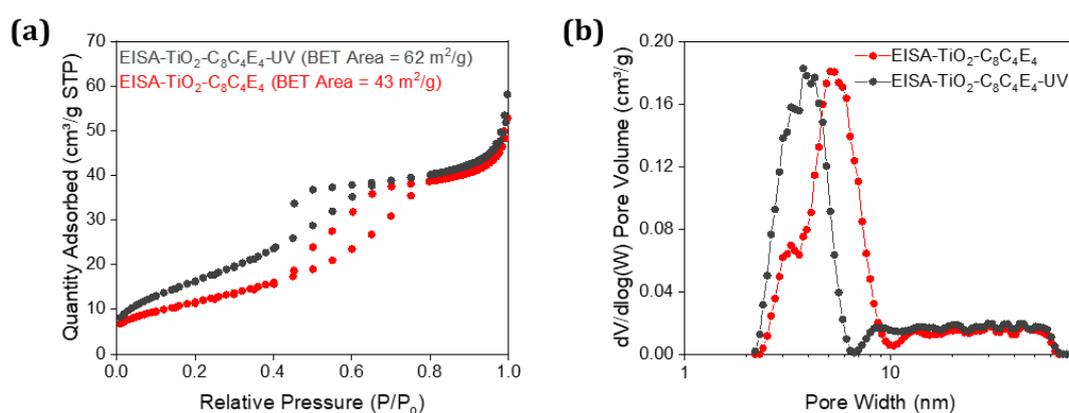
Figure 6.13. N_2 adsorptions (a) and pore size distribution (b) for titania synthesised using the EISA method and C$_8$AzoOC$_4$E$_4$ in either the native-*trans* (red) or *cis*-PSS (red).

6.3.2.5 Photocatalytic Activity

The photocatalytic activity of the titania particles was again investigated by repeating the previous measurement monitoring the degradation of an organic dye, methyl orange. The dye concentration was monitored every 15-20 minutes using UV-Vis absorption spectroscopy, with monitoring of the dye concentration using UV-Vis absorption spectroscopy. The degradation again followed *pseudo*-first order kinetics, with a rate equation of $\ln(C_0/C_t) = -kt$. (Figure 6.14) All absorption spectra can be found in the Appendix (A.6.12) with the associated rate constants available in Table 6.7.

Both titania candidates perform well with respect to their photocatalytic behaviour. In this case, the rate constants are higher than any of the rate constants obtained for the non-evaporative approach (highest previously was 0.95×10^{-3} s^{-1} for TiO$_2$-C$_8$C$_8$E$_4$) and are 48 and 82% higher compared to the same surfactant used for the non-evaporative synthesis using the surfactant in either the native *trans* or *cis*-PSS, respectively. The rate constants obtained for titania synthesised using the EISA approach are very similar for both UV and non-UV syntheses, with a different of only 0.1 s^{-1} occurring between the rate constants. It is anticipated that this difference is on the order of the error associated with the measurements, meaning that the higher rate constant calculated for EISA-TiO$_2$-C$_8$C$_4$E$_4$-UV may not be meaningfully higher than that calculated for EISA-TiO$_2$-C$_8$C$_4$E$_4$. There was insufficient titania synthesised to repeat the photocatalytic measurements to better gauge the uncertainty associated with the calculated rate constant. Both particles also have very similar crystallite sizes and morphologies, with EISA-TiO$_2$-C$_8$C$_4$E$_4$-UV having a 50% larger BET area than EISA-TiO$_2$-C$_8$C$_4$E$_4$. Any improvements to the photocatalytic performance obtained by using the surfactant in the *cis*-PSS could be attributed to this increased BET area in the first instance, as all other measured parameters have little variation.
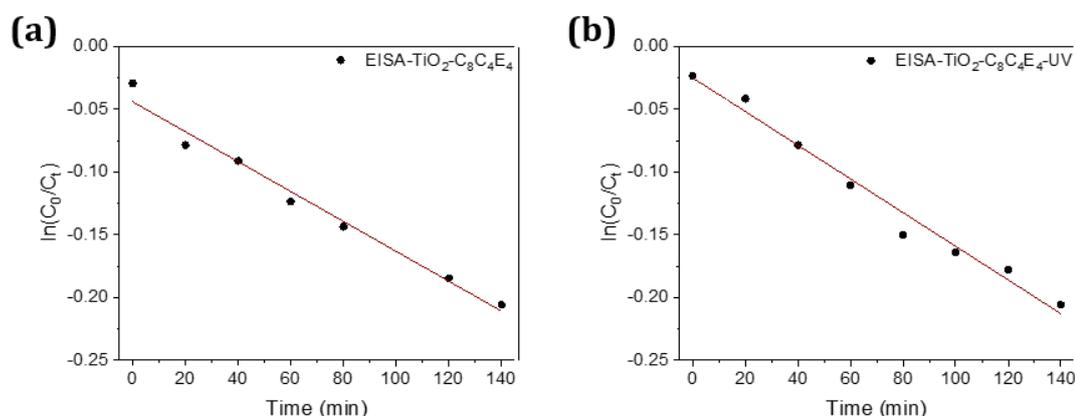
Figure 6.14. Photocatalytic decay of methyl orange by (a) EISA-TiO$_2$-C$_8$C$_4$E$_4$ and (b) EISA-TiO$_2$-C$_8$C$_4$E$_4$-UV follow pseudo-first order decay kinetics. The rate constants found were 1.2×10^{-3} s^{-1} and 1.3×10^{-3} s^{-1}, respectively.

Table 6.7. Photocatalytic *pseudo*-first order rate constant, k, and key physical properties (crystallite size, BET area) for titania samples synthesised with AzoPS using the EISA method.

Sample	k (s^{-1})	Crystallite Size (nm)	BET area (m^2 g^{-1})
EISA-TiO$_2$-C$_8$C$_4$E$_4$	1.2×10^{-3}	12.0	43
EISA-TiO$_2$-C$_8$C$_4$E$_4$-UV	1.3×10^{-3}	11.2	62

6.3.2.6 Comparison of Both Synthetic Approaches

Comparing these particles to those synthesised using the same AzoPS but with the non-evaporative approach shows that the EISA method results in a vastly different product for the titania synthesised using the AzoPS in the *cis*-PSS compared to the counterpart made using the non-evaporative method. For the titania made using the *trans*-AzoPS, a slight increase in crystallite size, from 9.4 to 12 nm, is observed between the non-evaporative and evaporative approaches, as well as an increase in overall particle size. There is a slight decrease in BET area, from 59 to 43 m^2 g^{-1}. Both titania products have a pore size distributed centred on 6-7 nm but the EISA approach resulted in a higher pore volume, as well as having a long plateau pore volume at high pore sizes. The photocatalytic rate constant increases by almost 50%, from 0.81 s^{-1} to 1.2 s^{-1} from the non-evaporative to the EISA approaches, implying that these differences in crystallite size and PSD have a significant effect on performance.

For the titania synthesised using the *cis*-PSS, the crystallite size remains the same across the two synthetic approach, although there is a clear change in morphology, with only spherical particles being formed for the EISA approach. The BET area also increases starkly for the EISA approach compared to the non-EISA approach, from 36 to 62 m^2 g^{-1}. The improved photocatalytic performance, with a rate constant increasing from 0.46 to 1.3 s^{-1} can be attributed to this increase in BET area, associated with the formation of exclusively spherical particles, rather than a variety of morphologies. The performance of EISA-TiO$_2$-C$_8$C$_4$E$_4$ and EISA-TiO$_2$-C$_8$C$_4$E$_4$-UV are very similar, with rate constant of 1.2×10^{-3} s^{-1} and 1.3×10^{-3} s^{-1} being obtained for each, respectively. The former possesses a higher crystallite size while the latter has a higher BET area and PSD shifted slightly to larger values.

It is clear that the EISA method results in a better product for photocatalytic purposes, particularly for the AzoPS in the *cis*-PSS. It is likely that the slow evaporation of solvent and gradual increasing of effective surfactant concentration allows for more uniform and consistent self-assembly compared to the perhaps more dynamic behaviour of the surfactant in a closed solution of a fixed volume. The formation of a mixture of morphologies for the non-evaporative approach seems to reflect the composition of the *cis*-photostationary state, which was found to be 63% *cis*-isomers. It is possible that the

remaining 37% *trans*-isomers facilitated the formation of spheres, as observed for the same approach using the surfactant in the native *trans*-state. The *cis*-isomers, or lack of *trans*, appears to have contributed significantly to the formation of more irregular structures such as flower-like crystals or long fibrils. However, it is clear that for the EISA approach this is not the case. As the EISA approach involves increasingly less volumes of liquid due to the evaporation process, it is possible that the increasing concentration of the surfactant, along with surface forces from the evaporation, result in a much more organised and ordered structure. In this case, it is possible to form spherical particles, regardless of the isomeric form of the AzoPS.

5.4 Conclusions

It has been shown that AzoPS have the ability to be used as template to form photocatalytic porous nanoparticles. The key trends observed for the non-evaporative synthesis are the formation of different morphologies (spherical *vs.* various) depending on whether the synthesis proceeded with the AzoPS in the native *trans*-state or the *cis*-PSS. It was also found that the syntheses using the *cis*-PSS had both higher crystallite sizes than their *trans* counterparts, but lower BET areas. This is attributed to the formation of non-porous morphologies such as flower-like crystals and long fibrils. For the syntheses using the AzoPS in the native *trans*-state, it was found that a higher crystallite size was associated with a higher BET area, implying that these two key parameters can be optimised together, rather than being a zero-sum scenario. This is a different perspective than that usually posited in the literature. The photocatalytic performance depends strongly on the irradiation conditions used, in all cases, the rate constant for the titania synthesised using the AzoPS in the *cis*-PSS is lower than that synthesised using its native *trans*-state counterpart.

The titania synthesised using the EISA approach using the non-photoresponsive analogue, Brij L4, was found to form both brookite and anatase phases, even before calcination occurs. This is an unusual result that reinforces the role of the surfactant as a key parameter for metal-oxide templating. Using the AzoPS $C_8AzoOC_4E_4$, particles slightly larger than those synthesised using the non-evaporative approach were formed. Here, the key difference between synthesis techniques is the uniformity of the particles, in both cases, using the surfactant in either the native *trans*-state or *cis*-PSS, resulted in the formation of spherical particles, as observed using TEM. Furthermore, a slight increase in crystallite size was associated with the EISA approach over the non-evaporative approach. This, in conjunction with the formation of uniform spheres and not mixed morphologies implies that the EISA synthesis yields a significantly better product for templating with AzoPS. The improved photocatalytic performance of the titania synthesised using the EISA method affirms this conclusion.

A common issue discussed in the area of surfactant-assisted templating for the formation of porous nanoparticles is the trade-off between BET area and crystallite size, and how both are crucial for good photocatalytic performance. Here, the best candidate from the non-evaporative approach, TiO_2-$C_8C_8E_4$, had both the highest crystallinity and BET area, reaffirming this conclusion. However, the general trend observed here is that the titania products with good crystallinity also had high BET areas, rather than one occurring at the expense of the other. It was also observed that spherical morphology and high BET areas are crucial, as the titania formed using the non-evaporative approach and

the *cis*-PSS showed very poor photocatalytic performance, despite possessing good crystallinity.

In summary, for the first time AzoPS have been used to template titania. Overall, it is clear that while AzoPS can be used as templates, the use of UV light to irradiate to the *cis*-PSS does not have a significant positive effect on the parameters of the product particle. It was hoped that an improvement in surface area or BET area would occur, but rather the *cis*-PSS tended to result in higher crystallite sizes, due to the formation of various morphologies. This variety of morphologies did not contribute to increase photocatalytic performance. In cases where a variety of morphologies were not obtained, (*e.g.* the EISA approach) the titania synthesised using the *cis*-PSS did result in higher BET areas but the final affect on performance was low, with similar rate constants obtained regardless of the isomeric form of the surfactant. It is clear from this that the template chosen does play a significant role on the final template particle, as quite different results were obtained whether a non-photoresponsive surfactant or an AzoPS was used.

Future work in this area would involve expanding the EISA method to use some of the other AzoPS, to see if the behaviour observed for $C_8AzoOC_4E_4$ was consistent across the surfactant family. In particular, $C_8AzoOC_8E_4$ would be interesting as this surfactant possessed the highest rate constant in the non-evaporative approach. Future work could also involve irradiation of either UV or blue light *in-situ*, rather than before the synthesis, to investigate if a more rapid isomerisation affected the particle morphology and size. However, results so far indicate that gradual changes in self-assembly behaviour, *i.e.* slow evaporation, result in a better nanoparticle product. As the EISA approach yielded the best product, thought to be a result of the inducement of alignment or improved self-assembly behaviour due to the evaporation process, the use of AzoPS to template films, rather than particles, could be very interesting. The possibility of π-π stacking between adjacent chromophores could have favourable consequences for the properties of the film, the disruption of which upon UV irradiation, could also be a worthwhile avenue of investigation.

5.5 References

1   D. A. H. Hanaor and C. C. Sorrell, *J. Mater. Sci.*, 2011, **46**, 855–874.

2   M. Xu, Y. Gao, E. M. Moreno, M. Kunst, M. Muhler, Y. Wang, H. Idriss and C. Wöll, *Phys. Rev. Lett.*, 2011, **106**, 1–4.

3   A. L. Linsebigler, G. Lu and J. T. Yates, *Chem. Rev.*, 1995, **95**, 735–758.

4   F. Huang, D. Chen, X. L. Zhang, R. A. Caruso and Y.-B. Cheng, *Adv. Funct. Mater.*, 2010, **20**, 1301–1305.

5   D. Chen and R. A. Caruso, *Adv. Funct. Mater.*, 2013, **23**, 1356–1374.

6   I. L. Violi, M. D. Perez, M. C. Fuertes and G. J. A. A. Soler-Illia, *ACS Appl. Mater. Interfaces*, 2012, **4**, 4320–4330.

7   C. K. Tsung, J. Fan, N. Zheng, Q. Shi, A. J. Forman, J. Wang and G. D. Stucky, *Angew. Chemie - Int. Ed.*, 2008, **47**, 8682–8686.

8   X. Wang, L. Cao, D. Chen and R. A. Caruso, *ACS Appl Mater Interfaces*, 2013, **5**, 9421–9428.

9   R. Zhang, A. A. Elzatahry, S. S. Al-deyab and D. Zhao, *Nano Today*, 2012, **7**, 344–366.

10   J. L. Vivero-Escoto, Y. D. Chiang, K. C. Wu and Y. Yamauchi, *Sci. Technol. Adv. Mater.*, 2012, **13**, 013003.

11   A. A. Ismail and D. W. Bahnemann, *J. Mater. Chem.*, 2011, **21**, 11686–11707.

12   W. Li, Z. Wu, J. Wang, A. A. Elzatahry and D. Zhao, *Chem. Mater.*, 2014, **26**, 287–298.

13   Y. Wang, L. Li, X. Huang, Q. Li and G. Li, *RSC Adv.*, 2015, **5**, 34302–34313.

14   K. (Guy) Vibulyaseak, B. Ohtani and M. Ogawa, *RSC Adv.*, 2020, **10**, 32350–32356.

15   S. Sugapriya, R. Sriram and S. Lakshmi, *Optik (Stuttg).*, 2013, **124**, 4971–4975.

16   T. Alapi, P. Sipos, I. Ilisz, G. Wittmann, Z. Ambrus, I. Kiricsi, K. Mogyorósi and A. Dombi, *Appl. Catal. A Gen.*, 2006, **303**, 1–8.

17   D. Chen, L. Cao, F. Huang, P. Imperial, Y. B. Cheng and R. A. Caruso, *J. Am. Chem. Soc.*, 2010, **132**, 4438–4444.

18   D. M. Antonelli and J. Y. Ying, *Angew. Chemie Int. Ed. English*, 1995, **34**, 2014–2017.

19   K. Cassiers, T. Linssen, M. Mathieu, Y. Q. Bai, H. Y. Zhu, P. Cool and E. F. Vansant, *J. Phys. Chem. B*, 2004, **108**, 3713–3721.

20   E. Beyers, P. Cool and E. F. Vansant, *Microporous Mesoporous Mater.*, 2007, **99**, 112–117.

21   E. Beyers, P. Cool and E. F. Vansant, *J. Phys. Chem. B*, 2005, **109**, 10081–10086.

22   D. M. Antonelli, *Microporous Mesoporous Mater.*, 1999, **30**, 315–319.

23   J. Wei, Y. Liu, J. Chen, Y. Li, Q. Yue, G. Pan, Y. Yu, Y. Deng and D. Zhao, *Adv Mater*, 2014, **26**, 1782–1787.

24   P. Kluson, P. Kacer, T. Cajthaml and M. Kalaji, *J. Mater. Chem.*, 2001, **11**, 644–651.

25   P. Yang, D. Zhao, D. I. Margolese, B. F. Chmelka and G. D. Stucky, *Nature*, 1998, **396**, 152–155.

26   B. C. J. Brinker, Y. Lu, A. Sellinger and H. Fan, *Adv. Mater.*, 1999, 579–585.

27   L. Mahoney and R. T. Koodali, *Materials (Basel).*, 2014, **7**, 2697–2746.

28   J. Zhang, Y. Deng, D. Gu, S. Wang, L. She, R. Che, Z. S. Wang, B. Tu, S. Xie and D. Zhao, *Adv. Energy Mater.*, 2011, **1**, 241–248.

29   I. Naboulsi, B. Lebeau, L. Michelin, C. Carteret, M. Bonne and J. L. Blin, *Microporous Mesoporous Mater.*, 2018, **262**, 1–12.

30   E. A. Barringer and H. K. Bowen, *J. Am. Ceram. Soc.*, 1982, **65**, C-199-C-201.

31   K. Cassiers, T. Linssen, M. Mathieu, Y. Q. Bai, H. Y. Zhu, P. Cool and E. F. Vansant, *J. Phys. Chem. B*, 2004, **108**, 3713–3721.

32   K. Zimny, C. Carteret, M. J. Stébé and J. L. Blin, *J. Phys. Chem. C*, 2011, **115**, 8684–8692.

33   K. Zimny, J. Ghanbaja and J. Blin, *New J. Chem.*, 2010, **34**, 2113–2117.

34   D. Chen, F. Huang, Y.-B. Cheng and R. A. Caruso, *Adv. Mater.*, 2009, **21**, 2206–2210.

35   F. Sauvage, D. Chen, P. Comte, F. Huang, Ḱ. L. Heiniger, Y. Cheng, R. A. Caruso and M. Graetzel, *ACS Nano*, 2010, **4**, 4420–4425.

36   A. Altomare, C. Cuocci, C. Giacovazzo, A. Moliterni, R. Rizzi, N. Corriero and A. Falcicchio, *J. Appl. Crystallogr.*, 2013, **46**, 1231–1235.

37   A. Le Bail, *Powder Diffr.*, 2004, **19**, 249–254.

38   J. Tauc, R. Grigorovici and A. Vancu, *Phys. Stat. Sol.*, 1966, **15**, 627–637.

39   J. Tauc, *Mat. Res. Bull.*, 1968, **3**, 37–46.

40   L. Chu, Z. Qin, J. Yang and X. Li, *Sci. Rep.*, 2015, **5**, 1–10.

41   J. Zhang, P. Zhou, J. Liu and J. Yu, *Phys. Chem. Chem. Phys.*, 2014, **16**, 20382–20386.

42   M. Rezaee, S. M. Mousavi Khoie and K. H. Liu, *CrystEngComm*, 2011, **13**, 5055–5061.

43   J. I. Langford and A. J. C. Wilson, *J. Appl. Crystallogr.*, 1978, **11**, 102–113.

44   Z. Zhang, S. Brown, J. B. M. Goodall, X. Weng, K. Thompson, K. Gong, S. Kellici, R. J. H. Clark, J. R. G. Evans and J. A. Darr, *J. Alloys Compd.*, 2009, **476**, 451–456.

45   K. A. Cychosz and M. Thommes, *Engineering*, 2018, **4**, 559–566.

46   I. Naboulsi, B. Lebeau, L. Michelin, C. Carteret, L. Vidal, M. Bonne and J. L. Blin, *ACS Appl. Mater. Interfaces*, 2017, **9**, 3113–3122.

47   K. M. Reddy, S. V. Manorama and A. R. Reddy, *Mater. Chem. Phys.*, 2003, **78**, 239–245.

48   R. W. G. Wyckoff, *Crystal Structures*, Interscience Publishers, New York, 2nd Editio., 1963.

Chapter 7

Conclusions and Future Work

Conclusions and Future Work

This thesis investigated the self-assembly behaviour of azobenzene photosurfactants, with particular emphasis on the relationship between self-assembly and macroscopic properties such as viscosity and the emergence of long-range order. Across four results chapters, which will be summarised in turn below, it has become clear that aqueous solutions of AzoPS are fascinating systems with a diverse range of light-responsive behaviours and applications.

Chapter 3 initially described the results of a SANS study with *in situ* UV-Vis absorption spectroscopy, to monitor the change in the self-assembled structure upon photoisomerisation of $C_8AzoOC_8E_4$. It was found the AzoPS transitioned between WLMs in the native *trans*-state and fractal aggregates in the *cis*-PSS. Further rheology measurements on solutions of both $C_8AzoOC_8E_4$ and $C_6AzoOC_4E_4$ confirmed flow behaviour consistent with WLMs, with $C_6AzoOC_4E_4$ possessing particularly interesting light-responsive flow behaviour. $C_6AzoOC_4E_4$ can reversibly transition between a high viscosity, viscoelastic fluid and a low viscosity, Newtonian fluid, through application of blue and UV light.

The combined UV-Vis-absorption-SANS approach presented here could be extended to a variety of systems to allow monitoring of the self-assembly process, as the only requirement is the presence of a characteristic absorption spectrum. The sample environment developed here is also accessible to other users at the Jülich Centre for Neutron Science in Garching, München. This technique would be of particular value to dynamic, non-equilibrium processes such as the controlled release of small molecules from self-assembled aggregates, *e.g.,* drug delivery, micellar catalysis. As $C_6AzoOC_4E_4$ demonstrates the ability to significantly alter its rheological behaviour on demand upon light-irradiation, the possibility of using this surfactant as a light-responsive drag-reduction/efficient heat-transfer fluid is worth exploring. Drag-reduction is a preferable characteristic for fluid transport but disfavoured when the fluid must pass through heat exchangers for heating and cooling applications. Therefore, the ability to switch easily between these two properties is much sought after. To date, no simple single-component salt-free fluid has been reported.[1] It is suspected that the inclusion of salts is a drawback to the multi-component fluid. Isomerisation to the *cis*-isomer is anticipated to create a non-drag reducing fluid with increased heat-transfer capabilities, as it is expected to have less turbulent flow than the *trans*-state. Friction measurements using a tribometer could also be useful for experimentally determining the difference between the coefficients of friction for the *trans* and *cis*-forms of AzoPS.

Chapter 4 focused further on the rheological behaviour of $C_6AzoOC_4E_4$, particularly the self-assembly behaviour under shear, measured using rheo-SANS. This work highlights the concentration-dependent behaviour of surfactants, with starkly different relaxation times and shear-dependent behaviour observed for the two solutions, 2.5 and 4 wt%, probed here. Using rheo-SANS, a phase transition to an aligned, sheet-like phase was found for the 2.5 wt% solution. The 4 wt% solution demonstrated interesting shear-thickening viscosity behaviour, with a structure consistent with WLMs observed across all shear rates. It is likely that shear-banding is emerging for these WLMs; it is thought shear banding likely occurs for all WLM solutions.[2]

There have been few reports integrating rheo-SANS with AzoPS, despite their potential as light-responsive rheological fluids. This work highlights the value of rheo-SANS as a technique to probe the shear-dependent properties of soft matter systems in detail. The focus of future work will be on measuring solutions of $C_6AzoOC_4E_4$ in the 1,2 plane (*i.e.,* an 'arial view' of the Couette cell), as well as quantifying the increase in branching with concentration. Possible techniques for this purpose are NMR diffusion studies and cryo-TEM imaging. A more detailed investigation into the shear behaviour after UV irradiation to fully form the *cis*-PSS would also be informative.

In Chapter 5, the self-assembly behaviour of all four AzoPS were investigated at high concentrations in terms of their ability to form photoresponsive LLC phases. Using POM and SAXS, all AzoPS were found to form LLC phases, typically either lamellar or hexagonal. These phases follow interesting trends in terms of the effect of concentration, molecular structure and isomeric form. For example, despite all AzoPS possessing the same packing parameter predictive of cylindrical aggregates in the *trans*-form, $C_2AzoO_4E_4$ formed exclusively lamellar phases, while $C_6AzoOC_4E_4$ and $C_8AzoOC_4E_4$ formed hexagonal and lamellar phases. For all AzoPS, UV light resulted in a loss of the LLC phase. It was shown that UV light could also be applied selectively through the use of a mask, allowing controlled deformation of the LLC template.

These single-component, photoresponsive LLC phases will allow new functional materials to be developed, in fact, future work based on these findings is already underway. This work involves creating light-responsive dispersions of LLC droplets (*cubosomes, hexosomes)*. These droplets retain the ordering of the parent LLC phase, but are dispersed in water so have significantly lower viscosities than the bulk LLC phase, allowing for better integrating with applications involving controlled delivery and release.[3]

Finally, in Chapter 6 the use of AzoPS as soft-templates for the formation of porous TiO_2 nanoparticles was demonstrated. This is the first report of AzoPS used to template

titania. Two different synthetic approaches were trialled, one non-evaporative and one using evaporation-induced self-assembly. The key finding of the non-evaporative method was the formation of diverse morphologies for the titania synthesised using the *cis*-AzoPS, while regular, spherical morphologies are found when the native *trans*-state is used as a template. This morphology difference propagated to differences in BET areas and crystallite size for each of the isomers used as templates. Using the evaporation-induced self-assembly approach, larger particles were formed, along with slightly larger crystallite sizes. As a result, better photocatalytic activity was observed (through the degradation of methyl orange) for the titania synthesised using the evaporation-induced self-assembly method. Potential avenues for future work would be the use of AzoPS to template films, or other structures where ordering along the π-π packing direction of the AzoPS is desirable. As this packing is easily disrupted for UV light, the potential for on-demand changes to key property remains.

There are some key findings consistent to all Chapters: (1) it is clear that the aromatic π-π interactions of the azobenzene core strongly influence the self-assembly of the AzoPS, whether through the formation of elliptical, rather than cylindrical, WLMs or LLC phases different to those predicted by the packing parameter. The aromatic core is a key difference which separates AzoPS from regular surfactants, not simply in terms of incorporating a photoresponse, but also in terms of influencing the packing behaviour of the native-*trans* monomer; (2) light irradiation strongly affects the properties of the AzoPS system. It is evident that the self-assembly behaviour of AzoPS depends greatly on the above two points, as well as concentration, molecular structure, applied shear and temperature. These parameters allow the macroscopic system properties to be manipulated, with the same simple AzoPS systems having the potential to be either viscous or watery, forming an ordered LLC phase or an isotropic solution, templating a spherical or flower-like titania aggregate

When this project began, SANS had rarely been combined with *in-situ* UV-Vis absorption spectroscopy, and never with *in-situ* irradiation to study the dynamic self-assembly of aggregates in solution. Since the publication of some of the work in this thesis, this combined technique has been used to probe controlled release from light-responsive micelles[4] and expanded to include the monitoring of structural changes using other kinds of spectroscopies.[5] The use of rheo-SANS to probe AzoPS systems was also a novel approach here, with the first published report of this arising for a photoactive betaine surfactant in 2021.[6] Furthermore, prior to this work there was only one report of an AzoPS forming wormlike micelles with tuneable rheological behaviour, for a gemini cationic structure.[7] The AzoPS in this thesis became the first neutral AzoPS reported to

form WLM with photoswitchable viscosities. During this time, responsive, viscoelastic solutions have evolved as topic of interest among other research groups, with zwitterionic AzoPS,[6] Se-based ionic liquid surfactants,[8] silicone oils[9] and polyacrylate solutions[10] all recently used to create various kinds of systems with switchable viscosities. In fact, using azobenzene as a means to design efficient light-responsive soft-matter systems warranted a review article in 2021,[11] following from other review articles on the topic in 2020,[12] 2018[13] and 2013[14]. Further developments in the field include using the results from AzoPS research to develop novel applications, such as electro-spun fibres doped with azobenzene-doped liquid crystals for precise photopatterning[15] and phase alignment,[16] and using photoswitchable surfactants to crate shape- and colour-changing polymer particles.[17] This thesis also broadened the family of light-responsive surfactants which can form LLC phases and provided the first report of using AzoPS to template mesoporous titania nanoparticles. It is clear there is a growing body of research on the topic of azobenzene in soft matter systems and that the results presented in this thesis formed part of the progress in that field. Altogether, AzoPS can form elegant systems which offer fascinating possibilities, with a diverse range of potential avenues for future research.

7.1 References

(1)   Shi, H.; Ge, W.; Oh, H.; Pattison, S. M.; Huggins, J. T.; Talmon, Y.; Hart, D. J.; Raghavan, S. R.; Zakin, J. L. *Langmuir* **2013**, *29* (1), 102.

(2)   Fardin, M.-A.; Casanellas, L.; Saint-Michel, B.; Manneville, S.; Lerouge, S. *J. Rheol. (N. Y. N. Y).* **2016**, *60* (5), 917.

(3)   Mulet, X.; Boyd, B. J.; Drummond, C. J. *J. Colloid Interface Sci.* **2013**, *393* (1), 1.

(4)   Akamatsu, M.; Kobayashi, K.; Iwase, H.; Sakaguchi, Y.; Tanaka, R.; Sakai, K.; Sakai, H. *Sci. Rep.* **2021**, *11* (1), 1.

(5)   Nakamura, M.; Okano, M.; Watanabe, S. *ACS Appl. Polym. Mater.* **2019**, *1* (11), 3008.

(6)   Butler, C. S. G.; King, J. P.; Giles, L. W.; Marlow, J. B.; Vidallon, M. L. P.; Sokolova, A.; de Campo, L.; Tuck, K. L.; Tabor, R. F. *J. Colloid Interface Sci.* **2021**, *594*, 669.

(7)   Song, B.; Hu, Y.; Zhao, J. *J. Colloid Interface Sci.* **2009**, *333* (2), 820.

(8)   Zhang, Y.; Chen, Z.; Zhao, Y. *Phys. Chem. Chem. Phys.* **2019**, *21* (27), 14734.

(9)   Gäbert, C.; Rosenstingl, T.; Linsler, D.; Dienwiebel, M.; Reinicke, S. *ACS Appl. Polym. Mater.* **2020**, *2* (12), 5460.

(10)   Wu, D.; Shi, Y.; Lv, K.; Wei, B.; Zhu, Y.; Yin, H.; Feng, Y. *Molecules* **2021**, *26* (13), 1.

(11)   Giles, L. W.; Marlow, J. B.; Butler, C. S. G.; Turpin, G. A.; De Campo, L.; Mudie, S. T.; Faul, C. F. J.; Tabor, R. F. *Phys. Chem. Chem. Phys.* **2020**, *22* (7), 4086.

(12)   Chen, S.; Costil, R.; Leung, F. K.; Feringa, B. L. *Angew. Chemie* **2021**, *133* (21), 11708.

(13)   Santer, S. *J. Phys. D. Appl. Phys.* **2018**, *51* (1), 013002.

(14)   Brown, P.; Butts, C. P.; Eastoe, J. *Soft Matter* **2013**, *9* (8), 2365.

(15)   Thum, M. D.; Ratchford, D. C.; Casalini, R.; Wynne, J. H.; Lundin, J. G. *ACS Appl. Nano Mater.* **2021**, *4* (1), 297.

(16)   Thum, M.; Ratchford, D. C.; Casalini, R.; Kołacz, J.; Lundin, J. G. *J. Mater. Chem. C* **2021**, 22.

(17)   Lee, J.; Ku, K. H.; Kim, J.; Lee, Y. J.; Jang, S. G.; Kim, B. J. *J. Am. Chem. Soc.* **2019**, *141* (38), 15348.

Appendix

Appendix to Chapter 2 – Experimental

A.2.1 Synthesis and Characterisation of AzoPS

Materials

Sodium nitrite (NaNO3, ≥99.0%), anhydrous potassium carbonate (≥99.0%), potassium iodide (KI, 99.0%), sodium hydride (60% w/w in mineral oil), tetraethylene glycol (99%), hydrochloric acid (HCl, conc. 37%), ethanol (HPLC grade), tetrahydrofuran (THF, HPLC grade), dichloromethane, acetone and were purchased from Sigma Aldrich. 4-hexylaniline (90%) was purchased from ChemCruz. Sodium hydroxide (NaOH, ≥97%) and chloroform (>99%) were purchased from Fisher Scientific and phenol (>99.0%) was purchased from BDH Chemical Ltd. England. 1,4-dibromobutane (>98%) was purchased from Alfa Aesar. All reagents and solvents were used as received unless otherwise stated.

Methods

The synthesis of the AzoPS was achieved through three steps: (1) the preparation of a hydroxyl precursor, 4-alkyl-4′-hydroxylazobenzene; (2) modification of the above to a bromoprecursor, 4-alkyl-4′-(2-bromo)alkyloxy azobenzene, via an S_N2 reaction; (3) addition of the neutral tetraethylene glycol head group to yield the final product.

2.1.1. Synthesis of C_nAzoOH (4-alkyl-4-hydroxyl azobenzene)

In a round-bottom flask (100 mL), 4-alkylaniline (20 mmol, 4-ethylaniline: 2.49 mL; 4-hexylaniline: 3.85 mL; 4-octylaniline: 4.57 mL) was dissolved in an acetone: water mixture (1:1, 50 mL) and HCl (37.5%, 0.048 mol, 4 mL) added. The resulting orange solution was placed in an ice bath and kept at 0 °C. Sodium nitrite (20 mmol, 1.38 g) was dissolved in distilled water (20 mL), cooled (1-2 °C) and added dropwise to the acidic alkylaniline solution. The orange solution was left to stir over ice for 5 min, to allow for diazonium salt formation. The solution was placed in the freezer until required. Separately, NaOH (20 mmol, 0.80 g), Na_2CO_3 (20 mmol, 2.12 g) and phenol (20 mmol, 1.88 g) were dissolved in distilled water (50 mL) and cooled until the solution temperature reached 1-3 °C. To the basic solution, the acidic diazonium salt solution was added dropwise, maintaining a temperature < 8 °C. An aqueous NaOH solution (6.5 mL, 2.5 mmol L^{-1}) was added dropwise to the basic phenol solution along with the acidic diazonium salt solution, in order to maintain a final pH of 10. The resulting yellow precipitate was filtered and washed with cold water. The product C_mAzoOH was recovered in the form of a yellow powder.

C$_6$AzoOH (1a)

^{1}H NMR (CDCl$_3$, 400 MHz, 25 °C): δ = 1.31 (t, J = 8 Hz, 3H), 2.75 (quart., J = 8 Hz, 2H), 6.96 (d, J = 8.8 Hz, 2H), 7.34 (d, J = 8.2 Hz, 2H), 7.82 (d, J = 8.3 Hz, 2H), 7.88 (d, J = 8.8 Hz, 2H) ppm.

^{13}C NMR (CDCl$_3$, 100 MHz, 25 °C): δ = 15.4, 28.8, 115.8, 122.6, 124.9, 128.5, 147.2, 150.9, 158.0 ppm.

FTIR: ν = 3163 (br.), 2960 (w), 2927 (m), 2848 (w), 1583 (s), 1505 (s), 1242 (s), 1131 (s) cm^{-1}.

Mass Spectrometry (CH$_3$Cl, m/z: APCI$^+$): Exact mass calculated: 226.1106 [M], Exacted mass obtained: 227.1168 [M+H]$^+$.

Melting Point: 85.1–86.2 °C.

Yield: 68%

C$_6$AzoOH (1b)

^{1}H NMR: (CDCl$_3$, 400 MHz, 25 °C): δ = 0.91 (t, J = 8 Hz, 3H), 1.34 (m, 6H), 1.68 (m, 2H), 2.67 (t, J = 9 Hz, 2H,), 5.06 (s, 1H.), 6.98 (d, J = 7 Hz, 2H), 7.33 (d, J = 8.4 Hz, 2H), 7.81 (d, J = 7.2 Hz, 2H), 7.88 (d, J = 8.4 Hz, 2H) ppm.

^{13}C NMR: (CDCl$_3$, 100 MHz, 25 °C): δ = 14.1, 22.6, 28.9, 31.3, 31.7, 35.9, 115.8, 122.5, 124.8, 129.1, 146, 147.2, 150.9, 158.2 ppm.

FTIR: ν = 3547 (w), 3292 (b), 2956 (s), 2916 (s), 2849 (s), 1646 (w), 1586 (s), 1478 (C-H, s), 1404 (, s), 1290 (s), 1142 (s), 830 (s) cm^{-1} .

Mass Spectrometry (CH3Cl, m/z: APCI$^+$): Exact mass calculated: 282.1732 [M], exact mass obtained: 281.1659 [M+H]$^+$.

Melting Point: 86.9 – 88.8 °C.

Yield: 74%

C$_8$AzoOH (1c)

^{1}H NMR: (CDCl$_3$, 400 MHz, 25 °C): δ = 0.90 (t, J = 7 Hz, 3H), 1.33 (m, 8H), 1.66 (m, 4H), 2.69 (t, J = 7 Hz, 2H,), 5.5 (s, br.,), 6.96 (d, J = 7.2 Hz, 2H), 7.32 (d, J = 9 Hz, 2H), 7.81 (d, J = 7.2 Hz, 2H), 7.88 (d, J = 8.4 Hz, 2H) ppm.

^{13}C NMR: (CDCL3, 100 MHz, 25 °C): δ = 14.2, 22.7, 29.3, 29.5, 31.3, 31.9, 35.9, 115.9, 122.5 125.1, 129.1, 146.1, 147.1, 150.6, 158.3 ppm.

FTIR: ν = 3427 (br), 2956 (s), 2923 (s), 2856 (s), 1586 (s), 1465 (s), 1243 (s), 1135 (s), 833 (s), 558 (s) cm^{-1} .

Mass Spectrometry (CH3Cl, m/z: APCI$^+$): Exact mass calculated: 310.2045 [M], exact mass obtained: 309.1977 [M+H]$^+$.

Melting Point: 87.2 – 88.8 °C.

Yield: 66%

2.1.2 Synthesis of bromoprecursor C_nAzoOC_mBr (4-alkyl-4'(bromo)alkoxy azobenzene)

 C_nAzoOH (1 eq., 10 mmol, 2.26 g for C_2AzoOH; 2.82 g for C_6AzoOH; 3.00 g for C_8AzoOH) was dissolved in acetone (25 mL). 1,4 di-bromobutane (2 eq., 20mmol, 2.39 mL), K_2CO_3 (2 eq., 20 mmol, 2.76 g) and KI (0.1 eq., 1 mmol, 0.17 g) were added to the reaction flask and the resulting dark red solution was stirred under reflux at 65 °C for 2 days with monitoring via thin layer chromatography (TLC, 9:1 cyclohexane: ethyl acetate). Acetone was removed via rotary evaporation and the product was dissolved in dichloromethane (DCM, 20 mL) and washed with water several times to remove the co-salt. DCM was removed via rotary evaporation and the product was recovered as an orange solid upon recrystallization from ethanol.

C_2AzoOC_4Br (2a)

¹H NMR: (CDCl$_3$, 400 MHz, 25 °C): δ = 1.31 (t, J = 8 Hz, 3H), 2.02 (m, 2H), 2.13 (m, 2H), 2.74 (m, J = 8 Hz, 2H), 3.53 (mt, J = 6 Hz, 2H), 4.11 (t, J = 6, Hz 2H), 7.01 (d, J = 9 Hz, 2H) 7.34 (d, J = 8.36 Hz, 2H) 7.83 (d, J = 8.32 Hz, 2H) 7.92 (d, J = 9 Hz, 2H) ppm.

¹³C NMR: (CDCl$_3$, 400 MHz, 25 °C): δ = 15.4, 27.8, 28.82, 29.4, 33.4, 67.2, 114.7, 122.6, 124.6, 128.5, 147.1, 147.1, 151, 161.1 ppm.

FTIR: ν = 2966 (w), 2920 (m), 2861 (w), 1609 (s), 1497 (s), 1236 (s), 1138 (s) cm^{-1}.

Mass Spectrometry: (CH$_3$Cl, m/z: APCI$^+$): Exact mass calculated: 360.0837 [M], exact mass obtained: [M+H] 361.0910.

Melting Point: 115.4 – 117.3 °C

Yield: 82%

C_6AzoOC_4Br (2b)

¹H NMR: (CDCl$_3$, 400 MHz, 25 °C): δ = 0.92 (t, J = 8 Hz, 3H), 1.35 (m, 6H), 1.68 (m, 2H), 2.06 (m, 4H), 2.7 (t, J = 6.6 Hz, 2H), 3.47 (m, 2H), 4.11 (t, J = 6 Hz, 2H) 7.03 (d, J = 8.8 Hz, 2H), 7.29 (d, J = 8.2 Hz), 7.81 (d, J = 8.3 Hz 2H), 7.9 (d, J = 8.9 Hz, 2H) ppm.

¹³C NMR: (CDCl$_3$, 400 MHz, 25 °C): δ = 14.1, 22.62, 27.9, 29, 31, 31.3, 32.5, 33.4, 35.9, 67.2, 119.7, 122.6, 124.6, 129.1, 145.9, 147.1, 151, 161.1 ppm.

FTIR: ν = 2914 (s), 2848 (w), 1602 (s), 1498 (s), 1380 (w), 1256 (s), 1133 (s) cm^{-1}.

Mass Spectrometry (CH$_3$Cl, m/z: APCI$^+$): Exact mass calculated: 416.1463 [M], exact mass obtained: 417.154 [M+H]$^+$

Melting Point: 136.2 - 137.5 °C

Yield: 85%

C$_8$AzoOC$_4$Br (2c)

^{1}H NMR: (CDCl$_3$, 400 MHz, 25 °C): δ = 0.91 (t, J = 7 Hz, 3H) 1.3 (m, 10H), 1.66 (m, 2H), 2.02 (m, 2H), 2.11 (m, 2H), 2.7 (t, J = 8 Hz, 2H), 3.54 (t, J = 7 Hz, 2H) 4.11 (t, J = 7 Hz, 2H), 7.01 (d, J = 8.9 Hz, 2H), 7.32 (d, J = 8.2 Hz, 2H), 7.82 (d, J = 8.2 Hz, 2H), 7.92 (d, J = 8.9 Hz, 2H) ppm.

^{13}C NMR: (CDCl$_3$, 100 MHz, 25 °C): δ = 14.1, 22.7, 27.9, 29.2, 29.3, 29.4, 29.5, 31.3, 31.9, 33.4, 35.9, 67.2, 114.7, 122.5, 124.6, 129.1, 145.9, 147.1, 151.2, 161.1 ppm.

FTIR: ν = 2929 (s), 2838 (m), 1606 (s), 1498 (m), 1452 (m), 1393 (w), 1250 (s), 1141 (s) cm^{-1} . **Mass Spectrometry** (CH$_3$Cl, m/z: APCI$^+$): Exact mass calculated: 444.1776 [M], exact mass obtained: 445.1849 [M+H]$^+$.

Melting Point: 138.4 – 140.1 °C

Yield: 67%

C$_8$AzoOC$_8$Br (2d)

^{1}H NMR: (CDCl$_3$, 400 MHz, 25 °C): δ = 0.91 (t, J = 8 Hz, 3H), 1.29-1.35 (m, 10H), 1.4 – 1.47 (m, 8H), 1.66 (quint., 2H), 1.86 (m, 4H), 2.69 (t, J = 7 Hz, 2H), 3.44 (m, 2H), 4.05 (t, J = 7 Hz, 2H), 7.01 (d, J = 9 Hz, 2H), 7.32 (d, J = 8.5 Hz, 2H), 7.81 (d, J = 8.6 Hz, 2H), 7.9 (d, J = 8.7 Hz, 2H) ppm.

^{13}C NMR: (CDCl$_3$, 100 MHz, 25 °C): δ = 14.1, 26, 29.2, 28.1, 28.5, 28.6, 28.7, 29.3, 29.3, 29.5, 31.4, 31.9, 32.7, 33.9, 35.9, 68.3, 114.7, 122.5, 124.6, 129.1, 145.8, 147, 151.1, 161.4 ppm.

Mass Spectrometry (CH3Cl, m/z: APCI+): Exact mass calculated: 500.2402 [M], exact mass obtained: 501.2473 [M+H]$^+$.

Melting Point: 119.8 - 121.2 °C

Yield: 80%

2.1.3. Synthesis of C$_n$AzoOC$_m$E$_4$ (4-alkyl-4'-(mono-tetraethylene glycol) alkyloxy azobenzene:

Tetraethylene glycol (5 eq., 28.1 mmol, 5.41 mL) was dried using molecular sieves. Dry tetraethylene glycol was then dissolved in dry THF (25 mL) in a round-bottomed flask (50 mL) under an inert N$_2$ atmosphere. To this NaH (60% in oil (w/w), 1.5 eq., 8.4 mmol, 0.346 g) was added and left to stir for 1 h under N$_2$. C$_m$AzoOC$_n$Br (1.0 eq., 5.6 mmol) was dissolved in dry THF (10 mL) and added to the reaction flask. The resulting red solution was refluxed at 65 °C for 24 h. Acetone was removed via rotary evaporation and the resulting red oil dissolved in dichloromethane (20 mL) and washed with water. The DCM layer was dried, filtered and the solvent was removed via rotary evaporation. Excess bromoprecursor was removed using a silica plug and washing with chloroform. The product was recovered as a red oil.

$C_2AzoOC_4E_4$ (3a)

¹H NMR: (CDCl₃, 400 MHz, 25 °C): δ = 1 (t, J = 8 Hz, 3H), 1.81 (m, 2H), 1.9 (m, 2H), 1.98 (m, 2H), 2.74 (t, J = 8 Hz, 2H), 3.65 (m, 16H) 4.09 (t, J = 6 Hz, 2H), 7.01 (d, J = 8.92 Hz, 2H), 7.33 (d, J = 8.24 Hz, 2H), 7.82 (d, J = 8.24 Hz, 2H), 7.9 (d, J = 8.92 Hz, 2H) ppm.

¹³C NMR: (CDCL₃, 600 MHz, 25 °C): δ = 15.5, 26, 26.1, 28.8, 61.7, 68, 70.2-70.9 (7 peaks) 72.64, 114.69, 122.6, 124.6, 128.49, 146.97, 147.04, 151.05, 161.38 ppm.

FTIR: ν = 3404 (br.), 2965 (w), 2933 (s), 2874 (w), 1589 (s), 1492 (m), 1249 (s), 1315 (s) cm⁻¹.

Mass Spectrometry (CH₃Cl, m/z: APCI⁺): Exact mass calculated: 474.2730. Exact mass obtained: 475.2779 [M+H]⁺.

Yield: 38%

$C_6AzoOC_4E_4$ (3b)

¹H NMR: (CDCl₃, 400 MHz, 25 °C): δ = 0.9 (t, J = 8 Hz, 3H), 1.22 (d, 2H), 1.33 (m, 6H), 1.66-1.9 (m, 6H), 2.69 (t, J = 8 Hz, 2H), 3.63 (m, 16H), 4.09 (t, J = 7 Hz, 2H), 7 (d, J = 8.88 Hz, 2H), 7.3 (d, J = 8.16 Hz, 2H), 7.8 (d, J = 8.2 Hz, 2H), 7.89 (d, J = 8.8 Hz, 2H) ppm.

¹³C NMR: (CDCl₃, 600 MHz, 25 °C): δ = 14.1, 22.6, 26.1, 28.9, 30.9, 31.3, 31.7, 35.4, 61.7, 68, 70-70.9 (7 peaks), 72.65, 114.68, 122.51, 124.55, 129.03, 145.8, 146.9, 151, 161.4 ppm

FTIR: ν = 3175 (br.), 2959 (w), 2926 (m), 2873 (w), 1603 (s), 1490 (m), 1256 (s), 1131 (m) cm⁻¹. **Mass Spectrometry** (CH₃Cl, m/z: APCI⁺): Exact mass calculated: 530.3356. Exact mass obtained: 531.3442 [M+H]⁺

Yield: 39%

$C_8AzoOC_4E_4$ (3c)

¹H NMR: (CDCl₃, 400 MHz, 25 °C): δ = 0.79 (t, J = 8 Hz, 3H), 1.18-1.23 (m, 12H), 1.55 (m, 2H), 1.71 (m, 2H), 1.8 (m, 2H), 2.57 (t, J = 8 Hz, 2H), 3.49 (m, 12H), 3.62 (m, 4H), 3.97 (t, J = 8 Hz, 2H), 6.9 (d, J = 8.92 Hz, 2H), 7.2 (d, J = 8.24 Hz, 2H), 7.7 (d, J = 8.2 Hz, 2H), 7.78 (d, J = 8.88 Hz, 2H) ppm.

¹³C NMR: (CDCl₃, 600 MHz, 25 °C): δ = 14, 22.6, 26, 25.9, 29.2, 29.4, 30.7, 31.2, 31.8, 35.73, 61.4, 67.9, 70- 70.8 (7 peaks), 72.5, 114.3, 122.7, 124.5, 129.0, 145.2, 146.8, 151.1, 160.9 ppm.

FTIR: ν = 3175 (br.), 2965 (w), 2926 (m), 2866 (w), 1596 (s), 1497 (s), 1248 (s), 1135 (s) cm⁻¹.

Mass Spectrometry (CH₃Cl, m/z: APCI⁺): Exact mass calculated: 558.3669. Exact mass obtained: 559.3714 [M+H]⁺.

Yield: 42%

C$_8$AzoOC$_8$E$_4$ (3d)

^{1}H NMR: (CDCl$_3$, 400 MHz, 25 °C): δ = 0.84 (t, J = 8 Hz, 3H), 1.26–1.54 (m, 24H), 1.78 (m, 2H), 2.63 (t, J = 8 Hz, 2H), 3.64 (m, 16 H), 3.99 (t, J = 7 Hz, 2H), 6.95 (d, J = 9 Hz, 2H), 7.25 (d, J = 8.32 Hz, 2H), 7.75 (d, J = 8.36 Hz, 2H), 7.84 (d, J = 8.96 Hz, 2H) ppm.

^{13}C NMR: (CDCl$_3$, 600 MHz, 25 °C): δ = 14.06, 22.61, 25.93, 29.2, 29.3, 29.2, 29.3, 29.3, 29.3, 30.9, 31.3, 31.8, 33.6, 35.8, 61.5, 68.3, 70.2-70 (7 peaks), 72.8, 114.6, 122.5, 124.5, 129, 145.8, 146.9, 151, 161.1 ppm.

 FTIR: ν = 3169 (br.), 2971 (w), 2928 (m), 2867 (w), 1594 (s), 1498 (s), 1247 (s), 1139 (s) cm^{-1}.

Mass Spectrometry (CH$_3$Cl, m/z: APCI$^+$): Exact mass calculated: 614.4295 [M]. Exact mass obtained: 615.439 [M+H]$^+$.

Yield: 47%

2.2 Critical Micelle Concentrations

The critical micelle concentrations (CMCs) of AzoPS in water (25 °C) were determined for the *trans*- and *cis*-isomers using surface tensiometry (ST) and dynamic light scattering (DLS). In ST the CMC is reached when the surface tension becomes independent of surfactant concentration. Using DLS the intensity of scattering light increases significantly upon the onset of micelle formation.

Table A.2.1 Critical micelle concentrations of the *trans*- and *cis*-isomers of the AzoPS determined using dynamic light scattering (DLS) and surface tensiometry (ST). The associated errors are given in brackets (standard deviation of three measurements)

AzoPS	CMC$_{trans}$ by ST (μM)	CMC$_{cis}$ by ST (μM)	CMC$_{trans}$ by DLS (μM)	CMC$_{cis}$ by DLS (μM)
C$_2$AzoOC$_4$E$_4$	52.2 (2.4)	56.8 (2.1)	34.4 (5.7)	34.1 (19.1)
C$_6$AzoOC$_4$E$_4$	37.1 (6.3)	29.5 (1.8)	22.9 (4.2)	23.7 (5.0)
C$_8$AzoOC$_4$E$_4$	17.8 (2.1)	19.9 (1.8)	11.4 (1.6)	12.4 (1.2)
C$_8$AzoOC$_8$E$_4$	108.6 (3.1)	125.9 (2.3)	102.7 (33.9)	124.0 (1.2)

A.2.3 Determining Composition of the Photostationary State

The degree of isomerisation (ID) in the cis-photostationary state (PSS) can be calculated as follows:

$$ID_{cis} = \frac{A_0(365) - A_{PSS}(365)}{A_0(365)} \times 100\% \qquad \text{Eq. A1}$$

where A_0(365) refers to the absorbance of the assembly of 100% *trans*-isomers at 365 nm and A_{PSS}(365) refers to the absorbance of the *cis*-PSS at 365 nm. Similarly, for reverse isomerisation, the degree of isomerisation for the *trans*-PSS is obtained by:

$$ID_{trans} = \frac{A_{PSS}(365)}{A_o(365)} \times 100\% \qquad \text{Eq. A2}$$

where A_{PSS}(365) now refers to the absorbance of the *trans*-PSS at 365 nm.

A.2.4 Calculations for Surfactant Dimensions and Packing Parameter

In order to calculate the packing parameter for each AzoPS, the surfactant tail length, l_c, tail volume V, and head group area a_e were determined. V and l_c were calculated by Traube's empirical volume additivity rule,[1] with the volume of the pendant alkyl chain, the azobenzene core, the oxy group and the spacer contributions are summed to obtain the total volume (Table A.2.2), and the length of the various components summed for the total length.. The Tanford equations (Equations S3, S4) are used to obtain the contributions of the components of each AzoPS.[2]

$$V = 26.9 \times a + 27.4 \qquad \text{(Eq. A3)}$$

$$l = 1.265 \times a + 1.5 \qquad \text{(Eq. A4)}$$

Where a is the number of -CH_2- carbons in the carbon chain. The contributions from the oxy group were obtained by ab initio calculations.[1,3] The length of the azobenzene moiety is 0.9 nm and 0.55 nm for the trans- and cis-isomers, respectively.[4-8] The molecular volumes of the *trans*- and *cis*-isomers of the azobenzene core were obtained from the Van Der Waals volume through computational calculations and estimated to be 0.176 nm^3 and 0.177 nm^3, respectively.[9] The head group area of ethylene glycol groups are difficult to determine[10] and are known to be dependent on the hydrophobic chain length.[10] However, these values can be approximated from the literature.[11,12] An estimation of the packing parameters (P) for AzoPS can be obtained and are summarized in Table A.3.

Table A.2.2. Contribution of components (volumes, lengths, effective areas) to packing parameter calculation using the additivity principle.

Contribution	Value	Method
Pendant Alkyl Chain Volume (nm^3)	$0.0269a + 0.0274$	Tanford Equations[2]
Spacer Alkyl Chain Volume (nm^3)	$0.0269a$	Tanford Equations[2]
Azobenzene Volume (nm^3)	$0.176/0.177$ (*trans/cis*)	Van der Waals Volume, MOPAC calculations[6]
Oxygen Volume (nm^3)	9.1×10^{-3}	Van der Waals Volume, *ab initio* calculaitons[1]
Pendant Alkyl Chain Length (nm)	$0.1265a + 0.15$	Tanford Equations[2]
Spacer Alkyl Chain Length (nm)	$0.1265a$	Tanford Equations[2]
Azobenzene Length (nm)	$0.9/0.55$ (*trans/cis*)	X-Ray Analysis[6]
Oxygen Group Length	0.28	DFT Calculations[3]
E_4 Effective Area	0.46	ST Study of $C_{12}E_4$ at 25 °C[11]

Table A.2.3. Packing parameters, *P,* for each AzoPS calculated using the packing parameter principle

AzoPS	P_{trans}	P_{cis}
$C_2AzoOC_4E_4$	0.39	0.46
$C_6AzoOC_4E_4$	0.41	0.47
$C_8AzoOC_4E_4$	0.42	0.47
$C_8AzoOC_8E_4$	0.45	0.49

Appendix to Chapter 3

3.1 Photostability of Azobenzene Cycling
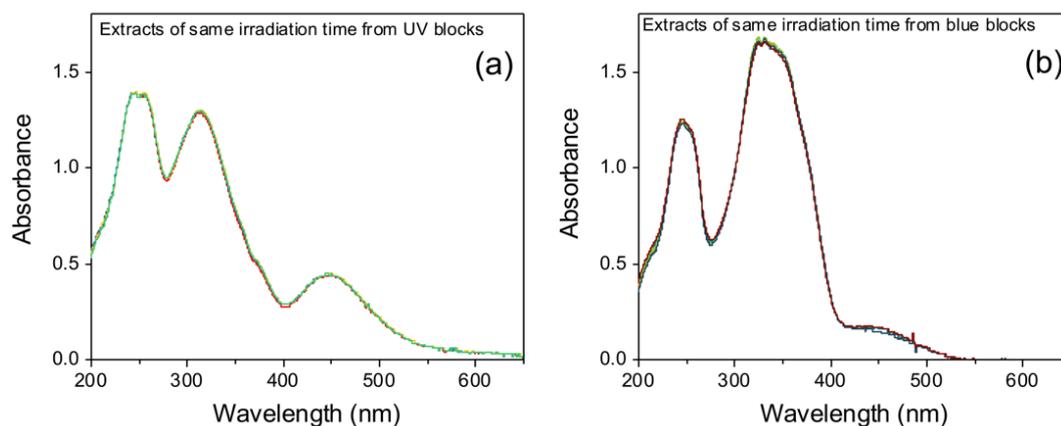
Figure A.3.1. $C_8AzoOC_8E_4$ can isomerise reversibly over several hours. UV-Vis absorption spectra of $C_8AzoOC_8E_4$ in D_2O (0.2 mM) (a) measured for a fixed UV irradiation time (365 nm) and (b) for a fixed blue light irradiation time (450 nm). Both sets of spectra were recorded during the repeated cycling of UV and blue irradiations, which were necessary to improve statistics in the SANS experiments.

3.2 Small-Angle Neutron Scattering Data and Fitting

3.2.1 Structural Parameters from SANS Model Fitting

Table A.3.1. Structural parameters obtained from SANS data for $C_8AzoOC_8E_4$ under blue light illumination in D_2O (0.2 mM) at 25 °C. For deconvolution into two models, dark grey refers to the flexible elliptical cylinder (FEC) model, while light grey refers to the elliptical cylinder model (EC). L_c is contour length, L_k is Kuhn length, L_{cyl} is cylinder length, r_m is the minor axis radius, a_r is the axis ratio, SLD refers to the scattering length density, χ^2 indicates the goodness-of-fit. X_{sol} is the calculated solvent fraction of the aggregates.

T (s)	Model	L_c	b (Å)	SLD (×10⁻⁶ Å⁻²)	χ^2	X_{sol}	L_{cyl} (Å)	r_m (Å)	a_r	SLD (×10⁻⁶ Å⁻²)	χ^2	X_{sol}
60	FEC	*	211.7	5.3	1.9	0.82	-	29.5	15.6	-	-	-
120	FEC	*	222.2	5.4	1.7	0.84	-	27.1	18.3	-	-	-
180	FEC	*	356.1	5.5	4.3	0.85	-	27.7	19.3	-	-	-
240	FEC	*	648.0	5.7	7.1	0.89	-	30.2	19.5	-	-	-
300	FEC/EC	*	243.9	5.7	0.7	0.89	366.8	32.2	5.1	5.3	2.7	0.82
360	FEC/EC	*	405.0	5.3	1.3	0.82	397.4	33.5	5.4	5.1	2.4	0.79
420	FEC/EC	*	636.2	5.7	1.8	0.89	615.0	34.4	5.1	5.1	2.2	0.79
480	FEC/EC	*	481.8	5.3	1.5	0.82	488.9	35.0	5.8	5.2	2.0	0.80
540	FEC/EC	*	446.0	5.3	1.2	0.82	589.2	36.1	5.7	5.0	1.7	0.77

* values for L_c lay outside the observation window of this experiment and are therefore not reported.

Table A.3.2. Structural parameters from SANS models for $C_8AzoOC_8E_4$ under UV light illumination in D_2O (0.2 mM) at 25 °C. For deconvolution into two models, dark grey refers to the flexible elliptical cylinder (FEC) model, while light grey refers to the elliptical cylinder model (EC). L_c is the contour length, L_k is the Kuhn length, L_{cyl} is the cylinder length, r_m is the minor axis radius, a_r is the axis ratio. For the fractal model, V_{fr} refers to the volume fraction, r is the radius of the constituent components, D is fractal dimension, L_{corr} is the correlation length. In all cases, SLD refers to the scattering length density, χ^2 gives an indication of the goodness-of-fit and X_{sol} is the calculated solvent fraction of the aggregates.

T (s)	Model	L_c	L_K (Å)	SLD (×10⁻⁶ Å⁻²)	χ^2	X_{sol}	L_{cyl} (Å)	r_m (Å)	a_r	SLD (×10⁻⁶ Å⁻²)	χ^2	X_{sol}
60	FEC/EC	*	517.7	5.1	7.3	0.79	587.7	41.2	5.7	4.8	7.8	0.73
120	FEC/EC	*	328.0	5.5	2.6	0.85	460.0	24.8	7.5	5.0	2.1	0.77
180	FEC/EC	*	711.0	5.1	2.3	0.79	446.4	22.1	9.2	4.5	2.5	0.68
240	-	-	-	-	-	-	-	-	-			
300	-	-	-	-	-	-	-	-	-			

T (s)	Model	D	r (Å)	SLD (×10⁻⁶ Å⁻²)	χ^2	X_{sol}	L_{corr} (Å)	
360	fractal	0.40	44.0	4.5	7.5	0.68	917.3	2.53
420	fractal	0.37	44.0	4.7	7.4	0.71	755.5	2.56
480	fractal	0.41	43.4	5.1	7.3	0.79	1856	2.56
540	fractal	0.36	42.4	5.5	6.7	0.85	1057	2.50

3.2.2 Comparison of Flexible Elliptical Cylinder Models
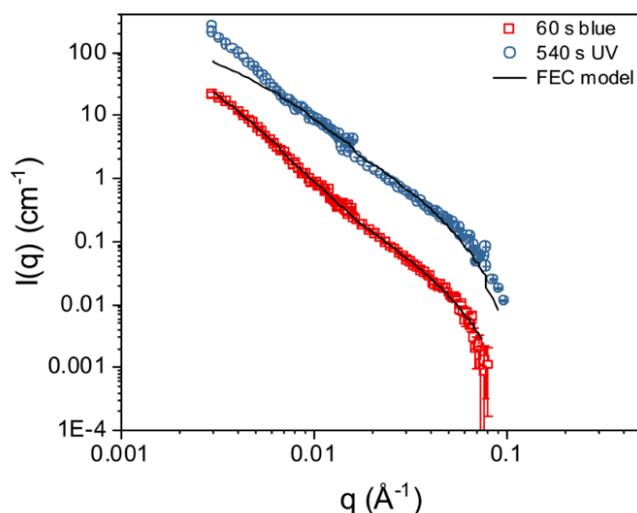
Figure A.3.2. SANS scattering profiles of $C_8AzoOC_8E_4$ after 60 s blue (red line) and 540 s UV (blue line) illumination. The black solid line indicates a fit to a flexible elliptical cylinder (FEC) model. The UV scattering curve has been offset by a factor of 10 for clarity.

3.2.3 Comparison of the Intensity of Small-Angle Neutron Scattering
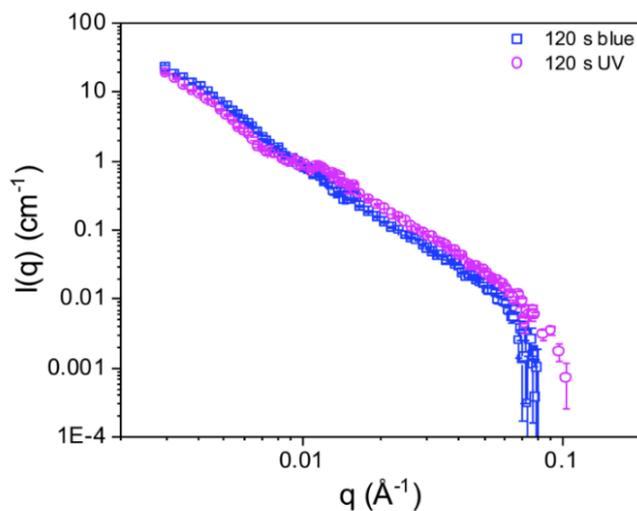
Figure A.3.3. SANS scattering profiles of **C$_8$AzoOC$_8$E$_4$** after 120 s of blue (blue line) and UV (pink line) irradiation. The scattering intensity is comparable under both conditions.

3.2.4 SANS Profiles at Equilibrium (0.2 mM)
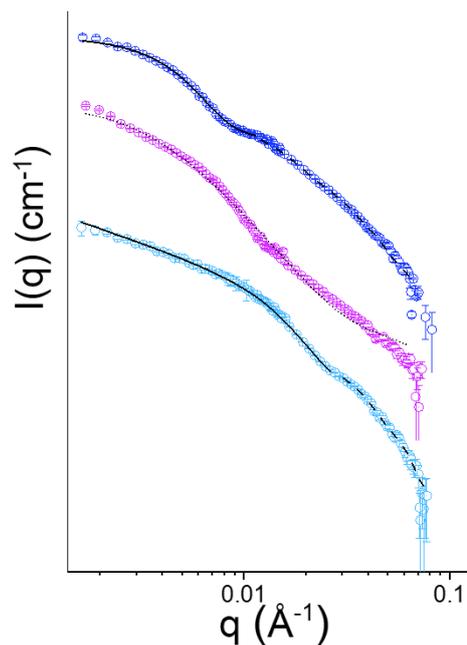
Figure A.3.4. SANS profiles of C$_8$AzoOC$_8$E$_4$ (0.2 mM in D$_2$O) in the native *trans*-dominant state (teal), and in the *cis*- (pink) and *trans*-PSS (blue) after UV and blue irradiation, respectively. Fits to a flexible elliptical cylinder model are shown with a black line, fits to an elliptical cylinder model with a dashed line and fits to the fractal model are shown with a dotted line. The scattering profiles have been offset for clarity.

3.2.5 SANS Profiles at Higher Concentration (1 mM)
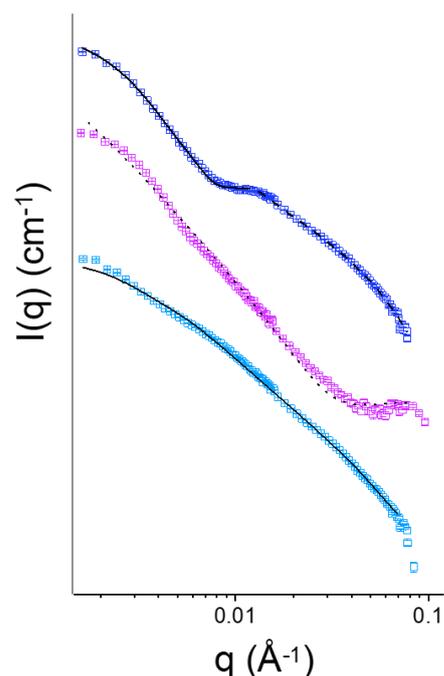
Figure A.3.5. SANS profiles of **C₈AzoOC₈E₄** (1 mM in D₂O) in the native *trans*-dominant state (teal), and in the *cis*- (pink) and *trans*-PSS (blue) after UV and blue irradiation, respectively. Fits to a flexible elliptical cylinder model are shown with a black line, fits to an elliptical cylinder model with a dashed line and fits to the fractal model are shown with a dotted line. The scattering profiles have been offset by a factor of 10 for clarity.

3.3 Retention of the *cis*-PSS after Rheology Measurements
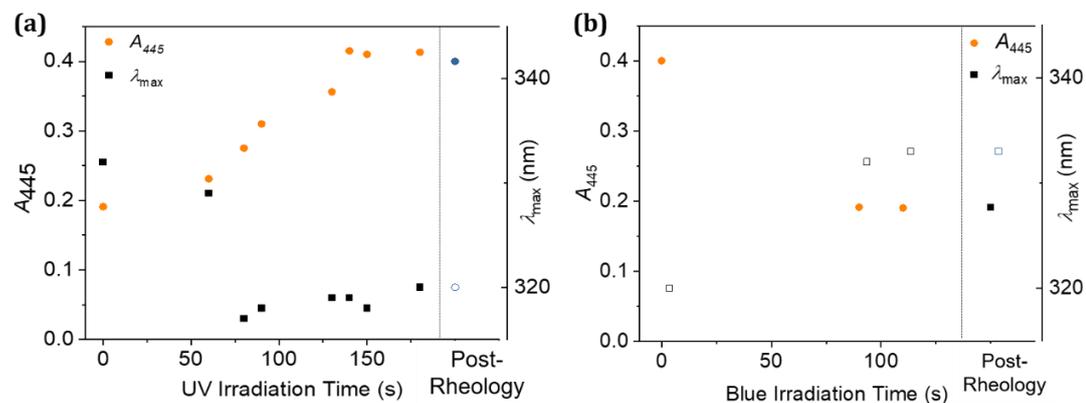
Figure A.3.6. UV-Vis absorption spectra were collected on aliquots of $C_6AzoOC_4E_4$ (2.5 wt% parent solution, aliquots diluted for UV-Vis absorption measurements) removed during the light irradiation process (either UV or blue) and after rheology measurements. (a) Under UV irradiation, the presence of the cis-isomer is characterised by the increase in the absorbance of the n $\rightarrow$ π^* band (445 nm) and a absorption maximum (λ_{max}) of 318 nm. (b) The return to the trans-isomer dominant state under blue irradiation is characterised by a decrease in absorption at 445 nm and λ_{max} of 332 nm.

3.4 Additional Cryo-TEM Images
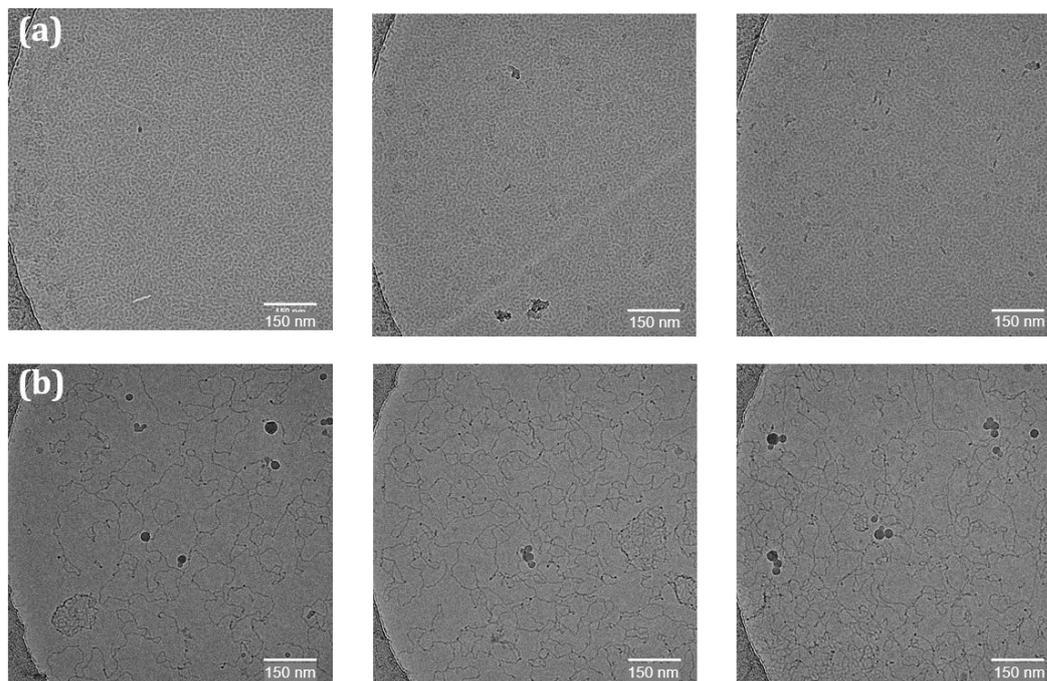
Figure A.3.7. Cryo-TEM images of $C_6AzoOC_4E_4$ (2.5 wt% in H_2O) before (a) and after (b) UV irradiation to form the cis-PSS**.**

3.5 Small-Angle X-Ray Scattering: Fitted Parameters and Models

Table A.3.3. Structural parameters obtained from SAXS data for *trans*- and *cis*-$C_6AzoOC_4E_4$ in H_2O (0.5 and 2.5 wt%) at 25 °C. R is the cylinder radius obtained from the best fit to the data using the model specified. Axis ratio is the proportion of minor to major axis for an elliptical cylinder, L_K is the Kuhn length obtained from the flexible cylinder model, L is the value for cylinder or contour length, SLD is the scattering length density of the sample (SLD solvent = -0.561 and SLD dry sample = 1.2 ×10^{-6} Å^{-2} for reference), PD_r is the polydispersity applied to the cylinder radius, PD_{Lk} is the polydispersity applied to the Kuhn length. All model fittings were performed in SasView.

Isomer	wt%	Model	R (Å)	Axis Ratio	L_K (Å)	L (Å)	SLD (×10^{-6} Å^{-2})	PD_r	PD_{Lk}	χ^2
trans	0.5	Cylinder	55.0	-	-	5055*	1.19	0.12		1.71
trans	2.5	Flexible Cylinder	59.5	-	677.4*	18186*	1.02	0.2	0.12	6.48
cis	0.5	Elliptical Cylinder	28.9	7.4	-	6664*	0.52	-	-	0.53
cis	2.5	Flexible Cylinder	41.5	-	175.7	4437*	0.99	-	-	1.01
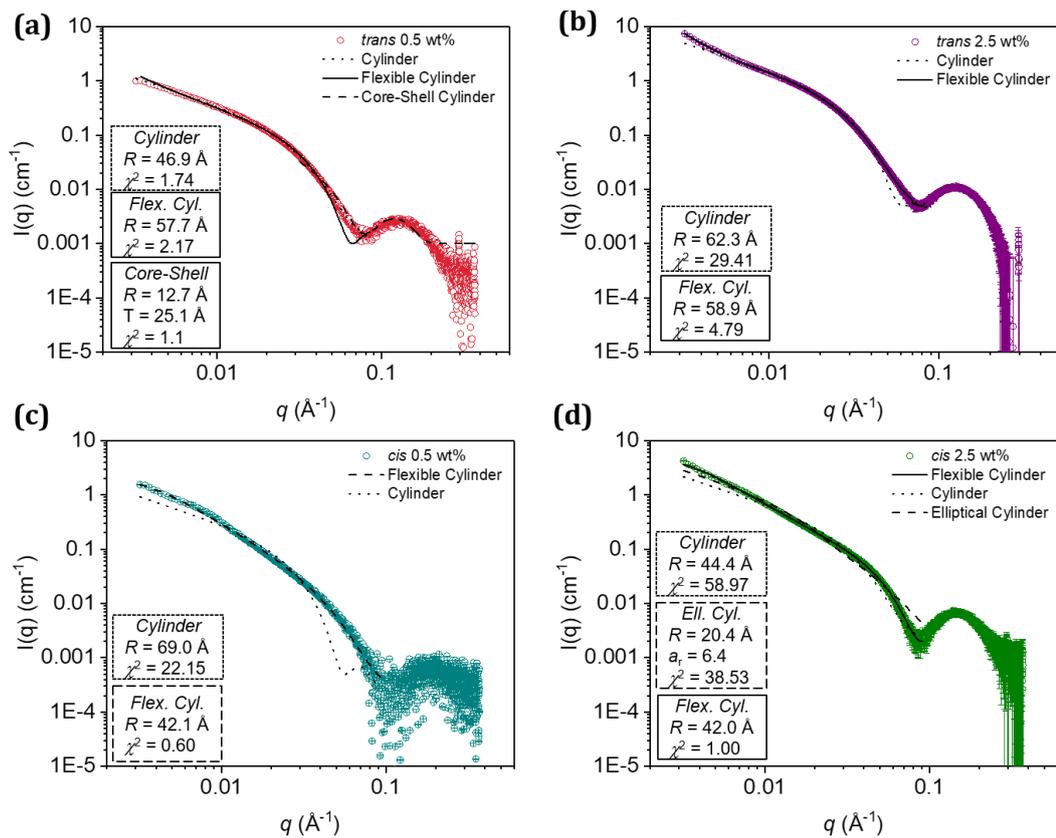
Figure A.3.8. SAXS profiles of $C_6AzoOC_4E_4$ in (a) the native *trans*-form at 0.5 wt% and (b) 2.5 wt% and (c) in the *cis*-PSS at 0.5 wt% and (d) 2.5 wt%. Fits to various cylindrical models are shown, with the associated parameters (R = radius, a_r = axis ratio, χ^2 = goodness-of-fit) shown in boxes on the left of each graph.

Appendix to Chapter 4

4.1 Supplementary Rheology Measurements
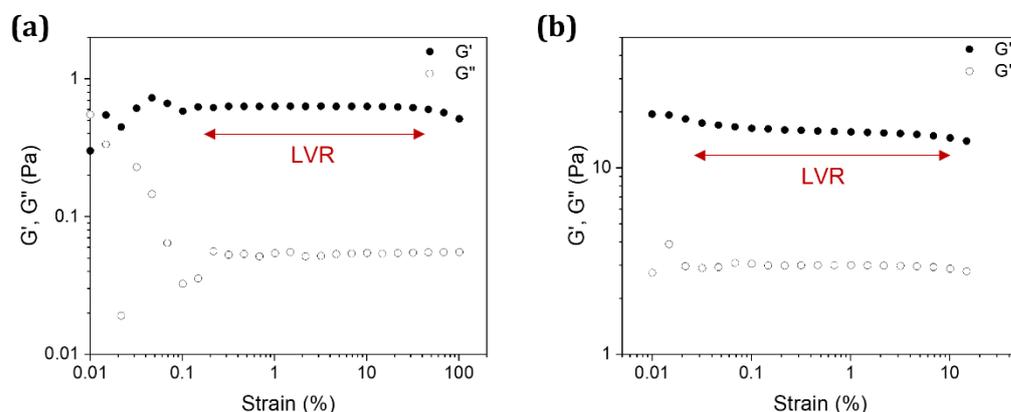
Figure A.4.1. Amplitude measurements to determine the linear viscoelastic range (LVR). Graphs shows storage (G') and loss (G") moduli as a function of % strain for (a) 2.5 wt% and (b) 4 wt% $C_6AzoOC_4E_4$.
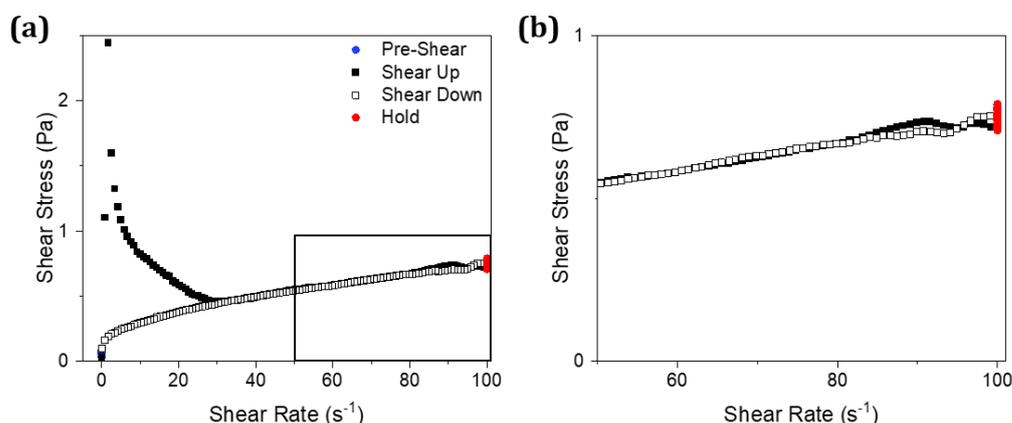
Figure A.4.2. Flow-rate measurements to determine time-dependent behaviour. (a) shows the shear-up ramp (black squares), hold step at 100 s^{-1} (red circles) and shear-down ramp (open squares). For the shear-up and shear-down ramps, 120 points were measured across the range 0.01-100 s^{-1} with points measured every 2.5 s. For the hold step, 50 points were measured at 100 s^{-1} with one point taken every 3.6 s. (b) shows a zoomed-in excerpt of the high shear region, showing two small hysteresis loops, one positive and one negative. The shear-thickening behaviour that occurred during the hold step can also be observed.

4.2 Additional Rheo-SANS Data and Analysis (2.5 wt%)
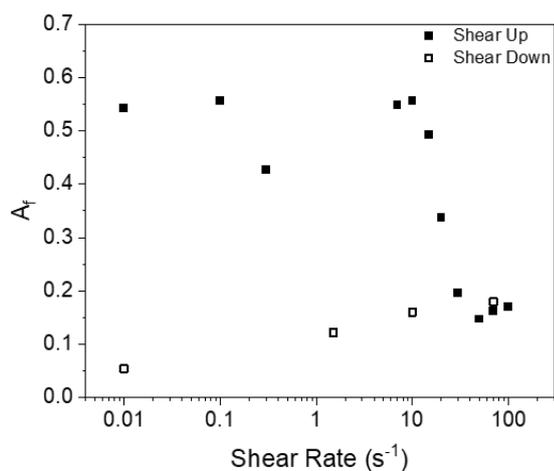
Figure A.4.3. Alignment factor as a function of shear rate for 2.5 wt% $C_6AzoOC_4E_4$ on shear-up (black squares) and shear-down (open squares) ramps, determined from annularly reduced data.
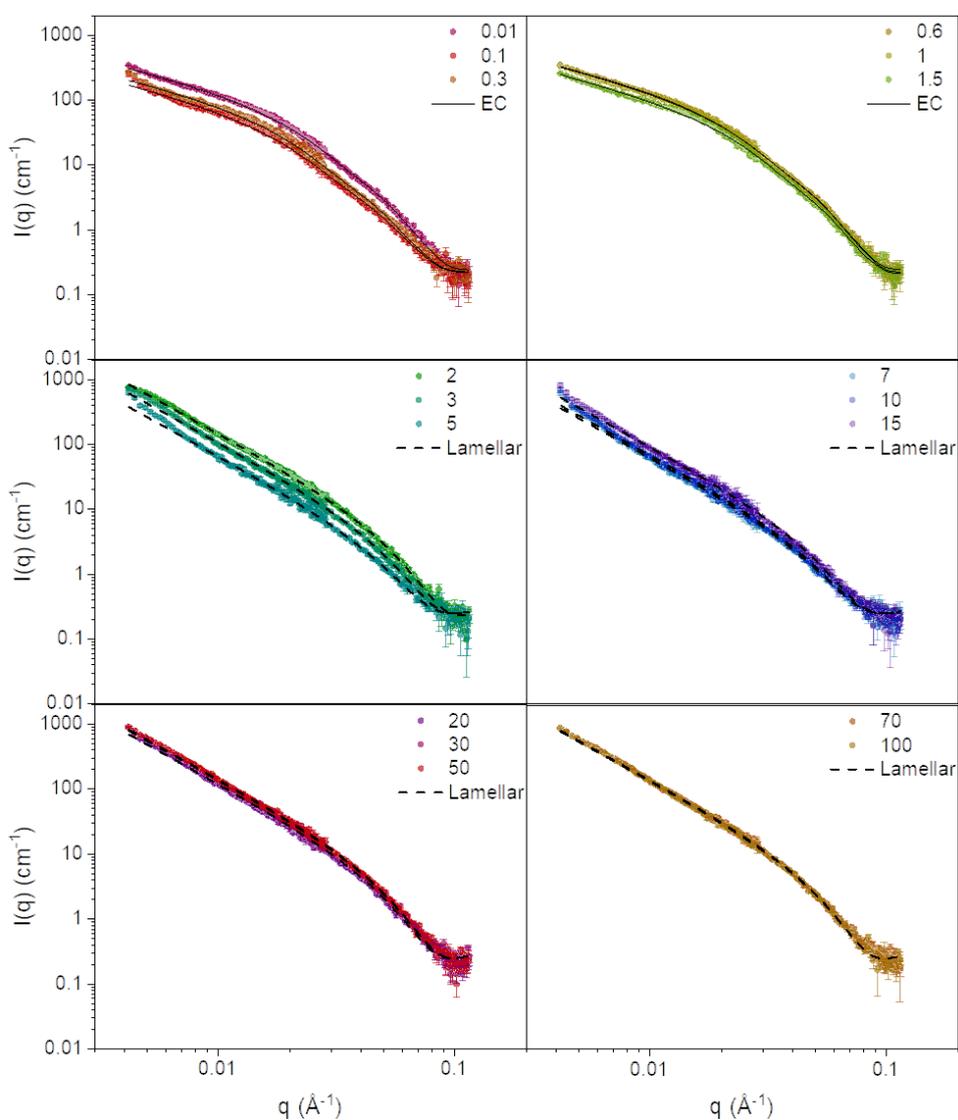
Figure A.4.4. Scattering profiles for 2.5 wt% $C_6AzoOC_4E_4$ in the horizontal direction, shear-up ramp. Models to elliptical cylinder (solid line) or lamellar (dashed line) model are fitted.
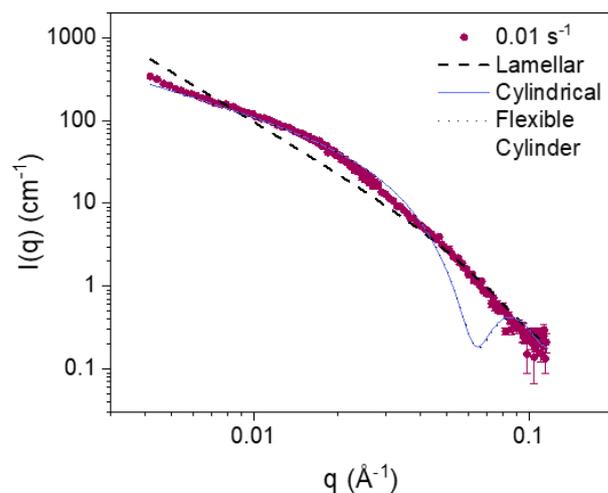
Figure A.4.5. Attempts to fit other models to the scattering profile at 0.01 s^{-1} in the horizontal direction for a 2.5 wt% aqueous solution of $C_6AzoC_4E_4$ on the shear-up ramp. The lamellar model (black dashed line), cylindrical model (blue solid line) and flexible cylinder model (black dotted line) were all inadequate to describe the scattering profile. An elliptical cylinder model was used to describe the scattering model in this case.
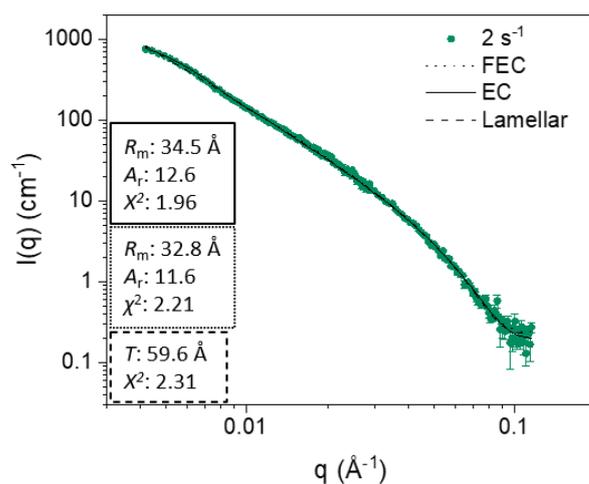
Figure A.4.6. Attempts to fit other models to the scattering profile at 2 s^{-1} in the horizontal direction for a 2.5 wt% aqueous solution of $C_6AzoC_4E_4$ on the shear-up ramp. The lamellar model (black dashed line), elliptical cylindrical model (black solid line) and flexible cylinder model (black dotted line) all described the scattering profile reasonably well, with low goodness-of-fit values, χ^2. The lamellar model was ultimately chosen as the physical parameters given by the cylindrical model describe a lamellar sheet in practice (high axis ratio, A_r, where major axis is 11-12 times the size of the minor axis, R_m). In general, when several models can describe the data, it is considered best to choose the model with the fewest fitting parameters, in this case the lamellar model, in which only thickness and SLD were varied, while for the (flexible) elliptical cylinder models, length, (Kuhn length), radius, axis ratio and SLD were all varied. At higher shear rates, the elliptical cylindrical models fitted the scattering profiles increasingly poorly and vice versa for the lamellar model.

Table A.4.1 Physical parameters obtained from fitting either an elliptical cylinder to a lamellar model to the scattering profiles in the horizontal direction for a 2.5 wt% aqueous solution of $C_6AzoC_4E_4$ on the shear-up ramp. The axis ratio describes the ratio of the long to short radius of the cylinder, SLD refers to the scattering length density of the scattering bodies in solution, scale is a multiplying factor in the fitting process, proportional to the volume fraction and χ^2 refers to the goodness-of-fit.

Shear Rate (s^{-1})	Model	Radius (Å)	Axis Ratio	Thickness (Å)	SLD (10^{-6} Å^{-2})	Scale	χ^2
0.01	Elliptical Cylinder	33.9	3.3	-	2.03	0.019	2.73
0.1	Elliptical Cylinder	34.0	3.6	-	3.35	0.020	1.71
0.3	Elliptical Cylinder	34.9	3.5	-	2.90	0.019	1.95
0.6	Elliptical Cylinder	33.3	3.4	-	2.00	0.020	1.86
1	Elliptical Cylinder	33.3	3.3	-	2.01	0.020	2.94
1.5	Elliptical Cylinder	32.9	3.1	-	2.71	0.024	3.49
2	Lamellar	-	-	59.6	2.23	0.023	2.31
3	Lamellar	-	-	63.0	2.90	0.023	4.24
5	Lamellar	-	-	64.0	2.57	0.019	3.13
7	Lamellar	-	-	65.2	3.07	0.014	3.02
10	Lamellar	-	-	65.4	2.83	0.014	3.09
15	Lamellar	-	-	65.4	2.45	0.015	3.56
20	Lamellar	-	-	65.2	2.21	0.017	3.46
30	Lamellar	-	-	64.2	2.06	0.019	2.87
50	Lamellar	-	-	64.2	2.24	0.020	2.67
70	Lamellar	-	-	64.4	2.49	0.024	2.80
100	Lamellar	-	-	64.4	2.27	0.020	2.52
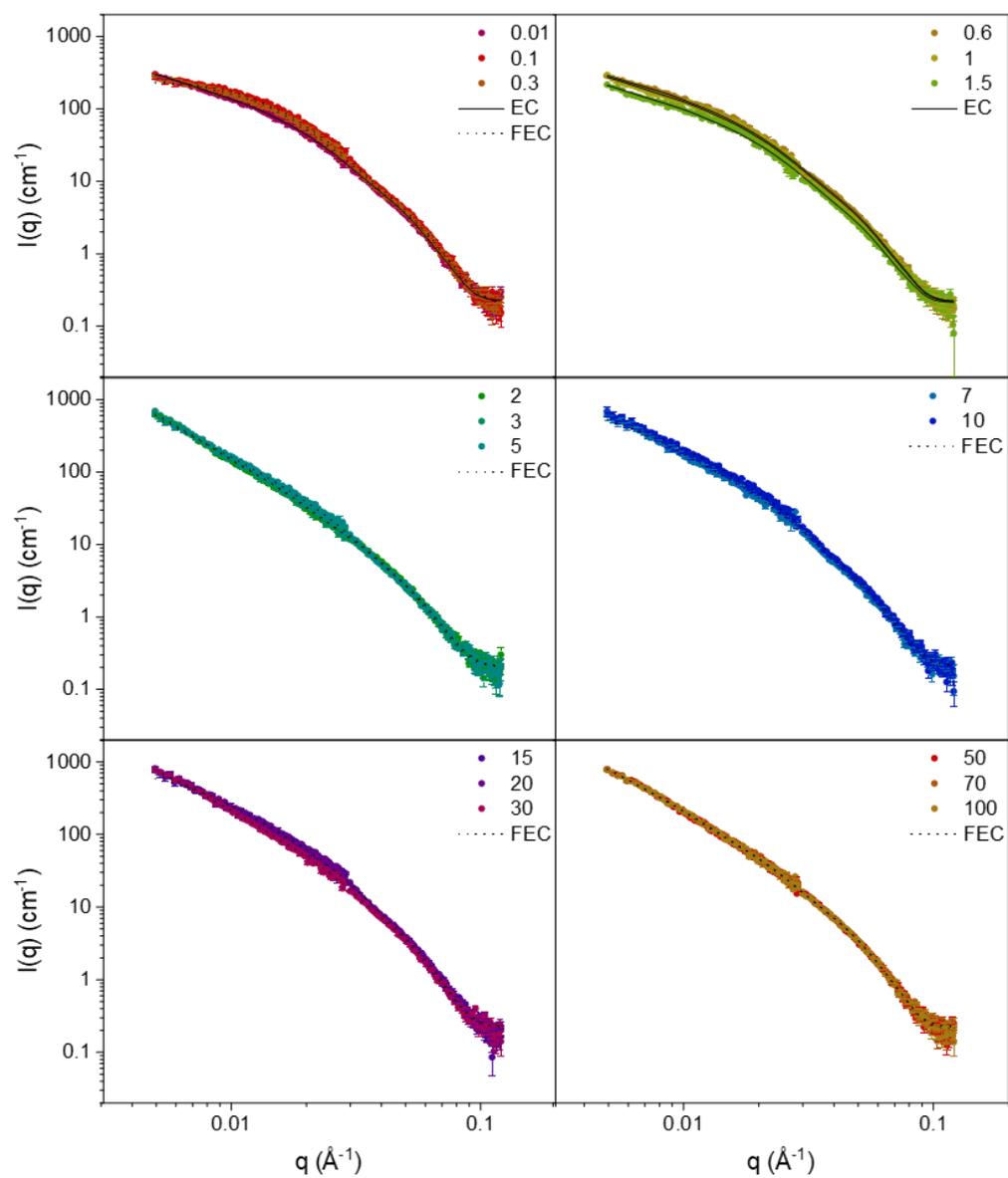
Figure A.4.7. Scattering profiles for 2.5 wt% $C_6AzoOC_4E_4$ in the vertical direction, shear-up ramp. Models to elliptical cylinder (solid line) or flexible elliptical cylinder (dotted line) model are fitted.
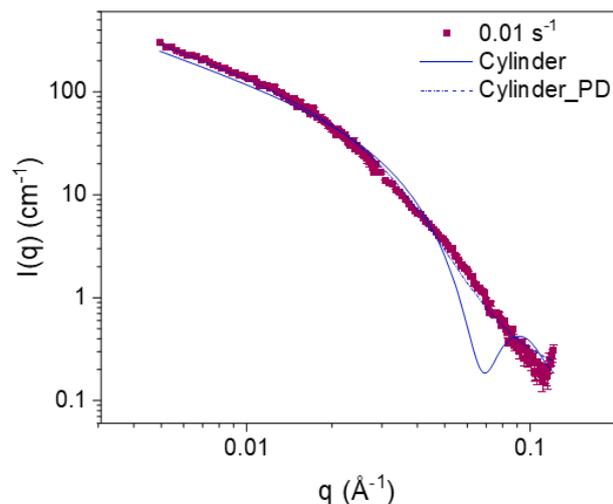
Figure A.4.8. Attempts to fit other model to the individual scattering profiles in the vertical direction for a 2.5 wt% aqueous solution of $C_6AzoC_4E_4$ on the shear-up ramp. The cylinder model is inadequate to fit the data. The cylindrical model with polydispersity (>0.6) on the radius described the profiles better but was still insufficient. In practice, an elliptical cylinder was used to fit the scattering profile, which is qualitatively not hugely different from a cylinder model with polydisperse radii.

Table A.4.2 Physical parameters obtained from fitting either an elliptical cylinder or flexible elliptical cylinder (FEC) to the scattering profiles in the vertical direction for a 2.5 wt% aqueous solution of $C_6AzoC_4E_4$ on the shear-up ramp. L_K is the Kuhn length, SLD refers to the scattering length density of the scatterers in solution, scale is a multiplying factor in the fitting process, proportional to the volume fraction, and χ^2 refers to the goodness-of-fit.

Shear Rate (s^{-1})	Model	Radius (Å)	Axis Ratio	L_K (Å)	SLD (10^{-6} Å^{-2})	Scale	χ^2
0.01	Elliptical Cylinder	33.3	3.5	-	3.00	0.014	1.60
0.1	FEC	30.9	3.3	142.4	3.13	0.014	2.00
0.3	FEC	31.2	3.2	177.1	3.85	0.022	1.63
0.6	Elliptical Cylinder	33.1	3.5	-	3.37	0.024	2.00
1	Elliptical Cylinder	33.3	3.5	-	2.73	0.019	1.89
1.5	Elliptical Cylinder	33.4	3.3	-	2.26	0.020	2.36
2	FEC	33.3	4.7	321.7	3.47	0.019	1.69
3	FEC	34.3	5.2	359.5	3.40	0.018	1.93
5	FEC	33.7	3.0	181.3	2.72	0.018	1.59
7	FEC	33.3	2.8	166.3	3.02	0.021	2.46
10	FEC	32.7	3.0	157.6	2.97	0.024	1.59
15	FEC	33.4	2.8	145.3	2.52	0.015	2.27
20	FEC	33.9	2.8	170.4	3.20	0.018	2.55
30	FEC	34.3	3.2	220.6	3.88	0.016	1.58
50	FEC	34.7	3.6	256.0	3.02	0.017	2.05
70	FEC	34.1	3.4	227.6	3.86	0.022	1.17
100	FEC	34.4	3.5	234.3	3.85	0.025	1.74
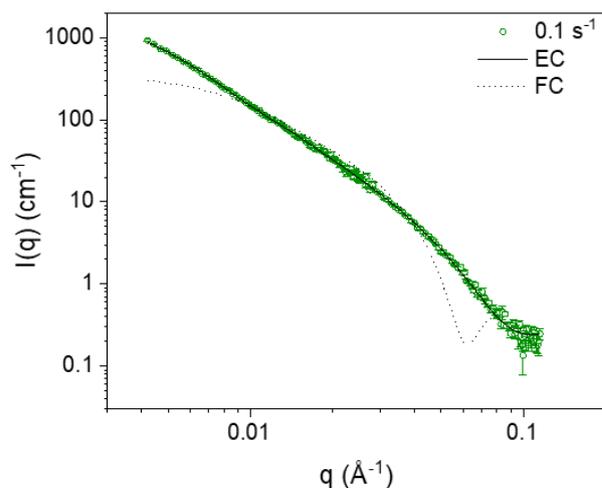
Figure A.4.9. Attempts to fit other models to the individual scattering profiles in the horizontal direction for a 2.5 wt% aqueous solution of $C_6AzoC_4E_4$ on the shear-down ramp. The elliptical cylinder model (EC, solid line) fits the data well but the physical parameters output described a fundamentally lamellar structure due to the very high axis ratio (Radius: 35.3 Å, Axis Ratio 11.1). The Lamellar model was chosen instead as it has fewer fitted parameters and still fits the data well (low χ^2). The lamellar model had an associated thickness of 65.2 Å, similar to the value of two radii. The flexible cylinder model (dotted line) was inadequate to describe the data.

Table A.4.3 Physical parameters obtained from fitting a lamellar model to the scattering profiles in the horizontal direction for a 2.5 wt% aqueous solution of $C_6AzoC_4E_4$ on the shear-down ramp. SLD refers to the scattering length density of the scatterers in solution, scale is a multiplying factor in the fitting process, proportional to the volume fraction, χ^2 refers to the goodness-of-fit. The value for thickness obtained is roughly twice the length of the surfactant tail length.

Shear Rate (s^{-1})	Model	Thickness (Å)	SLD (10^{-6} Å^{-2})	Scale	χ^2
100	Lamellar	64.4	2.27	0.020	2.53
70	Lamellar	64.3	2.10	0.019	2.57
50	Lamellar	63.5	2.41	0.023	2.38
30	Lamellar	64.1	2.41	0.022	1.92
20	Lamellar	64.1	2.03	0.018	1.92
15	Lamellar	64.0	2.20	0.019	2.65
10	Lamellar	64.5	2.03	0.018	2.18
7	Lamellar	64.3	2.39	0.022	2.70
5	Lamellar	64.8	2.08	0.019	2.78
3	Lamellar	64.3	1.90	0.018	2.90
2	Lamellar	64.5	1.75	0.017	3.03
1.5	Lamellar	64.1	1.96	0.019	2.80
1	Lamellar	64.1	2.28	0.022	2.80
0.6	Lamellar	64.2	2.10	0.020	3.17
0.3	Lamellar	64.0	2.67	0.028	3.35
0.1	Lamellar	64.5	2.54	0.026	3.44
0.01	Lamellar	65.2	2.89	0.031	3.76
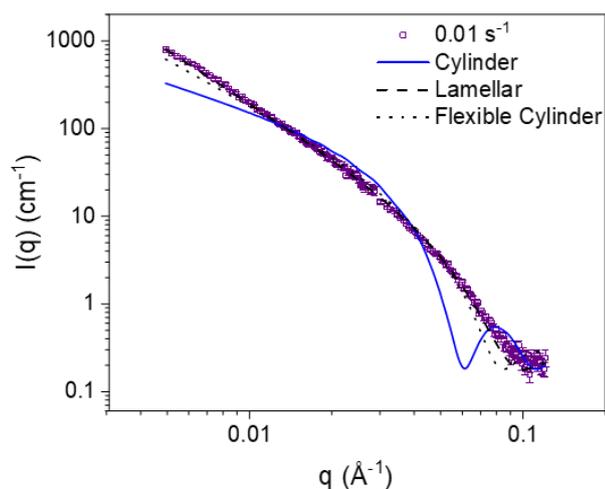
Figure A.4.10. Attempts to fit other model to the individual scattering profiles in the vertical direction for a 2.5 wt% aqueous solution of $C_6AzoC_4E_4$ on the shear-down ramp. A cylindrical model (blue line), lamellar model (dashed black line) and flexible cylinder model (dotted black line) were inadequate to describe the data. A flexible elliptical cylinder model was used in practice.

Table A.4.4 Physical parameters obtained from fitting a flexible elliptical cylinder (FEC) to the scattering profiles in the vertical direction for a 2.5 wt% aqueous solution of $C_6AzoC_4E_4$ on the shear-down ramp. L_K refers to the Kuhn length, SLD refers to the scattering length density of the scatterers in solution, scale is a multiplying factor in the fitting process, proportional to the volume fraction, χ^2 refers to the goodness-of-fit.

Shear Rate (s^{-1})	Model	Radius (Å)	Axis Ratio	L_K	SLD $(10^{-6}\ Å^{-2})$	Scale	χ^2
100	FEC	34.7	3.2	221.2	2.96	0.018	1.69
70	FEC	34.5	3.5	239.4	2.39	0.019	1.49
50	FEC	34.6	3.5	241.3	3.37	0.024	1.38
30	FEC	35.1	2.9	202.7	2.45	0.020	1.70
20	FEC	34.8	3.3	232.8	2.00	0.018	1.29
15	FEC	34.4	3.3	223.1	3.68	0.020	1.49
10	FEC	34.5	3.3	228.3	2.16	0.018	1.68
7	FEC	34.8	1.9	224.5	2.37	0.019	1.90
5	FEC	34.5	1.3	200.2	2.86	0.015	1.29
3	FEC	34.6	3.2	204.1	2.52	0.020	1.45
2	FEC	34.7	3.8	277.1	2.04	0.017	1.40
1.5	FEC	35.2	3.4	243.0	3.04	0.020	2.10
1	FEC	34.7	3.6	248.6	2.63	0.019	1.52
0.6	FEC	34.6	3.8	259.3	3.33	0.023	1.57
0.3	FEC	34.3	4.1	284.4	2.63	0.018	1.58
0.1	FEC	34.9	3.6	256.1	2.83	0.019	2.42
0.01	FEC	34.6	3.5	237.7	2.19	0.023	1.87
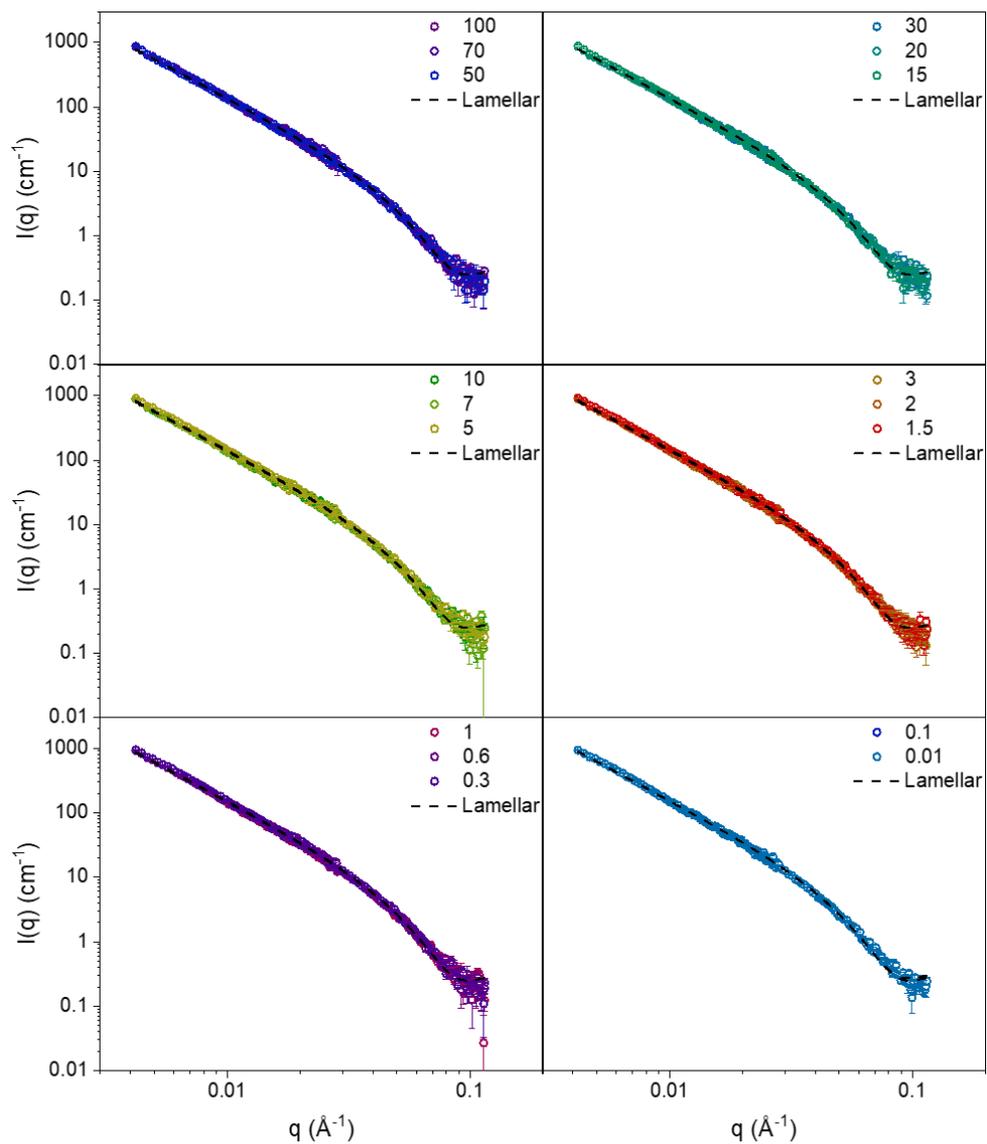
Figure A.4.11 Individual scattering profiles from a 2.5 wt% aqueous solution of $C_6AzoOC_4E_4$ for the horizontal direction (flow direction) on the shear-down ramp. A lamellar model (dashed line) is fitted to the scattering profiles.
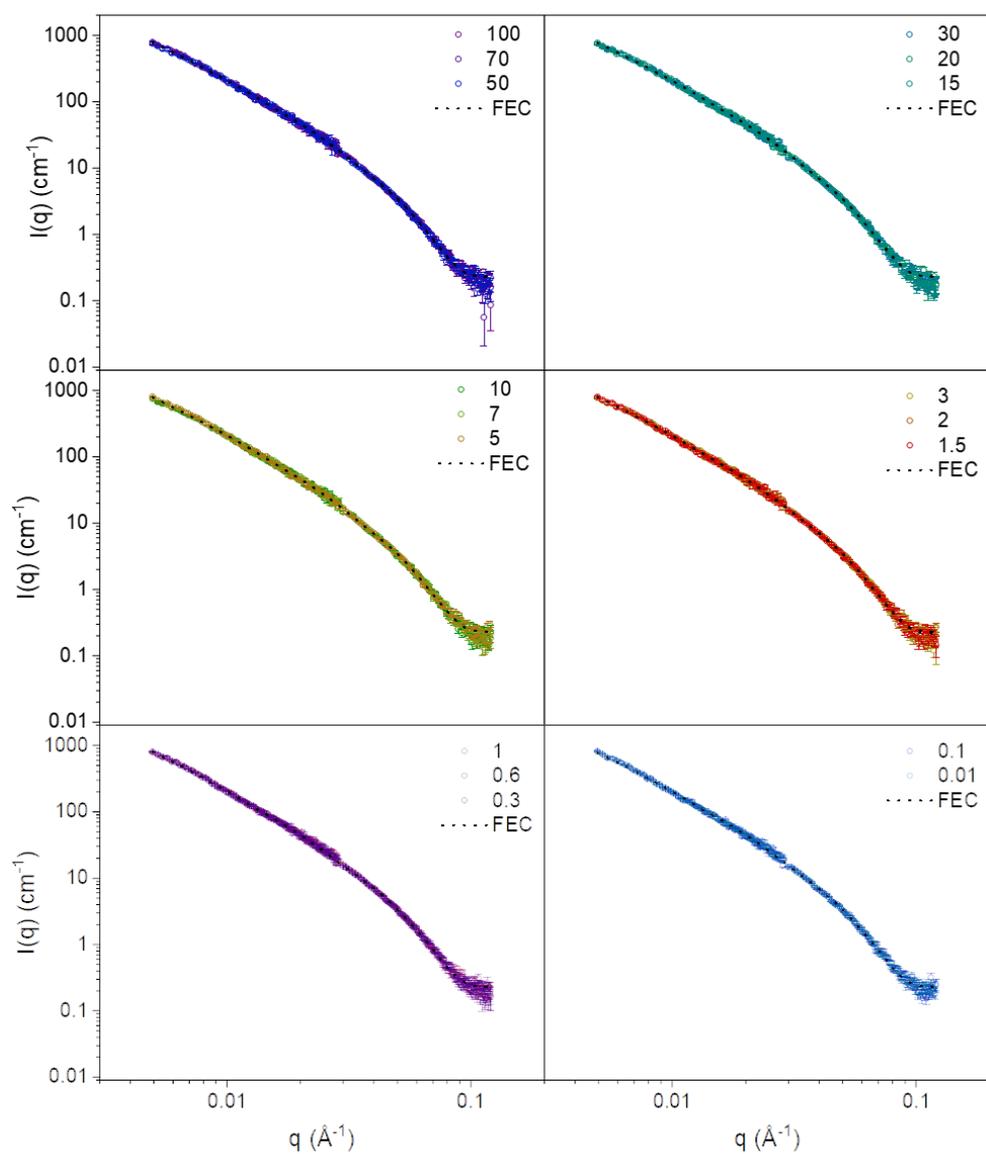
Figure A.4.12 Individual scattering profiles from a 2.5 wt% aqueous solution of $C_6AzoOC_4E_4$ for the vertical direction on the shear-down ramp. A flexible elliptical model (dotted line) is fitted to the scattering profiles.
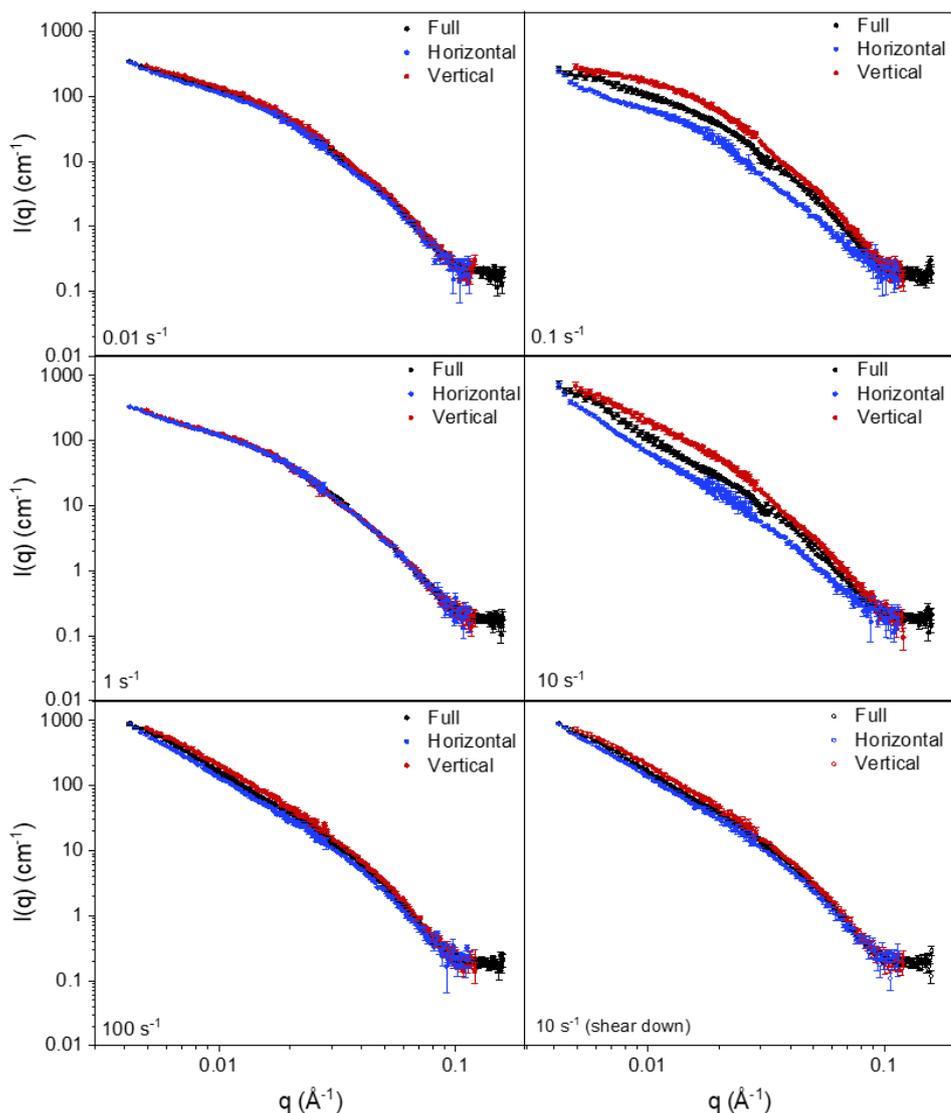
Figure A.4.13. Comparison of the scattering profiles that have been partially reduced in two perpendicular directions, horizontal (blue) and vertical (red) with the scattering profile that has been integrated and reduced over the full angular range (black). A selection of shear rates are shown across the shear-up ramp (solid circles) with one shear rate (10 s^{-1}) shown for the shear down ramp (open circles)
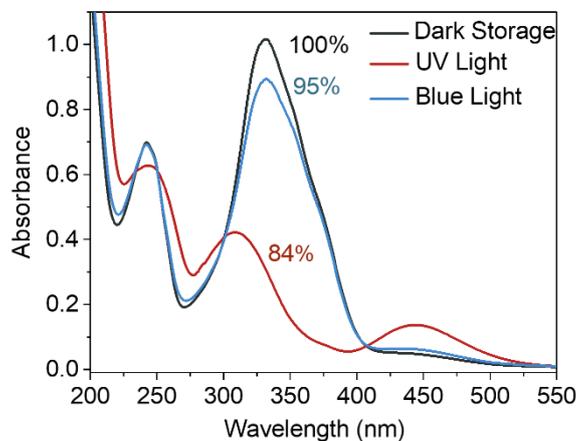
Figure A.4.14. UV-Vis absorption spectra for $C_6AzoOC_4E_4$ (above CMC in water). Asymmetry is evident in the absorption bands of the *trans*-isomer due to aromatic stacking of the planar azobenzene moieties, causing a blue-shift in the maximum.
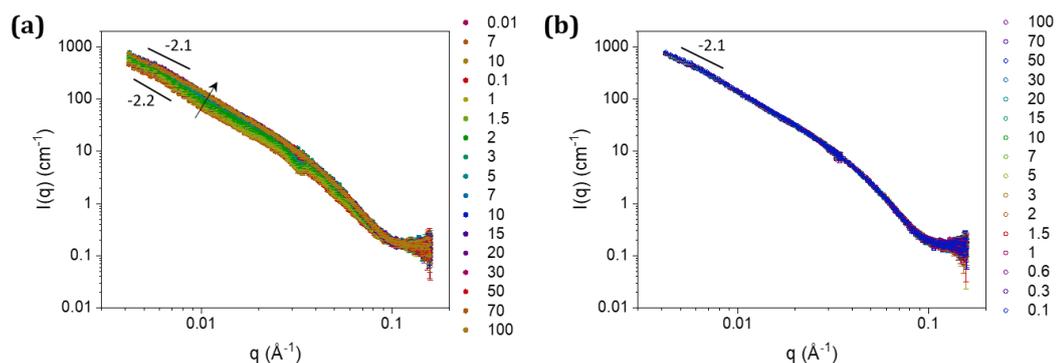
Figure A.4.15. 1D scattering profiles of $C_6AzoOC_4E_4$ (2.5 wt%) measured at 40 °C. (a) shows the scattering intensity as a function of scattering angle q for the shear-up ramp while (b) shows the intensity as a function of q for the shear-down ramp

Figure A.4.16. Photos of the colour change upon UV irradiation and photoisomerisation. The vial on the left contains 4 wt% $C_6AzoOC_4E_4$ in the native *trans*-state (orange) while the vial on the right shows 2.5 wt% C_6AzoOC_4E after UV irradiation (red). It should be noted that in the native *trans*-state, the 2.5 wt% solution is the same orange colour as the 4 wt% solution.
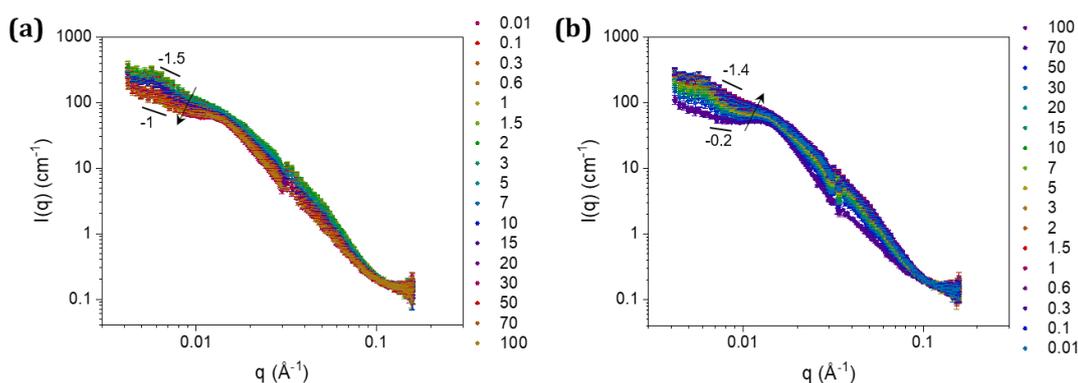
Figure A.4.17. Scattering profiles of a 4 wt% aqueous solution of $C_6AzoOC_4E_4$ in the native *trans*-form for the shear-up (a) and shear-down (b) ramps. The slope of the decay in scattering intensity at low q is indicated by solid line. The discontinuity at ~0.01 Å^{-1} is an artefact resulting from the process of merging the scattering intensity from two different detector distances.

Appendix to Chapter 5
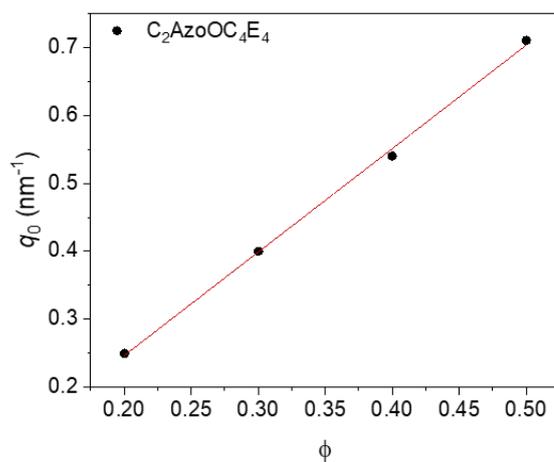
Figure A.5.1. Determination of the bilayer thickness of the lamellar LLC phase formed by $C_2AzoOC_4E_4$ in the native *trans*-state. The bilayer thickness is invariant with concentration, q_0 corresponds to the position of the first interference peak in the SAXS profiles and ϕ denotes the surfactant concentration in weight percent. The slope of the graph of q_0 *vs.* ϕ is $2\pi\delta$, where δ is the bilayer thickness.
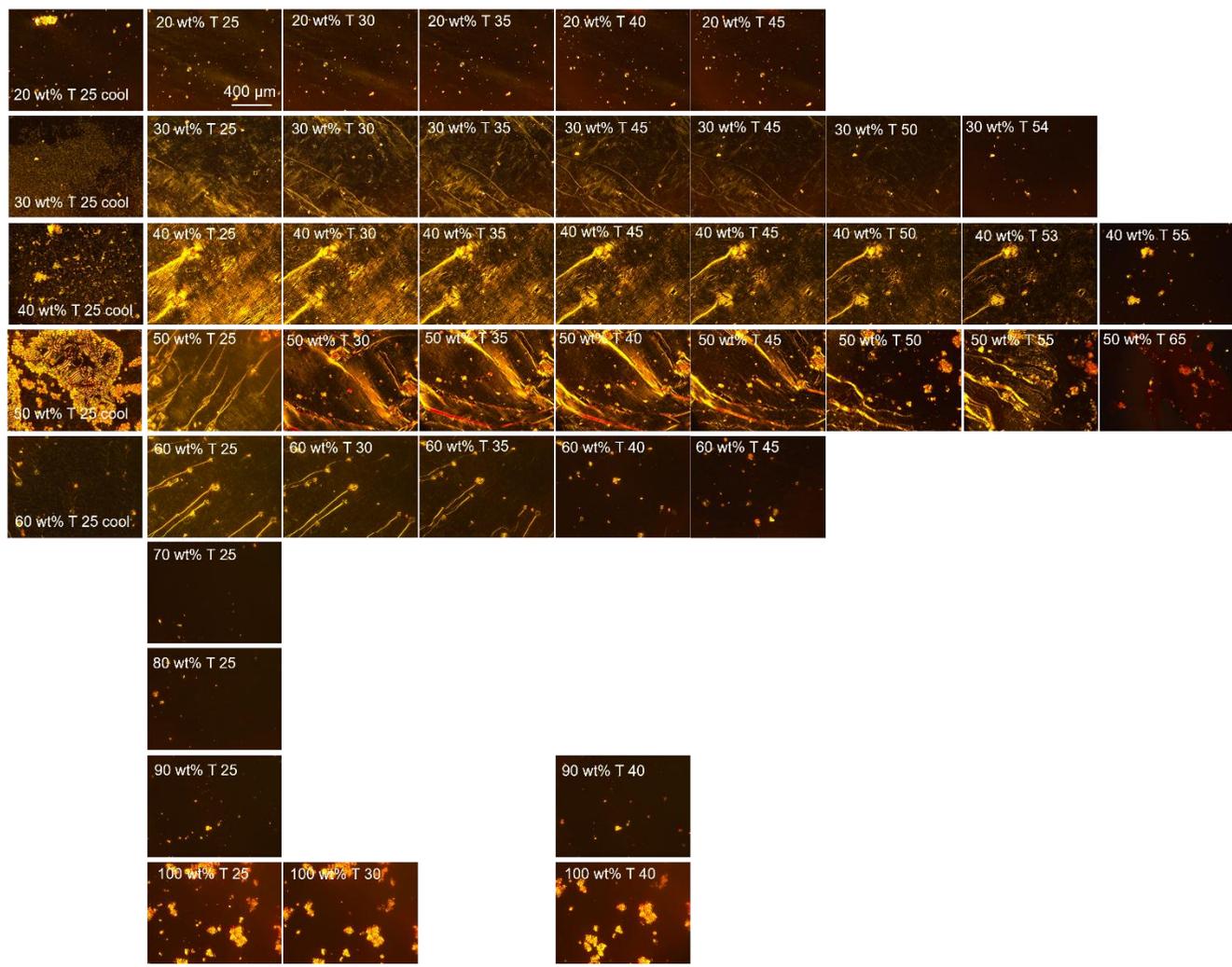
Figure A.5.2. POM images as a function of temperature for $C_2AzoOC_4E_4$
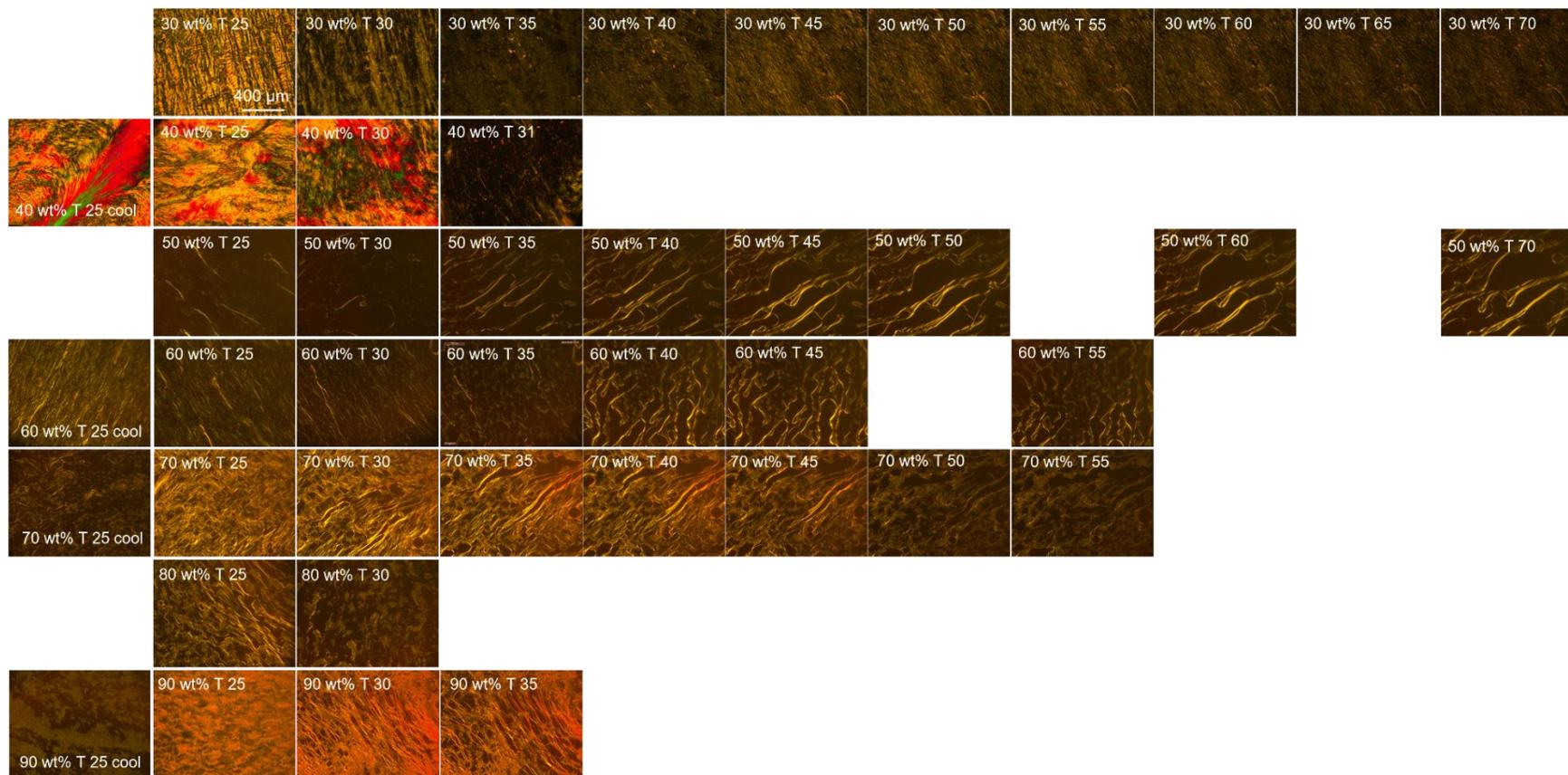
Figure A.5.3. POM images as a function of temperature for C₆AzoOC₄E₄
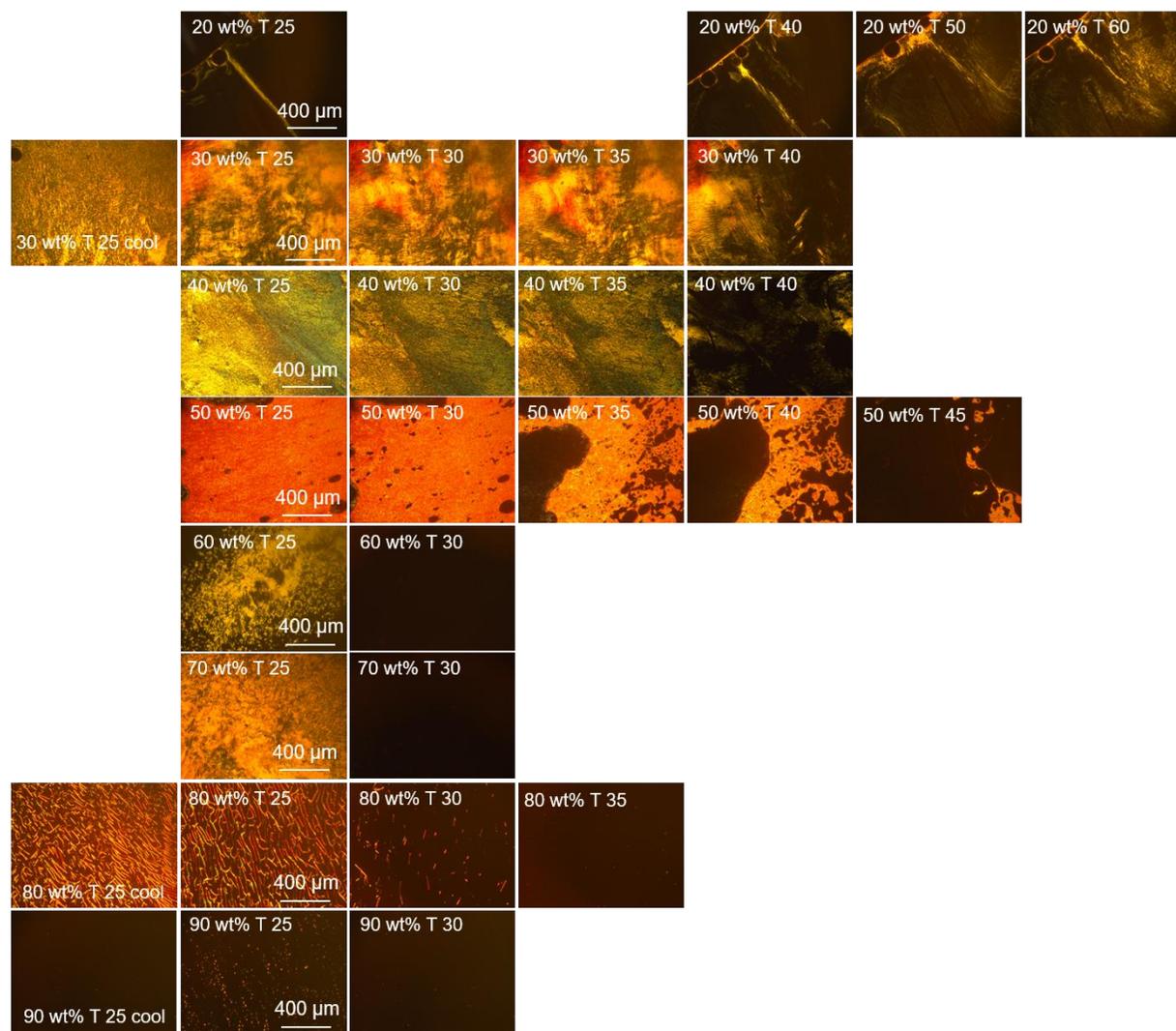
1Figure A.5.4. POM images as a function of temperature for $C_8AzoOC_4E_4$
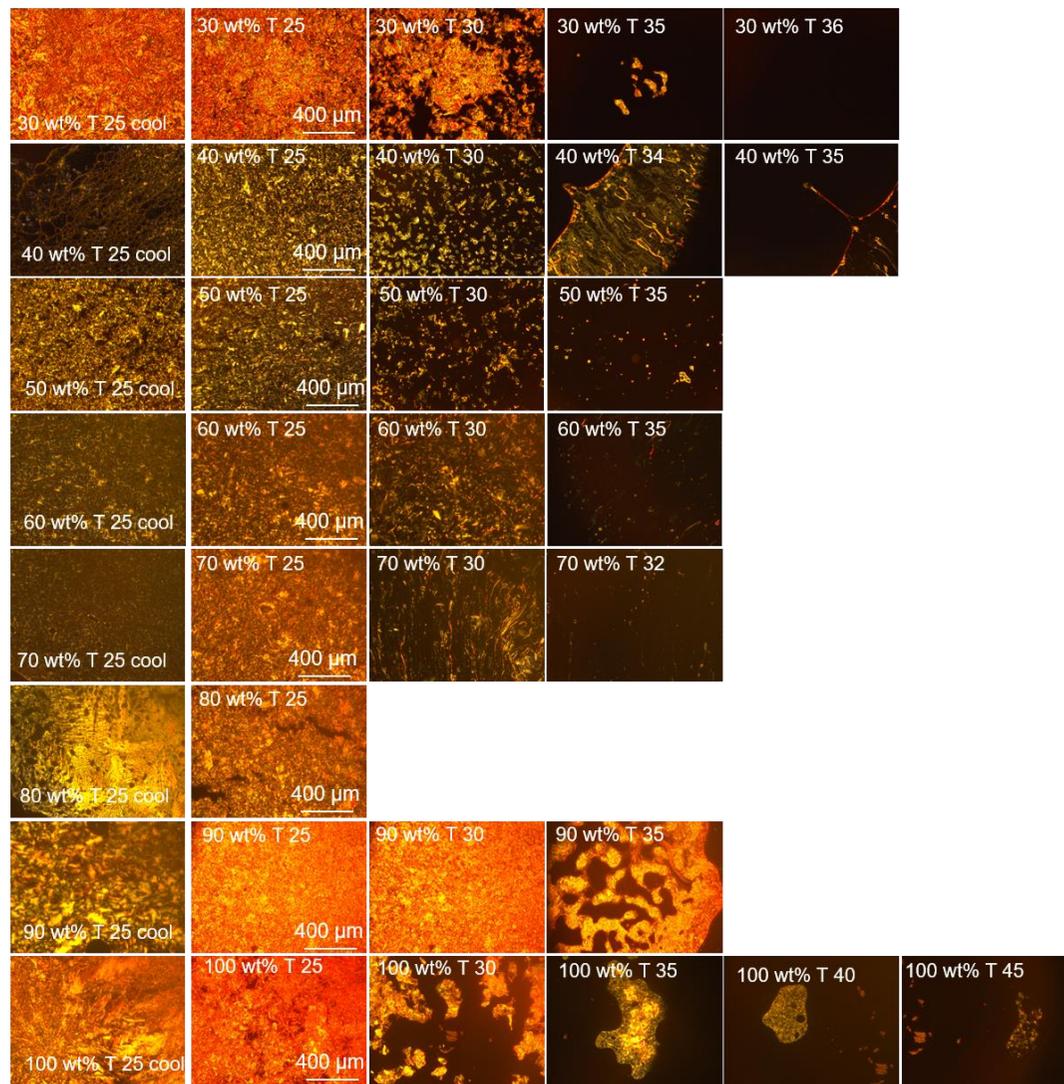
Figure A.5.5. POM images as a function of temperature for $C_8AzoOC_8E_4$
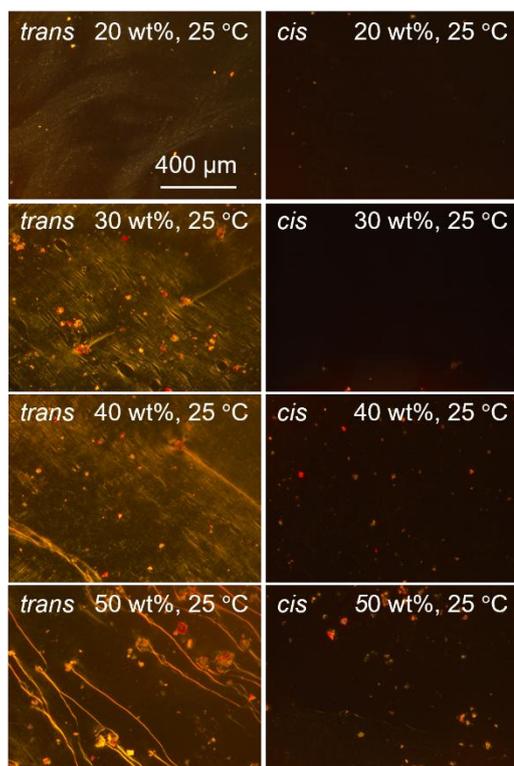
Figure A.5.6. POM images for solutions of $C_2AzoOC_4E_4$ before and after UV irradiation. Before irradiation the AzoPS is in the native *trans*-state and brightness and birefringent textures corresponding to lamellar LLC phases can be observed, while after UV irradiation the *cis*-PSS is formed and no indication of birefringent LLC phases is present.
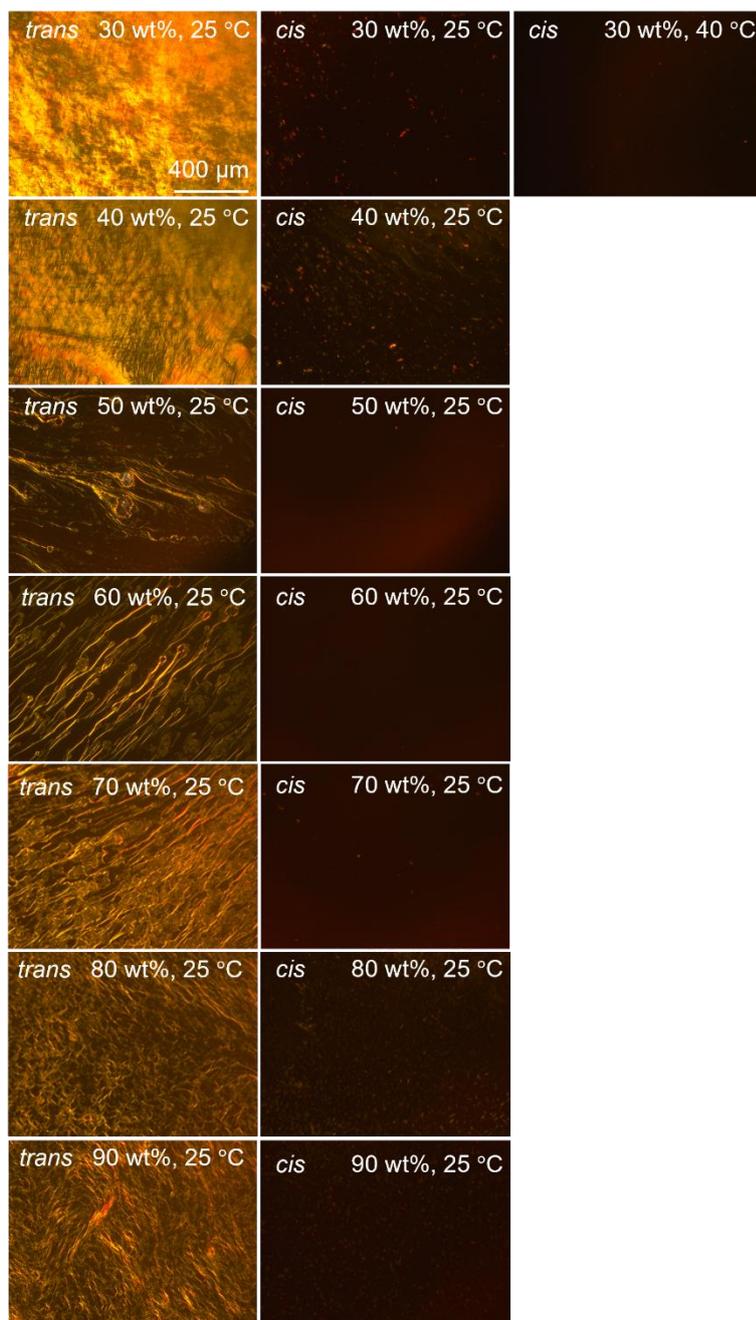
Figure A.5.7. POM images for solutions of $C_6AzoOC_4E_4$ before and after UV irradiation. Before irradiation the AzoPS is in the native *trans*-state and brightness and birefringent textures corresponding to either hexagonal or lamellar LLC phases can be observed, while after UV irradiation the *cis*-PSS is formed and no indication of birefringent LLC phases is present.
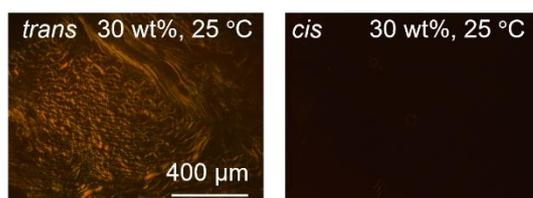
Figure A.5.8. POM images for a 30 wt% solution of $C_8AzoOC_4E_4$ before and after UV irradiation. Before irradiation the AzoPS is in the native *trans*-state and a texture corresponding to a hexagonal LLC phase can be observed, while after UV irradiation the *cis*-PSS is formed and no indication of a birefringent LLC phases is present.
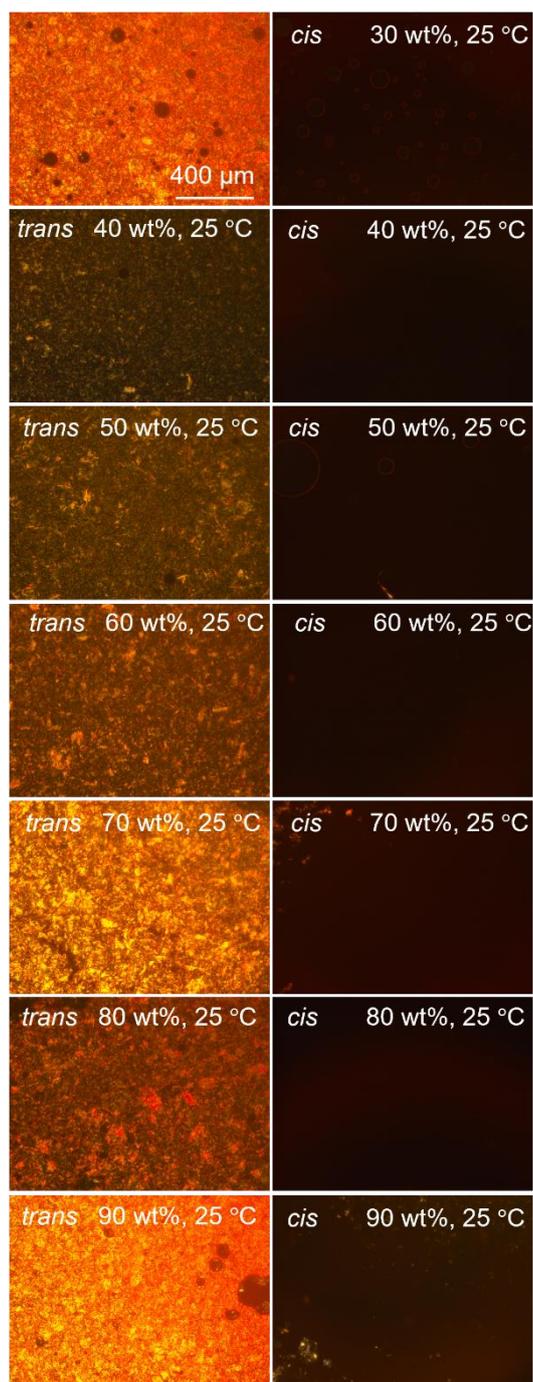
Figure A.5.9. POM images for solutions of $C_8AzoOC_8E_4$ before and after UV irradiation. Before irradiation the AzoPS is in the native *trans*-state and a crystalline texture can be observed in the POM images. After UV irradiation and formation of the *cis*-PSS, no indication of either crystallinity or birefringent LLC phases can be seen.
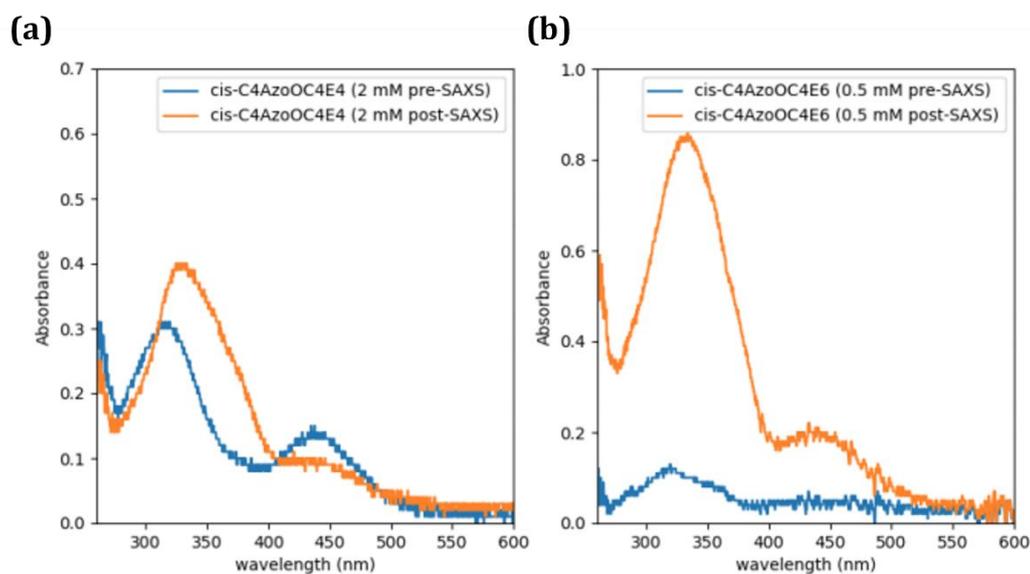
Figure A.5.10. SAXS accelerates the reverse isomerisation of the *cis*-isomers (a) and (b) show the UV-Vis absorption spectra for two ethylene glycol AzoPS of very similar molecular structures to the AzoPS reported here, and measured during the same experimental SAXS sessions under the same conditions. Clear reversion to the *trans*-form can be observed after SAXS measurement, highlighted by the red-shift of the π-π peak and decrease in the n-π* peak.
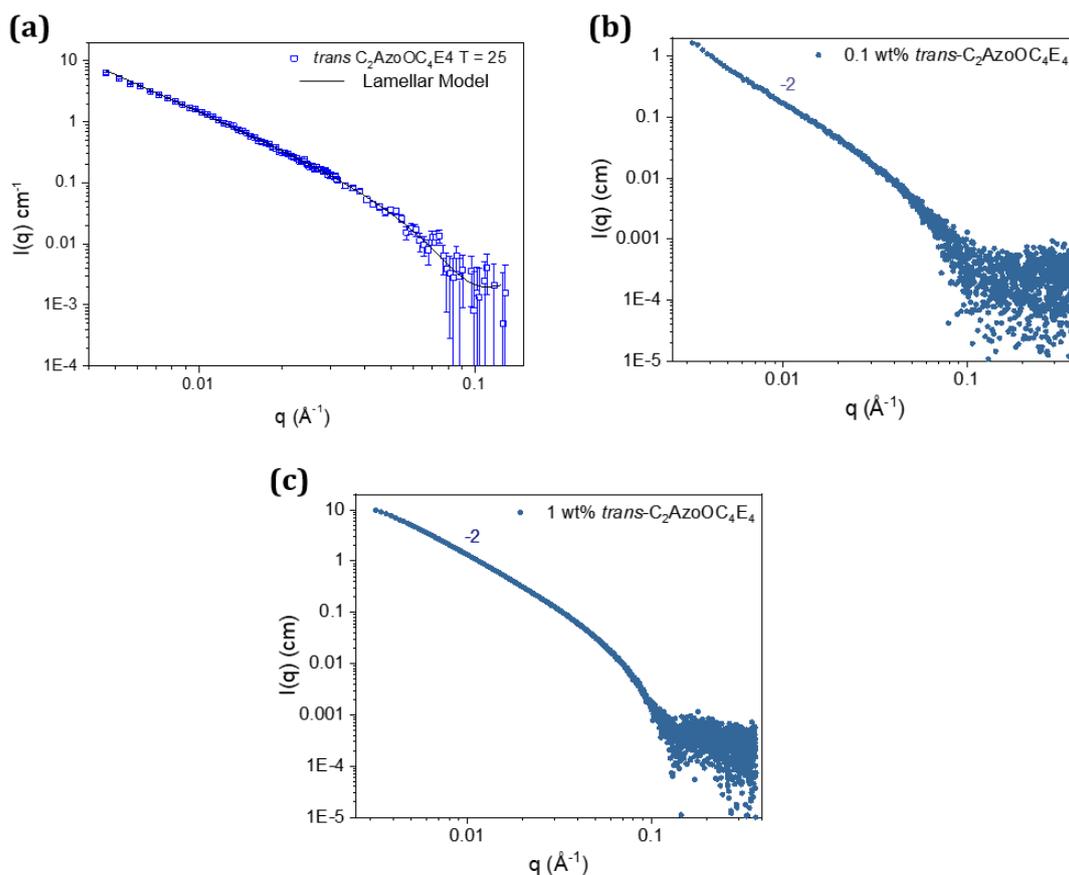
Figure A.5.11. At low concentration, $C_2AzoOC_4E_4$ self assembles into lamellar sheets, evidenced by a low q decay of q^{-2}. (a) shows a SANS profile at 0.05 wt% with a fit to a lamellar model shown in black (b) and (c) shows SAXS profiles at 0.1 and 1 wt% respectively, each with a decay consistent with lamellar sheets. All concentrations are above CMC*trans*.
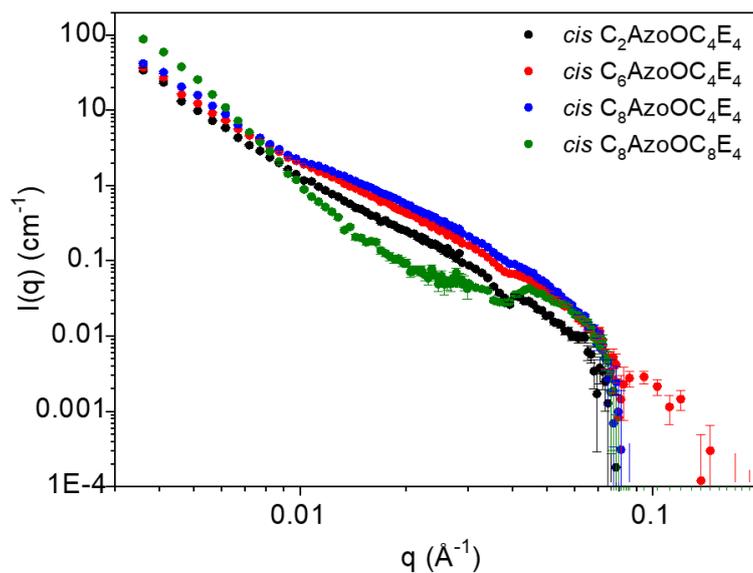
Figure A.5.12. Solutions of *cis*-AzoPS (0.05 wt%, 1mM in D$_2$O, >CMC$_{cis}$, T = 20 °C) show small-angle neutron scattering profiles, indicating aggregate behaviour in solution. A variety of different aggregate shapes are obtained. C$_2$AzoOC$_4$E$_4$ decayed as $q^{-2.9}$, indicating a mass fractal; the scattering profile of C$_6$AzoOC$_4$E$_4$ and C$_8$AzoOC$_4$E$_4$ were consistent with a flexible elliptical cylinder, albeit with an upturn at low q, and C$_8$AzoOC$_8$E$_4$ scattered as a fractal aggregate.

Appendix to Chapter 6
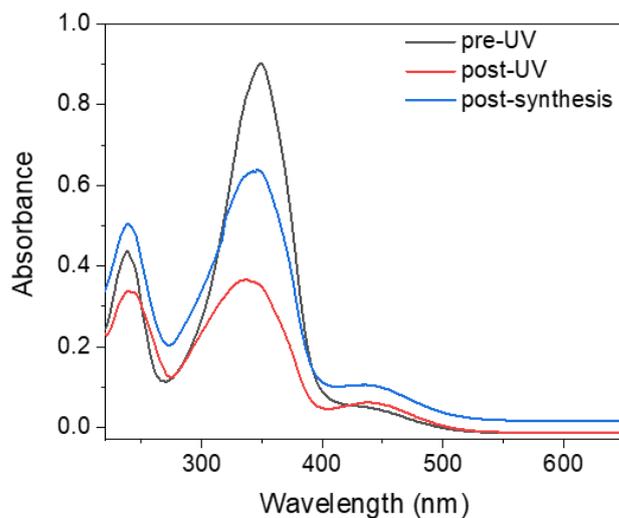
Figure A.6.1. UV-Vis absorption spectra of an aliquot of $C_6AzoOC_4E_4$ in EtOH used as a template to form titania nanoparticles using the non-evaporative sol-gel method. Spectra shown are: before UV irradiation (black), after UV irradiation to form the photostationary state (red) and after 24 hours static to form titania nanoparticles. The photostationary state (at 365 nm) was found to be 63% *cis*, with a 29% *cis* assembly remaining after the 24 hour static synthesis.
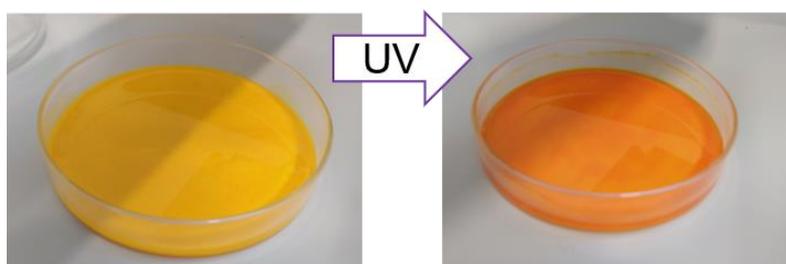
Figure A.6.2. Photographs of the hydrolysis step of the EISA approach. TTIP, AzoPS and EtOH are aged overnight and then poured into an open dish and irradiated with UV light for 30 minutes. A clear colour change is observed after UV irradiation. The solution is then left to evaporate to form the hydrolysed product.
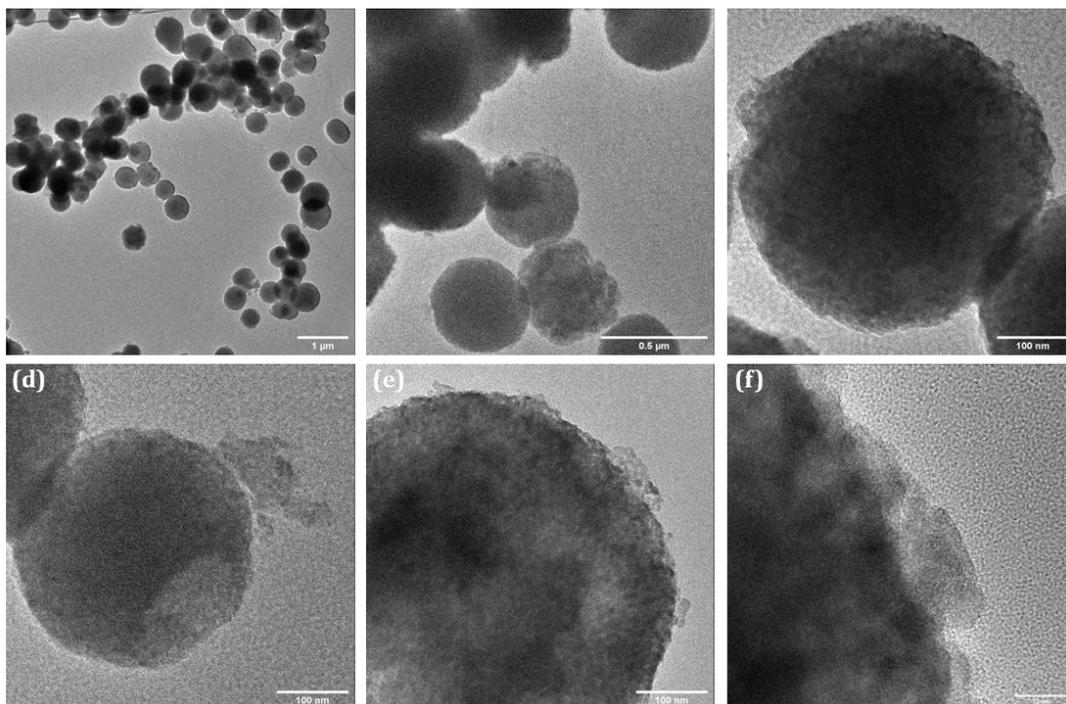
Figure A.6.3. TEM images of TiO$_2$-C$_8$C$_4$E$_4$ showing the formation of spherical particles, approximately 460 nm in diameter. (Figure a-d). The crystallite domains can be seen and are roughly 10 nm in size (Figure e-f)
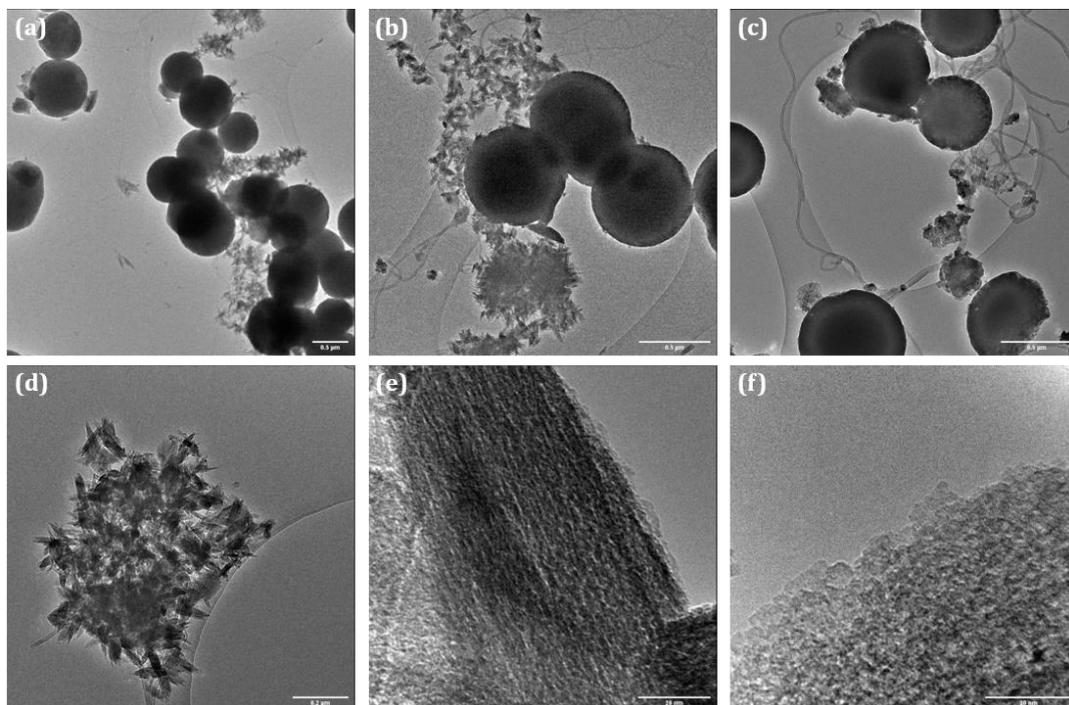
Figure A.6.4. TEM images of TiO$_2$-C$_8$C$_4$E$_4$-UV showing the formation of spherical particles, roughly 650 nm in diameter (Figure a-c). T variety of morphologies can be observed, from flower-like crystals (Figure a, b, d) to long fibrils (Figure c, e). The crystal domains can also be observed and are roughly 12 nm in size (Figure f).
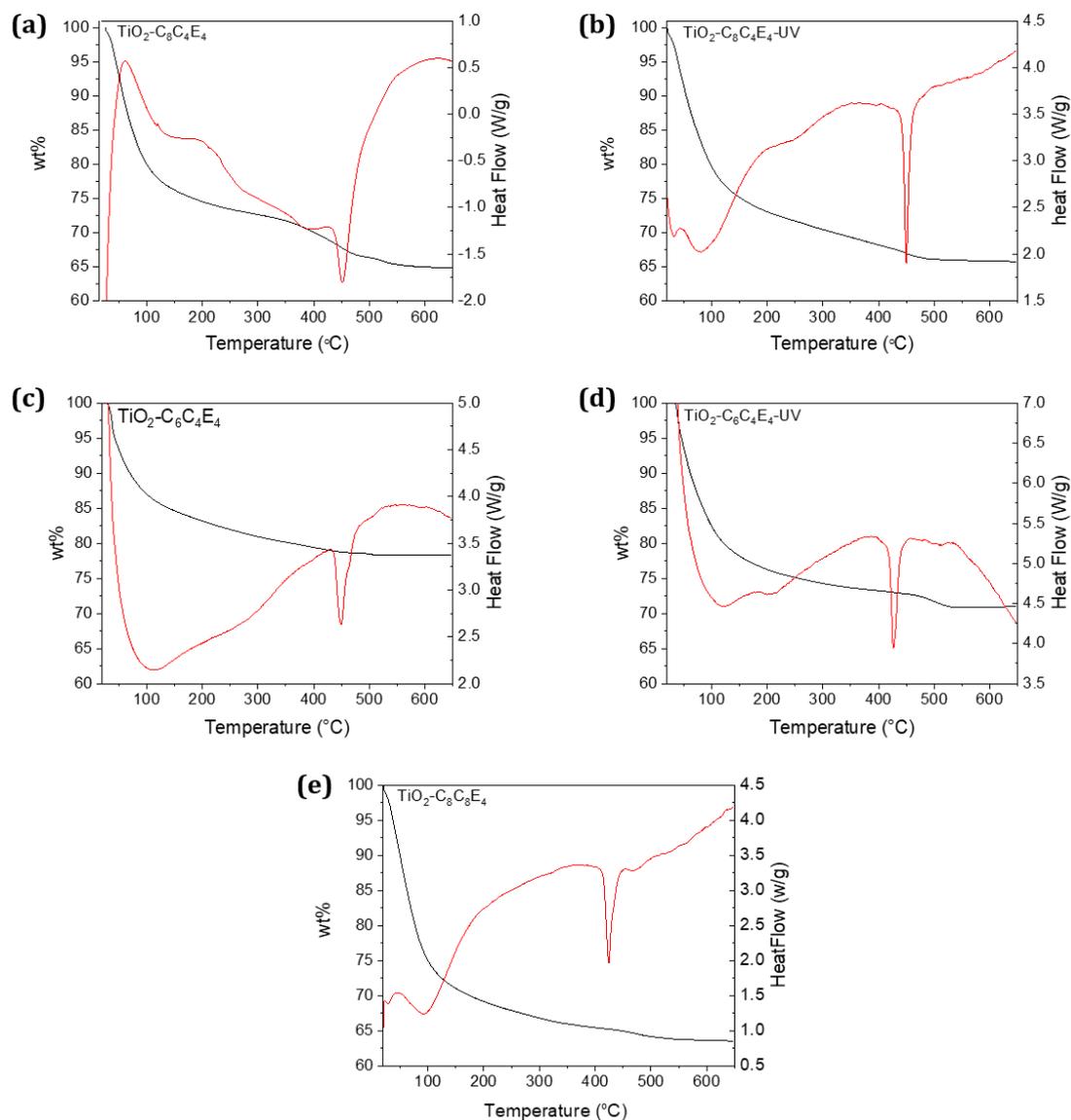
Figure A.6.5. SDT data for titania synthesised using the non-evaporative synthetic method, after the condensation step, before calcination at 450 °C. Heat flow is shown in red with wt% in black.
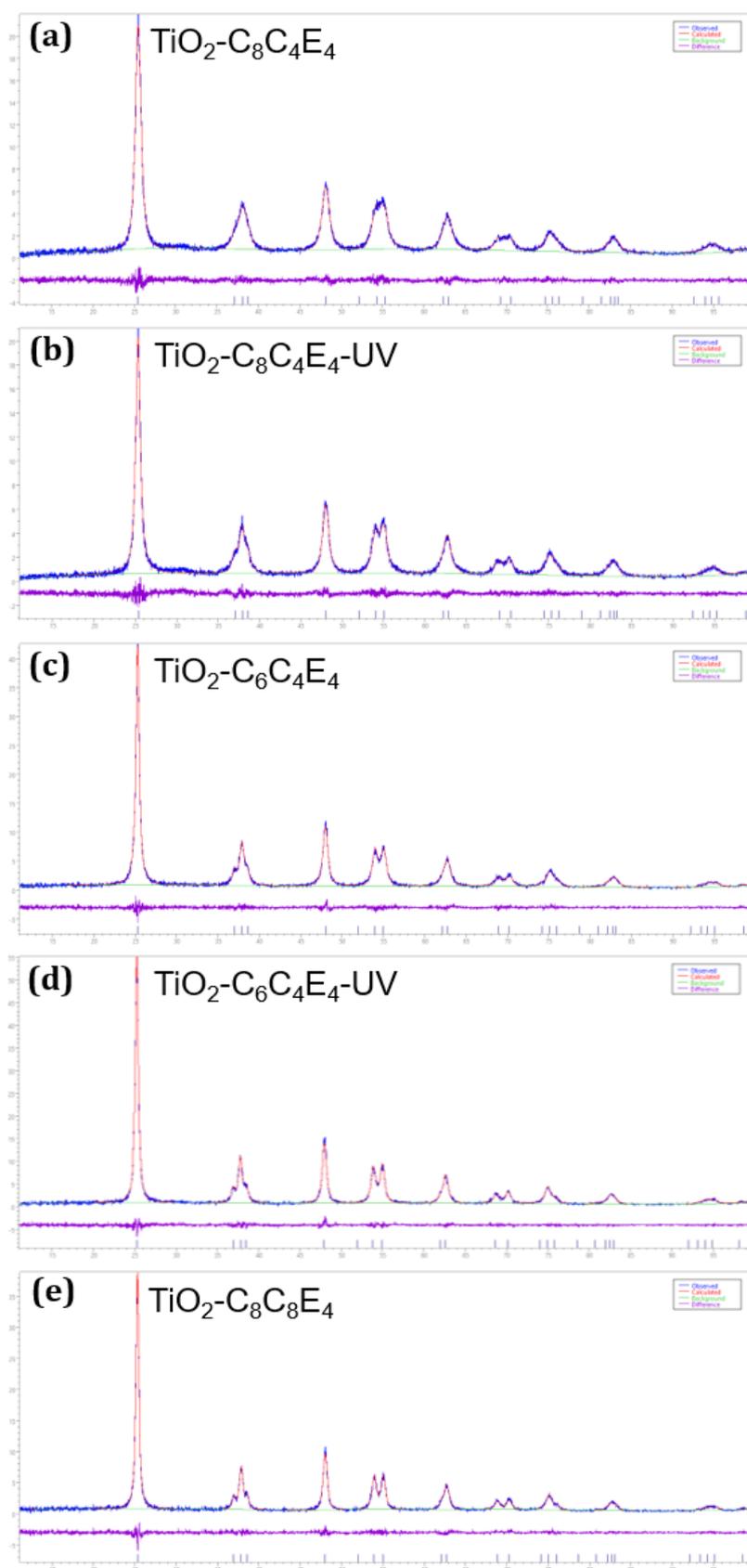
Figure A.6.6. Diffractograms of all five titania samples synthesised with the non-evaporative method after calcination. The measured diffraction pattern (blue) is fitted with the LeBail method[13] and Pearson peak fitting (red) with the background (green) determined using the Chebyshev method.[14] The difference between the fitted and measured data is shown in purple.

Table A.6.1. List of diffraction peak positions (2θ) and their corresponding interplanar distances (d) for each of the five calcined titania samples synthesised with AzoPS using the non-evaporative method.

| Peak	h k l	TiO$_2$-C$_8$C$_4$E$_4$		TiO$_2$-C$_8$C$_4$E$_4$-UV		TiO$_2$-C$_8$C$_8$E$_4$		TiO$_2$-C$_6$C$_4$E$_4$		TiO$_2$-C$_6$C$_4$E$_4$-UV	
		2θ (°)	d (nm)	2θ (°)	d (nm)	2θ (°)	d (nm)	2θ (°)	d (nm)	2θ (°)	d (nm)
1	101	25.40835	3.50259	25.34638	3.51101	25.29772	3.51766	25.29764	3.51767	25.25922	3.52293
2	103	37.06776	2.42329	37.06776	2.42329	36.97054	2.42944	36.99737	2.42774	36.90967	2.43331
3	004	37.96618	2.36799	37.96618	2.36799	37.84339	2.37539	37.89609	2.37220	37.77769	2.37937
4	112	38.64600	2.32788	38.64600	2.32788	38.56417	2.33263	38.57055	2.33226	38.50331	2.33618
5	200	48.09853	1.89016	48.09853	1.89016	48.01194	1.89336	48.00089	1.89377	47.93697	1.89615
6	202	52.05207	1.75551	52.05207	1.75551	51.94641	1.75883	51.94624	1.75883	51.86285	1.76146
7	105	54.10531	1.69363	54.10531	1.69363	53.93976	1.69844	53.99972	1.69670	53.84463	1.70122
8	211	55.13897	1.66430	55.13897	1.66430	55.03505	1.6672	55.02499	1.66748	54.94698	1.66966
9	213	62.23962	1.49040	62.23962	1.49040	62.10062	1.4934	62.10958	1.49320	61.99615	1.49566
10	204	62.85618	1.47725	62.85618	1.47725	62.69893	1.48058	62.72608	1.48000	62.59087	1.48287
11	116	69.03686	1.35931	69.03686	1.35931	68.82047	1.36305	68.89409	1.36177	68.69334	1.36526
12	220	70.38469	1.33654	70.38469	1.33654	70.24790	1.33881	70.23043	1.33910	70.12951	1.34078
13	107	74.40366	1.27398	74.40366	1.27398	74.14693	1.27775	74.24776	1.27627	74.00417	1.27987
14	215	75.27684	1.26136	75.27684	1.26136	75.07165	1.26429	75.11333	1.26370	74.93443	1.26627
15	301	76.14653	1.24910	76.14653	1.24910	75.99238	1.25125	75.97541	1.25149	75.8606	1.25309
16	206	78.94839	1.21165	78.94839	1.21165	78.70974	1.21472	78.77558	1.21387	78.56049	1.21665
17	008	81.17041	1.18399	81.17041	1.18399	80.86494	1.18769	80.99596	1.18610	80.7017	1.18968
18	303	82.32079	1.17034	82.32079	1.17034	82.13173	1.17255	82.13143	1.17256	81.98232	1.17431
19	224	82.87253	1.16394	82.87253	1.16394	82.66667	1.16632	82.68271	1.16613	82.51372	1.16809
20	312	83.29702	1.15908	83.29702	1.15908	83.11588	1.16115	83.10334	1.16129	82.96547	1.16287
21	314	92.40696	1.06716	92.40696	1.06716	92.17034	1.06928	92.18215	1.06918	91.99071	1.0709
22	217	93.62868	1.05642	93.62868	1.05642	93.3166	1.05913	93.40554	1.05836	93.12332	1.06082
23	305	94.47358	1.04919	94.47358	1.04919	94.21007	1.05143	94.24221	1.05116	94.02132	1.05304
24	321	95.31947	1.04210	95.31947	1.04210	95.10456	1.04389	95.07978	1.04410	94.92033	1.04543
25	109	98.88162	1.01388	98.88162	1.01388	98.47903	1.01694	98.64256	1.01570	98.25885	1.01863
26	208	100.29127	1.00339	100.2912	1.00339	99.91936	1.00612	100.0424	1.00522	99.69933	1.00775
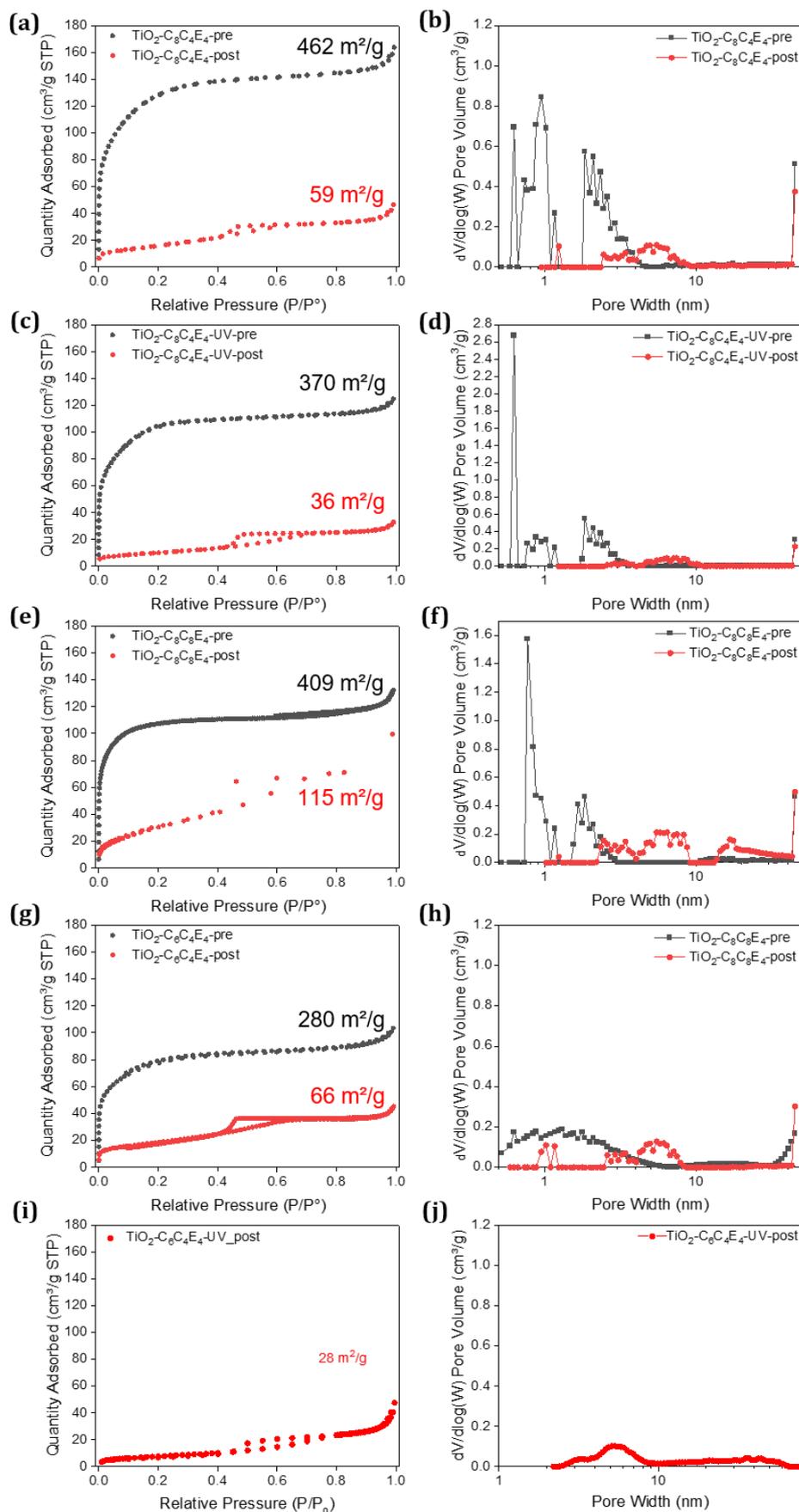
Figure A.6.7. N$_2$ adsorption-desorption isotherms (a, c, e, g) and pore-size distributions (b, d, f, h) before (grey) and after (red) calcination for the five titania samples synthesised using AzoPS with the non-evaporative sol-gel method.
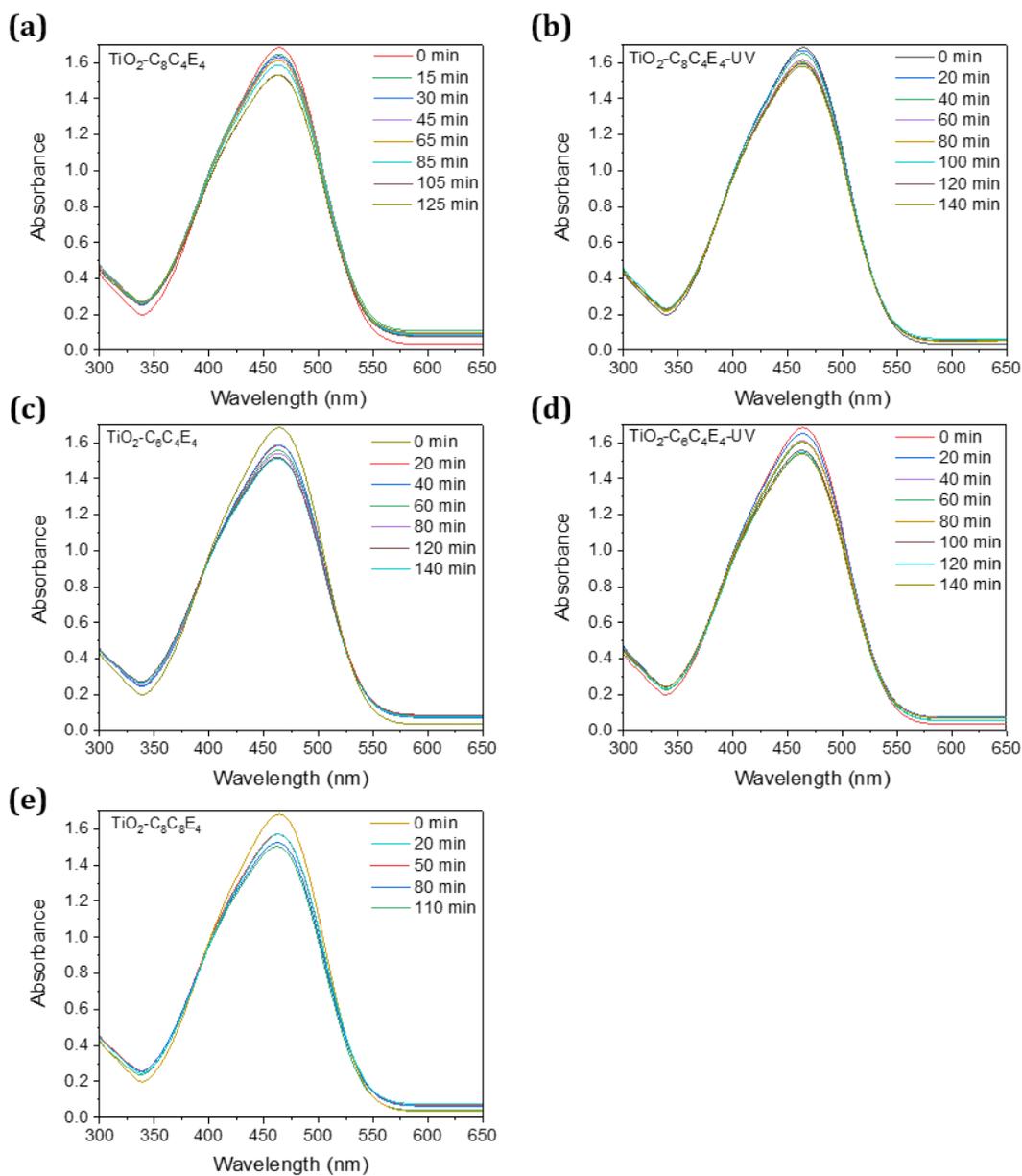
Figure A.6.8. UV-Vis absorption spectra of the various AzoPS used as templating agents for the non-evaporative approach. Aliquots were removed during the photocatalytic process to track the decomposition of methyl orange, evidenced by the decrease in absorbance and blue shift of the peak at 463 nm.
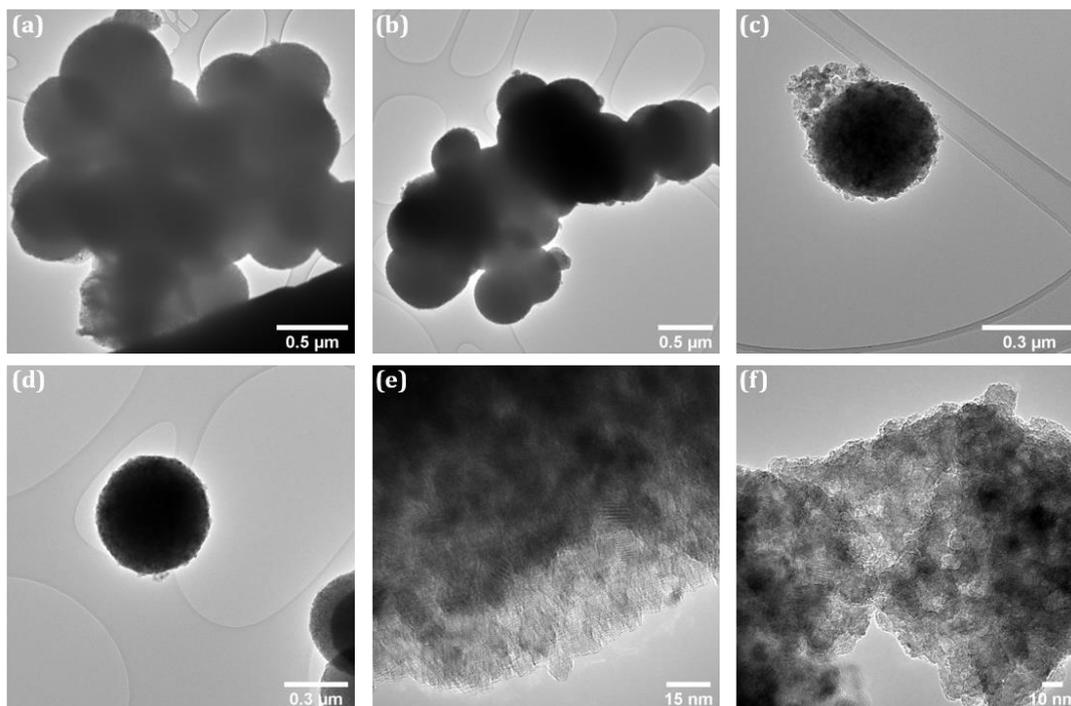
Figure A.6.9. TEM images of EISA-TiO$_2$-C$_8$C$_4$E$_4$ showing the formation of spherical particles, approximately 400-600 nm in diameter. (Figure a-d). The crystallite domains can be seen and are roughly 15 nm in size. (Figure e-f)
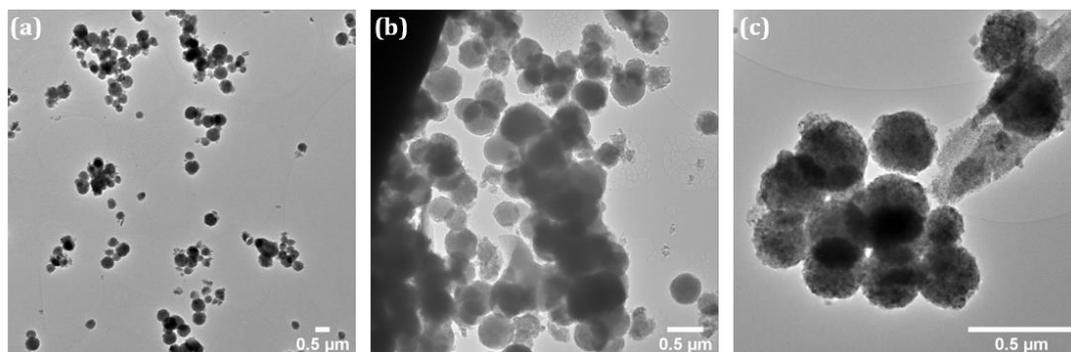

Figure A.6.10. TEM images of UV-EISA-TiO$_2$-C$_8$C$_4$E$_4$ showing the formation of spherical particles, approximately 400-600 nm in diameter. (Figure a-c)
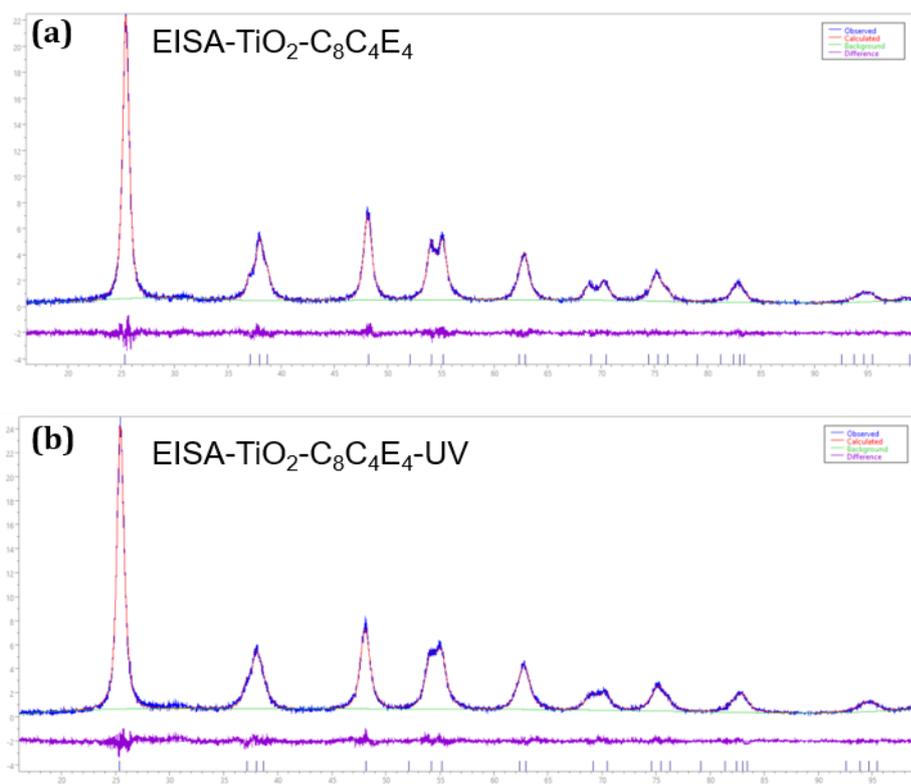
Figure A.6.11. Diffractograms of titania samples synthesised with the EISA method after calcination. The measured diffraction pattern (blue) is fitted with the LeBail method[13] and Pearson peak fitting (red) with the background (green) determined using the Chebyshev method.[14] The difference between the fitted and measured data is shown in purple.

Table A.6.2. List of diffraction peak positions (2θ) and their corresponding interplanar distances (d) for the calcined titania samples synthesised with AzoPS using the EISA method.

Peak	h k l	EISA-TiO$_2$-C$_8$C$_4$E$_4$		EISA-TiO$_2$-C$_8$C$_4$E$_4$-UV	
		2θ (°)	d (nm)	2θ (°)	d (nm)
1	101	25.37955	3.5065	25.38273	3.50607
2	103	37.10289	2.42108	37.13903	2.4188
3	004	37.98887	2.36662	38.05527	2.36265
4	112	38.69427	2.32509	38.70681	2.32436
5	200	48.17015	1.88751	48.16374	1.88775
6	202	52.12409	1.75325	52.131	1.75303
7	105	54.14869	1.69238	54.22602	1.69015
8	211	55.22124	1.66202	55.21709	1.66213
9	213	62.3238	1.48858	62.34304	1.48817
10	204	62.93178	1.47566	62.97235	1.4748
11	116	69.09904	1.35824	69.19498	1.35659
12	220	70.49789	1.33467	70.48777	1.33484
13	107	74.46188	1.27313	74.59063	1.27125
14	215	75.36832	1.26005	75.42819	1.2592
15	301	76.27099	1.24737	76.26257	1.24749
16	206	79.03473	1.21054	79.12358	1.2094
17	008	81.22693	1.18331	81.39243	1.18132
18	303	82.44978	1.16883	82.46216	1.16869
19	224	82.99409	1.16254	83.02569	1.16218
20	312	83.43477	1.15752	83.43304	1.15754
21	314	92.5544	1.06585	92.5834	1.06559
22	217	93.73834	1.05548	93.85791	1.05444
23	305	94.61586	1.04799	94.6692	1.04754
24	321	95.49445	1.04066	95.48145	1.04077
25	109	98.96668	1.01324	99.17516	1.01167
26	208	100.4022	1.00258	100.5637	1.00141
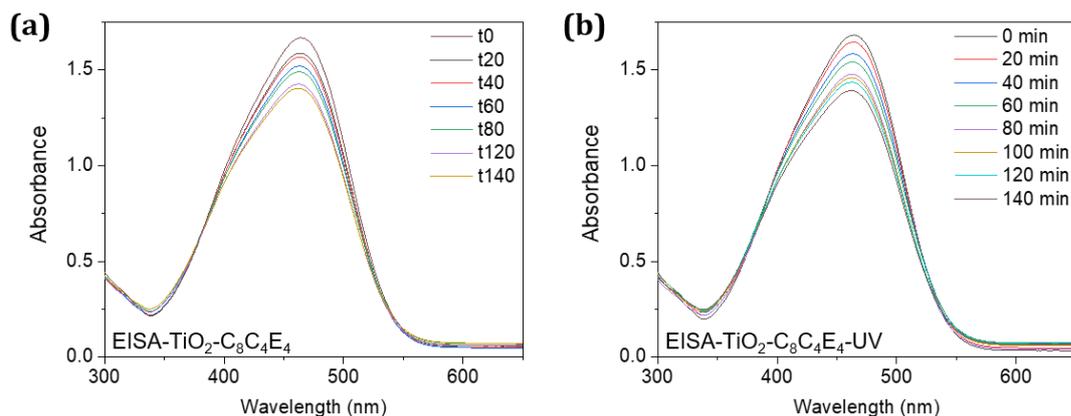
Figure A.6.12. UV-Vis absorption spectra of $C_8AzoOC_4E_4$ used as templating agents for templating titania with the EISA approach. Aliquots were removed during the photocatalytic process to track the decomposition of methyl orange, evidenced by the decrease in absorbance and blue shift of the peak at 463 nm.

Appendix References

(1)   H. Durchschlag and P. Zipper, in Ultracentrifugation, ed. M. D. Lechner, Steinkopff, Darmstadt, 1994, pp. 20-39

(2)   C. Tanford, J. Phys. Chem., 1972, 76, 3020-3024.

(3)   F. Agapito, B. J. C. Cabral and J. A. M. Simões, *Journal of Molecular Structure: THEOCHEM,* 2005, **719**, 109-114.

(4)   R. F. Tabor, R. J. Oakley, J. Eastoe, C. F. J. Faul, I. Grillo and R. K. Heenan, *Soft Matter*, 2009, **5**, 78-80.

(5)   G. S. Kumar and D. C. Neckers, *Chem. Rev.,* 1989, **89**, 1915-1925

(6)   E. Merino and M. Ribagorda, Beilstein *, J. Org. Chem*., 2012, **8**, 1071-1090

(7)   G. C. Hampson and J. M. Robertson, *J. Chem. Soc.* (Resumed), 1941, 409-413

(8)   M. Sato, T. Kinoshita, A. Takizawa and Y. Tsujita, *Macromolecules*, 1988, **21**, 1612-1616

(9)   K. Takeshita, N. Hirota and M. Terazima, *J. Photochem. Photobiol. A: Chem*., 2000, **134**, 103-109

(10)   R. Nagarajan, *Langmuir*, 2002, **18**, 31-38

(11)   M. J. Rosen, A. W. Cohen, M. Dahanayake and X. Y. Hua, *J. Phys. Chem*., 1982, **86**, 541-545

(12)   M. Carvell, D. G. Hall, I. G. Lyle and G. J. T. Tiddy, *Faraday Discuss. Chem. Soc.*, 1986, **81**, 223-237

(13)   Altomare, A.; Cocci, C.; Giacovazzo, C.; Moliterni, A.; Rizzi, R.; Corriero, N.; Falcicchio, A. *J. Appl. Crystallogr.* **2013**, *46* (4), 1231.

(14)   Le Bail, A. *Powder Diffr.* **2004**, *19* (3), 249